EXTRACTION OF THE $^1S_0$ NEUTRON-NEUTRON SCATTERING LENGTH FROM THE REACTION $\pi^- d \to \gamma nn$ USING MONTE-CARLO SIMULATION

by

Qiankun Chen

Department of Physics
Duke University

Date: _____

Approved:

_____
Richard L. Walter, Co-Supervisor

_____
Calvin R. Howell, Co-Supervisor

_____
Seog Oh

_____
Richard G. Palmer

_____
Werner Tornow

Dissertation submitted in partial fulfillment of the
requirements for the degree of Doctor of Philosophy
in the Department of Physics
in the Graduate School of
Duke University

1998

ABSTRACT

(Physics — Nuclear)

EXTRACTION OF THE $^1S_0$ NEUTRON-NEUTRON SCATTERING LENGTH FROM THE REACTION $\pi^- d \to \gamma nn$ USING MONTE-CARLO SIMULATION

by

Qiankun Chen

Department of Physics
Duke University

Date: _____

Approved:

_____
Richard L. Walter, Co-Supervisor

_____
Calvin R. Howell, Co-Supervisor

_____
Seog Oh

_____
Richard G. Palmer

_____
Werner Tornow

An abstract of a dissertation submitted in partial fulfillment of the requirements for the degree of Doctor of Philosophy in the Department of Physics in the Graduate School of Duke University

1998

Abstract

The neutron-neutron scattering length (a_{nn}) has been extracted using the $^2H(\pi^-, n\gamma)n$ data from the Exp1286 project performed at the Los Alamos Meson Physics Facility (LAMPF), Los Alamos National Laboratory. In the experiment, kinematically complete events were recorded. In the case of a "double event", the position and energy of the γ ray were recorded together with the time-of-flight (TOF) and position of one of the two outgoing neutrons from the $^2H(\pi^-, n\gamma)n$ reaction. In the case of a "triple event", the position and energy of a γ ray were measured together with the TOFs and positions of both outgoing neutrons.

To extract the neutron-neutron scattering length (a_{nn}), Monte-Carlo simulation techniques were used to generate γ-position spectra (such as γ_x ,γ_y), opening-angle spectra, γ-energy spectra and neutron TOF spectra that were eventually compared to the corresponding experimental spectra. The inputs to the Monto-Carlo simulation code were the theoretical double-differential cross section of the $\pi^- d \rightarrow nn\gamma$ reaction plus information regarding the interaction between neutrons of various energies and the materials with which they may collide with. The double-differential cross sections are sensitive to a_{nn} and the effective range of neutron-neutron interaction (r_{nn}). Data from $^1H(\pi^-, n)\gamma$ were used to calibrate the TOF spectra and to tune and test the simulation code. The value of a_{nn} was extracted by comparing the experimental TOF spectrum

with the Monte-Carlo simulated TOF spectrum and calculating χ^2 over the TOF region which is sensitive to a_{nn} . This was done for different θ_3 cuts and for different detector types. After taking into account the effects of neutron scattering, finite size of the target and neutron detectors, cross talk between adjacent detectors, and making appropriate corrections, the final result for a_{nn} is found to be -18.50 ± 0.47 fm, where 0.47 fm is the total uncertainty (including statistical, systematic and theoretical uncertainties).

This result is in excellent agreement with two previous determinations of a_{nn} using the same reaction, but different experimental techniques.

Acknowledgements

This project would never have been possible without the assistance of numerous people. My thanks go, first and foremost to my co-advisor Dr. Richard L. Walter. His patience, insight and encouragement were essential for the completion of this work.

Another person without whom this work would never have come to a fruition is my co-advisor Dr. Calvin R. Howell, whose expertise and assistance in all aspects of the project, from data acquisition to data analysis, from hardware to software, from theory to experiment, were indispensable. His help is greatly appreciated.

I am grateful to Dr. Werner Tornow for numerous helpful detailed discussions on the physics aspects of the project, for sharing his expertise on Monte-Carlo simulation, for allowing me to use some of his data files and to convert some of his FORTRAN codes to C codes.

Since I was unable to participate in the data acquisition at the Los Alamos National Laboratory (LANL), I am indebted to the following people for their efforts in data acquisition: C.R. Howell, A.H. Hussein, G. Mertens, C.F. Moore, C.L. Morris, A. Obst, E. Pasyuk, C.D. Roper, F. Salinas, I. Slaus, S.M. Sterbenz, W. Tornow, R.L. Walter, C. Whitley and M. Whitton.

Thanks go to Ben Gibson and W. Gibbs of LANL, who made numerous

calculations of the double differential cross sections for the $^2H(\pi^-, n\gamma)n$ reaction. I thank C. L. Morris of LANL for helping me to clarify some aspects of the experiment, such as the proton beam structure of the LAMPF primary beam and the veto signals.

Fellow graduate students Frank Salinas and Dinko Gonzalez Trotter ran the neutron detector efficiency code from the Physikalisch-Technische Bundesanstalt (PTB) many times so that I could do Monte-Carlo simulations for different conditions. I really appreciate all of their help.

Dr. Ivo Slaus is to be recognized for several discussions about the theoretical aspects of the experiment and the uncertainties concerning the theory.

My thanks extend to Scott T. Carman of Lawrence Livermore National Laboratory (LLNL), who replayed the data using the Q system and generated the data files required by the final data analysis.

Finally, I would like to thank my parents for their support and encouragement through my entire education.

This work is supported in part by U.S. DOE grant No. DEFG05-91-ER40619.

Contents

List of Tables

List of Figures

Chapter 1

Introduction

1.1 N-N Forces and Charge Symmetry

The study of nucleon-nucleon (N-N) forces is a fundamental topic in nuclear physics. The long-range interaction between two nucleons (protons or neutrons) is conceptually based on the exchange of virtual field quanta. In hadron physics, the lightest of these quanta is the pion. The pion plays a special role since it gives rise to the longest range component of the force.

In 1935 Yukawa stressed the analogy between the Coulomb force originating in the exchange of a photon and the nuclear force generated by the exchange of a meson, which he regarded as an elementary particle. Today, we know that unlike photons, mesons are composite particles. However, Yukawa's original idea is still very useful in describing the N-N interaction.

The physics of the N-N interaction can be divided into three major regions:

1. The long-distance region, $r > 2$ fm $= 1.5\ \lambda_\pi$ with λ_π being the pion Compton wavelength, where one-pion exchange dominates and where the quantitative behavior of the potential is well established;

2. The intermediate region, 0.8 fm $< r < 2$ fm, where the dynamical contributions to the potential from two-pion exchange compete with or exceed the one-pion exchange potential;

3. The inner region, $r < 0.8$ fm, which has a complicated dynamics not

readily accessible to a quantitative theoretical description. This region is expected to be influenced by heavy mesons and/or by quark-gluon degrees of freedom. It is often studied using a phenomenological approach.

Charge symmetry is another fundamental topic in physics. If the N-N interaction is charge symmetric, then the neutron-neutron (nn), and proton-proton (pp) interactions should be the same (excluding the Coulomb interaction). Numerous experiments in the past have shown that the N-N interaction is to a large extent charge symmetric. However, there is clear evidence for charge-symmetry breaking (CSB).

The charge independence of nuclear forces is one of the first "internal" (independent of space-time) symmetries that was postulated and examined. It has been generalized to other hadronic interactions of mesons and baryons and has been found to hold quite generally. This symmetry is broken by the electromagnetic and weak interactions.

Nucleon-nucleon scattering experiments and bound-state properties provide the best tools to examine the aforementioned topics. However, since there is no pure neutron target available that is analogous to a pure hydrogen target used in p-p scattering experiments, the best way to investigate the n-n interaction is using reactions which generate two neutrons among their products. The $^2H(\pi^-, n\gamma)n$ reaction is one of the simplest and most practical to interpret among such reactions. Due to the simplicity of this reaction, the neutron-neutron scattering length a_{nn} extracted from this reaction is the most accurate available.

1.2 The Neutron-Neutron Scattering Length

For a n-n system, assume one of the neutrons is at rest in the lab. system and each neutron has energy E_n in their c.m. system; then the incident neutron has energy $E_{lab} = 2E_n$ in the lab system. The corresponding DeBroglie wavelength in the c.m. system is

$$\lambda\!\!\!^{-} = \hbar/p = 6.44/\sqrt{E_{lab}/2}\ , \tag{1.1}$$

where E_{lab} is measured in MeV and $\lambda\!\!\!^{-}$ is given in fm, $\hbar$ is the Planck constant, and p is the neutron's momentum. The angular momentum squared of one nucleon relative to the other is

$$L^2 = l(l+1)\hbar^2\ . \tag{1.2}$$

If the range of the nuclear interaction is r_N (≈ 2.8 fm), then, we must have

$$b \leq r_N \tag{1.3}$$

for the nuclear force to be effective, where b is the impact parameter. The definition of angular momentum is

$$L = p\,b; \quad L = \hbar\sqrt{l(l+1)}\ . \tag{1.4}$$

The first of these two definitions holds in classical mechanics while the second one is valid in quantum mechanics. Thus, from Equations 1.2 and 1.4 we have

$$\sqrt{l(l+1)} \leq r_N/\lambda\!\!\!^{-}\ . \tag{1.5}$$

Using Equation 1.5 we see that, if $r_N < \sqrt{2}\lambda\!\!\!^{-}$ only the $l = 0$ partial wave interacts. From Equation 1.1 with E_{lab} less than 10 MeV, it follows that $\lambda\!\!\!^{-}$ is greater than 2.9 fm, i.e., $r_N/\lambda\!\!\!^{-} \approx 1 < \sqrt{2}$. The radial ${}^1S_0$ wave function $u(r)$ satisfies the following Schrödinger wave equation:

$$\left[\frac{d^2}{dr^2} + k^2 - \frac{2\mu}{\hbar^2}V\right] u(r) = 0\ , \tag{1.6}$$

where μ is the reduced mass of the nucleon-nucleon system and $k = \frac{1}{\lambda} = \frac{\sqrt{2\mu E_n}}{\hbar}$ is the wave number, and V is the potential energy of the system.

As $r \to \infty$, the nuclear potential $V \to 0$, and the Schrödinger Equation 1.6 has the solution

$$u(r) \to v(r) = \frac{\sin kr + \delta}{\sin \delta} = \cos kr + \frac{\sin kr + \delta}{k}(k \cot \delta) \ , \tag{1.7}$$

where δ is called the phase shift. If only the S wave ($l = 0$) contributes to the scattering, then the scattering is isotropic and the total cross section is given by

$$\sigma = 4\pi \sin^2 \delta / k^2 \ . \tag{1.8}$$

When k is very small, we have

$$k \cot \delta \approx -\frac{1}{a} + \frac{1}{2} r_0 k^2 \ , \tag{1.9}$$

where the symbol a is called the scattering length and r_0 is the effective range. The wave function $u(r)$, the effective neutron-neutron interaction range r_{nn} , and the neutron-neutron scattering length a_{nn} are shown in Figure 1.1.

At low energies the cross section reduces to $4\pi a^2$. Note that the scattering length represents the strength of interaction and not its range, as one might expect from its units. Figure 1.1 demonstrates the definition of a_{nn} .

The present status of the nucleon-nucleon scattering lengths is as follows:

1. The accepted value of a_{pp} is -17.3±0.4 fm, obtained from pp scattering [Mil90].

2. The average value of a_{nn} is -16.8±0.4 fm [Mil90] obtained from the $^2H(n, nn)p$ reaction. But a measurement just completed at the Triangle Universities Nuclear Laboratory (TUNL) by D.E. González Trotter reports a value of 18.7 ± 0.6 fm [Gon98].

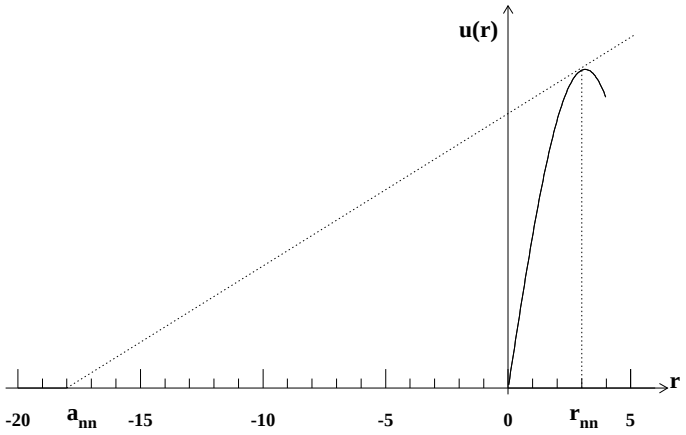

Figure 1.1: The slant dotted line is tangent to the wave function $u(r)$ at $r = r_{nn}$. The symbol r_{nn} stands for the effective range of the nn interaction.

3. Other reactions, such as $^3H(d, 2n)^3He$, $^3H(n, 2n)^2H$, or $^3H(t, 2n)^4He$, give a range for a_{nn} from -16 to -17 fm [Sch87, Sla89]. However, the theoretical methods used in extracting a_{nn} from these reactions are less reliable. In contrast, an exact theory exists for the three-nucleon system and rigorous calculations are possible.

4. So far, the most precise values of a_{nn} , obtained from the $^2H(\pi^-, n\gamma)n$ reaction, are -18.7±0.6 fm [Sch87] and -18.5±0.5 fm [Gab81]. These two results were obtained by the same research team using different methods; the first value was extracted from the time-of-flight (TOF) spectra of neutrons and the second value from a γ-ray energy spectrum. More details will be given about the method for extracting the values of a_{nn} from the $^2H(\pi^-, n\gamma)n$ reaction as the present dissertation proceeds.

Figure 1.2 summarizes the current situation for the experimental determina-

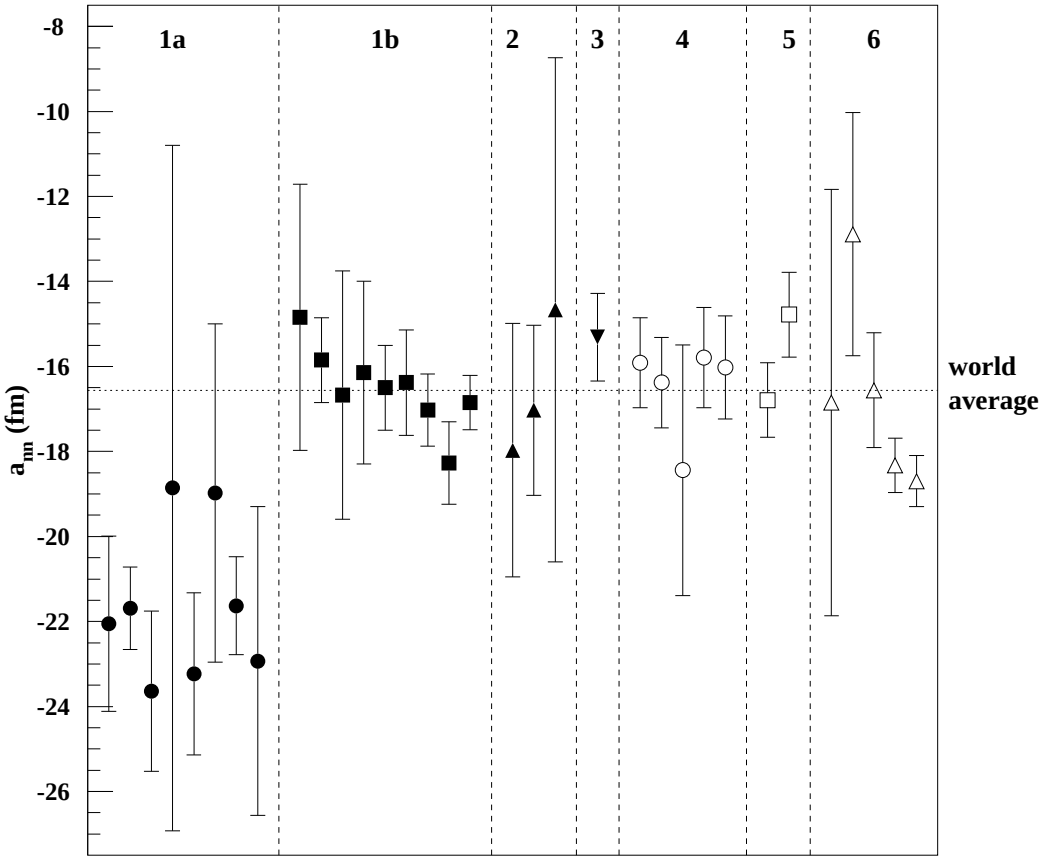

Figure 1.2: Current situation of the values of a_{nn} from different kinds of experiments; for a detailed explanation, see section 1.2.

tions of a_{nn} . The a_{nn} results are displayed for six different types of reactions: 1) $nd \rightarrow pnn$; 2) $nt \rightarrow dnn$; 3) $dd \rightarrow ppnn$; 4) $td \rightarrow {}^3He nn$; 5) $tt \rightarrow \alpha nn$; 6) $\pi^- d \rightarrow nn\gamma$. For each reaction the average a_{nn} can be calculated using

$$\overline{a_{nn}} = \frac{\sum \frac{a_{nn}(i)}{(\triangle a_{nn}(i)\ )^2}}{\sum \frac{1}{(\triangle a_{nn}(i)\ )^2}} \ , \tag{1.10}$$

where $a_{nn}(i)$ is the value obtained by the i^{th} experiment, and $\triangle a_{nn}(i)$ is the corresponding uncertainty. The uncertainty on the average value $\overline{a_{nn}}$ is given by

$$\triangle \overline{a_{nn}} = \sqrt{\frac{1}{\sum \frac{1}{(\triangle a_{nn}(i)\ )^2}}} \ . \tag{1.11}$$

All the data points in Figure 1.2 are taken from [Sla89] and the references mentioned therein. We will use fm as the unit for values of a_{nn} throughout the thesis. The values for reaction 1 are listed in Table 1.1.

Table 1.1: Values of a_{nn} from the reaction $n + d \rightarrow p + n + n$.

i	a_{nn}	$\triangle\ a_{nn}$	a_{nn}	$\triangle\ a_{nn}$
1	-22.05	2.07	-14.84	3.13
2	-21.69	0.97	-15.85	1.00
3	-23.64	1.89	-16.67	2.92
4	-18.86	0.06	-16.14	2.16
5	-23.23	1.92	-16.50	1.00
6	-18.98	3.99	-16.38	1.24
7	-21.63	1.15	-17.03	0.86
8	-22.93	3.63	-18.27	0.97
9			-16.85	0.6496

The left half of Table 1.1 (corresponding to 1a of Figure 1.2) lists values obtained in the kinematically incomplete experiments[1]. The weighted average

[1] In kinematically incomplete experiments, we cannot calculate the momenta of all outgoing particles from the measured quantities.

of these kinematically incomplete experiments yields

$$\overline{a_{nn}} = -22.01 \pm 0.60\,\text{fm} \ . \tag{1.12}$$

However, a reanalysis of some of these experiments using rigorous three-nucleon calculations yields quite a different result (ranging from -12.37 fm to -22.08 fm [Tor96]) for most of the afore mentioned experiments.

The right half of Table 1.1 (corresponding to 1b of Figure 1.2), which is for the kinematically complete experiments[2], and yields a weighted average of

$$\overline{a_{nn}} = -16.81 \pm 0.36\,\text{fm} \ . \tag{1.13}$$

Combining both the kinematically complete and incomplete results for a_{nn} from reaction 1 results in a weighted average of

$$\overline{a_{nn}} = -18.16 \pm 0.31\,\text{fm} \ . \tag{1.14}$$

The results for a_{nn} determined using reaction 2 are tabulated in Table 1.2. The weighted average of these results is

$$\overline{a_{nn}} = -17.12 \pm 1.60\,\text{fm} \ . \tag{1.15}$$

Table 1.2: Values of a_{nn} from reaction $n + t \rightarrow d + n + n$.

i	a_{nn}	$\triangle\ a_{nn}$
1	-17.97	2.98
2	-17.03	2.01
3	-14.67	5.94

For reaction 3 only one experimental measurement exists, which gives

$$\overline{a_{nn}} = -15.31 \pm 1.03\,\text{fm} \ . \tag{1.16}$$

[2]In kinematically complete experiments, we can calculate the momenta for all outgoing particles using conservation rules and the measured quantities.

For reaction 4 the results are tabulated in Table 1.3. The average value of a_{nn} from reaction 4 is

$$\overline{a_{nn}} = -16.12 \pm 0.552\,\mathrm{fm}\ . \tag{1.17}$$

Table 1.3: Values of a_{nn} from reaction $t + d \rightarrow {}^3H_e + n + n$.

i	a_{nn}	$\triangle\ a_{nn}$
1	-15.91	1.06
2	-16.38	1.06
3	-18.44	2.95
4	-15.79	1.18
5	-16.02	1.21

For reaction 5 the results are listed in Table 1.4. The average value of a_{nn} from reaction 5 is

$$\overline{a_{nn}} = -15.91 \pm 0.66\,\mathrm{fm}\ . \tag{1.18}$$

Table 1.4: Values of a_{nn} from reaction $t + t \rightarrow \alpha + n + n$.

i	a_{nn}	$\triangle\ a_{nn}$
1	-16.79	0.89
2	-14.78	1.00

For reaction 6 the results are given in Table 1.5. From the left half of Table 1.5, we have

$$\overline{a_{nn}} = -15.94 \pm 1.19\,\mathrm{fm}\ . \tag{1.19}$$

The overall result from reaction 6 is

$$\overline{a_{nn}} = -18.22 \pm 0.41\,\mathrm{fm}\ . \tag{1.20}$$

We would like to note that the two PSI results have relatively small error bars

Table 1.5: Values of a_{nn} from reaction $\pi^- + d \rightarrow \gamma + n + n$. The left part is from the literature before 1979. The two points on the right side were obtained at the Paul Scherrer Institut (PSI) after 1980. They are all different measurements, except that the two PSI points are from different analyses of the same measurement.

i	a_{nn}	$\triangle a_{nn}$	a_{nn}	$\triangle a_{nn}$
1	-16.85	5.02	-18.33	0.65
2	-12.89	2.864	-18.70	0.60
3	-16.56	1.358		

and therefore dominate the average value of a_{nn} in reaction 6.

Because the true value of a_{nn} is a fundamental parameter in nuclear physics, it is important to determine which of the above values are correct. The purpose of the present project is to establish which of the values in Equations 1.19 and 1.20 is the best determination of a_{nn} from the $^2H(\pi^-, n\gamma)n$ reaction. I would like to mention here that the present project is one of two related TUNL experiments to resolve the a_{nn} puzzle. The other experiment uses the $n + d$ breakup reaction to extract a_{nn} . Fellow graduate student D. Gonzalez Trotter's (now a postdoc fellow) Ph.D. dissertation [Gon98] focuses on the extraction of a_{nn} from the $n + d$ breakup reaction.

1.3 Motivation for the Project

The relative magnitudes of a_{nn} and a_{pp} can determine the magnitude of charge-symmetry breaking and the relative magnitudes of a_{nn} and a_{np} can determine the magnitude of charge-independence[3] breaking in the $^1S_0$ NN interaction. However, measuring these nucleon-nucleon scattering lengths reliably and with high accuracy has turned out to be an elusive experimental task. The neutron-

[3]The charge independence means that the NN interaction is the same for the nn, np or pp interaction.

neutron scattering length a_{nn} is difficult to measure directly because of the lack of a free neutron target. Measurements for studying the proton-proton scattering length a_{pp} are relatively easy, but the determination of the nuclear part of the scattering length is still somewhat model dependent because of the presence of the Coulomb force [Ban64, Gab79, Gla85, Hol85, Mil90, Tor96, Wat51, Wil72].

The most common way to measure a_{nn} is through nuclear reactions which produce three particles in the final state, at least two of which are neutrons. Each of the final state particles will have a range of momenta. The way in which the three particles share the total momentum is sensitive to the interaction between the neutrons [McV61].

The $^2H(n,nn)p$ is the reaction that has been most frequently used to measure a_{nn} . In this reaction there are three strongly interacting particles in the final state. However, the problem with this type of determination of a_{nn} is that the proton may affect the final-state interaction between the two neutrons and thus may complicate the theoretical interpretation of the experimental data [Wil72].

Twenty-five years ago Wilkinson [Wil72] proposed that it be a high priority for LAMPF (Los Alamos Meson Physics Facility) and other meson factories to use the $^2H(\pi^-,n\gamma)n$ reaction to measure a_{nn} . He considered this way to be a powerful approach because the $^2H(\pi^-,n\gamma)n$ reaction has only two strongly interacting particles in the final state. It is important to note that the theoretical interpretation of this reaction is much more reliable than that of the reactions with three strongly interacting particles in the final state in which the existence of a three-nucleon force is possible. Although all three outgoing

"particles" can be detected in the $^2H(\pi^-, n\gamma)n$ reaction, the counting rate is quite low for this triple coincidence measurement; usually only two "particles" are detected. However, the measurements of the momenta of two outgoing particles completely determines the momentum of the third "particle".

The energy distribution of the neutrons can be obtained via the measurement of a neutron time-of-flight (NTOF) spectrum by the following equation

$$t = 72.25l/\sqrt{E_n} \ , \tag{1.21}$$

where t is the time of flight measured in ns for a neutron over a flight path of length l measured in m, and E_n is the neutron energy in the lab system measured in MeV. For the $^2H(\pi^-, n\gamma)n$ reaction the neutron time-of-flight (NTOF) spectrum has two peaks as shown in Figure 1.3. An offset is added to the time of flight for the purpose of background subtraction and the spectrum reflects the neutron time of flight from the target to the detector. The left peak in Figure 1.3 is in the region where the relative kinetic energy between the two neutrons is high. This is the domain of quasi-free scattering (QFS), where the neutron in the deuteron acts as a spectator and gains almost no kinematic energy, and the proton in the deuteron nucleus absorbs the pion and generates a neutron and a γ ray. As a result, the energy of this neutron is similar to that in the $^1H(\pi^-, n)\gamma$ reaction. This QFS peak slowly falls off toward the region of low relative kinetic energies (longer time of flight). However, when the relative energy of the two neutrons becomes very small, the final state interaction (FSI) becomes important and is seen as a second peak in Figure 1.3. In the FSI region, the outgoing neutrons interact with each other more strongly than elsewhere in the NTOF spectrum, as one would expect from the relative closeness of the two trajectories.

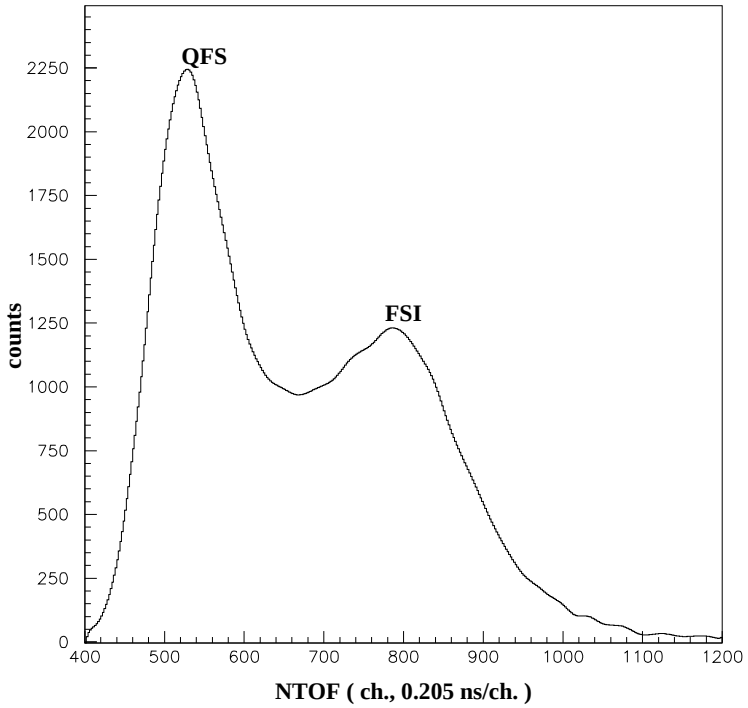

Figure 1.3: This NTOF spectrum demonstrates the QFS peak and the FSI peak. Time increases from left to right.

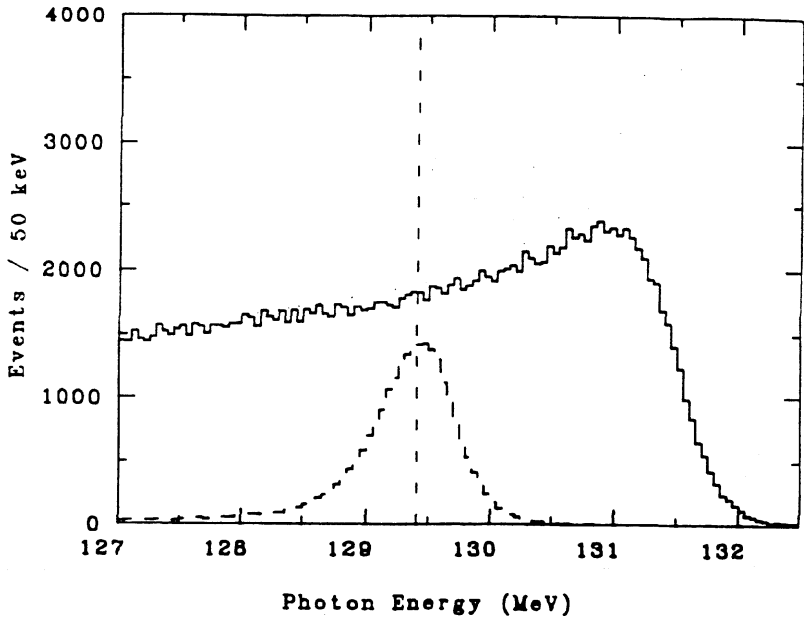

Figure 1.4: Photon-energy spectrum from π^- capture in ^1H and ^2H. The solid line is for π^- capture in ^2H, while the dashed line is for π^- capture in ^1H. A γ-ray energy resolution of about 0.5 MeV is required to observe such a spectrum. Scanned from [Hus92].

The upper end of the γ-ray energy spectrum for the $^2H(\pi^-, n\gamma)n$ reaction is shown as the solid curve in Figure 1.4. The energy of γ rays associated with neutrons in the QFS peak of Figure 1.3 is smaller than that of the γ rays associated with the neutrons in the FSI peak. The γ rays corresponding to the FSI region dominate, and the spectral region around the maximum photon energy shows an enhancement. The dashed curve in Figure 1.4 is the γ-ray energy spectrum for the $^1H(\pi^-, n)\gamma$ reaction. There is further discussion about the spectral shape below.

Early theoretical work of McVoy and Watson [McV61, Wat51] for the $^2H(\pi^-, n\gamma)n$ reaction showed that the neutron and γ-ray spectra are sensitive to the values of a_{nn} and the effective range r_{nn} of the neutron-neutron

interaction. In particular, the shape and height of the FSI peak in the neutron spectrum are sensitive to the value of a_{nn}. The shape of the FSI peak in the γ-ray spectrum is also sensitive to the value of a_{nn}, while the slope of the lower energy (approximately between 125 MeV and 130 MeV) part of the γ-ray spectrum is sensitive to r_{nn}.

Bander [Ban64] improved the earlier calculations of McVoy and Watson for the $^2H(\pi^-, n\gamma)n$ reaction and placed an estimate of 1 fm on the theoretical uncertainty of the a_{nn} determination. Further reduction in the theoretical uncertainty in a_{nn} has been achieved by several authors (for example, according to [Gib75b, Gib75a, Gib77], the theoretical uncertainty could be as small as 0.3 fm).

The summary of a_{nn} values in section 1.2 reveals sizable differences among the values of a_{nn} measured by $^2H(\pi^-, n\gamma)n$ experiments. One value is close to that measured in the $^2H(n, nn)p$ reaction in the kinematically complete experiments, and the other is larger by about 2 fm. If the latter result is confirmed by subsequent $\pi^- + d$ measurements, it might be a strong indication for the influence of a three-body force [Sla82]. Therefore, it is important to remeasure the value of a_{nn} from the $^2H(\pi^-, n\gamma)n$ reaction and to eliminate some of the confusion surrounding the determination of a_{nn}.

For the $^2H(\pi^-, n\gamma)n$ reaction the final state contains three particles: a γ ray and two neutrons. Because of this the γ-ray spectrum is not monochromatic. If there were only the γ-ray and one particle (say, a bound di-neutron) in the final state, the γ-ray spectrum would be monochromatic. If the two neutrons in the final state are not actually bound, but interact through an attractive potential, we can expect a tendency for them to recoil in the same direction with about

equal velocities, effectively acting like a single particle, and thus cause the γ-ray spectrum to be much more monochromatic than if there were no attractive n-n force. In other words, the effect of an attractive n-n interaction should be such as to make the γ-ray energy spectrum of Figure 1.4 show a pronounced peak near the high energy limit.

In the experiment we see a pronounced FSI peak in the TOF spectrum shown in Figure 1.3 and, as stated above, the peak shape and height are sensitive to a_{nn}. However, we can not directly calculate or extract a_{nn} from the experimental spectra alone. We must use a Monte-Carlo (MC) approach to simulate the experiment, taking into account all the factors that influence the shape of the spectrum, such as the geometrical arrangement of the target and detectors and multiple scattering. This folding process is necessary even if we were to attempt to unfold the spectrum (which we believe is impossible to do with significant accuracy). We would still need to do this through the reliance on theoretical calculations for particular points in the deuterium target and in the γ-ray and neutron detector, since the theory only provides information for the case of point geometry and no multiple scattering.

Hence, the main purposes of the Monte-Carlo simulation are:

1. to make corrections for γ-ray and neutron scattering and flux attenuation in the target system [4],

2. to account for the angular spread, i.e., the physical size of the neutron detectors,

3. to account for the energy-dependent efficiencies of the neutron detectors,

[4]Unless otherwise indicated, "target system" refers to both the deuterium or hydrogen liquid and the stainless-steel container. The latter is also referred to as the cryostat.

and

4. to determine a_{nn} by comparing the data with MC simulated spectra based on various N-N interactions.

In summary, with the MC code we use theoretical models of the n-n interaction and generate simulated spectra which are then compared with the actual measured spectra. By varying a_{nn} in the MC simulation, we can see how the match-up between simulated spectra and experimental spectra change and we can thus localize the range of permissible values.

In the discussion to follow, we will use the term "stopped π^-" to represent a π^- that has been slowed down in matter to the point where it is captured into an atomic orbit, i.e., to where it forms a mesonic atom. For such π^- atoms, the π^- will drop to states having a low principal quantum number n. In this case, the kinetic energy of the π^- is around 0.1 MeV (n=2). This kinetic energy is available in the $\pi^- + p$ or $\pi^- + d$ capture reaction and technically should be included in the kinematic relation. However, this energy is small relative to the Q-value of the π^- capture ($\sim$ 135 MeV) and can be neglected for the calculations and comparisons in the present discussion.

One may ask why pions should be used as probes instead of neutrons and protons, since all these particles interact according to the strong force? Part of the answer is that it is often difficult to sort out the properties of the probe particle from the properties of that which is being probed. For this reason it is important to use as many different types of probes as possible. Also, although pions and nucleons are all strongly interacting particles, they have different spins, different charge states, different mass and different momenta for a given energy. In addition, a stopped pion liberates about 140 MeV of energy upon

being captured without the introduction of angular momentum.

1.4 Brief Introduction to Exp1286

Experiment Exp1286 was performed in the summer of 1993 at the Los Alamos Meson Physics Facility (LAMPF). It was a measurement of the ${}^2H(\pi^-, n\gamma)n$ reaction. Pions were produced by bombarding a deuterium target with an 800 MeV proton beam. The reactions involved are the combination of the ${}^2H(p, n)pp$ reaction, the $H(n, \pi^-)pp$ reaction or the ${}^2H(p, \pi^-)ppp$ reaction. The beam intensity was about 1 mA, composed of 100 ps micro-pulses every 5 ns in macro-pulses of about 600 μs duration and frequency of 120 Hz.

The pions produced in the primary deuterium target were subsequently focussed and then slowed down by a beryllium slab in front of the liquid hydrogen or the deuterium target. The beryllium slab thickness was adjusted such that the reaction yield for ${}^2H(\pi^-, n\gamma)n$ was maximized.

Liquid scintillators were used for the neutron detectors because of their excellent timing resolution, and because of their pulse-shape characteristics which allows discrimination between neutron induced events and γ-ray induced events. The neutron detectors were arranged in such a way as to reduce cross talk between neutron detectors, to provide a strong sensitivity to different values of a_{nn} and to provide a good counting rate for a_{nn} events. Details of the experiment will be discussed in the next chapter.

1.5 Exit Channels for $\pi^- p$ and $\pi^- d$ Capture

1.5.1 The π^- Capture in Hydrogen

As mentioned earlier, measurements were done for π^- capture on both the hydrogen target and the deuterium target. There are two reactions for stopped π^- on protons:

$$\pi^- p \rightarrow n\gamma \ , \tag{1.22}$$

and

$$\pi^- p \rightarrow n\pi^0 \ . \tag{1.23}$$

The π^0 has a mean life of $(0.83 \pm 0.06\ ) \times 10^{-16}$ seconds. It will decay into two photons with a branching ratio of 98.8 %, to one photon, and a e^+e^- pair with a branching ratio of 1.17 %, to an e^+e^- pair with a branching ratio of 2×10^{-5} %.

The total energy released in the processes described by Equations 1.22 and 1.23 is

$$Q = m_\pi c^2 - \triangle = 139.5752 - 1.2935 = 138.2817 \text{ MeV} \ , \tag{1.24}$$

where $\triangle$ is the difference between the rest energies of the neutron and the proton.

In the reaction described by Equation 1.22, define E_γ as the energy of the photon, E_n the kinetic energy of the neutron, and m_n the mass of the neutron. Conservation of energy and momentum gives:

$$\frac{E_\gamma}{c} = \sqrt{2\, m_n\, E_n} \ ; \quad E_\gamma + E_n = Q \ . \tag{1.25}$$

Solving the above two equations yields:

$$E_\gamma = 129.376 \text{ MeV}, \text{ and } E_n = 8.907 \text{ MeV} \ . \tag{1.26}$$

Therefore, for 98.8% of the $\pi^- p$ capture reactions, monochromatic photons are produced from a stopped π^- beam.

For the reaction described by Equation 1.23, we define δ to be the mass difference between the π^- and π^0,

$$\delta = m_{\pi^-} - m_{\pi^0} = 139.5752 - 134.9739 = 4.6013\,\mathrm{MeV}\ . \tag{1.27}$$

Since $\delta > \triangle$, the π^0 mesons are produced with a kinematic energy E_0 described by the equations

$$E_0 + E_n = \delta - \triangle = 3.3078\,\mathrm{MeV} \tag{1.28}$$

and

$$\sqrt{2\,m_n\,E_n} = \sqrt{2\,m_0\,E_0}\ , \tag{1.29}$$

where m_0 is the mass of the π^0. Combining Equations 1.28 and 1.29 gives

$$E_0 = \frac{\delta - \triangle}{1 + m_0/m_n} = 2.892\,\mathrm{MeV}\ . \tag{1.30}$$

Using some algebra one obtains the minimum and the maximum energies of the photons for this process:

$$E_{\gamma_{min}} = \frac{m_0c^2 + E_0}{2} - \sqrt{\frac{E_0 m_0 c^2}{2}} = 54.96\,\mathrm{MeV}\ , \tag{1.31}$$

$$E_{\gamma_{max}} = \frac{m_0c^2 + E_0}{2} + \sqrt{\frac{E_0 m_0 c^2}{2}} = 82.90\ \mathrm{MeV}\ . \tag{1.32}$$

The energy spectrum of the photons is flat between the two limits $E_{\gamma_{min}}$ and $E_{\gamma_{max}}$.

1.5.2 The π^- Capture in Deuterium

For the capture of π^- on d, the possible exit channels are

$$\pi^- d \rightarrow nn\gamma\ , \tag{1.33}$$

$$\pi^- d \rightarrow nn\pi_0 \rightarrow nn\gamma\gamma \ , \tag{1.34}$$

and

$$\pi^- d \rightarrow nn \ . \tag{1.35}$$

Since the γ-ray spectrum does not exhibit a secondary maximum at about $m_\pi c^2/2$, one can conclude that the reaction (1.34) either does not occur or that it has a much smaller branching ratio than the reaction (1.33). Also, comparison between the γ-ray intensities observed with hydrogen and with deuterium indicates that only about 30 % of the capture processes occur via Equation 1.33. The remaining 70 % of the events do not generate γ-rays and correspond to the reaction shown in Equation 1.35.

1.6 Brief Introduction to Extracting a_{nn}

The way we extract a_{nn} is by comparing the experimental Neutron Time-Of-Flight (NTOF) spectra with the spectra obtained by a Monte-Carlo simulation that includes a theoretical N-N calculation. Different values of a_{nn} result in different simulated NTOF spectra. If we normalize these simulated NTOF spectra so that they have the same area (total counts) in the QFS peak area as the experimental spectrum, then the shapes in the region of the FSI peak are sensitive to the values of a_{nn}, as demonstrated in Figure 3.4. We then calculate the total χ^2 (which for our purposes is independent of the size of the chosen "bins") for the NTOF region around the FSI peak and we plot χ^2 vs. a_{nn}. The a_{nn} that corresponds to the minimum χ^2 (χ^2_{min}) is the a_{nn} value extracted from this experiment, and we label it as a_{nn0}. Since the χ^2 vs. a_{nn} curve is usually of parabolic shape, we determine two values of a_{nn} that correspond to (χ^2_{min} +

1), and are one standard deviation away from a_{nn0}. We will call these values the upper and lower limits of a_{nn}. Since the NTOF spectrum changes when different opening-angle cuts are applied(the opening angle is the angle between the γ direction and the neutron direction), we extract a_{nn} using a variety of opening-angle cuts. If the method is proper, these a_{nn} values should agree with each other within the assigned standard deviation. After we determine the a_{nn} value and the corresponding uncertainty for each opening-angle cut, we calculate the weighted average and assign a standard deviation on a_{nn}. For the final value of our measured a_{nn}, we will also assign a systematic uncertainty.

For convenience in later discussions, we use θ_3 to refer to the supplemental angle to the opening angle between the γ ray and neutrons.

1.7 Introduction to the Following Chapters

In Chapter 2 we present a detailed description of the experiment covering beam production, detectors, electronics, triggers and data acquisition. In Chapter 3 we describe the associated theory on how to extract a_{nn} from the NTOF spectrum for the reaction $\pi^- d \rightarrow nn\gamma$. In Chapter 4 we give a detailed description of the development of the Monte-Carlo simulation code. In Chapter 5 we report how the data analysis was performed and in Chapter 6 the final results from Exp1286 are reported.

Chapter 2

The Experiment

We start this chapter with a description of the experimental facility. Then we give some details about our experimental setup, from neutron detectors, γ-ray detector, trigger circuit, to data-acquisition system. We also present some experimental spectra obtained with the $^1H(\pi^-, n)\gamma$ reaction and the $^2H(\pi^-, n\gamma)n$ reaction.

2.1 Experimental Setup

In this section, we will give a brief introduction to the Los Alamos Meson Physics Facility and a detailed description of the experimental setup.

2.1.1 The Los Alamos Meson Physics Facility

As mentioned in Chapter 1, our experiment was performed at the Los Alamos Meson Physics Facility (LAMPF, also called the Clinton P. Anderson Meson Physics Facility in honor of the senator) in 1993. The layout of the facility is shown in Figure 2.1.

The LAMPF proton linear accelerator (linac) has high current capability, variable energy, good beam quality, no extraction loss, and low loss of internal beam. The design of the linac is described in much greater detail in [Ros69]. The linac can accelerate protons to energies between 212 and 800 MeV. From the injector, the proton beam enters the drift-tube linac and then the high-

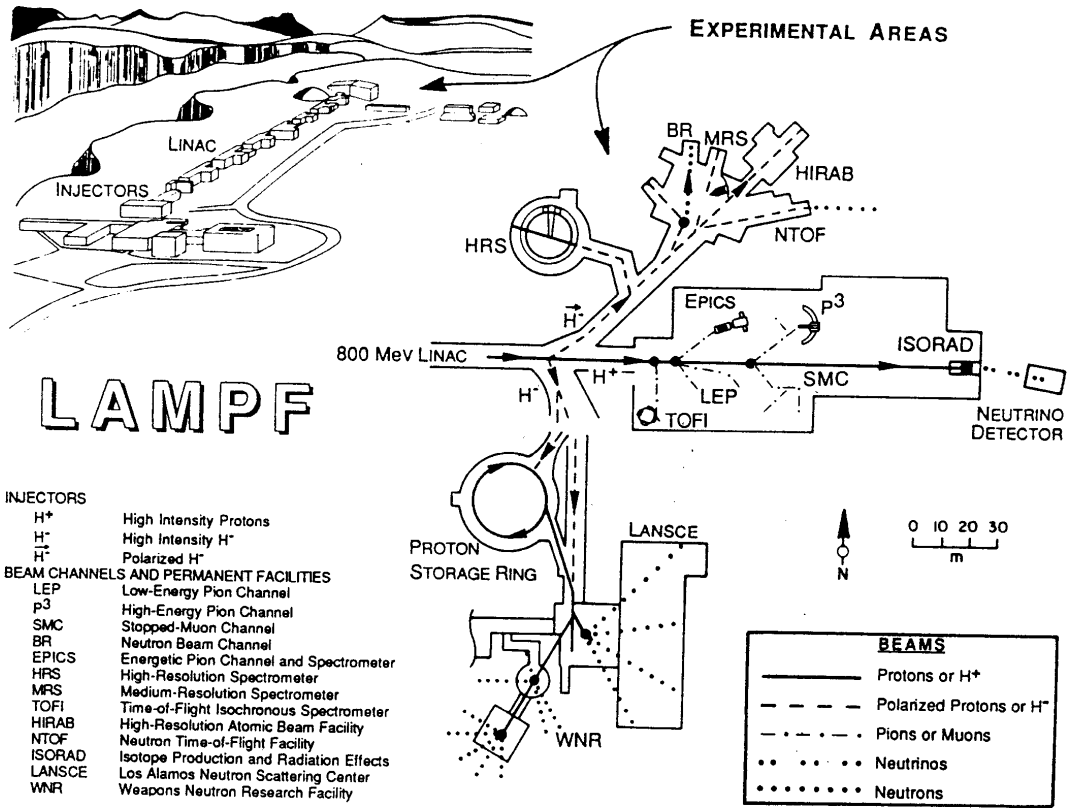

Figure 2.1: The experimental areas at LAMPF, scanned from [Eri91].

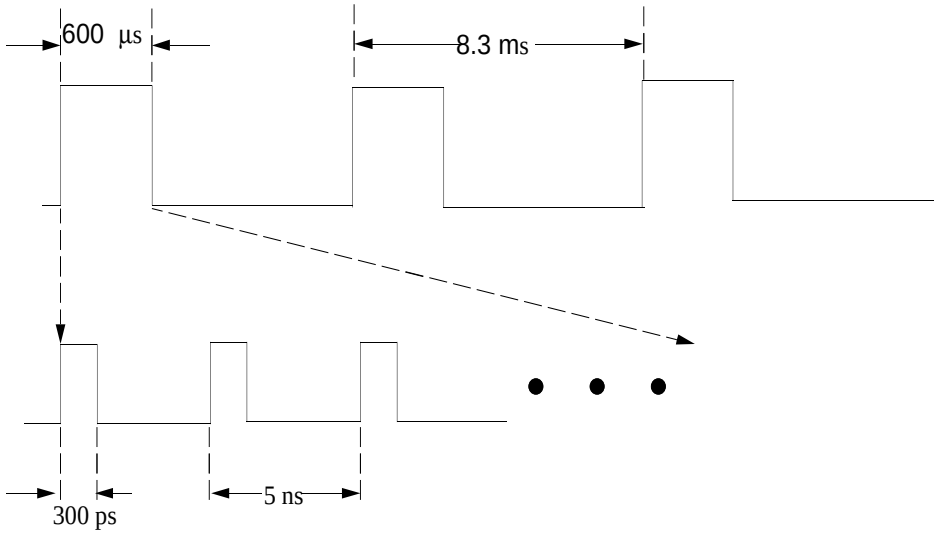

Figure 2.2: The structure of the proton beam used in Exp1286.

energy linac consisting of side-coupled resonant cavities. The accelerated protons can then be transported into three experimental areas. In our case the beam was switched to the meson area. In the meson area the proton beam traverses two or three targets to provide the pions and muons for the various experimental programs. Exp1286 used negative pions. A great advantage of the linac is the complete separation of the target region from the accelerator. This permits a separation of background radiation problems associated with each area. Typical target problems are in some respects similar to those found in reactor technology: radiation damage and disposal of radioactive materials, remote manipulation, heat transfer, corrosion, etc. Beyond the target area, the problems become ones of transport, purification, monitoring, detection, analysis, and focusing of secondary and tertiary beams. In Exp1286 the proton beam time structure is shown in Figure 2.2. A schematic view of the low-energy pion channel spectrometer is shown in Figure 2.3 [Ful73]. Pions of energy 48 MeV are produced in a rotating-wheel target by 800 MeV protons.

For our $\pi^- d$ or $\pi^- p$ capture experiment, it was important to stop the pions in the hydrogen or deuteron target. Therefore, it was necessary to slow the pions down prior to the target. In Exp1286, as shown in Figure 2.4, the pions were first slowed down from 48 MeV to about 20 MeV by a 4.45 cm thick beryllium block placed directly in front of the wall of the target chamber. The pion energies were further reduces to about 10 MeV by the 0.32 cm thick iron wall of the liquid target container. Finally, the pions were brought to a stop in the liquid hydrogen or the liquid deuterium and captured by a proton or deuteron. At this stage the ${}^1H(\pi^-, n)\gamma$ reaction or ${}^2H(\pi^-, n\gamma)n$ reaction could occur.

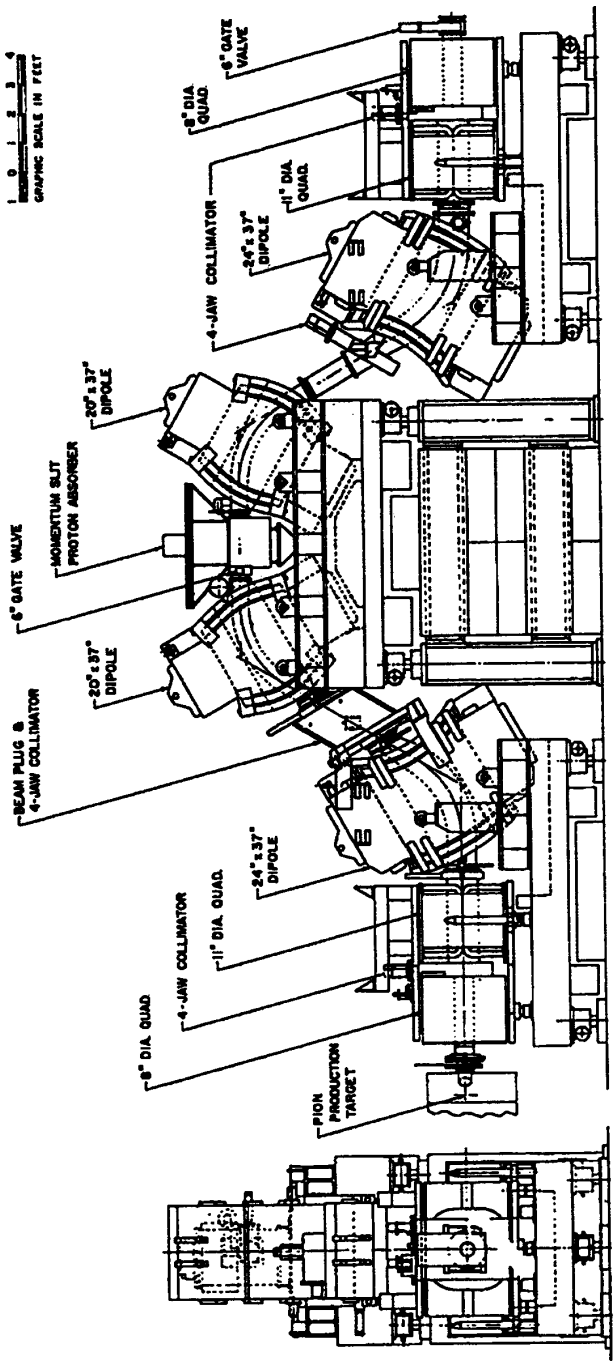

Figure 2.3: Front and side view of LAMPF low-energy pion channel. Height of beam centerline at entrance and exit is 5'0". Scanned from [Ful73].

2.1.2 Experimental Setup

The layout of the experimental setup is shown in Figure 2.4. The origin of our coordinate system is defined as the geometric center of the target chamber. It is possible that the center of the target chamber differs slightly from the center of the target itself due to misalignment. The z-direction was chosen to be along the path of the π^- beam, the y-direction is horizontal and perpendicular to the z-direction as shown in Figure 2.4 and the x-direction pointed vertically up. Veto paddles were placed in front of the neutron detectors and γ-ray detectors. They were made from plastic scintillators and were about 0.6 cm thick. In Exp1286, the events generated by charged particles were rejected by using the veto paddles.

2.1.3 The Target

There were two target sizes available for the target chamber used in Exp1286: the smaller one is 1.32" in diameter and 3" in height, the larger one is 2.36" in diameter and 4" in height. In order to maintain high enough counting rates, the larger one was used. The details of the target chamber are shown in Figure 2.5. Since we were using liquid hydrogen and liquid deuterium in the experiment, and hazards arise from cryogenic liquids, one must be careful when dealing with the target system and when being in the vicinity of the target. Reference [Nov93] says: "$\cdots$ hydrogen (or deuterium) gas is combustible over a wide range of mixtures in air (4 to 75%), and detonates when burned with air in confined spaces, particularly pipes. The key points of safe hydrogen (or deuterium) handling are: (1) be sure the entire hydrogen system is leak tight at the beginning, (2) make sure the system stays leak tight, (3) vent all hydrogen

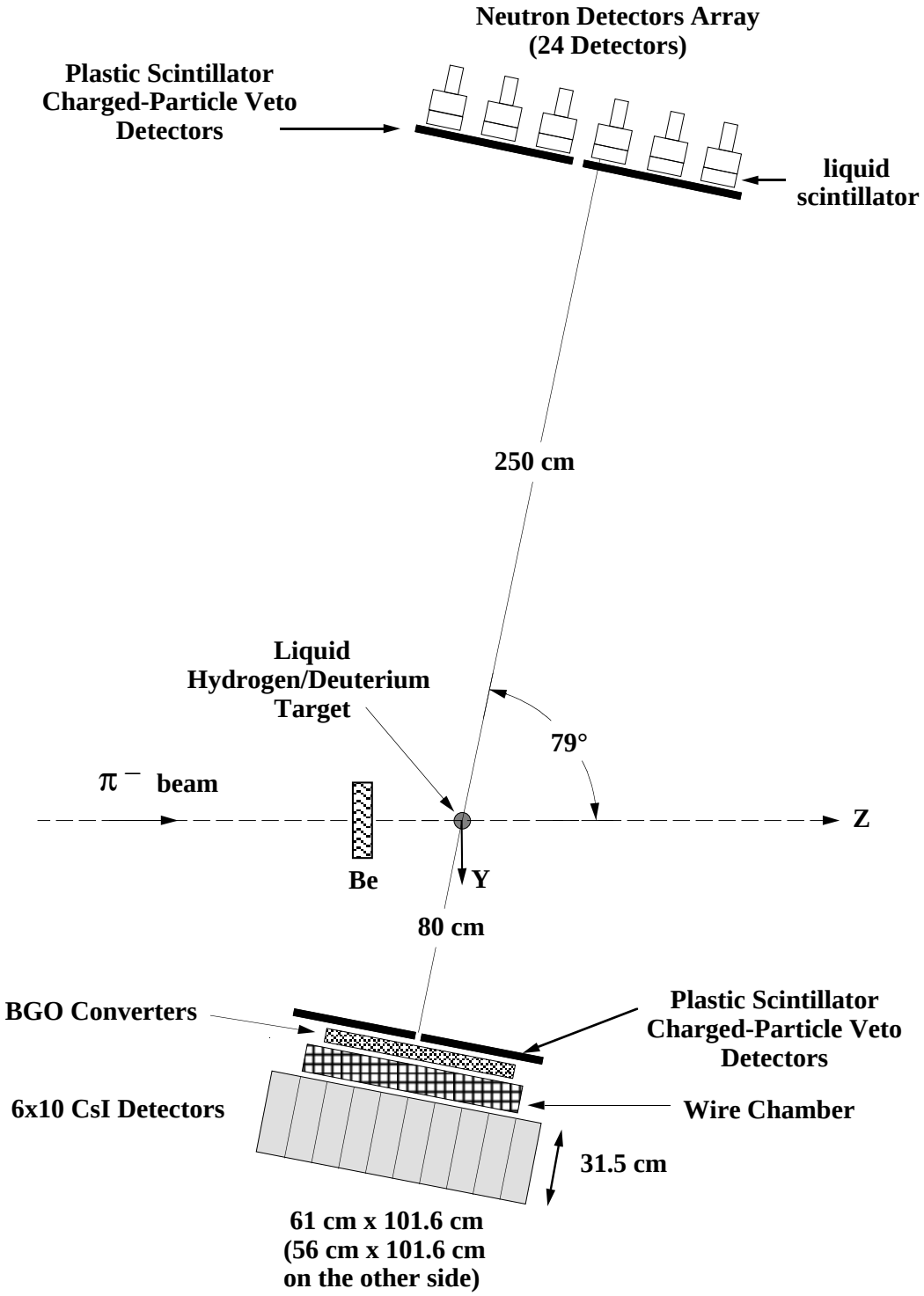

Figure 2.4: A schematic view of the experimental layout.

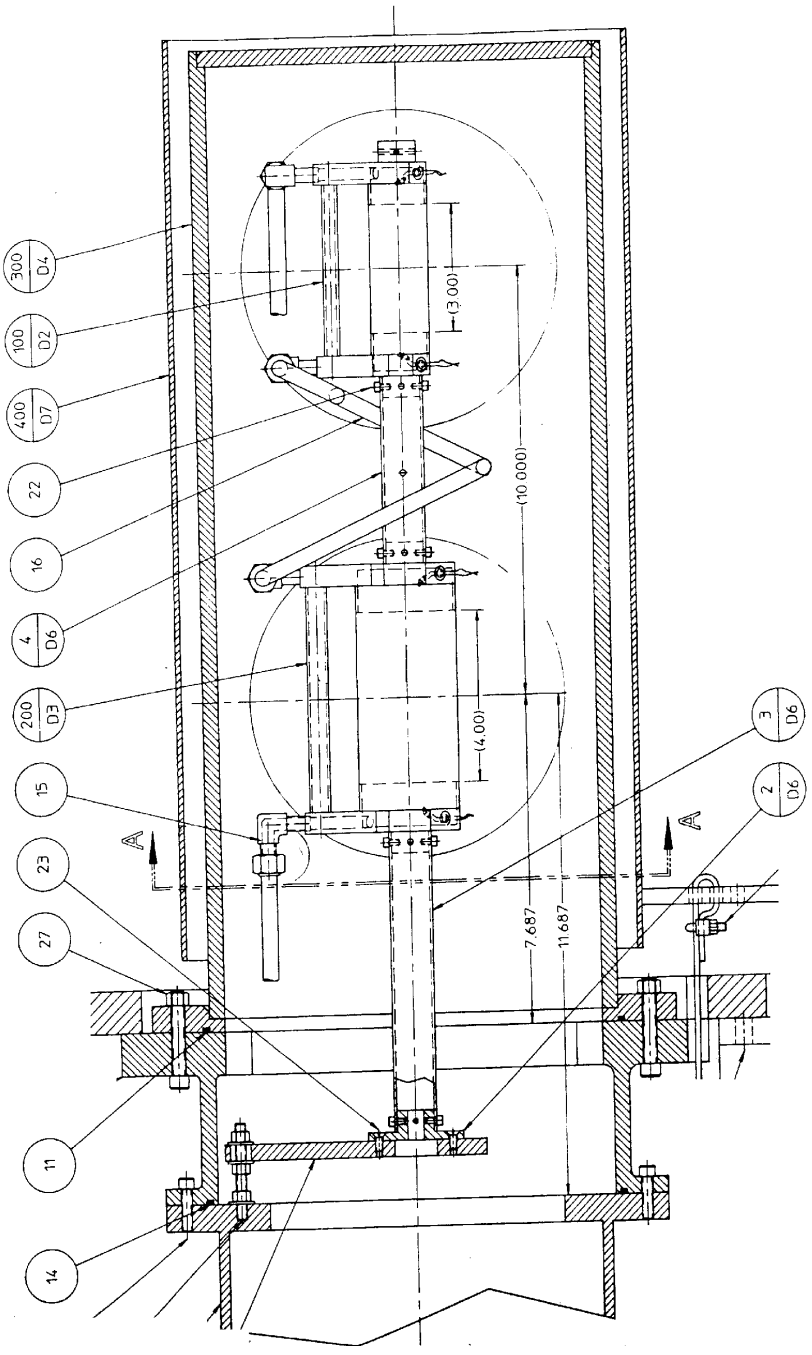

Figure 2.5: The target chamber used in Exp1286. Two target holders are shown here. The lower one (4″ high and 2.36″ in diameter) was used.

gas into a stack discharging in a safe location. Flush the stack with inert gas (preferably nitrogen) before planned discharges of hydrogen, (4) be sure that all hydrogen system components have the hydrogen removed and are purged before admitting air or doing any maintenance."

Ideally, the target would be either 100% pure hydrogen or deuterium. In analyzing the data it was noticed that there was 0.31% hydrogen contamination by number density in the deuterium target. See details in section 5.3.

2.1.4 The Neutron Detectors

Although only six neutron detectors are illustrated in the cross-sectional cut shown in Figure 2.4, we actually used twenty-four neutron detectors. These detectors were obtained from several sources: Argonne National Laboratory (2 types), Lawrence Livermore National Laboratory, and the Bicron Corp. The front view of the neutron-detector array is shown in Figure 2.6. Table 2.1 lists the positions and dimensions in inches of all the neutron detectors used in Exp1286. The detector positions are relative to the center of the coordinate system, which is very close to the centroid of the reactions in the target, but not exactly the same location. The positions listed are the distance to the face of the neutron detectors. The type 1 detectors use liquid organic scintillator BC519, the type 2 use BC 501, and type 3 use BC501A, and the type 4 use NE213. Since the neutron detectors are also sensitive to γ rays, the $n-\gamma$ discrimination technique (which utilizes the differences of the shapes of the pulses generated by neutron and γ rays) was employed to suppress the background events caused by γ rays in the neutron detectors. A suppression ratio of 20 to 1 was achieved. A segmented array of five charged-particle veto paddles covered the whole neutron-detector array.

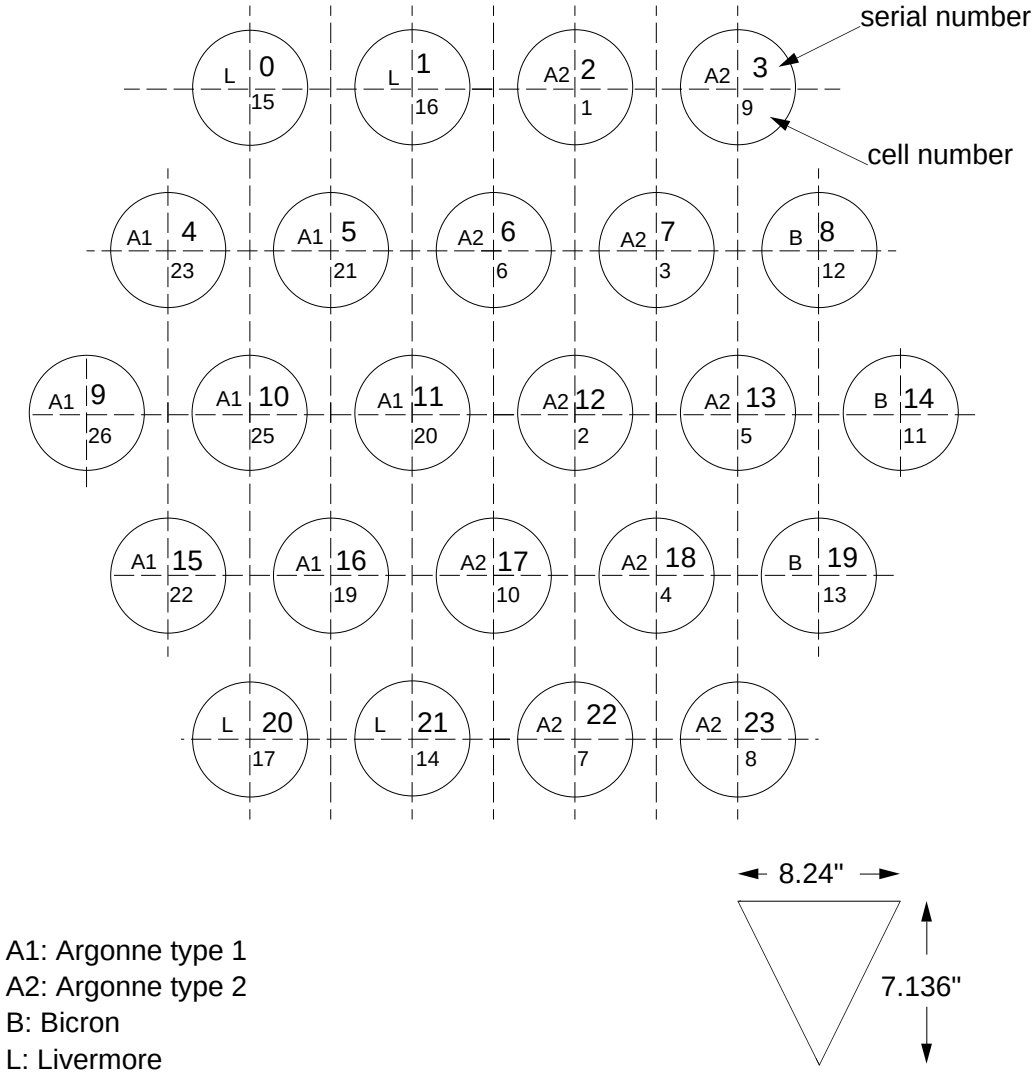

Figure 2.6: The neutron detector array in Exp1286. The detectors were aligned in a vertical plane that is parallel to the plane of the γ-ray detector. The scale gives the average separation distances for the detectors.

det. no.	x	y	z	tag no.	diam	thick	type
0	14.1132	-99.1121	4.7316	15	4.5	2.0	4
1	14.2089	-97.6600	12.7637	16	4.5	2.0	4
2	14.3166	-95.9872	20.8335	1	5.0	2.25	2
3	14.2890	-94.5165	28.9350	9	5.0	2.25	2
4	7.0962	-99.6029	0.7753	23	5.0	0.75	1
5	7.1191	-98.2621	8.6910	21	5.0	0.75	1
6	7.1704	-96.5564	16.7783	6	5.0	2.25	2
7	7.1798	-95.1055	24.9815	3	5.0	2.25	2
8	7.2352	-93.3752	32.9769	12	5.0	2.0	3
9	0.0259	-100.7302	-3.2577	26	5.0	0.75	1
10	0.1737	-99.2052	4.7233	25	5.0	0.75	1
11	0.1333	-97.5298	12.7241	20	5.0	0.75	1
12	0.0986	-95.9194	20.8758	2	5.0	2.25	2
13	0.1997	-94.4824	28.9841	5	5.0	2.25	2
14	0.1928	-92.6630	36.9792	11	5.0	2.0	3
15	-7.1470	-99.8760	0.5844	22	5.0	0.75	1
16	-7.0139	-98.3164	8.6821	19	5.0	0.75	1
17	-6.9679	-96.6514	16.7398	10	5.0	2.25	2
18	-6.9220	-95.1213	24.9194	4	5.0	2.25	2
19	-6.9015	-93.4439	33.0078	13	5.0	2.0	3
20	-14.1972	-99.1293	4.7238	17	4.5	2.0	4
21	-14.2096	-97.6897	12.7566	14	4.5	2.0	4
22	-14.0796	-95.9213	20.9147	7	5.0	2.25	2
23	-14.1353	-94.3909	29.0381	8	5.0	2.25	2

Table 2.1: Survey for all the neutron detectors used in Exp1286, where the first column (det. no.) refers to the serial number used in the Monte-Carlo code (written in C) while the tag no. is the detector number for internal referencing. All units are in inches.

2.1.5 The γ-ray Detectors

As shown in Figures 2.4 and 2.7, the γ-ray detection system consisted of four major parts: (1) a single veto paddle in front of the bismuth-germanate (BGO) converters, (2) the BGO converters (consisting of two planes of $0.25''$ thick BGO converters), (3) the tracking wire chambers (shown in Figure 2.7) and (4) the cesium iodide (CsI) detector array. The whole γ-ray detection system was one of the two arms of the Neutral Meson Spectrometer (NMS) constructed at LAMPF. The veto paddles were used to veto signals generated by charged-

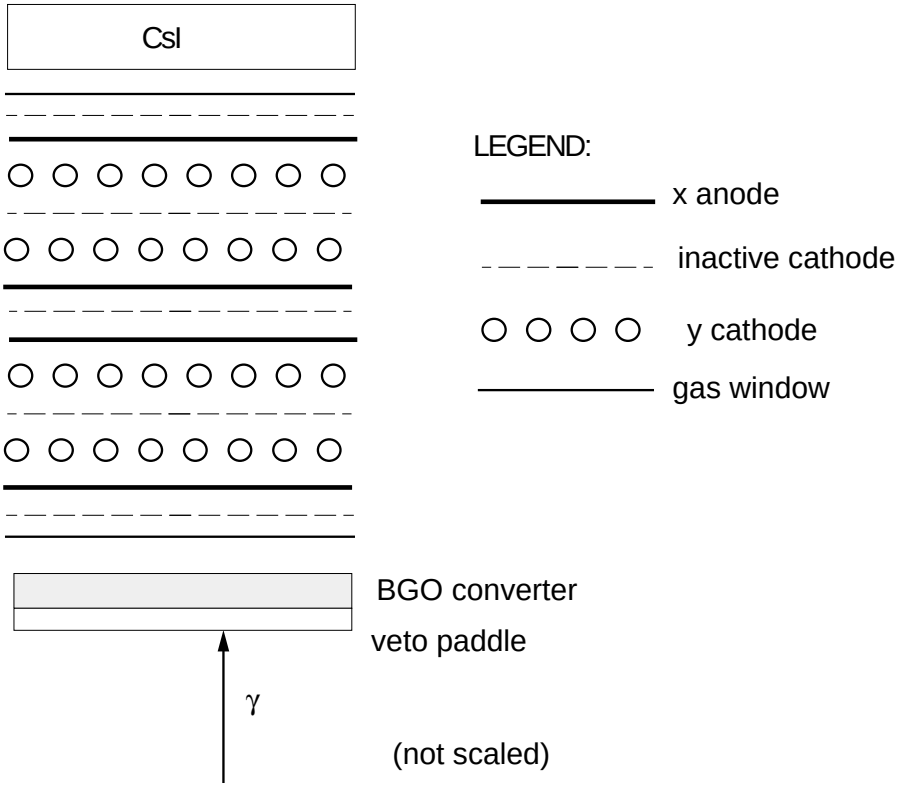

Figure 2.7: Schematic view of the wire chamber. The γ-ray first converts to e^+e^- showers in BGO crystals. The positions of the shower are then detected by the multi-wire proportional chamber (which is usually referred to as the wire chamber) between the BGO and the CsI detectors. Finally the γ-ray energy is detected by the CsI detector array behind the wire chamber.

particle events coming from the target and the Be slab. For example, a γ ray might hit the floor or the ceiling and generate charged particles which might be detected by the wire chamber and the CsI detectors. However, due to the existence of the veto paddles, such events were tagged and removed from the data set. The BGO crystals converted the γ ray into a charged-particle shower. The tracking wire chambers gave position signals telling where the charged particles emanated from the converter planes. With these position signals, we were able to reconstruct the vertex[1] where the charged-particle shower originated. The uncertainty for positions given by the wire chambers was about 100 μm, and the uncertainty in the position of the reconstructed vertex is less than 1 mm. This resolution is superior, especially in comparison to the size of the liquid target.

The CsI detectors behind the wire chamber were used to measure the γ-ray energy E_γ by collecting the remaining energy from the charged-particle shower following conversion. The CsI detectors consists of a 6×8 array of crystals. Each crystal was tapered so that both ends of the array approximately subtend the same solid angle at the target. The array was about 55 cm high, 102 cm wide and 30.5 cm deep.

2.1.6 Trigger Circuits and Data-Acquisition System

Figure 2.8 is a schematic view of the electronic trigger circuit used in Exp1286. We used 8mm tapes to record our data. For an event to be recorded on tape, the following conditions needed to be satisfied within the 450 ns window after the QDC gate (Figure 2.8) was opened:

[1]This reconstruction was done using the so-called Q system by Scott Carman of the Lawrence Livermore National Laboratory (LLNL) . A brief introduction to the Q system will be given in section 2.1.6.

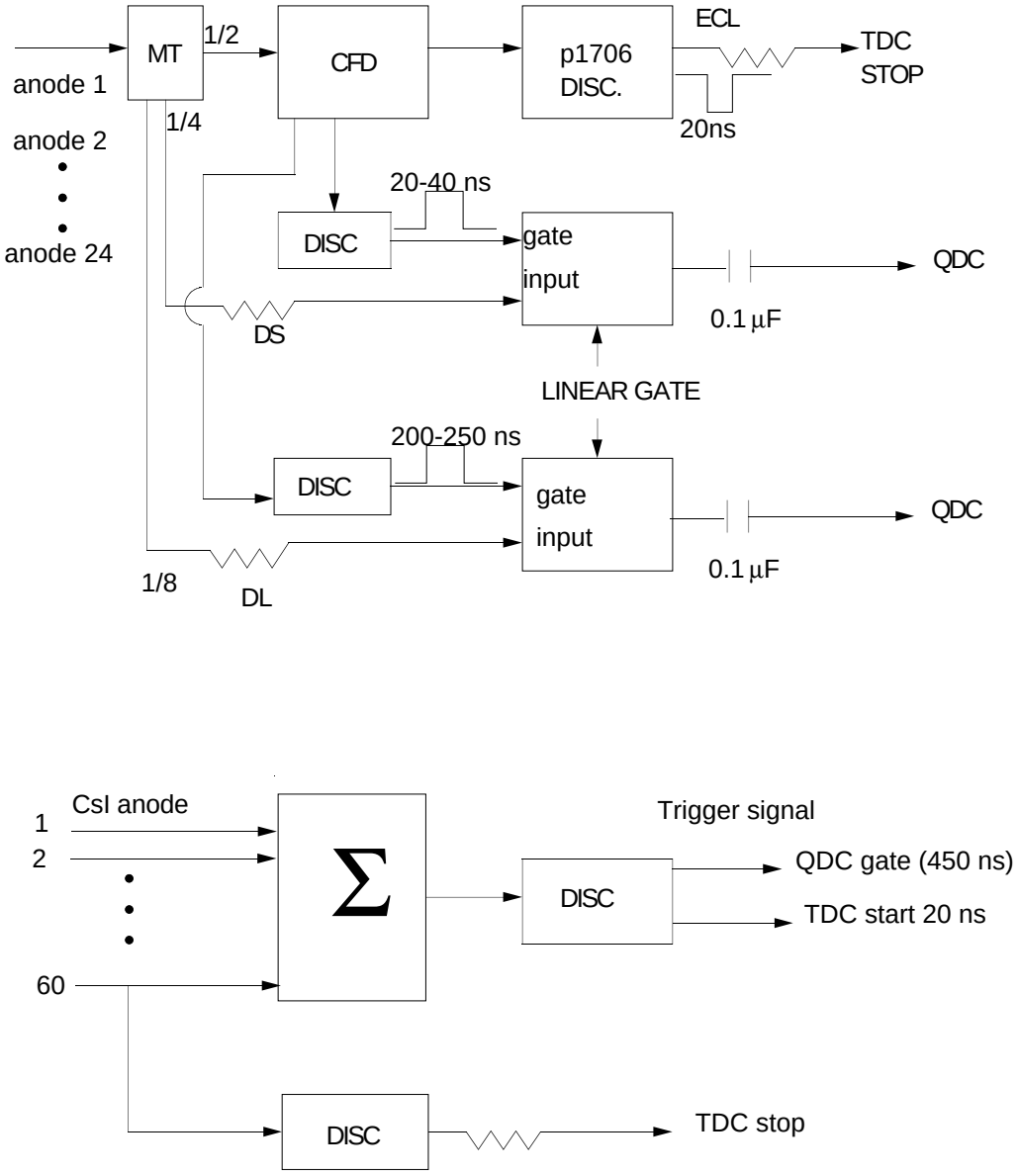

Figure 2.8: Block diagram of the trigger circuit.

1. No signal from the veto paddles (including the paddles in front of either the neutron detectors or the γ-ray detector).

2. At least one of the neutron detectors generated a signal higher than the preset threshold (equivalent to $\frac{1}{3} \times Cs$ as discussed later), so the neutron detector position information and the TOF signal were available.

3. The wire chamber generated a signal, which meant that the γ-ray position was determined.

4. At least one of the CsI γ-ray detector generated a signal, which meant the γ-ray energy was determined.

A schematic diagram of the data-acquisition system is shown in Figure 2.9. During the experiment, signals from detectors were first processed by the LAMPF user's electronics. Many of the electronic modules are Nuclear Instrument Modules (NIM). When these modules generated a trigger signal, the trigger module sent a Look-At-Me (LAM) signal to the Microprogrammed Branch Driver (MBD). The MBD determined which event was triggered and proceeded to acquire the CAMAC data from the event. The data were then transferred to the host computer (MicroVAX), where they were handled by the Los Alamos data acquisition system, Q. The so-called Q system was used for both data acquisition and data analysis. The following components are required for it to work properly: (1) a user-written set of FORTRAN codes for analysis and processing of data; (2) the Q Acquisition Language (QAL) compiler; (3) the real-time data-acquisition and replay system, Q; (4) the histogramming and display system H; (5) the data testing system T; (6) the dynamic parameter array system P; (7) the Q subroutine library QLIB.

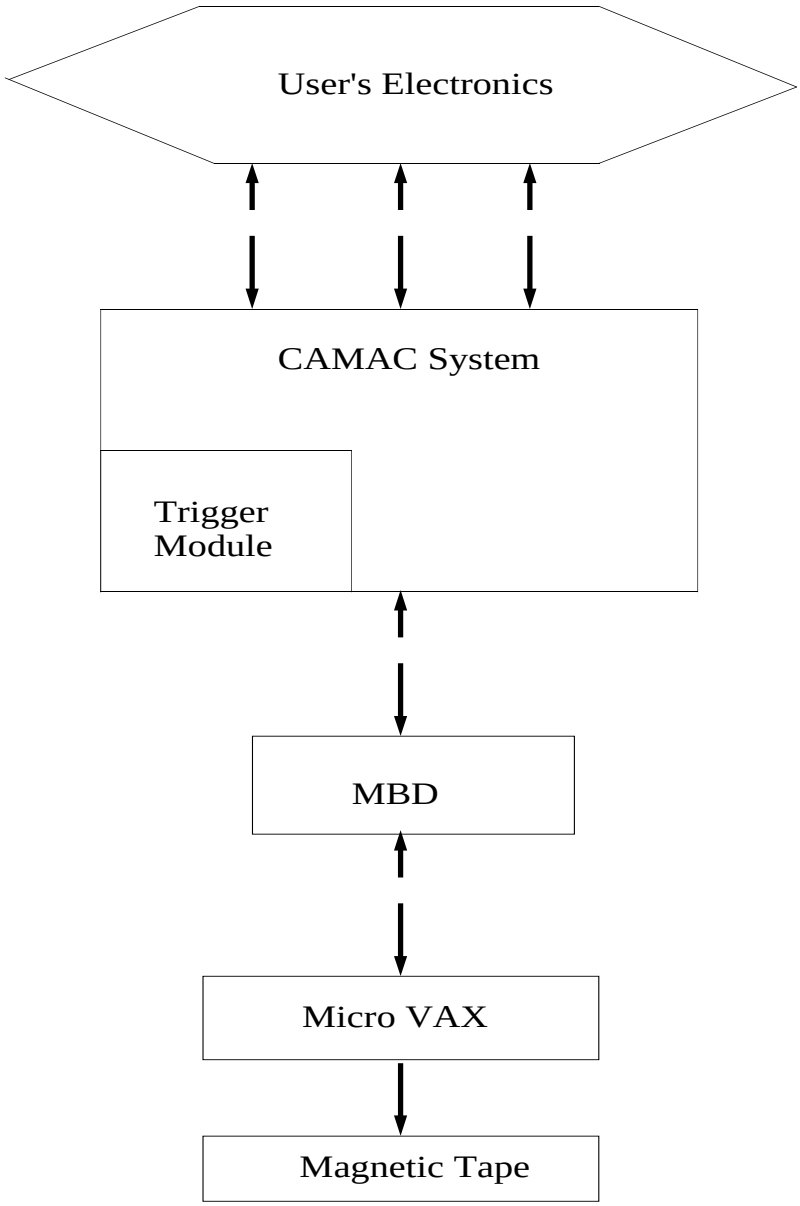

Figure 2.9: Schmatic view of the data-acquisition system.

2.1.7 Counting Rates

Given the counting rate in the neutron detector and the rate at which events were written to the data tapes, we can estimate the counting rate in the CsI detector from the counting rate for accidental events in the NTOF spectrum. For example, for the $^1H(\pi^-, n)\gamma$ reaction, we obtained 213,000 events in 65 minutes during run 316, i.e., 55 counts per second (cps) (for doubles plus triples). For the $^2H(\pi^-, n\gamma)n$ reaction, we acquired 211,000 events in 73 minutes during run 260, i.e., 48 cps (for doubles plus triples)[2]

In the entire TOF spectrum, about 50% of the counts are accidental events. Therefore, we obtain:

$$C_{acc} = 50\% * 50 \quad = \quad 25 \ \text{ cps} \tag{2.1}$$

$$\text{resolution time :} \quad \tau \quad = \quad 400 \text{ ns} \ . \tag{2.2}$$

For each neutron detector the counting rate is about 1000 cps, so for the neutron detector array, the counting rate is roughly $C_n = 20{,}000$ cps. Let C_{CsI} be the counting rate in the CsI detector array, then we have:

$$C_{acc} = \tau \ C_{CsI} \ C_n \ . \tag{2.3}$$

Therefore,

$$C_{CsI} = 3000 \ \text{ cps} \ . \tag{2.4}$$

2.2 Efficiency Measurement

Knowledge of the neutron detector efficiency is critical to the extraction of a_{nn} from experimental data. Fortunately, there exists a code called NEFF4

[2]Definition of double event and triple event: if the γ ray and one neutron are detected in an event, we call the event a double event, or for short a "double"; if the γ ray and two neutrons are detected in an event, we call the event a triple event or a "triple".

which was developed in the Physikalisch-Technische Bundesanstalt (PTB) at Braunschweig, Germany. This computer code can calculate the neutron detector efficiency, given the dimension of the neutron detector (for both the liquid scintillator and the aluminum/glass housing), the scintillator type, the direction of incident neutrons and the threshold. In Figure 2.10 we can see that the efficiency of the neutron detector rises rapidly above the detector threshold and then falls off to a nearly constant value. We can also see that the efficiency is very sensitive to the threshold, especially for low-energy neutrons.

It is convenient to use radioactive γ-ray sources to routinely set and check bias thresholds by choosing the pulse height at the Compton electron recoil edge at a known bias energy and then referencing all other biases to this single energy. We use the ^{137}Cs γ-ray source ($E_\gamma = 0.661$ MeV) and the Compton edge ($E_e \equiv 0.472$ MeV) as the reference standard. This is what we call "$1\times Cs$". So a bias of $1/4 \times Cs$ corresponds to a bias at $1/4 \times E_e$ electron energy. The light output in organic scintillators from recoiling electrons at one energy is greater than that for recoiling protons of the same energy. The relative light response functions have been measured for a variety of particle types. For example, according to [Tic92], for NE-213 scintillator, the light output for $E_e = 0.472$MeV $(1 \times Cs)$ corresponds to that for $E_p = 1.76$ MeV protons. Likewise, $(1/4 \times Cs)$ corresponds to $E_p = 0.76$ MeV. For neutron energies below 12 MeV, the efficiencies of the detectors is mainly due to $^1H + n$ reactions. At higher neutron energies, however, $^{12}C + n$ reactions can result in significant light output. These reactions may generate a proton, deuteron or one or more α-particles. When E_n is below 18 MeV, the following six neutron-carbon reactions need to be considered:

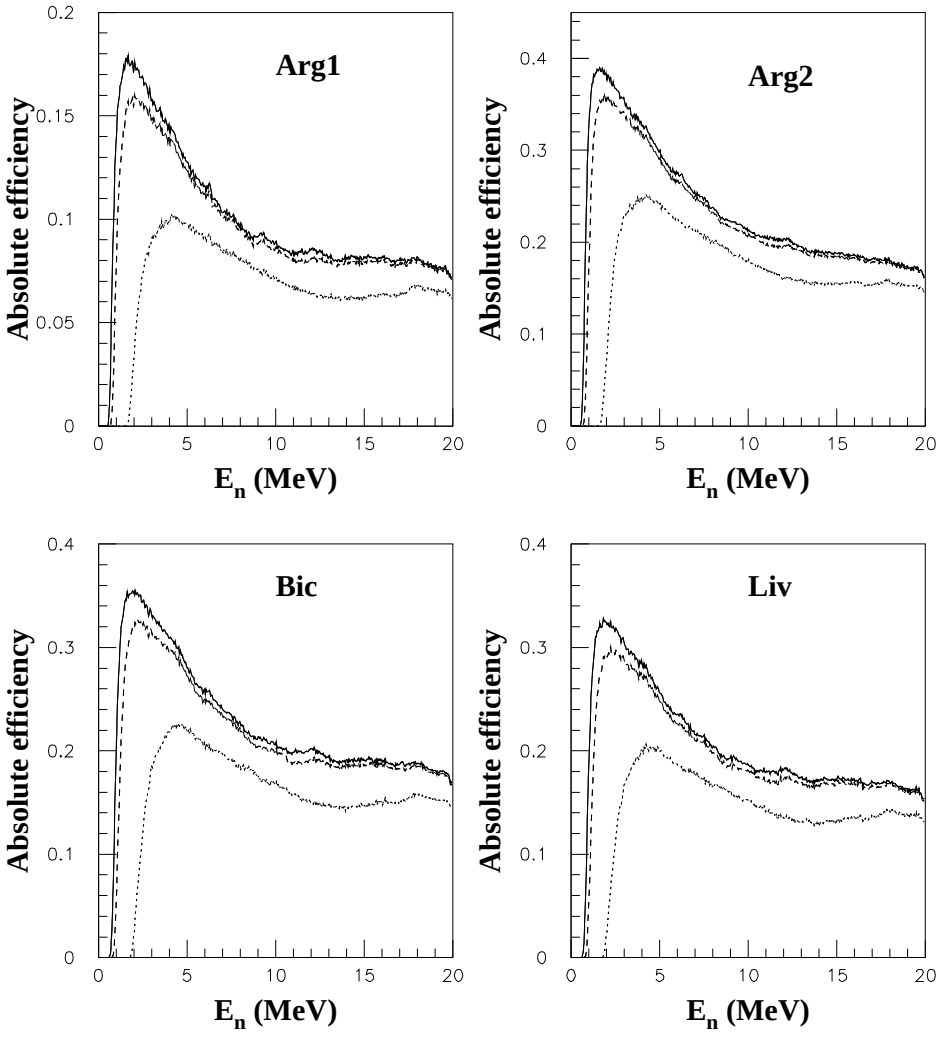

Figure 2.10: Neutron detector efficiencies calculated using the PTB code: detector types are labeled in each plot. Horizontal axes: E_n in MeV. Vertical axes: absolute detection efficiency. Solid curves are for the case of threshold equal to 1/4xCs, dashed curves are for the case of threshold equal to 1/3xCs, while dotted curves are for the case of threshold equal to 1xCs.

- $^{12}C(n,n_0)^{12}C$ and $^{12}C(n,n_1)^{12}C$ (Q=-4.44 MeV),
- $^{12}C(n,\alpha)^{9}Be$ (Q=-5.70 MeV),
- $^{12}C(n,n')3\alpha$ (Q=-7.28 MeV),
- $^{12}C(n,p)^{12}B$ (Q=-12.9 MeV),
- $^{12}C(n,d)^{11}B$ (Q=-13.7 MeV).

Reactions involving the elastic or inelastic neutron-carbon scattering do not directly result in any significant light output. However, the scattered neutrons from these two processes may subsequently scatter from ^{1}H and affect the efficiency quite a bit. Actually, elastic scattering from carbon followed by the $H(n,n)$ scattering is the dominant double scattering process when E_n is below 5.7 MeV. The $^{12}C(n,n')3\alpha$ reaction dominates over the single-scattering process $^{1}H(n,n)$ when the neutron energy is above 14 MeV. Generally speaking, light output from the emitted ^{9}Be, ^{11}B and ^{12}B nuclei are negligible compared to the light output from the lighter reaction products.

To check the efficiency of the neutron detectors, we conducted a series of efficiency measurements at the Triangle Universities Nuclear Laboratory (TUNL). There are two types of measured efficiencies, absolute and relative. We measured the absolute efficiencies. The absolute efficiency of a detector can be defined as the measured neutron yield (normalized to an absolute flux value) divided by the known cross section. In the absolute efficiency measurement, the shape and normalization of the efficiency function over an energy range are determined. In the present work, the efficiencies of the detectors were determined by measuring the neutron yields from the calibrated $^{2}H(d,n)^{3}He$ reaction. The cross-section values for the $^{2}H(d,n)^{3}He$ reaction measured by M.

Drosg [Dro78] at LANL were used as the standard values. For experimental details concerning this type of measurements, such as electronics, data analysis of the measurement and corrections to the data, and for details about the PTB efficiency code, refer to the Ph.D. dissertation of D.E. González Trotter [Gon98].

We used neutrons generated by the $^2H(d,n)^3He$ reaction, with energies from 5 MeV to about 13 MeV, to measure the absolute efficiency of each neutron detector. The following formula was used to extract detector efficiencies:

$$\epsilon(E_n) = \frac{Y_g(E_d,\theta)}{Y_n(E_n,\theta)} \ , \tag{2.5}$$

where E_d is the bombarding deuteron energy, E_n is the outgoing neutron energy, and θ is the reaction angle in the laboratory system. The symbol $Y_n(E_n,\theta)$ represents the number of neutrons incident on the front surface of the liquid scintillator in the detector per Beam-Current Integrator (BCI) count (given in units of μC), and $Y_g(E_d,\theta)$ stands for the experimental neutron yield per BCI from the deuterium gas and can be obtained directly from the measurement. The quantity $Y_n(E_n,\theta)$ can be calculated from

$$\begin{aligned} Y_n(E_n,\theta) = NI \times NT \times \Omega \times T_{gc}(E_n,\theta) \\ \times T_d(E_n) \times \sigma_g(E_n,\theta) \ , \end{aligned} \tag{2.6}$$

where $\sigma_g(E_n,\theta)$ stands for the known $^2H(d,n)^3He$ cross section in the laboratory system. The quantity $T_d(E_n)$ is the transmission probability through the entrance face of the detector[3] for a neutron of energy E_n. The total cross section (σ_t) values for aluminum obtained from ENDF/B-VI (Evaluated Neutron Data Format, B-VI is the version number of the data library) were used for the

[3]The cylindrical aluminum housing for the liquid scintillator is about 0.16 cm thick.

transmission calculation. The value $T_{gc}(E_n, \theta)$ is the transmission probability through the deuterium gas cell, for a neutron of energy E_n. This quantity is angle dependent because the path lengths of neutrons through the liner and wall of the gas cell changes with the emission angle.

In Equation 2.6, NI is the number of deuterons per μC incident on the gas cell, NT is the number of target nuclei per cm^2 across the length of the gas cell, and Ω is the solid angle subtended by the detector. The NI can be calculated using

$$NI = FS \times \frac{t}{q_d} \ , \tag{2.7}$$

where FS is the full-scale setting of the beam-current integrator (600 mA), t is the scale factor for the the beam-current integrator (0.01 s), and q_d is the charge of a deuteron. The NT can be calculated from

$$NT = \frac{P \times L \times NM}{R \times T} \ , \tag{2.8}$$

where P is the gas-cell pressure in bar, L is the length of the gas target, NM is the number of nuclei in the target gas per mole (12.05×10^{23} nuclei/mole), R is the universal gas constant (83.15 cm^3·bar/mole·Kelvin), and T is the gas temperature in Kelvin (293±2).

Figure 2.10 shows the comparison of calculations using the PTB code vs. data for the four types of neutron detectors we used in the project. As one can see, there is very good agreement in every case for the energy points we checked. Also, H. R. Setze did similar experiment before at TUNL [Set95] and showed that the PTB code does a very good job at low neutron energies (from threshold to 4 MeV). From the measurement and the PTB code calculation, we believe that we know the relative efficiency to better than ±2% of its value for the range of E_n considered.

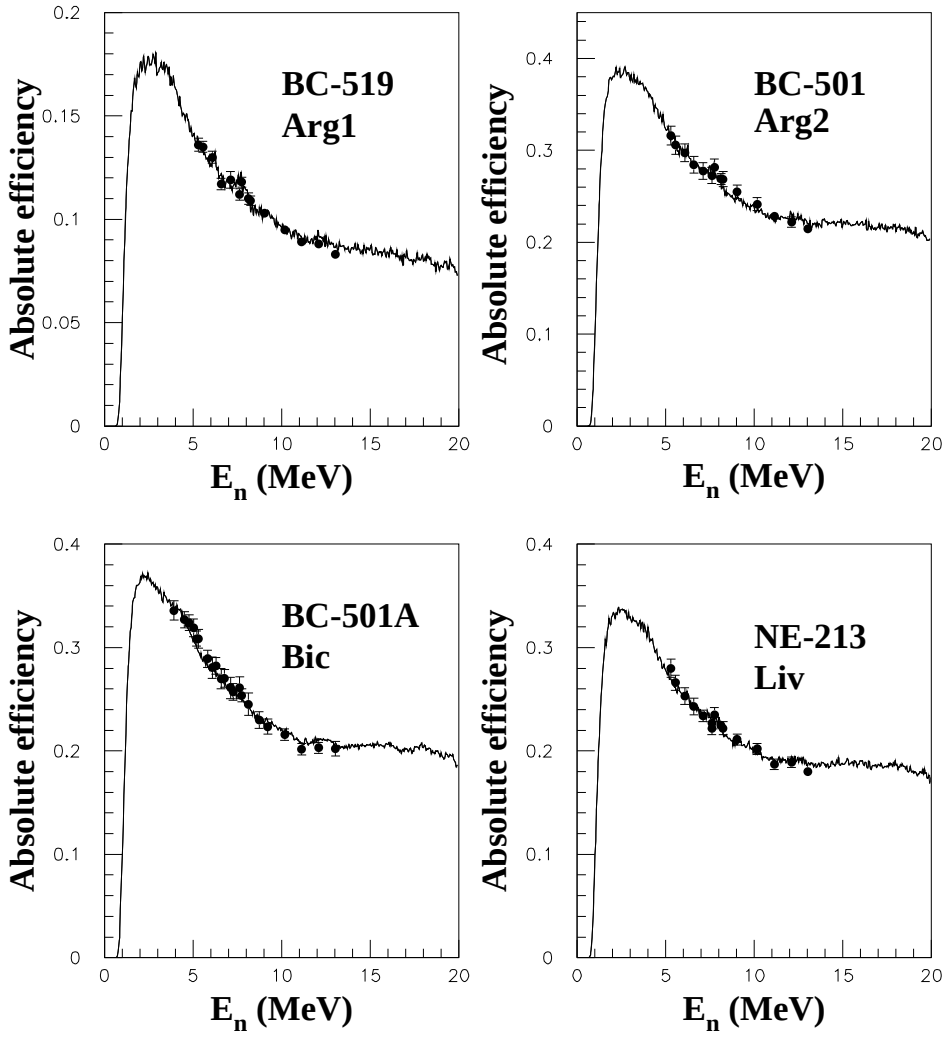

Figure 2.11: Neutron detector efficiencies: Curves are calculated results, while the symbols represent measured results. Threshold: 1/3 x Cs. In each plot, liquid scintillator type and detector type are shown. The sharp structures in the curves for the calculations mainly result from statistical uncertainties in the Monte-Carlo calculation (NEFF7).

2.3 Cross Talk Measurement

Since neutrons can interact with any nucleus, it is definitely possible that a neutron will scatter from the proton or the carbon nuclei of one liquid organic scintillator and then be detected by an adjacent detector. This phenomenon is called cross talk. In Figure 2.12, which is a plot of NTOF1 vs. NTOF2 for triple events, we can clearly see a band in the $|NTOF1 - NTOF2| < 10$ ns (10 ns is about 50 channels in Figure 2.12) region. These are cross talk events. We expect that such cross talk events exist in NTOF spectra for double events also.

We performed a measurement at the TUNL tandem accelerator using a honeycomb structure as shown in Figure 2.13 to measure the cross talk between the detectors used in Exp1286. First, we set up detector A alone and measured the yield per unit charge of integrated beam current (BCI). Then, we added six adjacent detectors (detectors 0 through 5) and measured the yield per unit charge again in detector A. Our data indicate that the yield increased by only 1.1%. This is a small number, and might have been ignored. However, such cross talk events are included in the Monte-Carlo simulation for Exp1286 and so no correction spectrum for this 1.1% amount of cross talk was subtracted from the measured data that are eventually compared to the calculated NTOF spectra.

2.4 Sample NTOF, γ_x , γ_y , E_γ and θ_3 Spectra

Figure 2.14 shows the θ_3 spectrum for the hydrogen target and the deuterium target. As a reminder, the angle θ_3 is defined as the angle between the neutron momentum and the negative of the γ-ray momentum. Since we are interested here only in comparing the shapes of the two spectra, the spectrum for the

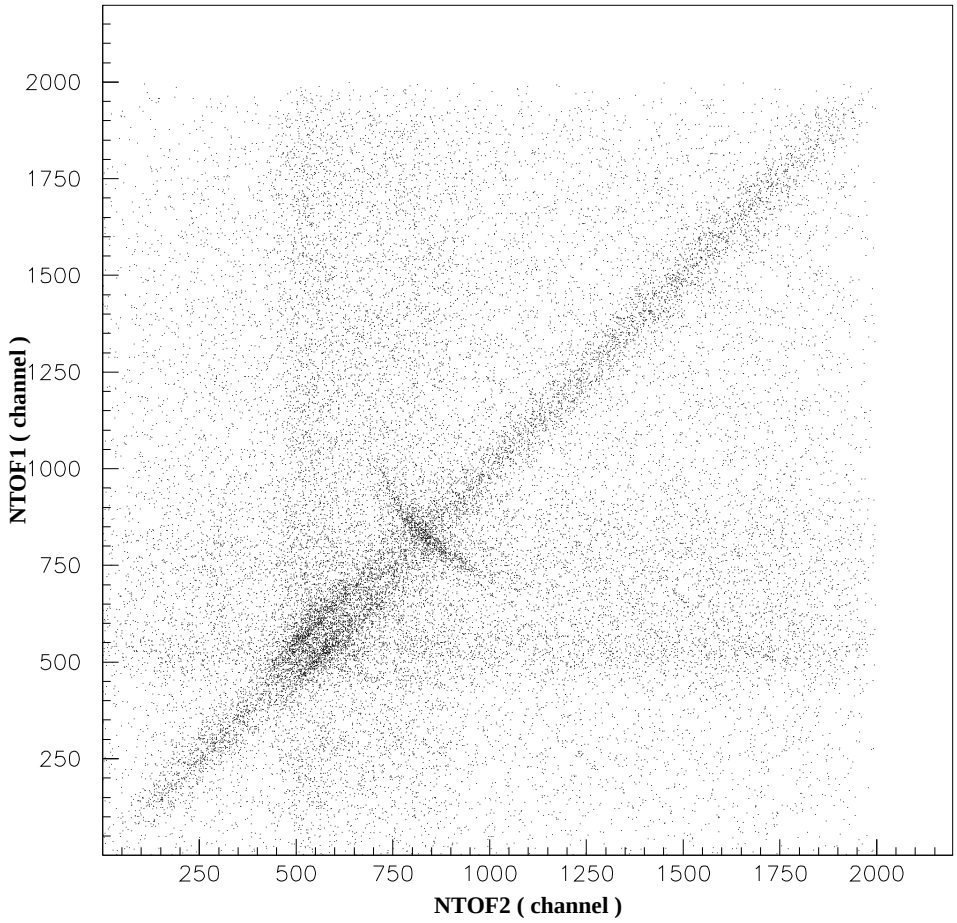

Figure 2.12: The TOF1 vs. TOF2 for the triple events from $\pi^- d \to nn\gamma$. Unit: channel numbers. The diagonal darker area from the lower left corner to the upper right corner indicates cross talk. Each channel corresponds to 0.205 ns.

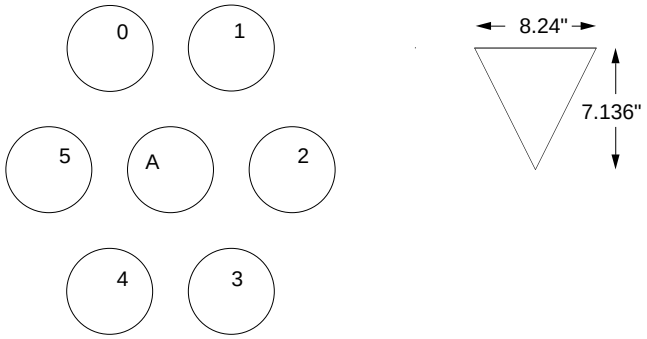

Figure 2.13: Experiment setup for cross talk measurement

deuterium target was normalized to have the same height as the spectrum for the hydrogen target. Obviously, and as expected from kinematics, the peak positions are quite different. Except for the case where neutron is scattered in the target, the angle between the detected neutrons and the corresponding γ ray must be 180° (that is, $\theta_3 = 0$) for the ${}^1H(\pi^-, n)\gamma$ reaction. If the target were a point target and the neutron and γ-ray detectors were point detectors, the θ_3 spectrum would be a spike peaked at zero, since the γ ray and the neutron from the ${}^1H(\pi^-, n)\gamma$ reaction always move in opposite directions. However, due to finite geometry, multiple scattering and cross talk (these issues will be discussed in detail later), the observed peak occurs at about 0.07 radian. This is justifiable and understandable considering the finite-geometry effects.

In Exp1286 we determined the position of the γ ray with the wire chamber to a high accuracy of about 1.2 mm. However, the resolution for the neutron position is 67% of the neutron detector radius R. In our simulation described later we always assume that neutrons are detected at the center of the neutron detectors, as far as the θ_3 calculation is concerned, because in the experiment we only know which detector detected the neutron, but no specific information is available from the experimental data regarding the neutron position. Let

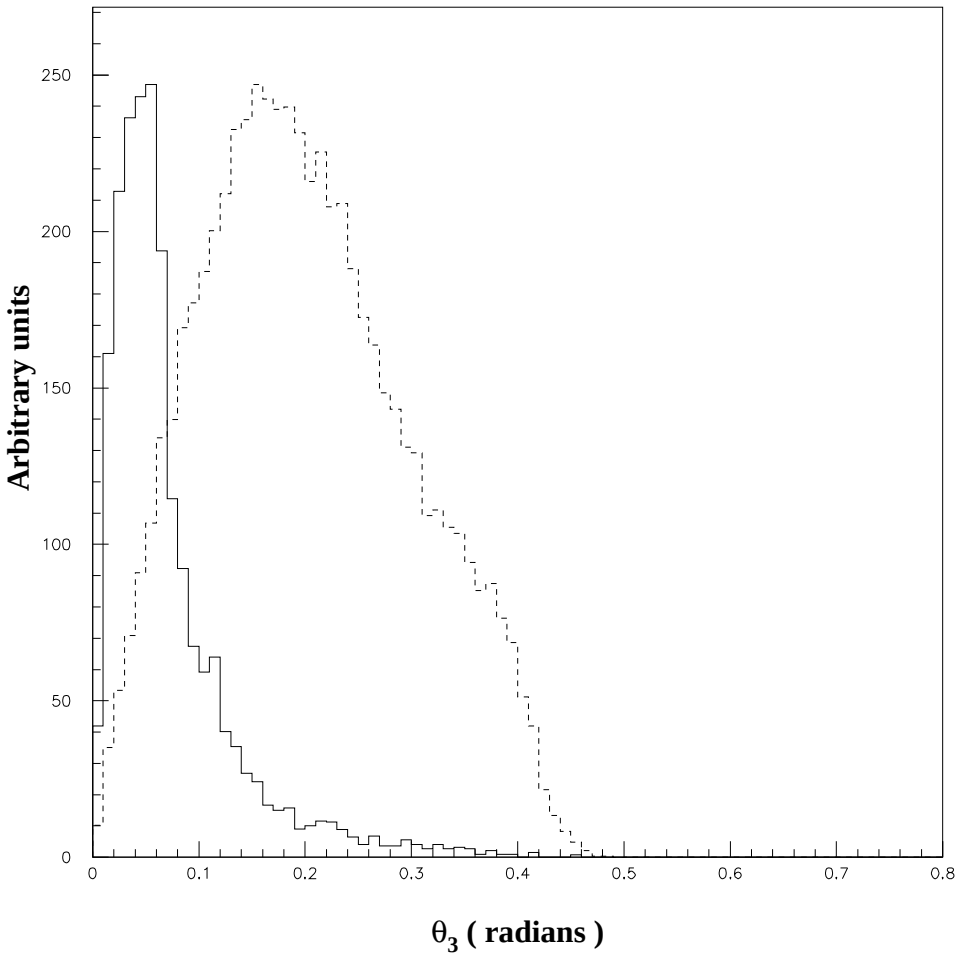

Figure 2.14: The experimental θ_3 spectra for the hydrogen target vs. that for the deuterium target after background subtraction. The solid curve is for the hydrogen target and the dashed curve is for the deuterium target. We are comparing the shape only.

us define D_{nd} to be the distance from the center of the coordinate system to the center of the neutron detector, which is approximately 250 cm. Then, the uncertainty in neutron position, $67\%R$, introduces an uncertainty in θ_3 of $\arctan(0.67\ R/D_{nd})$. Therefore, we define

$$\delta\theta_3^{(ndet)} = \text{atan}(0.67\ R/D_{nd}) = 0.018 \text{ radian.} \tag{2.9}$$

Here the superscript $(ndet)$ indicates the uncertainty is due to the finite size of the neutron detectors. Part(a) of Figure 2.15 illustrates the uncertainty in θ_3 cause by the uncertainty in neutron position.

Unfortunately, the finite geometry of the target causes larger uncertainties in θ_3 . Part(b) of Figure 2.15 illustrates this situation. The opening angle θ_3 is the same as the θ_t shown in this figure. But the angle we used in the simulation as θ_3 is θ_c. From part(b) of Figure 2.15 we can easily see the uncertainty due to the finite size of the target

$$\delta\theta_3^{(tar)} = |\theta_c - \theta_t| = \angle PGO + \angle PCO\ . \tag{2.10}$$

Let us define $D_{\gamma d}$ as the distance from the target to the wire chamber, D_g as the distance from P to line CO and D_n as the distance from point P to line GO. Then on the average, $\angle PCO$ is the average D_g over the average D_{nd}, and $\angle PGO$ is the average D_n over $D_{\gamma d}$. The values of D_g and D_n are approximately the same. Considering the fact that the target is 10 cm in height, it is reasonable to let $D_g = D_n = 3$ cm. Also, $D_{\gamma d}$ is around 80 cm. Therefore, from Equation 2.10 we have

$$\delta\theta_3^{(tar)} = \arctan(3.0/80.0) + \arctan(3.0/250) = 0.049 \text{ radian}\ . \tag{2.11}$$

If we combine Equations 2.9 and 2.10, the uncertainty caused by finite geometry is

$$\delta\theta_3 = \sqrt{(\delta\theta_3^{(tar)})^2 + (\delta\theta_3^{(tar)})^2} = 0.052 \text{ radian}\ . \tag{2.12}$$

This is smaller than the 0.07 discussed above in reference to Figure 2.15. The reason is that events due to multiple scattering and cross talk lead to a larger θ_3 , and we did not take those processes into account in obtaining Equation 2.12.

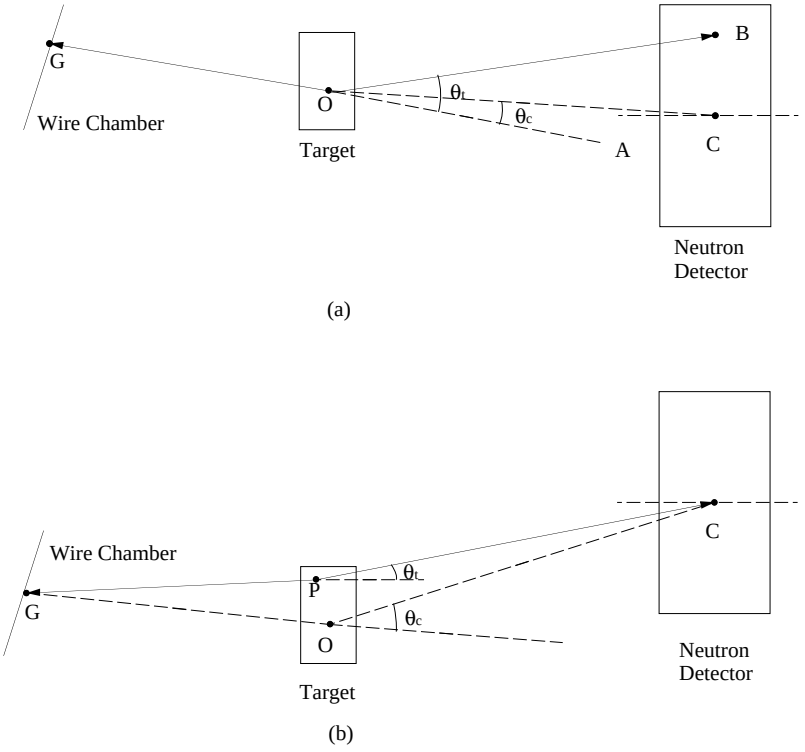

Figure 2.15: Uncertainty in θ_3 caused by finite size of a single neutron detector (top) and finite size of the target (bottom). Here C is the center of the neutron detector, O is the center of the target, and P, B and G are random points in the target, neutron detector and the wire chamber, repectively.

In the case of the hydrogen target, the angle between the γ ray and the neutron has to be $180°$ to conserve energy and momentum. Clearly, the spectrum in Figure 2.14 is much wider for the case of the deuterium target, because here the angle between the γ ray and one of the two neutrons could be anywhere from $0°$ to $180°$, whether or not the detected neutron was scattered before it

reached the neutron detector. As will be shown later, the θ_3 spectra for both cases agree with the Monte-Carlo simulated spectra.

Now let us examine the shapes of some other experimental spectra. First, let us look at Figure 2.16. The top left part of Figure 2.16 shows the vertical position spectrum of the γ ray (γ_x) for the hydrogen target (solid curve) and the deuterium target (dashed curve) for detector 2. Obviously, the γ-ray position is much more restrained by the neutron position in the case of the ${}^1H(\pi^-, n)\gamma$ reaction than in the case of the ${}^2H(\pi^-, n\gamma)n$ reaction. The same is true for the top left plot in Figure 2.16, where the shapes of the γ_y spectra for the same detector but for the two different reactions are compared. The bottom left plot of Figure 2.16 is a comparison of the shapes of the neutron time-of-flight (NTOF) spectra for detector 2 for the two different reactions. Obviously, the neutrons are almost mono-energetic for the ${}^1H(\pi^-, n)\gamma$ reaction and have a wide range of energies for the ${}^2H(\pi^-, n\gamma)n$ reaction. The bottom right plot of Figure 2.16 is a comparison of the shapes of the γ-ray energy spectra associated with neutron detector 2 for the two reactions. Due to the poor energy resolution of the γ-ray detection system, the differences in the shapes are not so big as in Figure 1.4, which was quoted from the proposal for Exp1286. Figure 2.17 is essentially the same as Figure 2.16 except that it is for θ_3 cut 2, which is a requirement for θ_3 being between 0.05 to 0.10 radian. Since we are now restricting the angle θ_3, the shapes of the γ_x and γ_y spectra change a lot for the ${}^2H(\pi^-, n\gamma)n$ reaction. For the ${}^1H(\pi^-, n)\gamma$ reaction, most of the counts in the spectra shown in Figure 2.17 are due to the finite size of the target and the neutron detector.

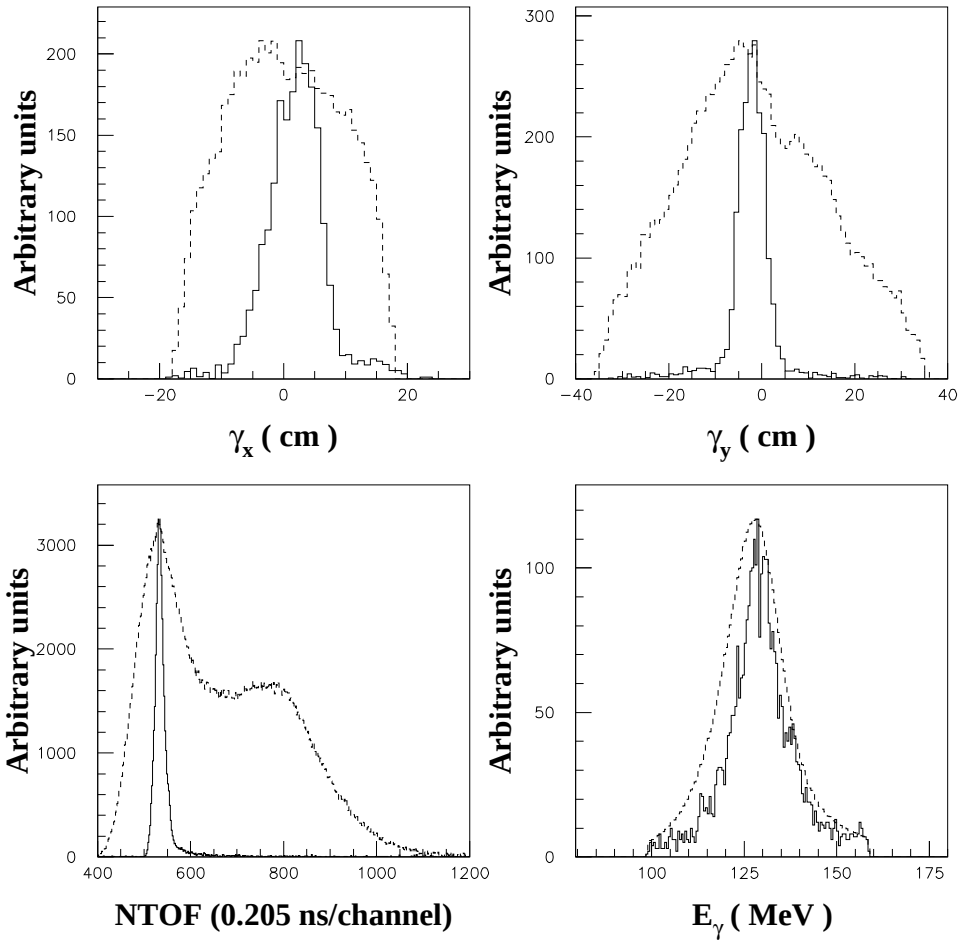

Figure 2.16: The experimental γ_x , γ_y , NTOF and E_γ spectra for the hydrogen target vs. that for the deuterium target for detector 2 after background subtraction, no θ_3 cuts applied. The solid curves are for the hydrogen target and the dashed curves are for the deuterium target. The curves for the two targets have been normalized to the maximum number of counts/channel to enable comparison of the shapes.

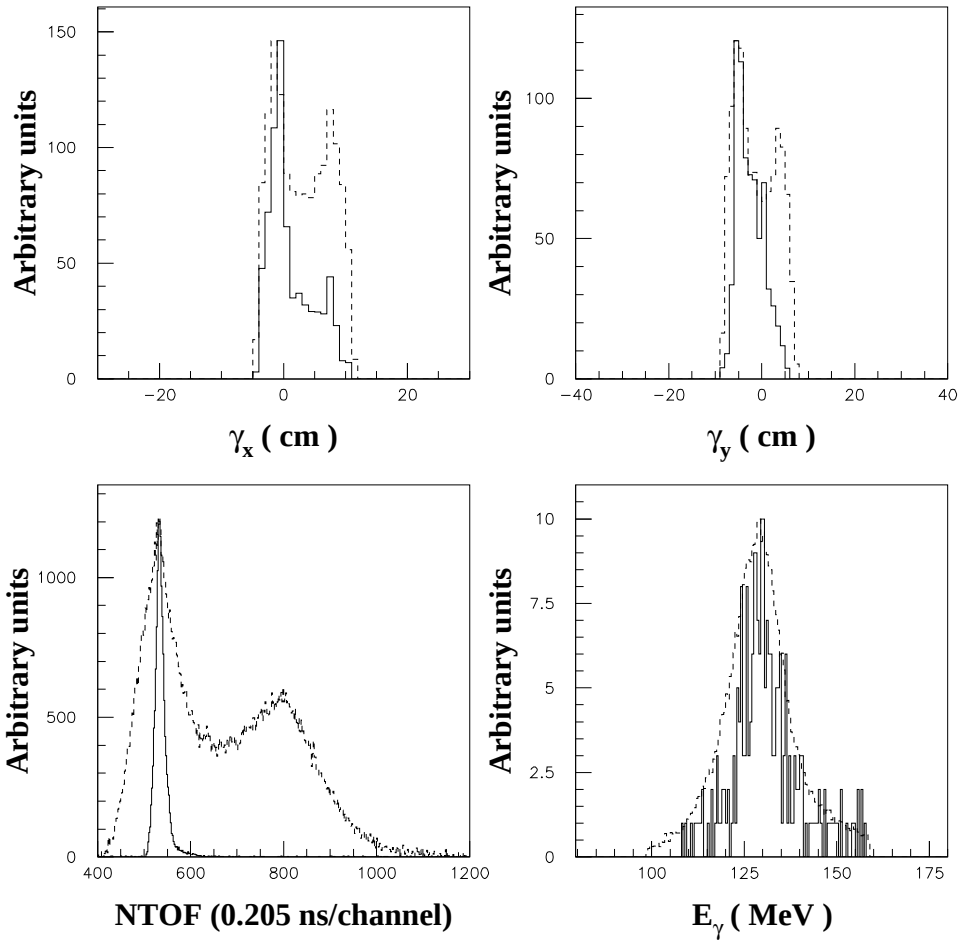

Figure 2.17: The experimental γ_x , γ_y , NTOF and E_γ spectra for the hydrogen target vs. that for the deuterium target after background subtraction for θ_3 between 0.05 and 0.1 radian. The solid curves are for the hydrogen target and the dashed curves are for the deuterium target. The curves for the two targets have been normalized to the maximum number of counts/channel to enable comparison of the shapes.

2.5 Discussion of Neutron Scattering and Cross Talk in the Experiment

The significance of neutron scattering and cross talk can be illustrated by comparing the simulated two-dimensional (2D) γ-ray position spectrum with direct neutron contributions only and the data as shown in Figure 2.18. For easier understanding of the issue, we choose the hydrogen target. The top part of Figure 2.18 is the simulated 2D γ-ray position spectrum for detector 2 without considering the contributions from neutron scattering or cross talk. The bottom plot is the 2D γ-ray position for the same detector from the $^1H(\pi^-, n)\gamma$ experiment with the central part deleted in order to show the effect of multiple scattering and cross talk. When we do the same deletion for the top part in Figure 2.18 we only see a blank frame, which indicates no counts beyond the border of the central hole in the bottom part of Figure 2.18. From the simulated θ_3 spectrum for the $^1H(\pi^-, n)\gamma$ reaction, there are no counts beyond 0.20 radian, if there is no neutron scattering in the target and if there is no cross talk between neutron detectors. Thus, we conclude that to obtain a proper description of the experimental spectrum we must include neutron scattering in the target and cross talk between neutron detectors.

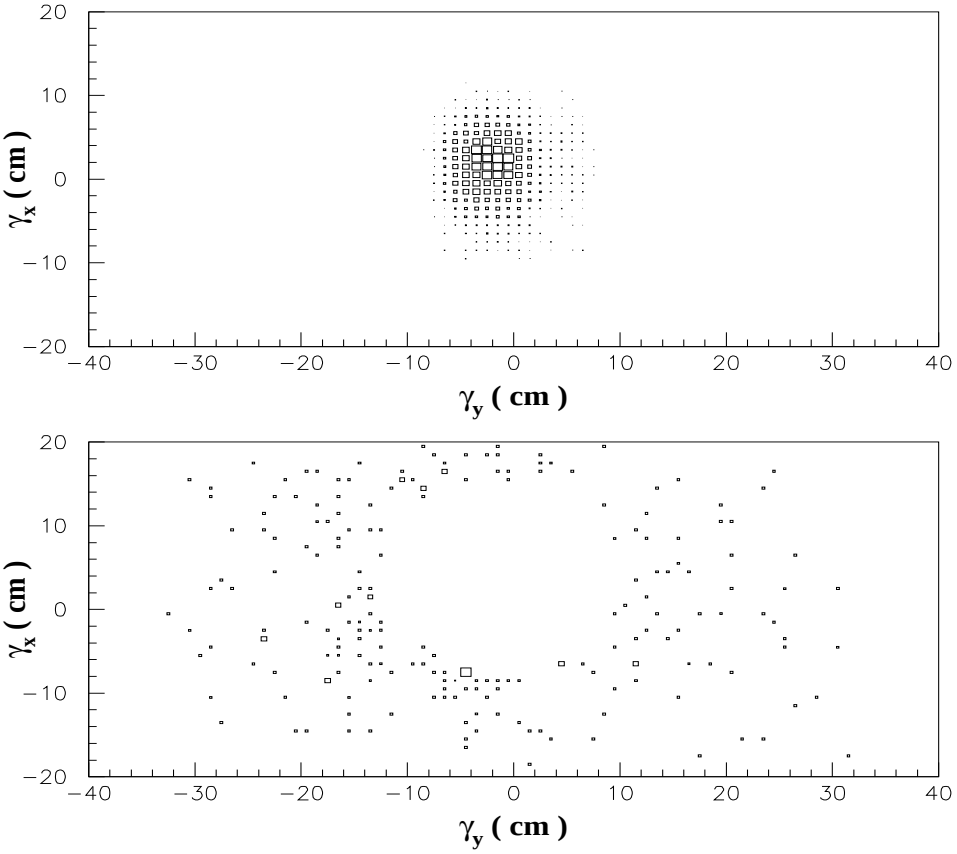

Figure 2.18: The top plot is a 2D γ-ray position spectrum corresponding to detector 2 by Monte-Carlo simulation for direct neutrons only. The bottom plot is the 2D γ-ray position spectrum for detector 2 from the $^1H(\pi^-, n)\gamma$ data with the central part removed in order to show the effect of multiple scattering and cross talk. The symbols in the upper figure represents slices through the data at the different levels ranging from 1 to 1000 events and the four symbols in the lower figure represent the levels of 1, 2, 3 and 4 events.

Chapter 3

Theory

In this chapter, we will provide some background information about the problem we are dealing with and describe the theoretical model we used in the calculation of the double differential cross sections for the $^2H(\pi^-, n\gamma)n$ reaction.

3.1 General Approach

The nucleon-nucleon (N-N) interaction is one of the most fundamental issues in nuclear physics. N-N refers to three kinds of interactions: proton-proton (p-p), neutron-proton (n-p) and neutron-neutron (n-n) interaction. Due to the lack of free neutron targets, our understanding of the p-p and n-p interactions is considerably better than that of the n-n interaction. Our present knowledge of the $^1S_0$ n-n scattering parameters comes mainly from the final state interaction, where two neutrons are present in the final state. The major focus of the present dissertation concerns the magnitude of the charge-symmetry breaking (CSB) part of the N-N force in the $^1S_0$ state.

3.1.1 Charge-Symmetry Breaking

For nuclear systems of A nucleons, one defines a charge-symmetry operator P_{cs} through the relations:

$$P_{cs} = e^{i\pi T_2} \text{ and } \ T_2 = \sum_{i=1}^{A} T_2(i) \ , \tag{3.1}$$

where $T_2(i)$ is the isospin component for nucleon i along the y-axis. The function of the charge-symmetry operator is to change d quarks to u quarks and u quarks to d quarks. When it acts on a nucleon, it changes the isospin. In other words, it converts a neutron state to a proton state or a proton state to neutron state according to the following equations:

$$P_{cs}|nkm>=|pkm> \ , \tag{3.2}$$

and

$$P_{cs}|pkm>=-|nkm> \ , \tag{3.3}$$

where $|nkm>$ stands for a neutron with momentum k and magnetic quantum number m, and $|pkm>$ stands for a proton with momentum k and magnetic quantum number m. If charge symmetry is valid, then

$$[P_{cs}, H] = 0 \ . \tag{3.4}$$

This implies that the system must be identical under neutron-proton exchange. However, the following pieces of evidences show that charge symmetry is broken to some extent:

1. The Nolen-Schiffer anomaly (NSA) [Nol69]. This is the discrepancy that exists between the binding energies of mirror nuclei after taking the n-p mass difference and the calculated e.m. correction into account. The discrepancy is about 100-400 keV for mirror nuclei with $A = 13$ to 41 and is considerably larger than the uncertainties [Sat76].

2. The 80 ± 19 keV discrepancy between the measured and calculated binding energies of ^3He and ^3H is a clear indication of charge-symmetry breaking (CSB).

3. From the nucleon-nucleon measurements we mentioned in Chapter 1,

$$a_{nn}^N \neq a_{pp}^N \ , \tag{3.5}$$

where the superscript N indicates only contributions from nuclear forces are considered.

4. The experimental results from the $\vec{n} + p \rightarrow n + p$ reaction are different from those for the $\vec{p} + n \rightarrow n + p$ reaction [Abe86, Knu90, Wil87]. The observation was that the analyzing power A_y^n for the former reaction is different from A_y^p for the latter reaction.

In [Hen69] the authors demonstrated that most of the CSB can be attributed to: (1) the mass difference between the d quarks and u quarks, which is $m_d - m_u \approx 4$ MeV and (2) the electro-magnetic interaction differences of the u and d quarks.

For hadronic interactions,

$$\delta V_{CSB} \approx \frac{\Delta m}{m_u + m_d} \approx 1\% \ . \tag{3.6}$$

Where $m_u \approx 6$ MeV and $m_d \approx 10$ MeV, and $\Delta m \approx 4$ MeV.

The calculated value based on one of the most recent NN models for the difference between a_{nn} and a_{pp} is [Mil90]

$$\Delta a_{CSB}^{calc} = a_{pp}^N - a_{nn}^N = 1.5 \pm 0.5 \text{ fm} \ . \tag{3.7}$$

Based on the well determined value for a_{pp} and various a_{nn} measurements made using the $^2H(n, nnp)$ reaction prior to 1980,

$$\Delta a_{exp}^{calc} = (-17.3 \pm 0.4) - (-17.1 \pm 0.4) \text{ fm} = -0.2 \pm 0.6 \text{ fm} \ . \tag{3.8}$$

That is, there is no sign of CSB. However, if we use the a_{nn} results obtained from the $^2H(\pi^-, n\gamma)n$ reaction after 1980, we have

$$\Delta a_{exp}^{calc} = (-17.3 \pm 0.4) - (-18.8 \pm 0.3) \text{ fm} = 1.5 \pm 0.5 \text{ fm} \ , \tag{3.9}$$

which is, by construction, in excellent agreement with Equation 3.7.

There is a tendency [Mil90] to disregard the a_{nn} results from the ${}^2H(n, nnp)$ reaction both because the analyses were performed using inadequate theoretical models and because of the possibility of a three-nucleon-force (3NF) affecting the interpretation of the data. Therefore, the a_{nn} value determined from the ${}^2H(\pi^-, n\gamma)n$ reaction has become a crucial quantity.

3.1.2 Calculation of Cross Sections for π^- Capture

Generally speaking, given the initial state ϕ_i and the Hamiltonian H of the system, the transition matrix element to a final state ϕ_f is $< \phi_i|H|\phi_f >$. The transition rate is the product of the transition matrix element squared and some phase-space factors.

In the case of ${}^2H(\pi^-, n\gamma)n$ reaction, ϕ_f is model dependent. The deuteron is a loosely bound system, with the neutron and proton spending a considerable fraction of the time outside the region usually taken to be the range of the nuclear force. Hence, the effects due to the overlapping of their meson fields is small. This conclusion is even more convincing considering the fact that the absorption of a $\pi-$meson by a proton is a high energy process which should not be affected much by the presence of a weakly bound neutron. Thus, the absorption with subsequent γ-ray emission in deuterium is basically the same as in hydrogen except it is modified by the momentum distribution of the proton in the deuteron and by the nn interaction in the final state. The parameters a_{nn} and the effective range r_{nn} are the most important ones to determine the strength of the nn interaction. Stating this another way, we say that the transition matrix is dependent on a_{nn} and r_{nn} .

The basics of the theory of the $^2H(\pi^-, n\gamma)n$ reaction is described in [Wat51] and [McV61]. There are two modes of π^- capture, $\pi^- + d \rightarrow n + n$ and $\pi^- + d \rightarrow n + n + \gamma$. The latter occurs about 30% of the time. The final state contains two neutrons in both cases. However, in the first case, due to the conservation of momentum and energy, the momenta of the outgoing neutrons are not dependent on the final-state interaction. In the case of $\pi^- + d \rightarrow n + n + \gamma$, the way in which the total momentum is distributed among the two neutrons and the photon is sensitive to the interactions between the reaction products. The interactions in the final state are the $n_1\gamma$ interaction, the $n_2\gamma$ interaction and the nn interaction. We know that the $n\gamma$ interaction is very weak compared to the nn interaction. This leaves the nn interaction as the main factor which determines the spectra of the final state momenta. The momenta of the neutrons can be measured very accurately using the time and position information from a time-of-flight spectrometer. These features make the $^2H(\pi^-, n\gamma)n$ reaction an excellent choice for the purpose of measuring the nn scattering length a_{nn} .

Knowing that the nn force is attractive, its qualitative effect on the neutron energy spectra is easy to see for the $\pi^- + d \rightarrow n + n + \gamma$ reaction. The neutrons have a range of recoil energies only because of the three-body final state. If the two neutrons were strongly bound as a "di-neutron", the "di-neutron" would recoil with a unique energy of about 4.8 MeV. If there were no interactions among the outgoing particles, then, the energy spectrum of the neutrons would be flat. However, the reality is somewhere between the two extremes. On one hand, the nn force is not strong enough to bind the two neutrons as a "di-neutron"; on the other hand, the nn force tends to equalize the neutron recoil velocities and produces a peak in the energy spectrum of

each neutron at about 2.4 MeV. The stronger the force is, the sharper the peak is. Therefore, the width of the neutron energy spectrum is a good measure of the nn interaction.

The ${}^2H(\pi^-, n\gamma)n$ capture occurs from the lowest mesonic Bohr orbit, so, considering the Q-value of about 130 MeV for the π^- capture reaction, the π^- is essentially at rest in the lab system. Take the linear momenta of the outgoing neutrons to be $\vec{p}_1$ and $\vec{p}_2$, respectively, and the momentum of the γ ray to be $\vec{q}$. Then, momentum conservation gives:

$$\vec{p}_1 + \vec{p}_2 + \vec{q} = 0 \ . \tag{3.10}$$

Since the three momenta must lie in a plane, we have six variables for the three particles. Conservation of energy and momentum give us four constraints for these six variables, thus, only two variables are independent. We will choose the two variables to be the energy E_1 of one of the neutrons and the angle θ_3 between the neutron momentum $\vec{p}_1$ and the axis along $-\vec{q}$, i.e., the direction opposite to the γ-ray emission.

For convenience, let us introduce two more variables. One is $\vec{p}$, the relative nn momentum between the two neutrons in their c.m. system, the other is $\vec{P}$, the total momentum of the c.m. system of the two neutrons in the lab system. Obviously,

$$\vec{p} = \frac{1}{2}(\vec{p}_1 - \vec{p}_2) \ , \tag{3.11}$$

$$\vec{P} = \vec{p}_1 + \vec{p}_2 \ . \tag{3.12}$$

The energy of the two neutrons is then $(p_1^2 + p_2^2)/2m_n = (p^2 + P^2/4)/m_n = (p^2 + q^2/4)/m_n$, by momentum conservation. Therefore, the total energy of the three outgoing particles is $q + (p^2 + q^2/4)/m_n$, which must be equal to the

initial total energy. Here, we assumed that $\hbar = c = 1$. It is now clear that p is uniquely determined by the γ-ray momentum q.

Since we want to measure a_{nn} in the $^1S_0$ state, the $^1S_0$ state requires the nn relative momentum p to be small. McVoy's paper [McV61] gives a nice figure showing the contours of $k = constant$ (and $p = constant$) in the E_1-θ_3 plane.

According to Watson [Wat51, Wat52], the energy dependence of the matrix element for the $^2H(\pi^-, n\gamma)n$ capture process in the $\vec{p} \to 0$ limit can be estimated using the zero-range approximation for the nn interaction. In the $\vec{p} \to 0$ limit, only the S-wave is important. Assume $\psi_s(r)$ is the singlet S-state wave function for the nn system, the matrix element will have the form

$$M_s = \int \psi_s^*(r)\ f(r)\ dr\ , \tag{3.13}$$

where $f(r)$ represents all the other factors. In the zero-range approximation,

$$\psi_s(r) = \sin(\frac{pr + \delta}{pr})\ , \tag{3.14}$$

where $\delta(p)$ is the S-state nn phase shift. Since we are using the natural units, (pr) is dimensionless. Substituting Equation 3.14 into 3.13, we find

$$M_s(p) = \frac{\delta}{p}\left[\int f(r)\cos(pr)d^3r + \cot(\delta)\int f(r)\sin(pr)d^3r\right]\ . \tag{3.15}$$

From the effective-range expansion

$$p\cot\delta = -\frac{1}{a} + \frac{1}{2}r_0p^2\ , \tag{3.16}$$

where a is the scattering length and r_0 is the effective range of the nn interaction, it is easy to see that $\cot\delta \to \frac{-1}{pa}$ as $\vec{p} \to 0$, so the integral involving $\sin(pr)$ goes to 0 at least as fast as p. If we assume that $|a| \gg R_d$ (the radius

of deuteron) and $pR_d \ll 1$, then the p dependence of the integrals is negligible compared to that of $\sin\delta/p$. In this limit, the p dependence of $M_s(p)$ is

$$M_s(p) = \frac{\sin(\delta(p))}{p} \ . \tag{3.17}$$

When p is small enough, we can ignore the p^2 term in Equation 3.16. That is:

$$\cot\delta = -\frac{1}{pa} \ . \tag{3.18}$$

Thus,

$$\sin\delta = \frac{pa}{\sqrt{1+p^2a^2}} \ . \tag{3.19}$$

Therefore the energy dependence of the cross section is simply

$$|M_s(p)|^2\Omega = \frac{1}{1+p^2a^2}\Omega \ , \tag{3.20}$$

where Ω is the appropriate phase-space factor, which depends on the pair of observables. When E_1 and θ_3 are observed,

$$\Omega = \frac{2\pi m_n^2 k^2 p_1}{m_n + k - p_1\cos\theta_3} dE_1 d\Omega_1 \ . \tag{3.21}$$

The condition for using Equation 3.20 is that $\frac{1}{2}r_0 a p^2 \ll 1$. Some detailed calculations show that this is equivalent to $p/\mu \ll 0.19$, with μ being the pion mass. This means that we must have

$$k \ \geq \ 130.9 \text{ MeV} \ , \tag{3.22}$$

$$\theta_3 \ \leq \ 20^\circ \tag{3.23}$$

on the E_1-θ_3 plane. The corresponding range of the relative energy $E = p^2/M$ of the two neutrons in their c.m. system is

$$E < 750 \text{ keV} \ . \tag{3.24}$$

To get the energy distribution at a specific θ_3 or the angular distribution for a specific neutron energy, one only needs to integrate Equation 3.20 over energy or angle. Watson and Stuart [Wat51] used a similar method to calculate the energy spectrum of the photons, i.e., the distribution of k, which is directly related to p. However, it is a less practical method because (1) the width of the k distribution is the same as that of the neutron energy distribution (about 2 MeV), (2) the γ-ray energy is peaked at about 130 MeV while the neutron energy peaked at about 2.4 MeV, and (3) an energy resolution of about 200 keV is required in order to extract a_{nn}. This latter problem is much easier to handle experimentally for the neutrons than for the γ rays. However, if the two neutrons act like a bound "di-neutron", then the γ-energy peak would be shifted considerably. Using this fact, Phillips and Crowe [Phi54] were able to conclude that a_{nn} is negative. Since Equation 3.20 is independent of the sign of the scattering length, it is important to have this independent determination of it.

Now, assume that the recoil momentum from the photon emission is initially absorbed entirely by the proton of the deuteron and that the transition matrix element is the same for the proton in the deuteron as it is for a free proton. This is equivalent to saying that the energy gained by the spectator neutron is entirely due to its interaction with the other nucleon. In coordinate space, the transition operator for a process in which momentum $-\Delta$ is transferred to the proton has the form $e^{-i\Delta\cdot\vec{r}_1}T(\vec{q}_i,\vec{q}_f)$, where $\vec{r}_1$ is the position of the proton and $\vec{q}_i$ and $\vec{q}_f$ are the initial and final relative momenta of the neutron relative to the proton in the c.m. system of the deuteron. In our case, $\Delta = \vec{q}$, so the

matrix element for radiative capture in deuterium can be written as

$$M = \int [e^{-i\vec{q}\cdot(\vec{r}_1+\vec{r}_2)/2}\psi_p(\vec{r}_1-\vec{r}_2)]^* e^{-i\vec{q}\cdot\vec{r}_1} T\phi(\vec{r}_1-\vec{r}_2)\xi d^3\vec{r}_1 d^3\vec{r}_2 \ , \tag{3.25}$$

where $\psi_p(\vec{r}_1-\vec{r}_2)$ is the wave function for the relative motion of the two neutrons in their c.m. system, ϕ is the wave function of the deuteron and ξ is the wave function of the pion in its Bohr orbit.

The approximations employed in the calculation are:

1. assume the impulse approximation is valid,
2. assume the wave function of the pion is constant over the volume of the deuteron,
3. approximation to $\psi_p(\vec{r})$,
4. approximation to $\phi(\vec{r})$, both S and D waves,
5. and neglect the momentum dependence of $T(\vec{q}_i, \vec{q}_f)$.

For the S-wave part of the deuteron wave function, i.e., $\phi_0(r)$, we use the Chew-Goldberger expression [Che50]

$$\phi_0(r) = \frac{N(e^{-\alpha r} - e^{-\beta r})}{r} \ , \tag{3.26}$$

where $\alpha = \sqrt{Me_d}$ and $\beta = 7\alpha$, and e_d is the deuteron binding energy.

Based on these approximations, it is not very difficult to calculate the energy distribution or angular distribution of the outgoing particles from the $^2H(\pi^-, n\gamma)n$ reaction.

3.2 Theoretical Approach Used in This Work

The details of the theory used in the calculation is given in [Gib75b, Gib75a, Gib77, Gib78] and the references cited in these articles. Nevertheless, I will give a brief description here.

The ${}^2H(\pi^-, n\gamma)n$ process can be visualized as in Figure 3.1. For this reaction, assume $\vec{p}_1$ and $\vec{p}_2$ are the momenta of the two neutrons and $\vec{q}$ is the momentum of the emitted photon (all momenta are measured in the laboratory frame). Define $\theta_{\gamma n}$ as the angle between the photon and neutron number 1, and θ_{nn} as the angle between the two neutrons. Conservation of energy and momentum gives:

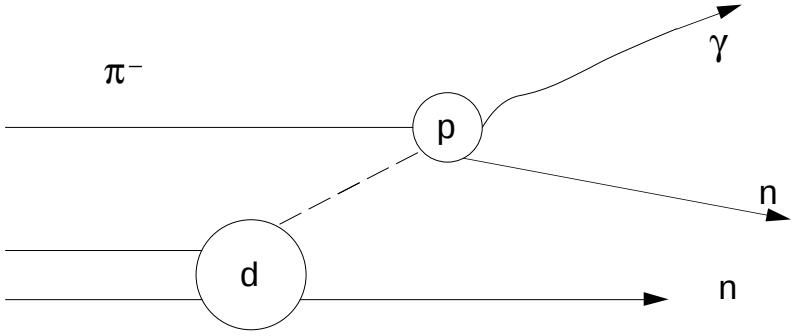

Figure 3.1: The ${}^2H(\pi^-, n\gamma)n$ reaction.

$$\vec{q} + \vec{p}_1 + \vec{p}_2 = 0 \tag{3.27}$$

$$q + \frac{1}{2m}(p_1^2 + p_2^2) = m_\pi - B_d - (m_n - m_p) \ . \tag{3.28}$$

The relative momentum of the two neutrons is

$$\vec{p} = \frac{1}{2}(\vec{p}_2 - \vec{p}_1 \ ) \ . \tag{3.29}$$

In the Exp1286 project, we measured the momenta of the photon and of one or both neutrons. This means we did a kinematically complete experiment.

For such an experiment, the differential spectrum (unnormalized) is described by

$$\frac{dN}{dx} \approx J(x) \mid< f \mid H' \mid i >\mid^2 p_1 p_2 \ , \tag{3.30}$$

where x is the variable of interest, the neutron TOF in our case. The phase-space factor $p_1 p_2$ is transformed to the appropriate TOF variable by means of the Jacobian $J(x)$. The H' is the transition operator for radiative pion absorption, which is taken from the non-relativistic reduction of the Chew-Goldberger-Low-Nambu (CGLN) amplitude for the radiative absorption of a pion by a nucleon [Che57b]. Since we are only interested in neutrons with very low relative momentum (the FSI area in the TOF spectrum), it is sufficient to consider H' to be of the form

$$H' = (A + B\vec{\sigma} \cdot \vec{\epsilon}) \ \exp(i\vec{q} \cdot \vec{r}/2) \ , \tag{3.31}$$

where $\vec{\sigma}$ operates on the proton spinor, $\vec{\epsilon}$ is the polarization vector of the photon and $\vec{r}/2$ represents the position vector of the proton from the center of mass of the deuteron, and A and B are constants, and are constrained by $\mid A \mid \ll \mid B \mid$ [McV61, Che57b]. The transition matrix element $< f \mid H' \mid i >$ can be written as

$$< f \mid H' \mid i >= \int d^3r \ \phi_\pi(r/2) \ \phi_d(r) e^{i\vec{q}\cdot\vec{r}/2} \phi_{nn}^{s(t)}(p, r) \ , \tag{3.32}$$

where $\vec{r}$ is the relative separation between the two neutrons. Thus, it is obvious that we have to evaluate integrals of this form to obtain the transition amplitude $< f|H'|i >$. In Equation 3.32 $\phi_{nn}^{s(t)}(p, r)$ represents the final state of the two neutrons having a relative separation $\vec{r}$ and a relative asymptotic momentum $\vec{p}$. The superscript $s(t)$ refers to the singlet (triplet) spin state,

$\phi_d(r)$ describes the initial deuteron, and $\phi_\pi(\frac{1}{2}r)$ is the initial-state pion wave function evaluated at the position of the proton.

The scattering length a_{nn} enters the expression through the phase shift of the $^1S_0$ part of $\phi_{nn}(p,r)$. The phase shift is determined in the effective range approximation by

$$p\ \cot\delta_0(p) = -\frac{1}{a_{nn}} + \frac{1}{2}r_{nn}p^2\ , \tag{3.33}$$

where δ_0 is the phase shift and r_{nn} is the effective range.

In early papers, the deuteron wave function was calculated using Reid's soft-core potential [Rei68], including the D state. Since deuterium is an isotope of hydrogen, the strong Stark mixing [Leo71] experienced by pionic deuterium insures that all captures occur from S orbitals. Thus, the only atomic effect on the spectrum comes from differences in atomic energy levels which are small enough to be neglected. The principle modification to the wave function of the bound pion from a constant wave function is due to the presence of the neutron. The shape of the modified pion wave function was estimated by using the Born approximation on an optical potential consisting of the π-neutron amplitude multiplying the neutron density in the deuteron. The P-wave contribution is negligible in this case [Kre69] so only S-wave scattering was assumed. Therefore ϕ_π is of the form:

$$\phi_\pi(r) \sim 1 + a_{\pi n}\left[\frac{1}{r}\int_0^r r'^2\rho(r')dr' + \int_r^\infty r'^2\rho(r')dr'\right]\ . \tag{3.34}$$

This function shows a decrease of about 15% at $r = 0$ from the constant model at $r = 50$ fm, the position where the change is a maximum. Therefore, it may safely be believed that higher-order terms in the Born series will not introduce errors in the correction larger that 15%. A zero-range wave function was used

in $\phi_{nn}(p,r)$ for the ${}^1S_0$ neutron-neutron scattering state:

$$\phi_{nn}^{ZR}(p,r) = j_0(pr)\ \cos\delta_0 + n_0(pr)\ \sin\delta_0\ , \tag{3.35}$$

where $j_0(pr)$ and $n_0(pr)$ are the spherical Bessel and spherical Neumann functions in the notation of Messiah [Mes61]. We can simplify it to

$$\phi_{nn}^{ZR}(p,r) = \frac{\sin(pr+\delta_0)}{pr}\ , \tag{3.36}$$

where δ_0 is the nn ${}^1S_0$ phase shift. Recall Equation 1.9, we have

$$p\cot\delta_0(p) = \frac{1}{a_{nn}} + \frac{r_{nn}p^2}{2}\ . \tag{3.37}$$

For the zero-range model to be a good approximation, we want the r_{nn} term to be one order of magnitude smaller than the a_{nn} term, i.e.,

$$\frac{\frac{r_{nn}p^2}{2}}{-\frac{1}{a_{nn}}} < 0.1\ . \tag{3.38}$$

Therefore, we must have

$$p < \sqrt{\frac{-0.2}{a_{nn}r_{nn}}}\ . \tag{3.39}$$

If we use $r_{nn} = 2.8$ fm and $a_{nn} = -18$ fm, then $p < 0.063$ fm^{-1} (which is about 12 MeV/C, using $\lambda = \hbar/p$). We will only choose the experimental data which satisfy this criteria when analyzing the data obtained from Exp1286. Note that this is not a very simple constraint.

3.2.1 Wave Functions of Incident Particles Used in the Calculation

The radial parts of the wave functions for the deuterons and the pions are shown in Figure 3.2. The pion wave function is suppressed by 15% at $r = 0$ compared with that at large r.

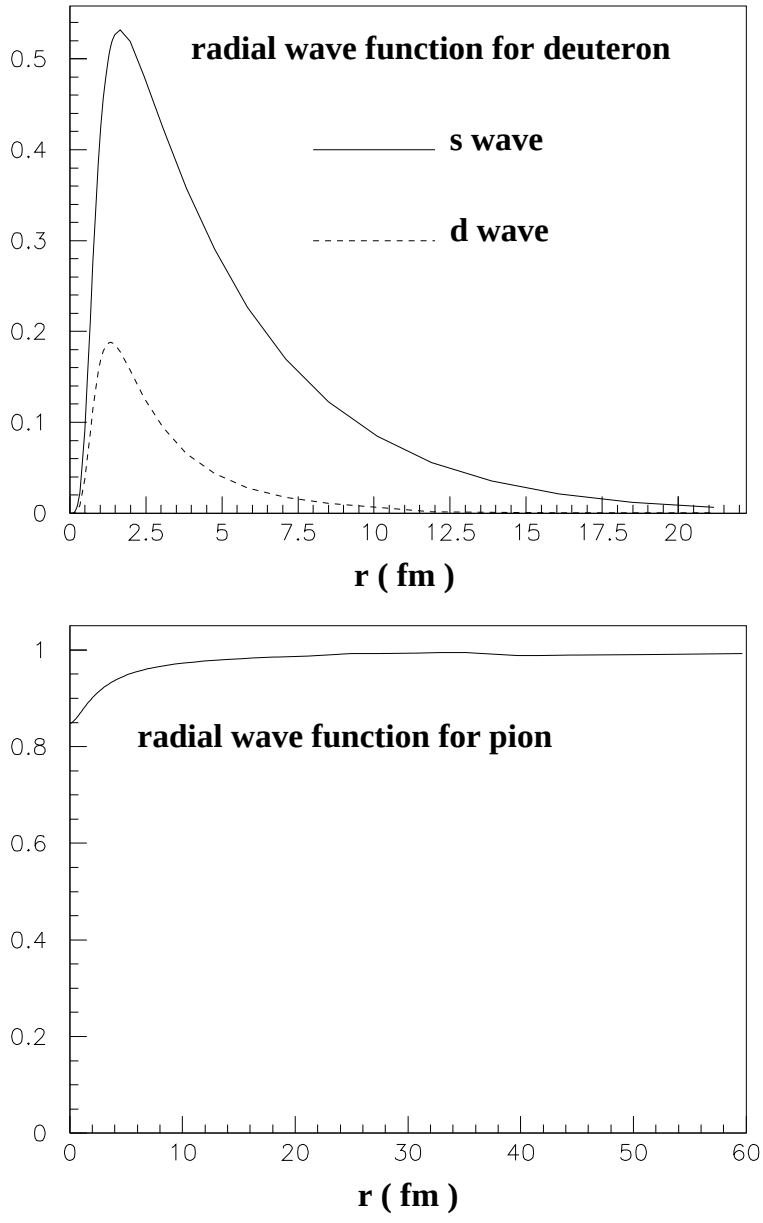

Figure 3.2: Wave functions of deuterons and pions used in the theoretical calculations. Source: [Gib97].

3.2.2 Neutron-Neutron Potential

For a N-N subsystem, the earliest and most commonly used separable potential models of the nucleon-nucleon interaction are those of Yamaguchi [Yam54] for the ${}^3S_1$ and ${}^1S_0$ channels,

$$V(p,p') = -g(p)g(p') \tag{3.40}$$

with the form factor

$$g(p) = \frac{\gamma}{\alpha^2 + p^2} \ , \tag{3.41}$$

which depends on two parameters γ and α. These parameters are determined by requiring that the potential reproduces the low-energy parameters a_{nn} (the scattering length) and r_{nn} (the effective range) in each channel. But this does not provide a short-range repulsion or a tensor force, hence, it must be generalized as

$$V_{ll'}(p,p') = -g_l(p)g_{l'}(p') + h_l(p)h_{l'}(p'); \ \ l,l' = 0,2 \ . \tag{3.42}$$

This type of model was first constructed by Tabakin [Tab] for the case of the nucleon-nucleon S-, P-, and D-waves and later by Mongan [Mon68, Mon69] for the case of all the partial waves with $J \leq 4$.

3.2.3 Theoretical Approximations and Uncertainties

Table 3.1 tabulates the individual uncertainties contributing to the extracted a_{nn} under different situations (source: [Gib75b, Gib75a]). The first column indicates reasons for the uncertainties. That is:

- A. n-n scattering wave function

	Reason for a_{nn} uncertainty	θ_{nn}= 5	10	20	30
A1	Zero range	-0.219	-0.282	-0.596	-1.337
A2 (i)	η matching ψ	-0.006	-0.011	-0.024	-0.051
A2 (ii)	$\eta = -5p$	+0.066	+0.078	+0.115	+0.152
A2 (iii)	$\eta = -0.5$	-0.325	-0.181	-0.121	-0.134
A3	Forbidden state final-state	0.000	0.000	+0.002	+0.006
B1	RSC deuteron, S state	-0.071	-0.088	-0.173	-0.329
B2	Hulthén deuteron	-0.082	-0.104	-0.204	-0.408
B3	Forbidden-state deuteron	-0.074	-0.092	-0.179	-0.346
C	r_{nn} = 2.6 fm	+0.038	+0.024	-0.038	-0.160
D1	$\delta_1 = 0.1p^2$	+0.002	+0.004	+0.008	+0.022
D2	$A/B = 0.1$	-0.032	-0.041	-0.094	-0.216
E	ψ_π= const.	-0.100	-0.129	-0.272	-0.590
F1	Complete forbidden state	-0.075	-0.096	-0.183	-0.359
F2	Hulthén plus zero range	-0.382	-0.496	-1.066	-2.500
F3	Hulthén plus zero range plus ($l > 0$) $\equiv$ 0	-1.475	-1.958	$\|\triangle a\| > 2.6$	$\|\triangle a\| > 2.6$

Table 3.1: The difference $\triangle a_{nn}$ in the value of a_{nn} extracted from the analysis and the value used to generate the pseudo data for various assumptions described in section IV of [Gib75b, Gib75a]. Column one stands for variations in the model, and A refers to n-n scattering wave function, B to the deuteron bound-state wave function, C to the effective range, D to the higher partial waves, E to the pionic wave function and F to the combined effects of all.

1. A1 indicates the difference between the zero-range model and the phase-shifted asymptotic wave function.

2. A2 stands for the differences caused by changes in the interior wave function ($r < R$) via adding a term of the form $\eta r^3(r-R)^3/pr$ to the $^1S_0$ partial wave. The parameter η was chosen in three different ways: (i). by matching the third derivative at R, (ii). by setting η to $-5p$, which corresponds to adding a constant to the wave function ψ over the range of interest, (iii). setting η to -0.5, which introduces an unphysical $1/p$ dependence to the wave function. For further details, one can refer to [Pic73].

3. A3 is the uncertainty caused by the possibility that the nucleons are composite particles and in a deeply bound state that is forbidden

by the Pauli principle.

- Deuteron bound-state wave function B1 covers the difference caused by the mix-in of the D state in the deuteron. Most estimates of the percentage of the D state range from 4% to 7%. B2 covers the uncertainly caused by the variations in the shape of the S-state wave function. B3 is due to similar effects as described earlier for A3.

- Effective range. This is the difference caused by changing r_{nn} from 2.8 fm to 2.6 fm.

- Higher partial waves. Considering the fact that only neutrons with relative energies of less than 35 MeV are considered, only the ^3P waves may be phase shifted significantly besides the $^1S_0$ partial wave. D1 is the difference attributed to the ^3P partial wave when maximizing the phase shift δ_1 to $0.1p^2$ radians. D2 is the difference between A/B equal to 0.1 and A being zero.

- Pionic wave functions.

- Combined effects: F1 to F3 are all due to the combination of the effects mentioned above.

3.3 Theoretical Predictions for the $\pi^- d \to nn\gamma$ Reaction

In this section, we present the results of calculations provided by our collaborators W.R. Gibbs and Ben Gibson of LANL. The calculation assumes that the target is a point target. Hence it is assumed that there is no multiple

scattering inside the target and no attenuation in the deuteron target. Also, the γ-ray detectors are assumed to be point detectors that can measure the energy and position of every incident γ exactly, and have an absolute efficiency of 100%. The neutron detectors are assumed to be point detectors that can detect the energy and position of every incident neutron exactly, and have an absolute efficiency of 100%; The γ rays are assumed to be detected at a fixed point. Under these assumptions, the energy spectrum and angular distribution of the outgoing neutrons from the $\pi^- d \to nn\gamma$ reaction are shown in Figures 3.3 to 3.7.

These figures demonstrate the theoretical predictions for the angular distribution of neutrons at different energies, and energy spectra at different opening angles (OA) based on a_{nn} and other parameters such as r_{nn} , R (effective radius of the neutron) and V (neutron-neutron potential). However, a_{nn} is by far the most sensitive factor for the theoretical predictions, so we will concentrate on variations with respect to a_{nn} .

From Figure 3.3, we notice several features. There are two prominent peaks: the FSI peak around $E_n = 2.4$ MeV and the QFS peak around $E_n = 9$ MeV. Also relatively speaking, there are more FSI neutrons (around 2.5 MeV) at larger opening angles then at smaller opening angles. Last, there are more total neutrons at larger opening angles.

From Figure 3.4, we notice that the FSI peak ($E_n = 2.4$ MeV) is around TOF = 120 ns for a flight path of 2.55 m, while the QFS peak ($E_n = 8.9$ MeV) is around TOF = 62 ns for the same flight path. Relatively speaking there are more neutrons around the FSI peak for larger values of a_{nn} than for smaller values.

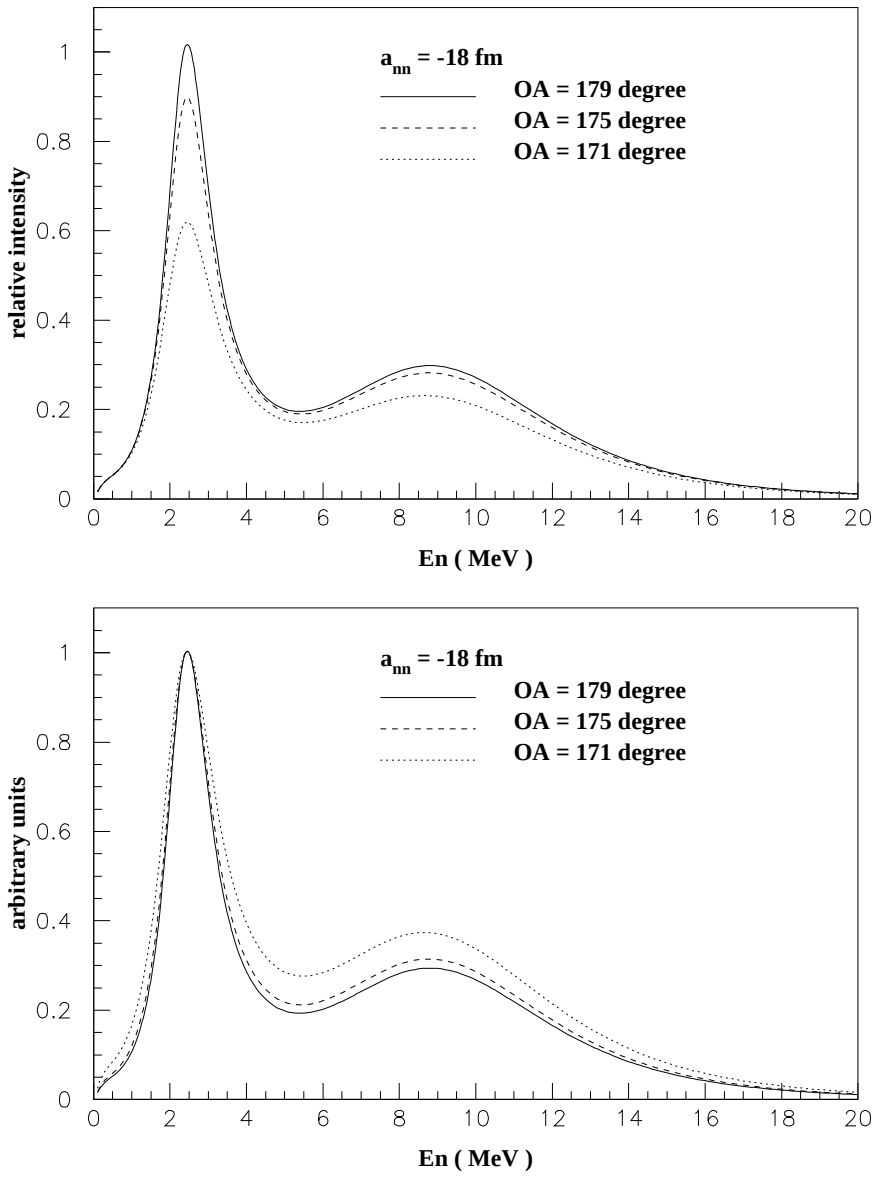

Figure 3.3: The E_n spectra at different opening angles for a specific a_{nn}. The opening angle (OA) refers to the angle between the γ-ray direction and the neutron direction. The top plot shows the relative intensity at different angles, while the curves are normalized to the same height in the bottom plot.

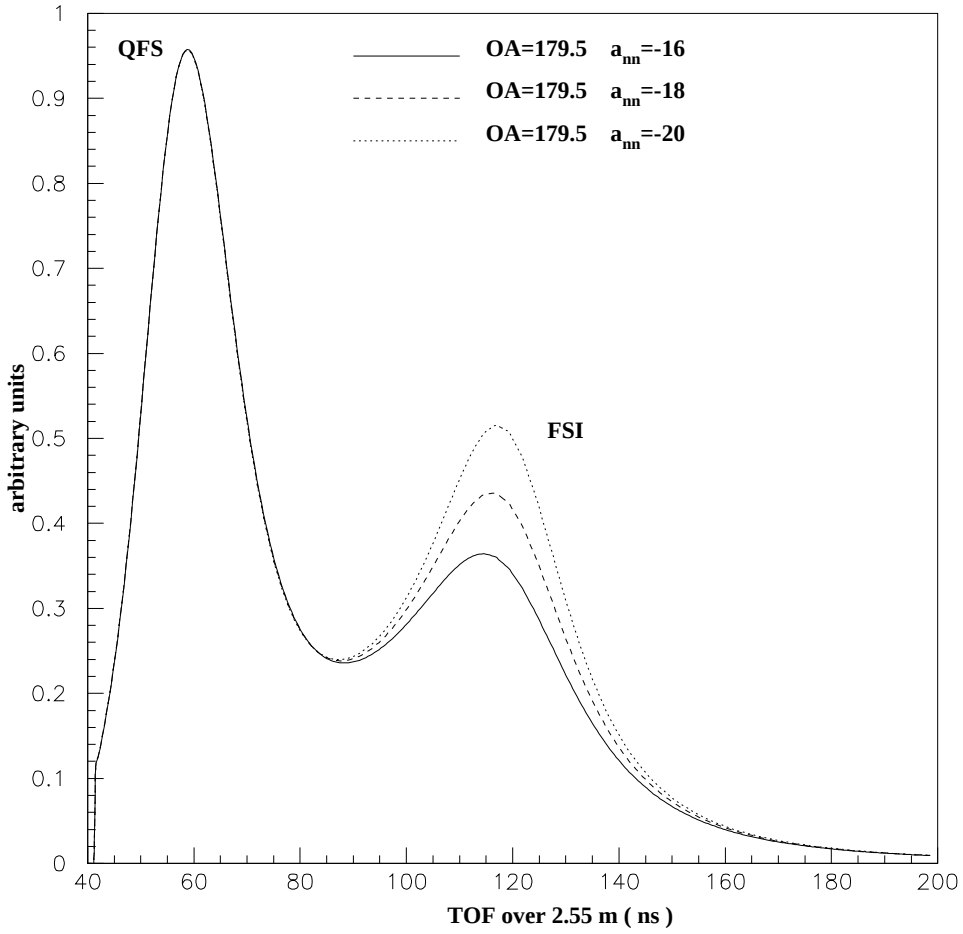

Figure 3.4: This figure shows the shapes of the TOF spectra for different a_{nn} at the opening angle of 179.5° , which refers to the angle between the γ-ray momentum and the neutron momentum. All the curves are normalized to have the same area in the QFS peak region.

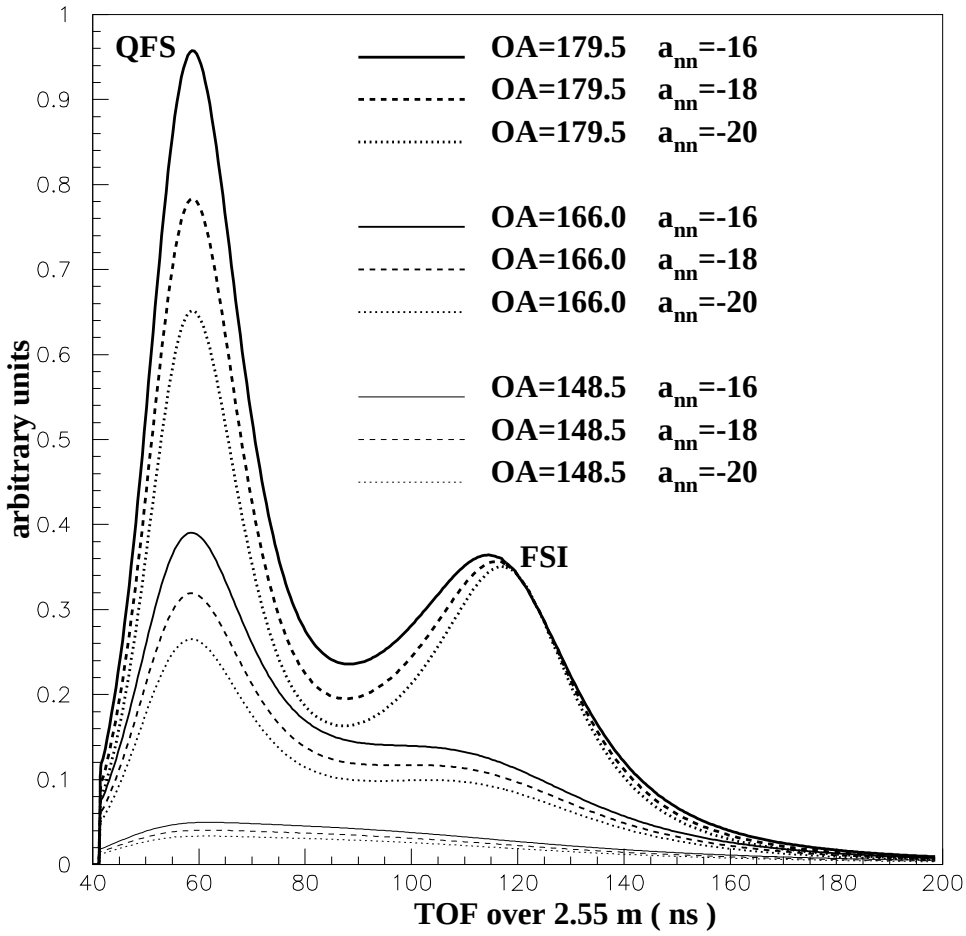

Figure 3.5: The E_n spectra at different opening angles and different a_{nn}. Opening angle (OA) refers to the angle between the γ-ray direction and the neutron direction. All the curves reflect the relative magnitude of double differential cross sections, with the maximum double differential cross section set to one in the data set for each value of a_{nn}.

Figure 3.5 is very similar to Figure 3.4. The difference is that in Figure 3.4 the curves were normalized to have the same height and in Figure 3.5 the curves are not normalized. Therefore, the relative magnitude of the double differential cross sections for the $^2H(\pi^-, n\gamma)n$ reaction are shown in Figure 3.5 for different values of a_{nn} and different opening angles.

In Figure 3.6, a_{nn} is fixed to be -18 fm. The top plot tells us that there are relatively more 2.5 MeV neutrons than 9 or 19 MeV neutrons per unit energy and per unit solid angle. In the bottom plot of the same figure, the curves in the top plot were normalized to have the same height. We can see that for the $^2H(\pi^-, n\gamma)n$ reaction the angular distribution of neutrons is more forward peaked for 2.5 MeV neutrons than that for 9 MeV or 19 MeV neutrons.

From Figure 3.7, where we only detect neutrons in a narrow energy bin around $E_n = 9$ MeV, one sees that there are relatively more neutrons when the absolute value of a_{nn} is smaller (i.e., when the n-n interaction is stronger), all other conditions being the same. Also, relatively speaking, when the absolute value of a_{nn} is smaller, the angular distribution for 9 MeV neutrons is more forward peaked.

The details regarding how to pick up a neutron energy and an opening angle for one of the outgoing neutrons from the $\pi^- d \to nn\gamma$ reaction will be discussed in section 4.1.

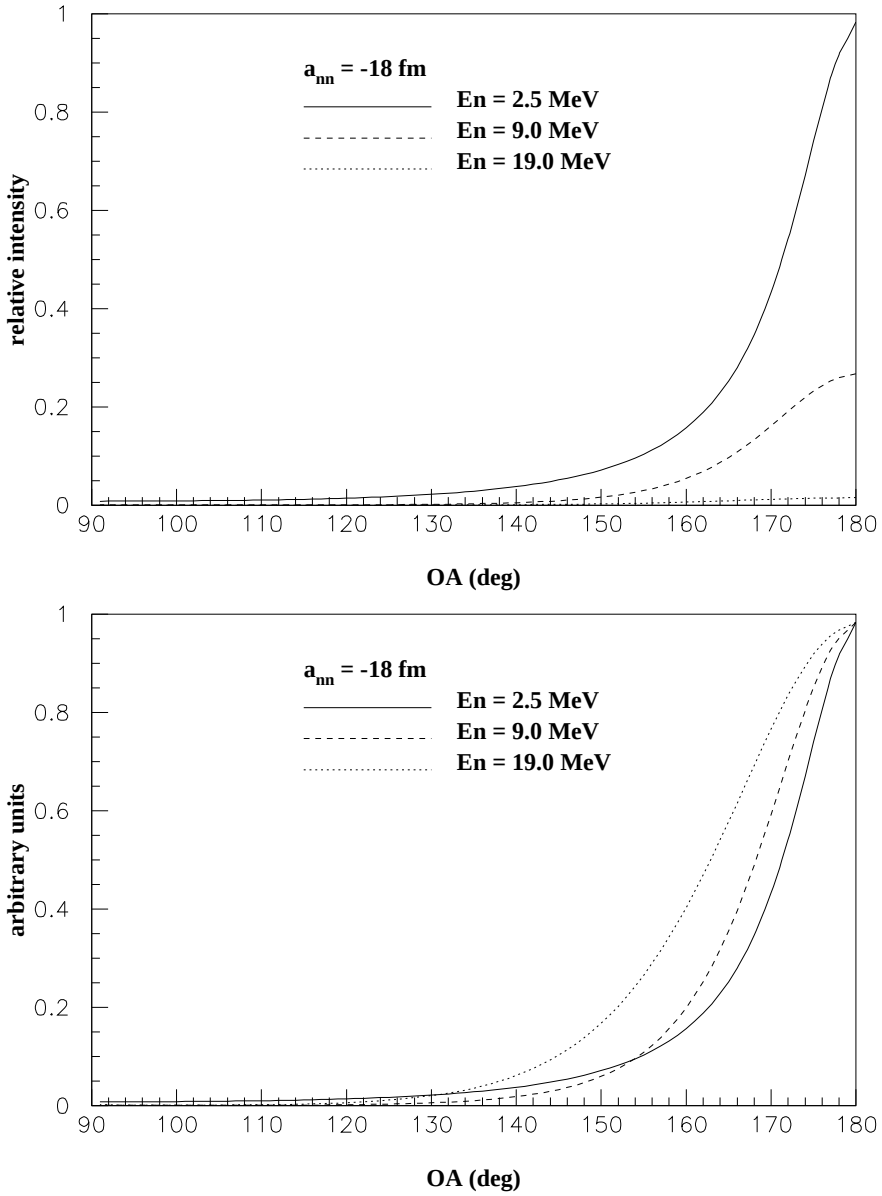

Figure 3.6: Angular distribution for different E_n for a specific a_{nn}. The top plot shows the relative intensity at different energies, while the curves are normalized to the same height in the bottom plot.

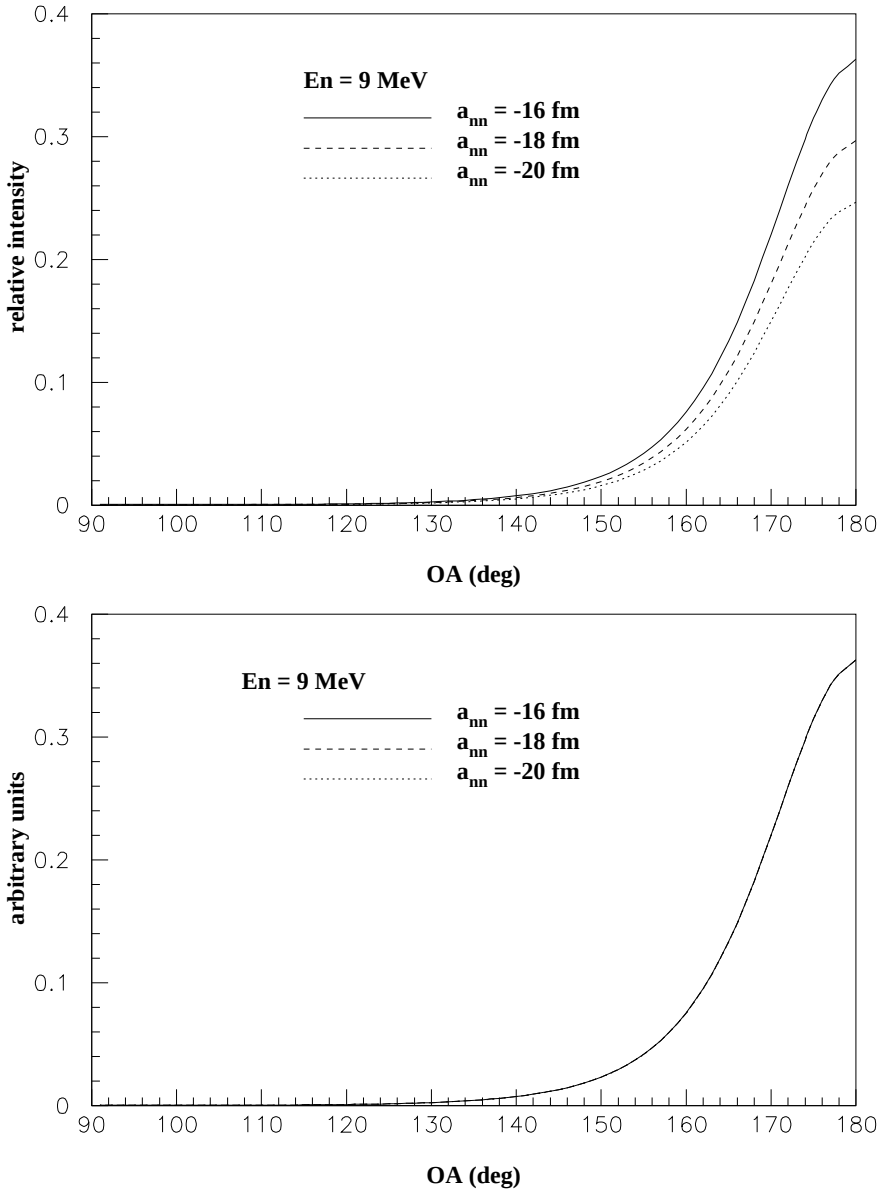

Figure 3.7: Angular distribution for different a_{nn} at 9 MeV. The top plot shows the relative intensity at different a_{nn} , while the curves are normalized to the same height in the bottom plot

Chapter 4

Monte-Carlo Simulation

In this chapter, we describe the event generation and particle tracking procedure for the LAMPF Exp1286 experiment. We start by explaining how the double differential cross sections were used to choose the energy and direction of emitted neutrons in the simulation of the $^2H(\pi^-, n\gamma)n$ reaction. Next, detector calibration parameters are determined using the $^1H(\pi^-, n)\gamma$ two-body capture reaction. The accidental coincidence events from data taken with the incident π^- beam on the deuterium target are used to determine the position-dependent efficiency of the γ-ray detector. The geometry parameters for the experimental setup were determined from an optical survey. Comparisons of data with the MC simulations were used to verify the geometry parameters. After the determination of the critical experimental parameters, the simulation is used to model the effects of the finite geometry of the setup, neutron scattering and reactions in the target materials and neutron scattering in the neutron detectors.

4.1 Event Generation

In this section, the procedure used to choose the E_n and direction of the first emitted neutron from $^2H(\pi^-, n\gamma)n$ reaction in the Monte-Carlo simulation is described. The choices are based on the relative double differential cross-section calculations of Gibbs and Gibsons (see section 3.3) for the $^2H(\pi^-, n\gamma)n$ reac-

tion. The relative double differential cross sections were tabulated as follows:

	j	0	1	$\cdots$	n_c	$n_c + 1$
i	$E_i \setminus \theta_j$	180.0	179.5	$\cdots$	1.5	0.0
0	0.0	p(0,0)	p(0,1)	$\cdots$	p(0,n_c)	p(0,n_c +1)
1	0.1	p(1,0)	p(1,1)	$\cdots$	p(1,n_c)	p(1,n_c +1)
2	0.2	p(2,0)	p(2,1)	$\cdots$	p(2,n_c)	p(2,n_c +1)
$\vdots$	$\vdots$	$\vdots$	$\vdots$	$\cdots$	$\vdots$	$\vdots$
199	19.9	p(199,0)	p(199,1)	$\cdots$	p(199,n_c)	p(199,n_c +1)
200	20.0	p(200,0)	p(200,1)	$\cdots$	p(200,n_c)	p(200,n_c +1)
201	E_{max}	p(201,0)	p(201,1)	$\cdots$	p(201,n_c)	p(201,n_c +1)

where n_c is the number of angles computed by Gibbs and Gibson (see section 3.3). They provided values of the matrix elements $p(i,j)$ for i between 1 and 200 (including 1 and 200) and for j between 1 and n_c. A matrix of this type was generated for several values of a_{nn} and r_{nn} . These matrices were eventually used to extract values for a_{nn} from the experimental spectra through the Monte-Carlo simulation. Calculations for each table were made at 200 discrete energies, from 0.1 to 20 MeV in 0.1 MeV steps and at n_c angles, making a matrix of $(200 \cdot n_c)$ grid points. A linear interpolation was used to obtain values at energies and angles between grid points. Outside the energy and angle ranges of the computed matrix elements, a linear extrapolation was used. To be more specific, the following extrapolations were made:

1.

$$p(201, j) = 0 \text{ for } j = 0, 1, \cdots, n_c, n_c + 1 \ . \tag{4.1}$$

2.

$$p(0, j) = 2.5\, p(1, j) - 1.5\, p(2, j) \text{ for } j = 1, 2, \cdots, n_c \tag{4.2}$$

3.

$$p(i,0) = p(i,1) - \frac{\theta_0 - \theta_1}{\theta_1 - \theta_2}(p(i,2) - p(i,1)\ )$$
$$\text{for } i = 0, 1, 2, \cdots, 200\ . \tag{4.3}$$

4.

$$p(i, n_c + 1) = p(i, n_c) - \frac{\theta_{n_c} - \theta_{n_c+1}}{\theta_{n_c-1} - \theta_{n_c}}\ (p(i, n_c) - p(i, n_c - 1)\ )$$
$$\text{for } i = 0, 1, 2, \cdots, 200\ . \tag{4.4}$$

The steps used to choose the energy for the first emitted neutron (E_n) from the $^2H(\pi^-, n\gamma)n$ reaction are described below.

1. The (relative) angle-integrated cross section was calculated at each energy in the matrix.

$$\sigma(E_i) = \sum_{j=0}^{n_c} \frac{1}{2}\ (p(i,j)\ \sin\theta_j + p(i,j+1)\ \sin\theta_{j+1}\ )\ (\theta_{j+1} - \theta_j\ )$$
$$\text{for } i = 0, 1, \cdots, 200, 201\ . \tag{4.5}$$

2. The angle-integrated cross sections were used to generate an energy-dependent relative probability distribution, i.e., the probability (relatively speaking) for E_n of the first emitted neutron to be between E_i and E_{i+1} is given by

$$P_{en}^{rel}[i] = \frac{\sigma(E_{i+1}) + \sigma(E_i)}{2}\ (E_{i+1} - E_i)\ . \tag{4.6}$$

We compute the relative probability that the first emitted neutron will have an energy between 0 and E_i, $P_e^{rel}[i]$, to be

$$P_e^{rel}[0] = 0\ . \tag{4.7}$$

$$P_e^{rel}[i] = \sum_{k=0}^{i-1}\ P_{en}^{rel}[k] \text{ for } i = 1, 2, \cdots, 199, 200, 201\ . \tag{4.8}$$

3. The distribution was normalized to unity, i.e.,

$$P_e[i] = \frac{P_e^{rel}[i]}{P_e^{rel}[201]} \text{ for } i = 0, 1, 2, \cdots, 199, 200, 201 \ . \tag{4.9}$$

4. Using a random number generator, we picked a probability between 0 and 1.0 for emitting a neutron of energy E_n from the $^2H(\pi^-, n\gamma)n$ reaction. If this randomly chosen probability falls between $P_e[i]$ and $P_e[i+1]$, then, the corresponding E_n is between E_i and E_{i+1}. Using an interpolation routine a value for E_n was obtained. The routine took into account the non-uniformity of the probability between E_i and E_{i+1}.

Once E_n was chosen, the next step was to choose the opening angle, θ, between the first emitted neutron and the γ ray. The following procedure was used.

1. A solid-angle weighted relative probability distribution was computed.

$$P_s(i,j) = p(i,j) \ \sin\theta_j \text{ for } j = 0, 1, 2, \cdots, n_c, n_c + 1 \ . \tag{4.10}$$

2. The relative probability for the opening angle to be between θ_j and θ_{j-1}, $P_{ang}^{rel}(i,j)$, is

$$P_{ang}^{rel}(i,0) = 0 \ , \tag{4.11}$$

and

$$P_{ang}^{rel}(i,j) = \frac{P_s(i,j-1) + P_s(i,j)}{2} \ (\theta_{j-1} - \theta_j \ ) \ ,$$
$$\text{for } i = 0, 1, 2, \cdots, 200, 201 \text{ and } j = 1, 2, \cdots, n_c, n_c + 1 \ . \tag{4.12}$$

3. The relative probability that a neutron with energy E_i is emitted between angle θ_0 and θ_j, $P_{oa}^{rel}(i,j)$, is

$$P_{oa}^{rel}(i,0) = 0 \tag{4.13}$$

and

$$P_{oa}^{rel}(i,j) = \sum_{k=0}^{j-1} P_{ang}^{rel}(i,k) \qquad (4.14)$$

$$\text{for } j = 1, 2, \cdots, n_c, n_c + 1 \ .$$

4. The probability array was normalized as follows:

$$P_{oa}(i,j) = \frac{P_{oa}^{rel}(i,j)}{P_{oa}^{rel}(i,n_c+1)}$$

$$\text{for } i = 0, 1, 2, \cdots, 200, 201 \text{ and for } j = 1, 2, \cdots, n_c, n_c + 1 \ . \qquad (4.15)$$

The algorithm worked as follows: if E_n happens to be E_i and a random number between $P_{oa}(i,j)$ and $P_{oa}(i,j+1)$ was picked, then an opening angle between θ_{j+1} and θ_j was selected. If E_n was not exactly equal to an E_i in the matrix, we interpolated the angular distribution:

$$tmpa(j) = r_i \ P_{oa}(i,j) + r_{i+1} \ P_{oa}(i+1,j) \qquad (4.16)$$

$$\text{for } j = 0, 1, 2, \cdots, n_c, n_c + 1 \ ,$$

where

$$r_i = \frac{E_{i+1} - E_n}{E_{i+1} - E_i} \ , \qquad (4.17)$$

$$r_{i+1} = \frac{E_n - E_i}{E_{i+1} - E_i} \ . \qquad (4.18)$$

Obviously,

$$r_i + r_{i+1} = 1 \ . \qquad (4.19)$$

Using the interpolated angular distribution, a number between 0 and 1.0 was randomly selected. The values of tmpa(j) and tmpa(j+1) were just below and above the random number. By inference, the opening angle must be between θ_j and θ_{j+1}. As in the case of the neutron-energy selection, the fact that θ is not uniformly distributed between θ_j and θ_{j+1} was taken into account.

4.2 Procedures Followed in the Monte-Carlo Simulation Code

In the previous chapters, we reviewed the experimental data from Exp1286, and the predictions from the collaborating theorists, W. R. Gibbs and B. F. Gibson. One might want to ask: what is the purpose of the Monte-Carlo (MC) simulation? The reason is that the theoretical predictions do not account for the finite geometry, neutron scattering and reactions in the target materials and neutron scattering in the neutron-detector array. Therefore, we have to simulate these effects. The MC simulation averages the point-geometry predictions over the finite geometry of the experimental setup and over the energy, position and time resolution of the detection system. It incorporates into the predictions the effects due to neutron scattering in the target materials, neutron attenuation in the target materials and air and scattering in the neutron-detector array.

In our simulation of each event, the natural progression of the particles from the reaction site in the target to the detectors is followed. This scheme has the advantage over forced-scattering simulations in that the contributions from each scattering process are internally consistent, thereby avoiding the need for normalization factors between scattering processes, as are often needed in forced-scattering simulations. The disadvantage is efficiency. In our scheme only a small fraction of the incident pions result in detected events, as opposed to the 100% in forced-scattering simulations. Details of the event generation and particle tracking MC simulation code are given below.

Figure 4.1 shows the flow chart of the MC code. Each event is simulated as follows.

1. A random position is picked inside the target cell (liquid deuterium/hydrogen). Each point is weighted by the experimentally determined distribution of stopped pions in the target. The determination

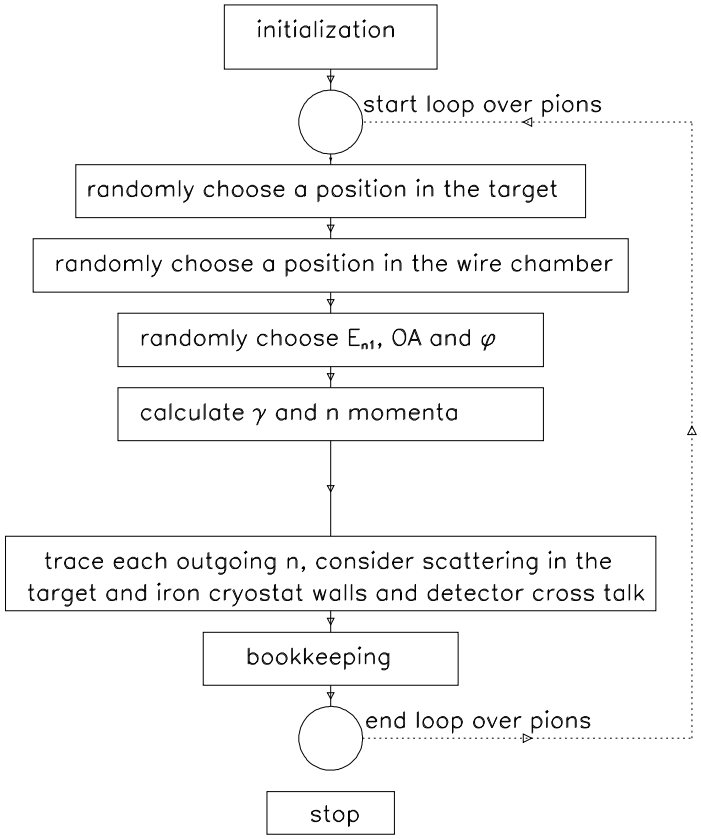

Figure 4.1: Flow chart of the Monte-Carlo simulation code.

of the stopped pion distribution in the target is described in section 4.2. For the purpose of this discussion, we use the simple radial dependent beam intensity shown in Figure 4.2 in the vertical direction and a uniform density in the other two directions.

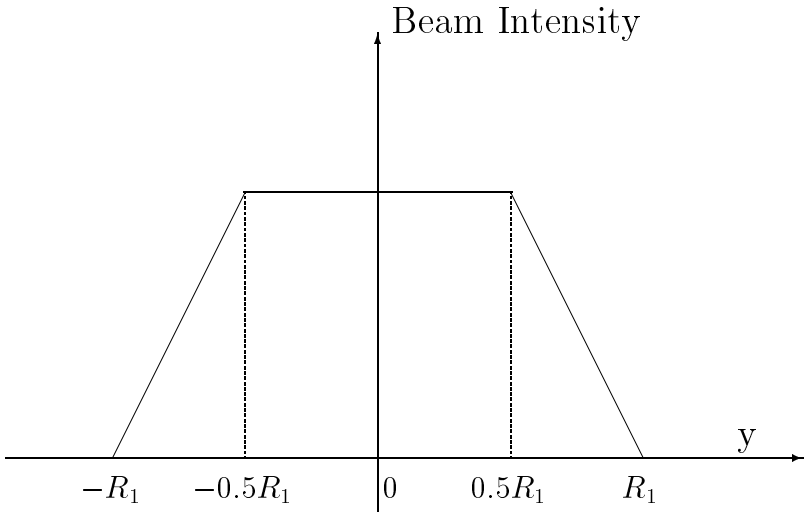

Figure 4.2: A sample beam profile along the y direction, which is the horizontal direction perpendicular to the beam direction. R_1 is the radius of the target.

2. A random direction for the outgoing γ for either the ${}^1H(\pi^-, n)\gamma$ reaction or the ${}^2H(\pi^-, n\gamma)n$ reaction is chosen [1]. The choice of the γ-ray direction is constrained to the solid angle subtended by the wire chamber. The assumption of equal probability in all directions for the emissions of γ rays makes sense because the capture processes (either the ${}^2H(\pi^-, n\gamma)n$ reaction or the ${}^1H(\pi^-, n)\gamma$ reaction) are almost solely due to S-wave capture, i.e., contributions from P-waves and higher angular momentum states are negligible, making the cross section isotropic in the c.m. system, which is the same as the lab system for the capture of stopped pions.

[1] We did experiments with either a hydrogen target or a deuterium target. Therefore, simulations were made for both the ${}^1H(\pi^-, n)\gamma$ reaction and the ${}^2H(\pi^-, n\gamma)n$ reaction.

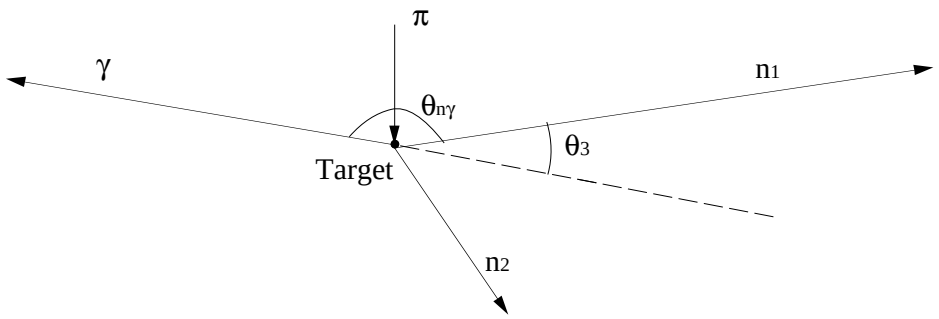

Figure 4.3: Definition of θ_3.

3. For the $^2H(\pi^-, n\gamma)n$ reaction, the E_n and neutron-gamma opening angle ($\theta_{n\gamma}$) of one of the outgoing neutrons are chosen. The angle θ_3 is the supplement of the opening angle between the γ ray and the neutron and is defined in Figure 4.3. The frequency of the selected E_n values are distributed according to the calculated double-differential cross sections using the procedure described in the previous section. A schematic view of a direct neutron from the liquid target to the detectors is shown in Figure 4.4. After an E_n value is selected, a value for θ_3 is picked. The frequency of the θ_3 values is determined from the angular dependence of the cross section at each neutron energy. For the hydrogen target, this step is skipped, since in $\pi^- p$ capture the neutron and γ ray are always emitted in opposite directions with fixed energies, 8.9 MeV for the neutron and 130 MeV for the γ ray.

4. The next step is to choose a direction for the same outgoing neutron. The choice of θ_3 in the previous step defines a cone of directional vectors for the neutron momentum. A direction on the cone is randomly chosen to set the direction of the neutron. In this case, every direction along the conic lines are equally probable, since the differential cross sections have no azimuthal dependency. This step is skipped for the hydrogen target, since the $\pi^- p$ capture has a two-body final state, only one neutron and

the γ ray. In that case the neutron direction is exactly opposite to that of the γ.

5. The momentum of the second neutron and the energy of the γ are calculated using conservation of linear momentum and energy. This step is skipped for the hydrogen target, because in that case, the neutron energy is fixed at 8.9 MeV. The attenuation of the γ rays in the target components due to Compton scattering and positron-electron pair production is negligible.

6. Next, each neutron is tracked through the target material towards the neutron-detector array. To check whether the neutron scatters before exiting the liquid, a random number x between 0.0 and 1.0 is generated. If the value of x is less than the probability for neutron elastic scattering, then the neutron is scattered once before transporting it to the cryostat wall. A schematic of a neutron that scatters once in the liquid deuterium target before being detected is shown in Figure 4.5. For this event, the neutron labeled n_1 was headed away from the neutron-detector array before being scattered in its direction. This type of event results in a gain in the number detected neutrons and is referred to as "in-scattering". The gains from "in-scattering" events are countered by the loss due to attenuation, i.e., a neutron was headed toward a detector but was scattered to or reacted at an angle outside the solid angle of the array. The probability for neutron elastic scattering in a material is

$$prob_{sc} = 1 - \exp(-n_t \, l \, \sigma_{el}(E_n)) \ , \tag{4.20}$$

where l is the distance an unscattered neutron would travel before leaving the material, n_t is the number density of the target nuclei and $\sigma_{el}(E_n)$ is the total elastic scattering cross section for neutrons in the target material. Refer to Figure G.1 and Figure D.1 for the neutron total elastic scattering cross section for hydrogen and deuterium, respectively. If the

neutron scatters, then a location in the target must be chosen as the scattering site. The distance l_x between the π^- capture site and the neutron scattering position is

$$l_x = l \frac{\ln(1-x)}{\ln(1-prob_{sc})} \ . \tag{4.21}$$

Then the time of flight (TOF) for a flight path of l_x for neutrons with energy E_n is calculated. The energy of the neutron scattered to an angle ψ is calculated using conservation of linear momentum and energy. The distribution of the ψ values is determined by the shape of the differential cross section $\sigma(\psi)$ for elastic scattering. The probability for an elastic scattering having the scattering angle between ψ and $\psi + \delta\psi$ is

$$P_{sc}(\psi, \delta\psi) = \frac{\sigma(\psi)\sin\psi d\psi}{\int_0^\pi \sin\psi'\sigma(\psi')d\psi'} \ . \tag{4.22}$$

For np scattering at low energies, the angular distribution takes the shape of $\cos(\psi)$ in the lab. system, where ψ is the scattering angle in the laboratory system and is always less than 90 degrees. For nd scattering, the angular distributions are available from the National Nuclear Data Center (NNDC) at Brookhaven National Laboratory (BNL). The nd total cross section increases rapidly with decreasing energy at energies below 10 MeV. Since most of the neutrons generated from the $^2H(\pi^-, n\gamma)n$ reaction have energies of less than 10 MeV, the attenuation of neutrons in the deuterium target must be included in the simulation. Because the probability for the $^2H(n, nnp)$ breakup reaction and the $^2H(n, n')$ inelastic scattering are very small compared to that for nd elastic scattering at neutron energy below 10 MeV, only elastic scattering is considered in the simulation of scattering. However, elastic and non-elastic processes are included when accounting for attenuation. In the case of the hydrogen target, the total cross section is almost exactly the same as the elastic scattering cross section.

7. Similar to the previous step, each neutron is tracked through the stainless steel wall of the cryostat. First, it is determined if a scattering process occurs in the wall. The probability of scattering within the stainless steel wall depends on the position where the neutron enters the wall and the direction it is moving. The total elastic cross section for $Fe(n,n)$ scattering is shown in Figure F.1. The same procedure used to handle scattering in the deuterium (or hydrogen) is followed. For neutrons that scatter in the iron, the TOF is calculated from the last interaction site in the liquid target to the scattering location in the wall. A schematic of a $\pi^- d$ capture neutron scattering in the steel wall before reaching the neutron detector is shown in Figure 4.6. The event depicted there would contribute to the in-scattering gain. The energy of the scattered neutron is calculated using nFe elastic scattering kinematics.

   The probability of a neutron scattering from the cryostat wall was determined using a multi-step procedure. We started by randomly picking a scattering angle based on the neutron energy and scattering-angle dependent experimental cross sections. The differential cross sections for neutron elastic scattering were obtained from NNDC at BNL. Then the energy of the scattered neutron was computed. Each neutron was then tracked. If it hit a neutron detector, it was detected with a specific weight factor. The weight factor was the product of the neutron transmission factor inside the liquid target, the neutron transmission factor in the air between the liquid target and the target wall, the transmission factor in the target wall, the transmission factor in the air between the target wall and the neutron detector, and the efficiency of the neutron detector. Also, if the neutron was scattered inside the liquid target, the transmission before and after the scattering was considered separately. This was also done when the neutron scattered inside the cryostat wall. The absolute detection efficiency of a neutron detector depends on the detector

dimensions, the scintillator type, the threshold setting, and the neutron direction and energy.

In addition to tracking the neutrons from the target to the detector array, effects due to neutron "cross talk" between the detectors was simulated. A neutron can be scattered either by a proton or a carbon nucleus in the liquid scintillator of one detector and be detected in an adjacent detector. We call this process "cross talk". Details about cross talk will be discussed later.

When neither outgoing neutron hit a neutron detector, the simulation was ended for the current event. We refer to a simulated event in which the outgoing γ and one of the outgoing neutrons are detected, as a double-coincidence event or a "double". A simulated event in which the outgoing γ and both of the outgoing neutrons are detected is called a triple-coincidence event or a "triple". In each simulation the following statistical information is recorded: the number of neutrons that hit each detector, the number of detected neutrons that are scattered inside the liquid target, the number of detected neutrons that are scattered inside the iron wall, the number of double events, the number of triple events, for the triple events, the distribution of the angle between the two outgoing neutrons.

8. For each event ("double" or "triple"), an informational array was output to a binary data file[2] for later analysis. The array (named datsum[17] in C, which was defined as an array of short integers with 17 elements) had the following structure (I shall use another font to describe this array):

```
datsum[1]  = DET1 # (id number)
datsum[2]  = DET2 # for triples (0 for doubles)
```

[2]A binary file takes only about one third of the disk space a corresponding ASCII file needs to store the same amount of information.

```
datsum[3]  = energy of neutron 1 (unit: 0.01 MeV)
datsum[4]  = energy of neutron 2 (unit: 0.01 MeV, = 0 for
             doubles)
datsum[5]  = tag* for neutron 1
datsum[6]  = tag* for neutron 2 (0 for doubles)
datsum[7]  = DET1 TOF channel,
datsum[8]  = DET2 TOF channel, (= 0 for doubles)
datsum[9]  = gamma energy (unit: 0.01 MeV)
datsum[10] = gamma x coordinate channel (unit: 0.01 cm)
datsum[11] = gamma y coordinate channel (unit: 0.01 cm)
datsum[12] = gamma z coordinate channel (always 0)
datsum[13] = #1 opening angle channel  (unit mrad)
             (angle between gamma and the neutron detected
               by DET1)
datsum[14] = #2 opening angle channel  (unit mrad)
             (angle between gamma and the neutron detected
               by DET2, 0 for doubles
datsum[15] = weight1, (weight factor for neutron detected
             by det. DET1)
datsum[16] = weight2, (weight factor for neutron detected
             by det. DET2, 0 for doubles)
```

The tags are as follows:

```
* tag=0 if the neutron is not scattered before it reaches
        the neutron detector
  tag=1 if the neutron is scattered in liquid target before
        it reaches the neutron detector
  tag=2 if the neutron is scattered in iron wall before it
        reaches the neutron detector
  tag=5 if the neutron is scattered by a proton in the liquid
```

```
        scintillator before it is detected by an adjacent
        neutron detector
  tag=6 if the neutron is scattered by a carbon nucleus in the
        liquid scintillator before it is detected by an
        adjacent neutron detector
```

The above procedure was repeated for 2×10^8 incident π^- mesons. With this number of pions, a statistical precision of $\pm 1\%$ was obtained in the QFS peak of the aggregate NTOF spectra for the entire array for a 0.05 radian wide cut on θ_3 . The histograms were managed using the HBOOK software package from CERN. The standard histograms that were accumulated during a simulation were the distribution of π^- reaction positions inside the target, the distribution of neutron energies, the distribution of kinetic energies of neutron 1 versus that of neutron 2 for triple events, the distribution of the opening angle of neutrons for doubles, and the neutron TOF for each detector and the entire detector array. Though the distribution of TOF's of each detector is nearly identical, there are noticeable differences in their TOF spectra due to differences in the time offsets and the time calibrations (see Table 4.1). In the neutron TOF spectra TOF_{ch} is related to the physical TOF (TOF_{ns}) by

$$TOF_{ch}(i) = \frac{TOF_{ns}(i) - TOF\_OFF_{ns}(i)}{nsperch(i)} \ , \tag{4.23}$$

where variable i is the neutron detector number (it ranges from 1 to 26), and subscripts ch and ns indicate the units (channels or nanoseconds) used for the TOF. The TOF_OFF parameter is the TOF offset in ns, and $nsperch(i)$ is the time calibration (ns/ch) for the i-th neutron detector. Refer to Table 4.1 for detailed information about $nsperch(i)$.

The tenability of the results from the MC simulation was checked using simple computations with realistic approximations. The details are described in Appendix H.

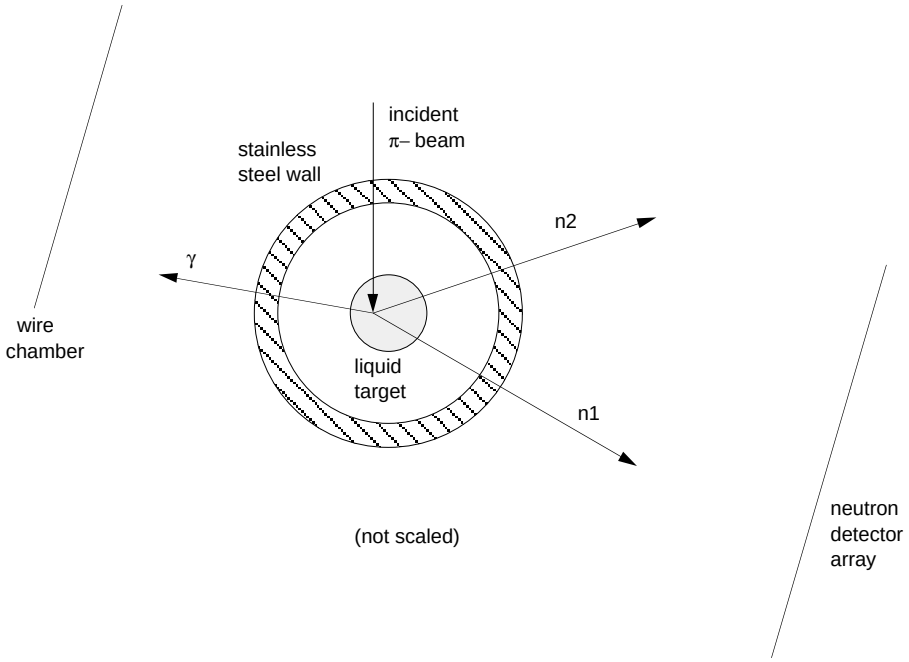

Figure 4.4: A schematic view of events from direct neutrons.

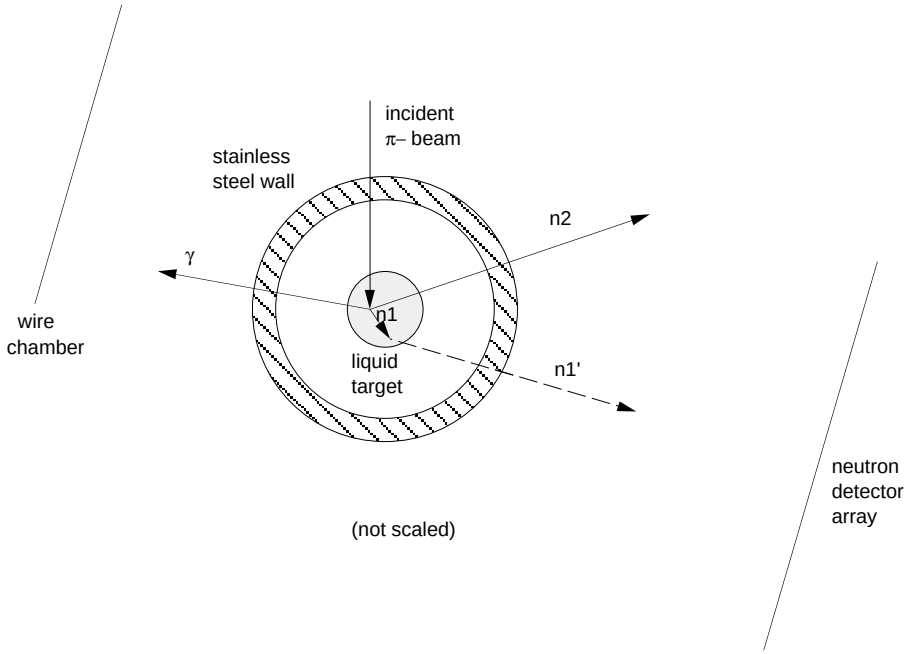

Figure 4.5: A schematic view of neutron scattering inside the liquid target.

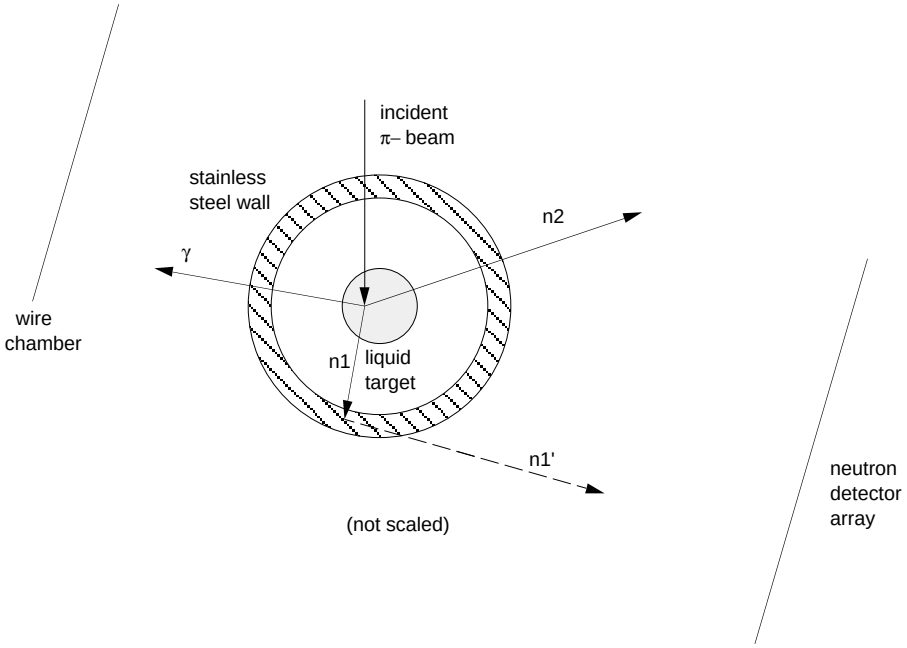

Figure 4.6: A schematic view of neutron scattering inside the stainless steel wall.

4.3 Sensitivity of Neutron-Flux Attenuation to Target Size

The value of a_{nn} was extracted from the shape of the measured neutron TOF spectra. The experimental TOF spectra was fitted with the theoretical predictions from the Monte-Carlo simulations using only two adjustable parameters, a normalization factor and a_{nn} . More than 95% of the detected neutrons had energies in the range from 0.5 MeV (just above threshold) to 12.0 MeV. Because the total cross sections for low-energy neutron interactions in materials are very energy dependent, the shape of the detected neutron energy distribution (TOF spectra) is critically influenced by the amount of target material (deuterium or hydrogen and iron) the neutrons traverse from the site of their creation in the target to the detector array. The neutron attenuation (out-scattering probability) depends on the dimensions and density of the deuterium/hydrogen target,

the thickness of the cryostat wall, and the stopped pion distribution inside the liquid target. In this section, we explore the sensitivity of the TOF spectra to the radius of the liquid deuterium target.

Shown in Figure 4.7 are predictions of TOF spectra for three liquid deuterium targets with different radii (R = 0.0 cm, R = 1.78 cm and R = 3.00 cm). The relative cross-section calculation of Gibbs and Gibson for the $^2H(\pi^-, n\gamma)n$ reactions were used to generate the TOF spectra. In each case the π^- was captured at the center of the target and the neutrons were transported through the half of the target on the side of the neutron-detector array. The effects of attenuation in the cryostat wall and in the air between the detector array and the cryostat were omitted in the calculations. All TOF distributions in Figure 4.7 are the results of tracking neutrons from 5 million $^2H(\pi^-, n\gamma)n$ reactions. The influence of the attenuation on the shape of the neutron TOF spectrum is clearly demonstrated in the top half of Figure 4.7. The neutrons from the point target are transported to the detectors without attenuation. The other two TOF curves include the neutron attenuation through half (one radius) the target diameter. The TOF spectra for the three target sizes were normalized at the peak of the QFS enhancement (see section 1.3) to illustrate the influence of attenuation on the shape of the TOF spectrum. The absolute attenuation factors are shown in the bottom half of Figure 4.7. The radius of the target used in our experiment was 3.00 ± 0.10 cm. The uncertainty in the target size is due to bulging of the 0.005 mil thick mylar cell under pressure; the mylar cell holds the liquid deuterium/hydrogen. Using the sensitivity calculations presented here, we infer that the 0.10 cm uncertainty in the target radius produces a less than 0.1 fm uncertainty in our determination of a_{nn} .

The ratio in the bottom plot of Figure 4.7 is defined as

$$ratio = \frac{\text{counts for radius} = 1.78 \text{ cm } (3.00 \text{ cm})}{\text{counts for radius} = 0.00 \text{ cm}} \ . \qquad (4.24)$$

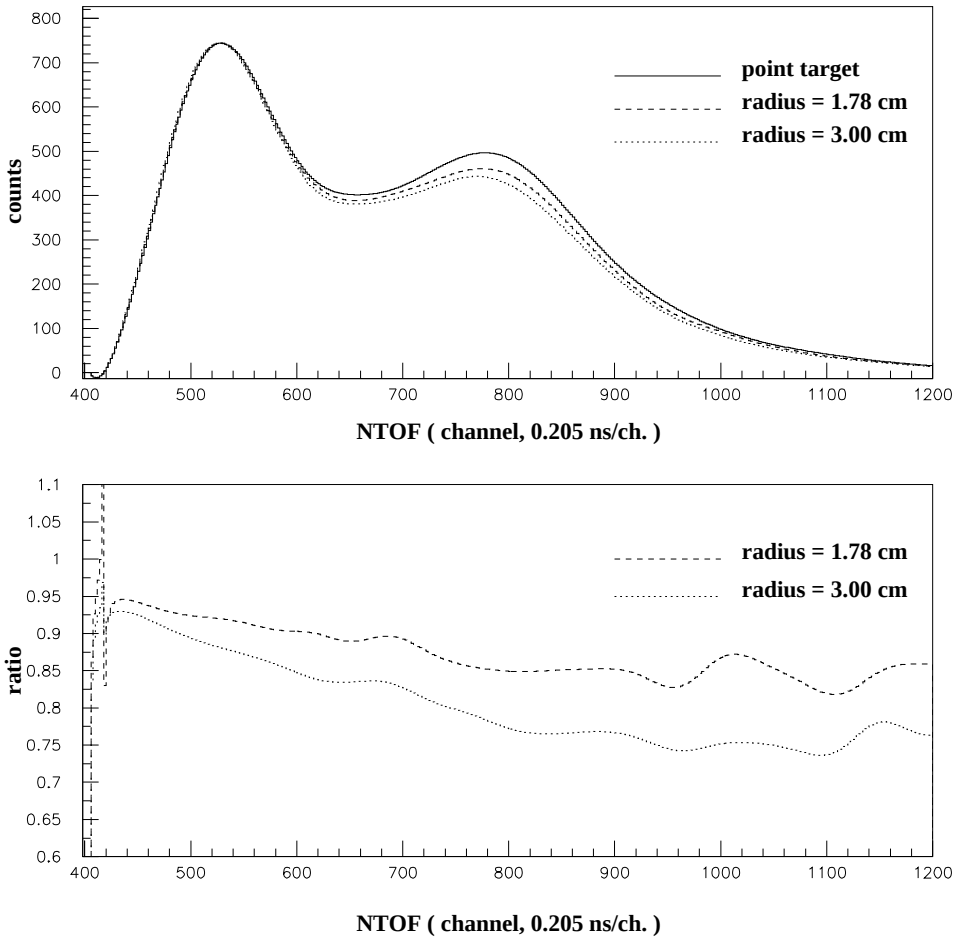

Figure 4.7: Top plot shows the neutron TOF spectra for three different target radii (solid curve for R = 0.00 cm, dashed curve for R = 1.78 cm and dotted curve for R = 3.00 cm). The spectra ae normalized at the QFS peak. The bottom plot shows the ratio of TOF spectra to the spectrum for the point target.

4.4 Determination of Experimental Setup and Detector Calibration Parameters

Because the $^2H(\pi^-, n\gamma)n$ reaction has three particles in the final state, particle energy and momentum conservation rules do not sufficiently restrict the particles' relative emission angles and energies for this reaction to be useful in determining experimental setup parameters to the accuracy needed for input to computer simulations. Therefore, we used the kinematically simpler $^1H(\pi^-, n)\gamma$ reaction, because it has only two particles in the exit channel causing the relative emission angles and energies to be tightly constrained by energy and momentum conservation rules. Special calibration runs were made with the target cell filled with liquid hydrogen instead of deuterium. The feature of the $^1H(\pi^-, n)\gamma$ capture reaction that the neutron and γ ray are always emitted in exactly opposite directions (like the γ rays in e^+e^- annihilation) proved to be an impressively valuable diagnostic tool. The $^1H(\pi^-, n)\gamma$ reaction was used to:

1. Verify the experimental geometry parameters determined from optical survey measurements;

2. Determine the time resolution of each neutron detector with respect to the γ-ray detector;

3. Determine the energy resolution of the CsI detector;

4. Determine (with a reasonable certainty) the stopped π^- distribution in the target;

5. Determine the out-scattering (attenuation) and in-scattering in the liquid target and the cryostat wall;

6. Determine the neutron scattering between detectors (cross talk).

All parameters determined from the $^1H(\pi^-, n)\gamma$ calibration data were used in the simulations of the $^2H(\pi^-, n\gamma)n$ reaction. Minor adjustments were made to the stopped π^- distribution in the target to account for slight difference in π^- beam tunes between the calibration runs and the production runs. The six items enumerated above are discussed in the subsections to follow.

4.4.1 Verification of the Experimental Setup Geometry

Optical surveys of the experimental setup were done immediately before data acquisition and at the end of the experiment. The positions of the center of the front face of each neutron detector were logged in the survey. All values were measured relative to the fudicial marks in the LEP cave. In both surveys, the origin was at the pivot point of the NMS detector crates. Because of differences in the calibration input in the two surveys, the origin of the coordinate systems differed by about 1.8 cm. Because the operator had more confidence in the second survey, we used the data from it in the simulations. The primary focus of the first set of simulations was to make certain that the geometry data taken from the optical survey and other sources were correct. The critical factors were the coordinates and dimensions of the target, the wire chamber and the neutron detectors, and the orientation of the wire chamber.

We obtained good agreement between the simulation and the $^1H(\pi^-, n)\gamma$ data. The quality of the agreement gave us confidence in the measured geometry parameters. There was only one significant adjust needed. Because there are only two particles in the exit channel of the $^1H(\pi^-, n)\gamma$ capture reaction and the π^- is captured at rest, there is a one-to-one correspondence between the position where the neutron hit a neutron detector and the position of the associated γ ray at the plane of the WC. It is this rigid relationship between the relative directions (always emitted exactly in opposite directions) of the emitted neutron and γ ray that makes the $^1H(\pi^-, n)\gamma$ reaction a powerful tool for

high precision geometry and dosage tomography measurements. The geometry parameters were checked by comparing the data for positions of the image of each neutron detector with that from the simulation. A consistent description of the centroids of the images of the neutron detectors in the WC could only be achieved by shifting the center of the hydrogen target down stream by about 1 cm from the origin of the survey coordinate system. The same geometry parameters were used in the MC simulation of the ${}^2H(\pi^-, n\gamma)n$ reaction.

4.4.2 Determination of Detector Time Resolution

The neutron time-of-flight (NTOF) spectra for the ${}^1H(\pi^-, n)\gamma$ reaction determine the effective time calibration (the product of the time per channel of the time-to-digital converter (TDC) and the mean particle flight path) and resolution of each neutron detector. By identifying two peaks of particles with well-known TOF, the prompt γ peak and the neutron peak from the ${}^1H(\pi^-, n)\gamma$ reaction in the NTOF spectra and the flight-path distances from the survey, we were able to determine the time per channel in the NTOF spectrum for each detector. Since the critical calibration procedure for converting from TOF to particle energy is the product of the TDC time-per-channel conversion factor and the flight-path length, precise knowledge of them separately is not necessary. So by fixing the distance between the liquid hydrogen target and each neutron detector to the value obtained from the optical survey, we were able to deduce the effective TDC time calibration (the TDC conversion factors needed to describe the experimental NTOF for the ${}^1H(\pi^-, n)\gamma$ reaction).

The flight-path lengths in the second column of Table 4.1 were computed from the optical survey data. The distances are from the center of the liquid hydrogen/deuterium target to the center of the detector. The channel number of the centroid of the prompt γ-ray peak in the NTOF spectrum of each detector is listed in the third column of Table 4.1. Because the counting statistics in the

γ-ray peak were better for the $^2H(\pi^-, n\gamma)n$ data than for the $^1H(\pi^-, n)\gamma$ data, the γ-ray centroids were taken from the NTOF spectra for the $^2H(\pi^-, n\gamma)n$ data. The channel centroid of the peak for the 8.868 MeV neutrons from the $^1H(\pi^-, n)\gamma$ capture reaction is listed in the fourth column of Table 4.1. The effective time calibrations of the NTOF spectra are given in the fifth column of Table 4.1 and were calculated as described below.

The prompt γ peak in the NTOF spectra is mainly due to secondary γ rays created by the stopping of e^+e^- in the CsI crystals. The 130 MeV γ rays from the $^1H(\pi^-, n)\gamma$ reaction creates an e^+e^- shower in the Bismuth-Germanate-Oxide (BGO) detector. The shower is stopped in the CsI array, and the energy in the shower is measured. The high-energy e^+ and e^- lose energy in the CsI crystals by e^+e^- pair creation and Coulomb scattering. The positrons eventually collide with their matter counterpart, electrons, and anhilate into two 511 keV γ rays. Some photons are detected by the neutron detectors. The γ rays from the process $\pi^- + d \rightarrow \pi^0 + n + n \rightarrow \gamma + \gamma + n + n$ are rejected by the software requirement put on the γ-ray energy (E_γ) in the data replay between 99 and 159 MeV.

The effective time calibration were computed as follows. Let the distance from the target center to the center of the CsI crystals be $D_{\gamma d}$ (= 80.64 cm), then the total flight-path length of the prompt γ rays is

$$l_\gamma = 2 * D_{\gamma d} + l_{det} \ , \tag{4.25}$$

where l_{det} is the distance from target center to a neutron-detector center.

The centroids of peaks from the prompt γ rays and the 8.868 MeV neutrons are denoted as $TOF(\gamma)$ and $TOF(n)$ respectively, as shown in Figure 4.8. The effective time calibration of each NTOF spectrum is given by

$$tcal = \frac{TOF(n) - TOF(\gamma)}{\frac{l_{det}}{v_n} - \frac{l_\gamma}{c}} \ , \tag{4.26}$$

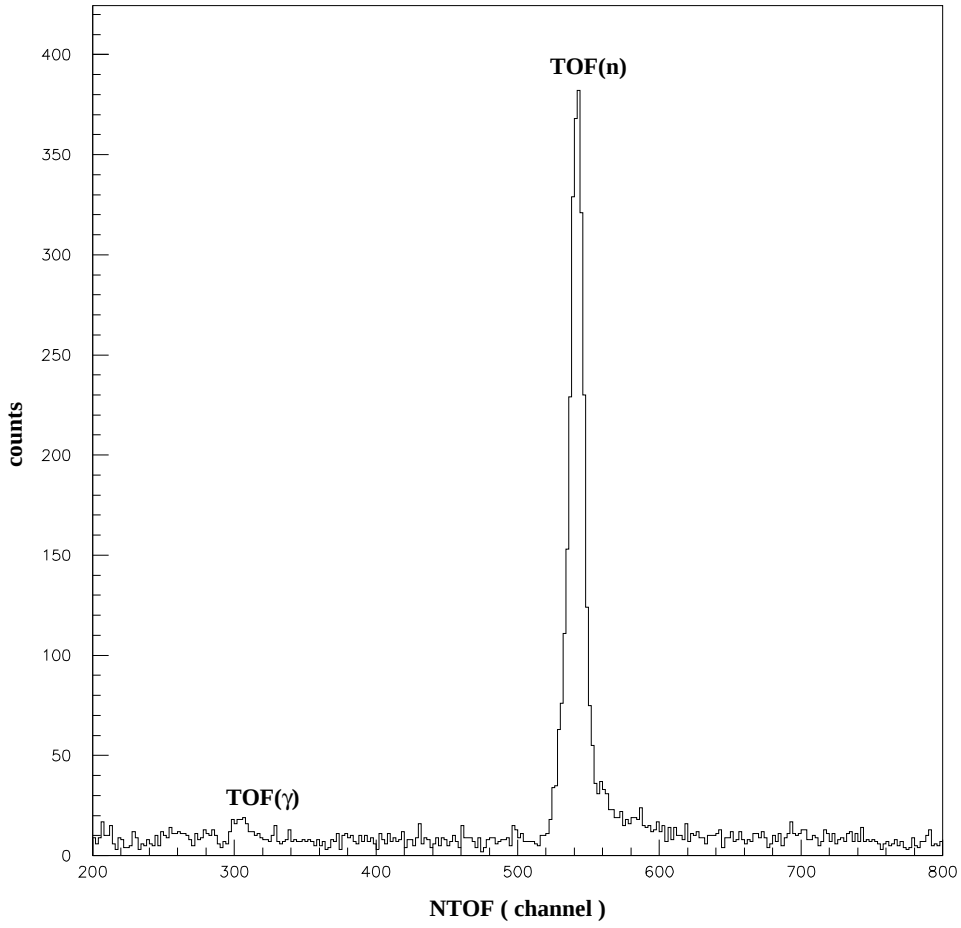

Figure 4.8: NTOF spectrum for detector 2 from ${}^1H(\pi^-, n)\gamma$ data. The γ-ray peak position TOF(γ) and neutron peak TOF(n) were used in the time calibration described in section 4.4.2.

where, v_n (= 0.0412 m/ns) is the speed of 8.868 MeV mono-energetic neutrons from the $^1H(\pi^-, n)\gamma$ reaction, and c (= 0.300 m/ns) is the speed of light in air. The effective time calibration obtained from the NTOF spectra of the $^1H(\pi^-, n)\gamma$ data and the $^2H(\pi^-, n\gamma)n$ data are listed in Table 4.1. The average time per channel is 0.205 ± 0.001 ns/channel.

Det#	l_{det} (m)	$TOF(\gamma)$	$TOF(n)$	tcal(ns/chan)
1	2.562	301.1	533.2	0.208
2	2.532	306.0	541.0	0.203
3	2.543	297.4	528.7	0.207
4	2.541	302.0	538.1	0.202
5	2.548	296.5	530.6	0.205
6	2.535	302.4	532.0	0.208
7	2.556	291.4	530.4	0.201
8	2.571	282.2	520.0	0.204
9	2.578	298.8	529.2	0.211
10	2.535	303.2	537.0	0.204
11	2.569	297.3	535.7	0.203
12	2.557	297.5	533.7	0.204
13	2.557	295.5	528.7	0.206
14	2.562	305.9	537.9	0.208
15	2.584	305.0	553.4	0.196
16	2.565	299.2	534.1	0.206
17	2.581	309.7	549.4	0.203
19	2.532	289.1	524.2	0.203
20	2.518	294.6	519.6	0.210
21	2.533	292.5	520.5	0.209
22	2.563	308.6	544.0	0.205
23	2.558	302.3	543.5	0.200
25	2.543	303.7	532.0	0.210
26	2.582	290.7	524.2	0.208

Table 4.1: Time calibration of TOF spectra.

The peaks in the experimental NTOF spectra for the 8.868 MeV neutrons from the $^1H(\pi^-, n)\gamma$ reaction have full widths measured at half maximum (FWHM) of 10 to 20 channels, depending on the detector type. For

measurements with a point-geometry setup and perfect electronics, the peak would be a δ function (have zero width). The spread in peak widths is mainly attributable to: (1). the finite size of the target and the neutron detectors, which results in the dispersion of the flight path; (2). neutron scattering inside the target material causes dispersion in the energy and flight-path length of the emitted neutrons; (3). neutron scattering in the detector array causes a dispersion in the flight-path length; and (4). the electronic resolution of the photo-multiplier tubes and trigger electronics. The effects of neutron scattering in the target materials and in the detector array will be discussed in more detail in the sections to follow. The resolution $\sigma_t^{exp}(i)$ of each detector for measuring neutron time of flights was obtained by fitting the 8.868 MeV neutron peak in the NTOF spectrum for the $^1H(\pi^-, n)\gamma$ reaction with a Gaussian function. The MC simulations were used to infer the electronic time resolution $\sigma_t^{elec}(i)$ for each detector by setting it equal to zero. In these simulations the width of the neutron peak was due solely to finite-geometry effects $\sigma_t^{fgeo}(i)$. A simulated NTOF spectrum is shown in comparison to the spectrum measured with detector 2 (Figure 4.9).

The $\sigma_t^{elec}(i)$ was obtained by comparing the experimental NTOF spectrum to the simulated NTOF spectrum with $\sigma_t^{elec}(i)$ set to zero (spectrum plotted with dashed line in Figure 4.9) and using the equation

$$\sigma_t^{exp}(i) = \sqrt{(\sigma_t^{fgeo}(i))^2 + (\sigma_t^{elec}(i))^2} \ . \tag{4.27}$$

The i denotes the neutron detector number. The results are shown in Table 4.2.

4.4.3 Calibration of γ-ray Detector Energy Resolution

During the data replay we observed that the energy resolution of the γ-ray detector was about 15 MeV, which is considerably larger than the 1 MeV design specifications of the Neutron Meson Spectrometer (NMS). Why was the

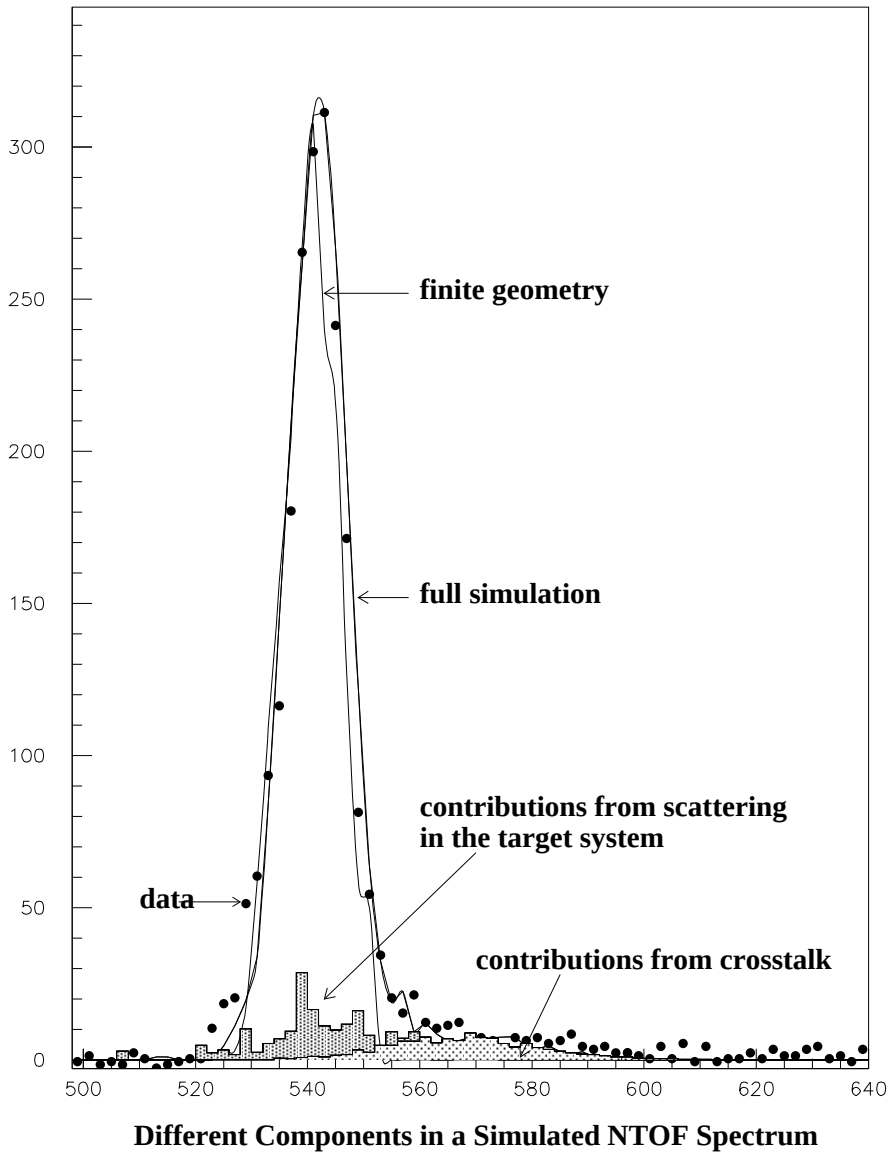

Figure 4.9: Comparison of experimental NTOF spectrum with the simulated one for detector 2 for the ${}^1H(\pi^-, n)\gamma$ reaction.

detector #	$\sigma_t^{exp}(i)$	$\sigma_t^{fgeo}(i)$	σ_t^{elec}
1	4.45	2.70	3.54
2	4.78	2.65	3.98
3	6.49	2.72	5.89
4	4.81	2.58	4.06
5	5.11	2.62	4.39
6	5.08	2.47	4.44
7	4.36	2.65	3.46
8	6.85	2.74	6.28
9	4.96	2.72	4.15
10	5.13	2.69	4.37
11	5.79	2.71	5.12
12	5.14	2.59	4.44
13	4.92	3.29	3.66
14	7.14	2.36	6.74
15	4.18	2.60	3.27
16	3.94	2.44	3.09
17	5.18	2.58	4.49
19	6.18	1.90	5.88
20	5.70	1.81	5.40
21	4.68	1.93	4.26
22	5.82	2.05	5.45
23	7.72	3.96	6.63
25	6.77	1.89	6.50
26	6.01	2.05	5.65

Table 4.2: This table displays the total NTOF resolution due to finite-geometry effects, and the electronic time resolution of each neutron detector. Units for $\sigma_t^{exp}(i)$, $\sigma_t^{fgeo}(i)$ and σ_t^{elec} are in channels.

γ-ray energy (E_γ) resolution so poor? The answer is still not certain, but some interesting features were noticed in our investigations onto the cause for the poor resolution. We studied the relationship between E_γ and other observables, such as the position of the γ ray at the WC (γ_x and γ_y) and the pulse height of the signals from the neutron detectors. We noticed that the energy resolution of the γ detectors had some position dependency. The position dependency was different in the vertical (γ_x) and horizontal (γ_y) directions. As shown in Figure 4.10 as γ_x is changed, the centroid of the E_γ peak basically stays in the same channel number, while the width of peak changes with γ_x . In the horizontal direction both the centroid and the width of the E_γ peak change. with γ_y , see Figure 4.11. A significant portion of the resolution is due to the γ_y dependence.

4.4.4 Stopped-Pion Distribution in the Target

The energy dependence of the neutron attenuation in the liquid deuterium target causes the shape of the NTOF spectrum to depend on the distribution of the stopped pions in the target. Neutrons from the $\pi^- d$ capture near the edge of the target cell on the side of the neutron detectors are attenuated in exiting the target less than those on the opposite side of the target. Therefore, the NTOF spectrum resulting from reactions at these two extreme locations in the target have different shapes. The ratio of the counts in the nn FSI enhancement (E_n = 2.5 MeV at the maximum) to those in the QFS peak (E_n = 9.0 MeV at maximum) is higher for reaction sites on the neutron-detector side of the target than for sites on the γ-detector side. Since a_{nn} is determined from the shape of NTOF spectrum, a reasonably accurate description of the stopped-pion ($\pi^- d$ capture sites) distribution inside the liquid deuterium target is needed to reduce uncertainties in the extracted value of a_{nn} . The $^1H(\pi^-, n)\gamma$ reaction was used to make tomographic measurements of the stopped π^- distribution inside the

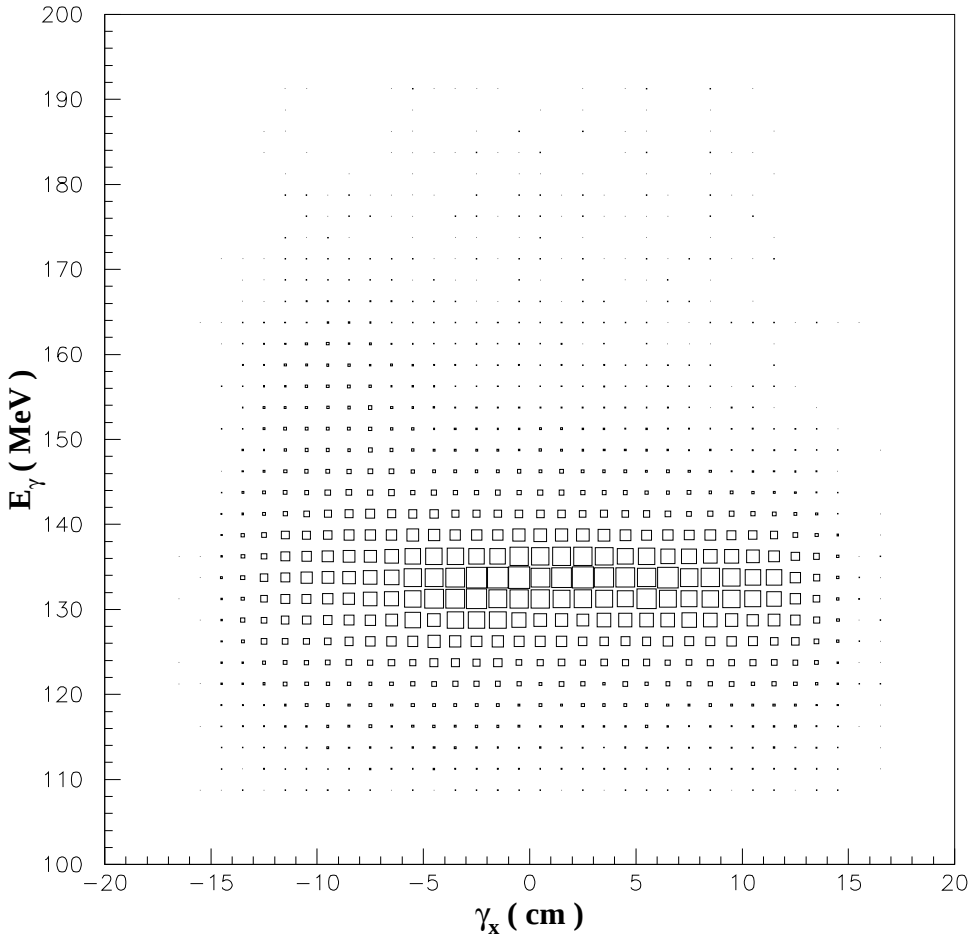

Figure 4.10: The γ-ray energy (E_γ) for the $^1H(\pi^-, n)\gamma$ reaction as a function of the γ-ray vertical position (γ_x) at the plane of the WC.

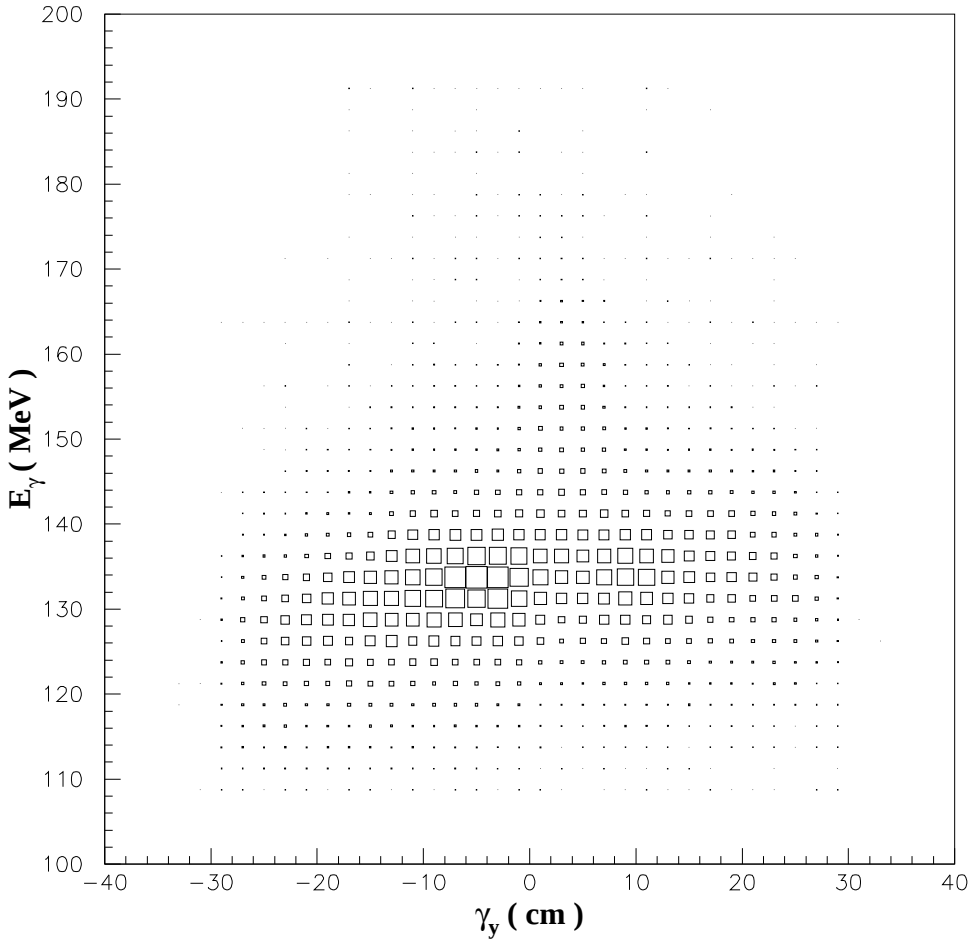

Figure 4.11: The γ-ray energy (E_γ) for the $^1H(\pi^-, n)\gamma$ reaction as a function of the γ-ray horizontal position (γ_y) at the plane of the WC.

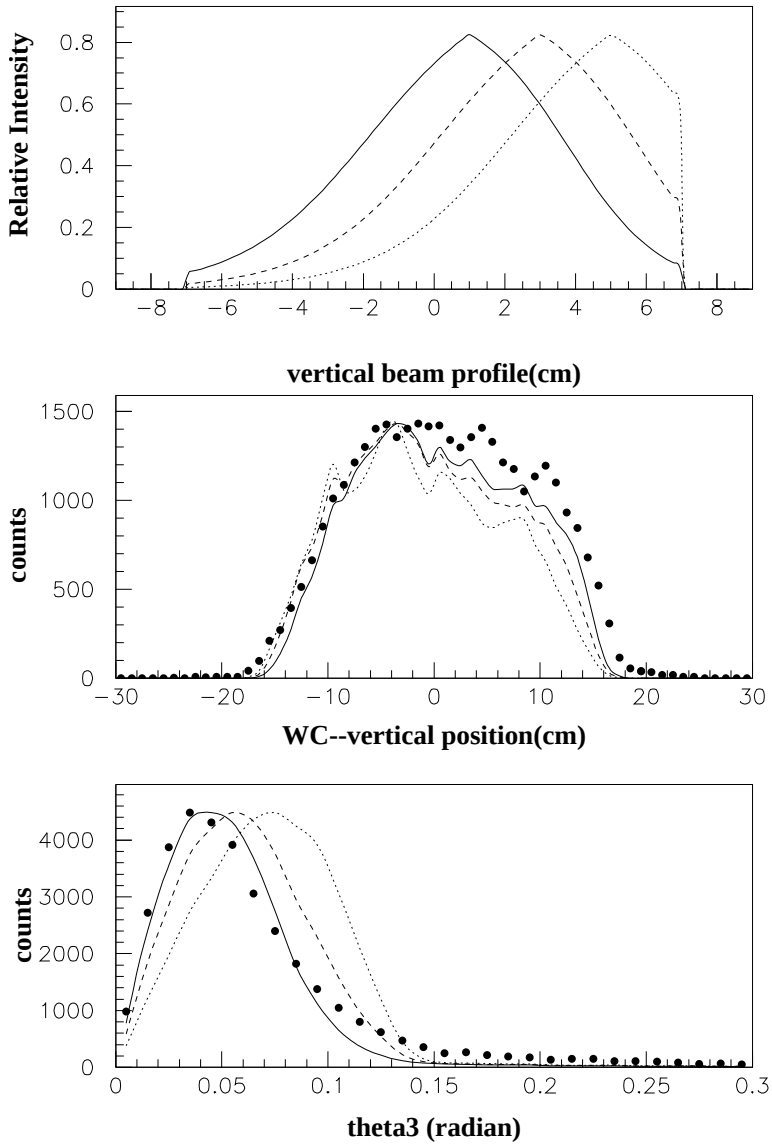

Figure 4.12: MC simulations to illustrate the sensitivity of the vertical position of the γ rays at the WC plane and θ_3 to the centroid of the stopped π^- distribution in the hydrogen target. The simulations were made for the three different distributions in the top plot. The WC-position spectrum is the image of the entire neutron-detector array. The dots indicate experimental data and same type of curves were used for each π^- distribution.

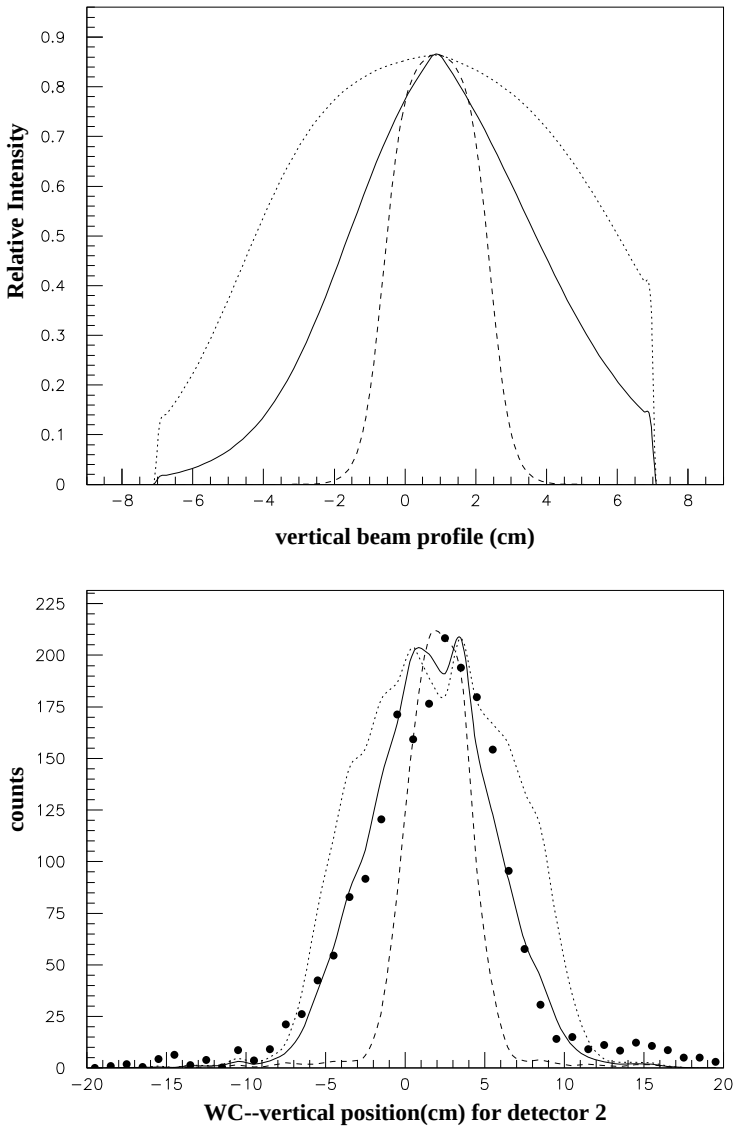

Figure 4.13: MC simulations to illustrate the sensitivity of the image of the neutron detector 2 in the WC to the vertical profile of the stopped π^- distribution in the hydrogen target. The simulations were made for the three different distributions in the top plot. The dots indicate experimental data and same type of curves were used for each π^- distribution.

target. The sensitivity of our experimental setup to the dimension of the target and the diagnostic capabilities of our instrumentation when used with the $^1H(\pi^-, n)\gamma$ reaction are illustrated in Figure 4.14. The spectra in Figure 4.14 are from two MC simulations, one with a point target (Figure 4.14 (a) and the dashed profiles in parts (c) and (d)), and the other with a uniform stopped π^- distribution within the dimensions of our target cell (6 cm diameter $\times$ 10 cm high). In both simulations the true sizes of the neutron detectors were used. The image of detector 1 in the WC and the x and y projections are displayed. The distribution of stopped π^- in the hydrogen target was determined using the MC simulation to fit three kinds of spectra, the γ_x spectrum, the γ_y spectrum and the θ_3 spectrum. The sensitivity of our technique to the shape and position of the π^- distribution inside the target is illustrated in Figure 4.12 to 4.16.

In the figures of the stopped π^- profile in the target, the x direction is vertical, the y direction is horizontal (perpendicular to beam direction), and the z direction is along the beam axis. The +x axis points up, the +y axis points toward the γ detector and the +z axis points in the direction of the incident π^- beam.

Since the liquid hydrogen and deuterium targets were operated at the same temperature and pressure, their nuclear number densities were the same within 10%, implying that their stopping powers for π^- mesons were the same within a few percent. Consequently, differences in the stopped π^- distribution in the deuterium target from that in the hydrogen target was solely due to differences in the π^- beam tune in the hydrogen-target runs from that in the deuterium target runs. The π^- distribution determined using the $^1H(\pi^-, n)\gamma$ reaction was used in the simulations of the $^2H(\pi^-, n\gamma)n$ reaction with only modest adjustments to account for the differences in the beam tune. The main change being the centroid of the π^- distribution in the deuterium target was about 1 cm higher than with the hydrogen target.

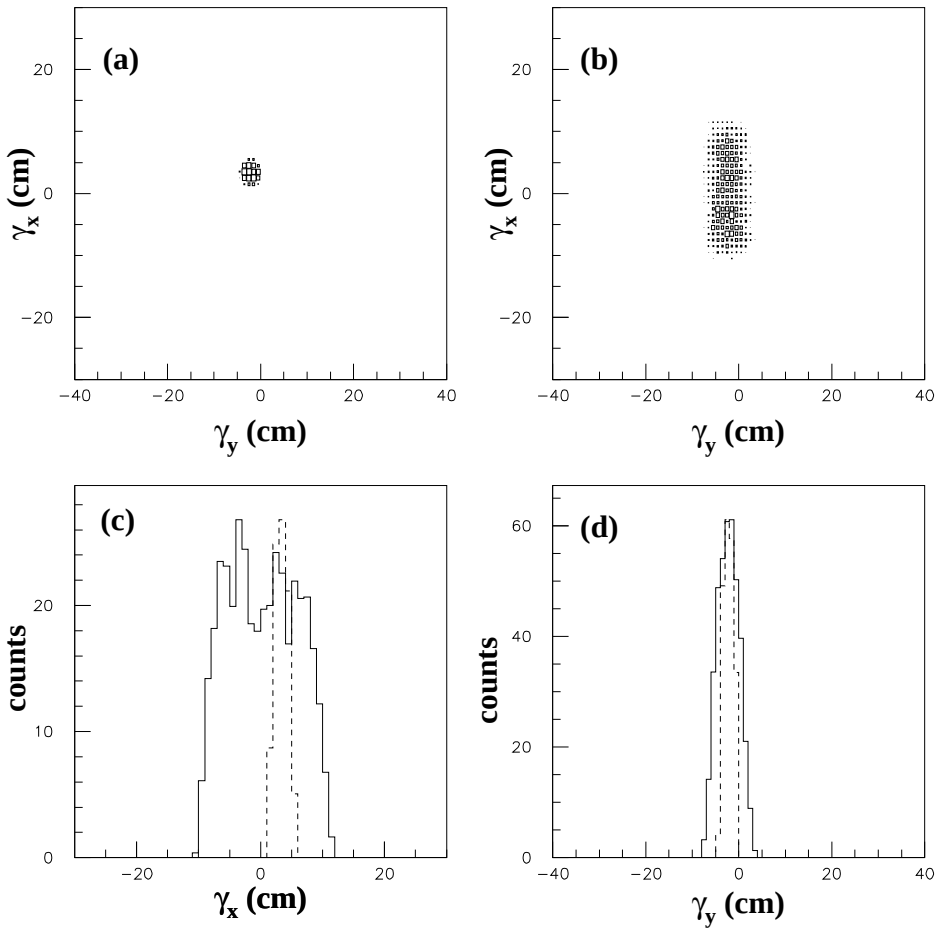

Figure 4.14: The effects of the finite target size on the γ-ray position spectra for detector 2. Plot (a) is the simulated two-dimensional image of detector on the plane of the wire chamber in the case of point target. Plot (b) is the same as (a) except it is for the case of finite-size target. Plot (c) is the projection of plot (a) and (b) onto the γ_x axis with the solid-curve profile for the projection of plot (b) and dashed-curve profile for the projection of plot (a). Plot (d) is the same as plot (c) except it is the projection onto the γ_y axis.

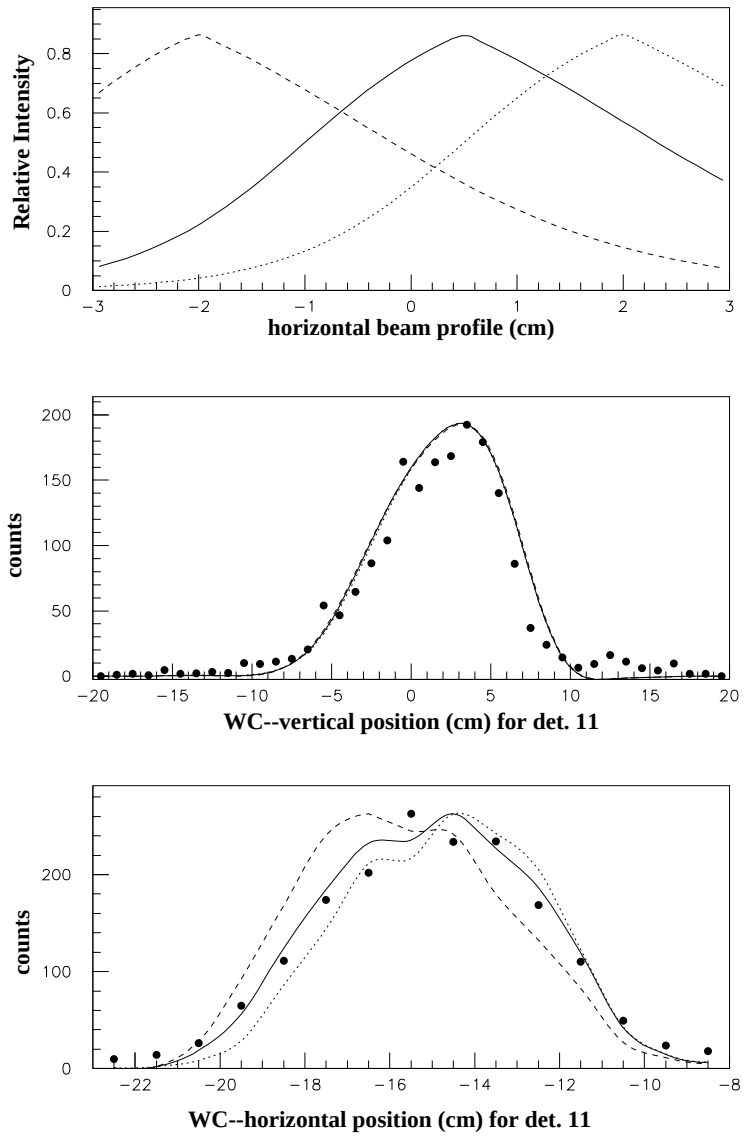

Figure 4.15: MC simulations to illustrate the sensitivity of the vertical and horizontal positions of the γ rays at the WC plane to the centroid of the stopped π^- distribution in the hydrogen target. The simulations were made for the three different distributions in the top plot. The WC-position spectrum is the image of neutron detector 11. The dots indicate experimental data and same type of curves were used for each π^- distribution.

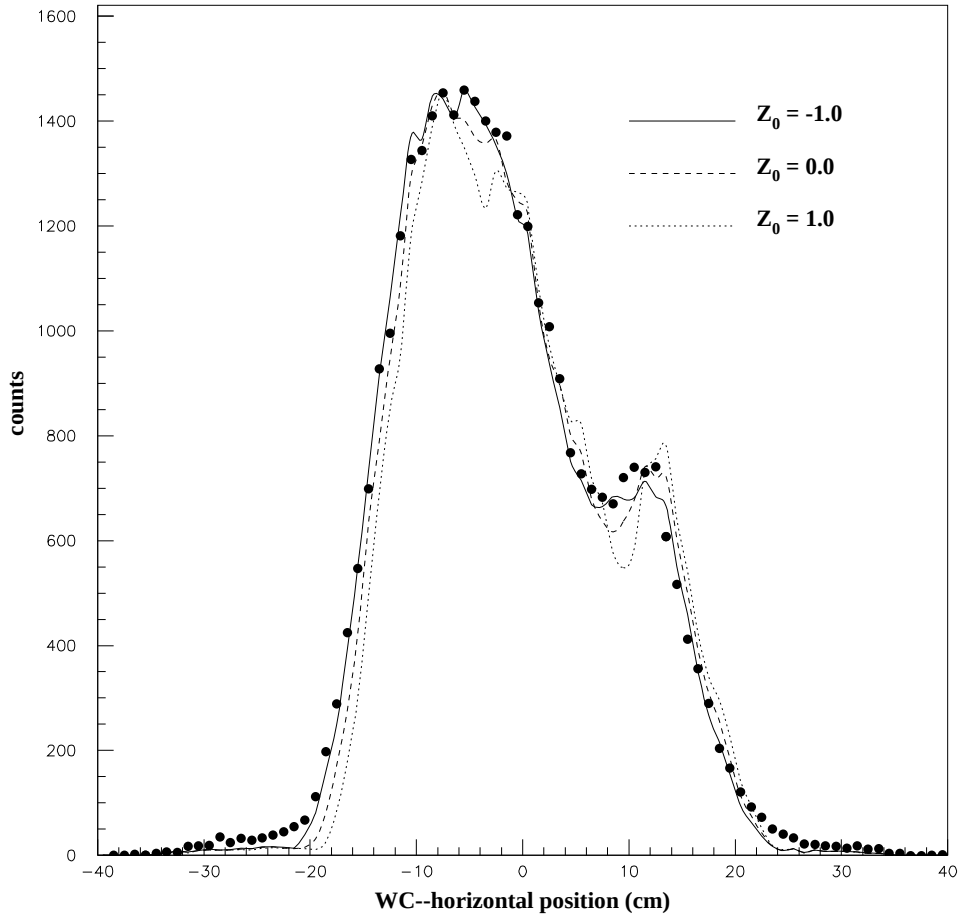

Figure 4.16: MC simulations to illustrate the sensitivity of the horizontal position of the γ rays at the WC plane to the centroid of the stopped π^- distribution in the hydrogen target. The simulations were made for three different distributions with the centroid of the beam profile along beam direction being -1, 0 and 1, respectively (in cm). The WC-position spectrum is the image of the entire neutron-detector array. The dots indicate experimental data.

4.4.5 Effects of Scattering

The γ rays associated with the neutrons from the $^1H(\pi^-, n)\gamma$ capture reaction that are transported to the neutron-detector array without scattering produce a clear image of each neutron detector at the plane of the wire chamber. The detector images are blurred by scattering, as shown in Figure 4.17 for detector 2. The γ-ray position distribution in Figure 4.17 were generated using the MC simulation code for the $^1H(\pi^-, n)\gamma$ reaction. The distribution in the top plot is due to γ rays associated with neutrons that travel directly (without scattering) from the site of the $\pi^- p$ capture inside the target to detector 2. The position distribution at the bottom of Figure 4.17 is produced by γ rays that are associated with neutrons that scatter once in the target material (liquid hydrogen cell and cryostat wall) before hitting detector 2. In both plots, γ_x and γ_y are the vertical and horizontal positions, respectively, of the γ ray at the plane of the wire chamber. As shown in the bottom plot, the effect of neutron scattering in the target is to randomize the direction of the associated γ ray.

The simulated NTOF spectrum for the neutrons from the $^1H(\pi^-, n)\gamma$ reaction that directly travel to detector 2 without scattering is shown in the top plot in Figure 4.18. The NTOF spectrum for neutrons that scatter in the target material once before hitting detector 2 is shown in the bottom plot. Since the scattering process shifts the neutron energy to lower values, the scattered neutrons on average have a longer TOF than the direct ones, as shown in the bottom plot in Figure 4.18 and in Figure 4.9.

4.4.6 Effects of Cross Talk and Cross Talk Determination

As mentioned earlier, cross talk refers to the process in which some neutrons are scattered by the proton or carbon nuclei in a liquid scintillator and are then detected by an adjacent detector. The probability for cross talk is of course

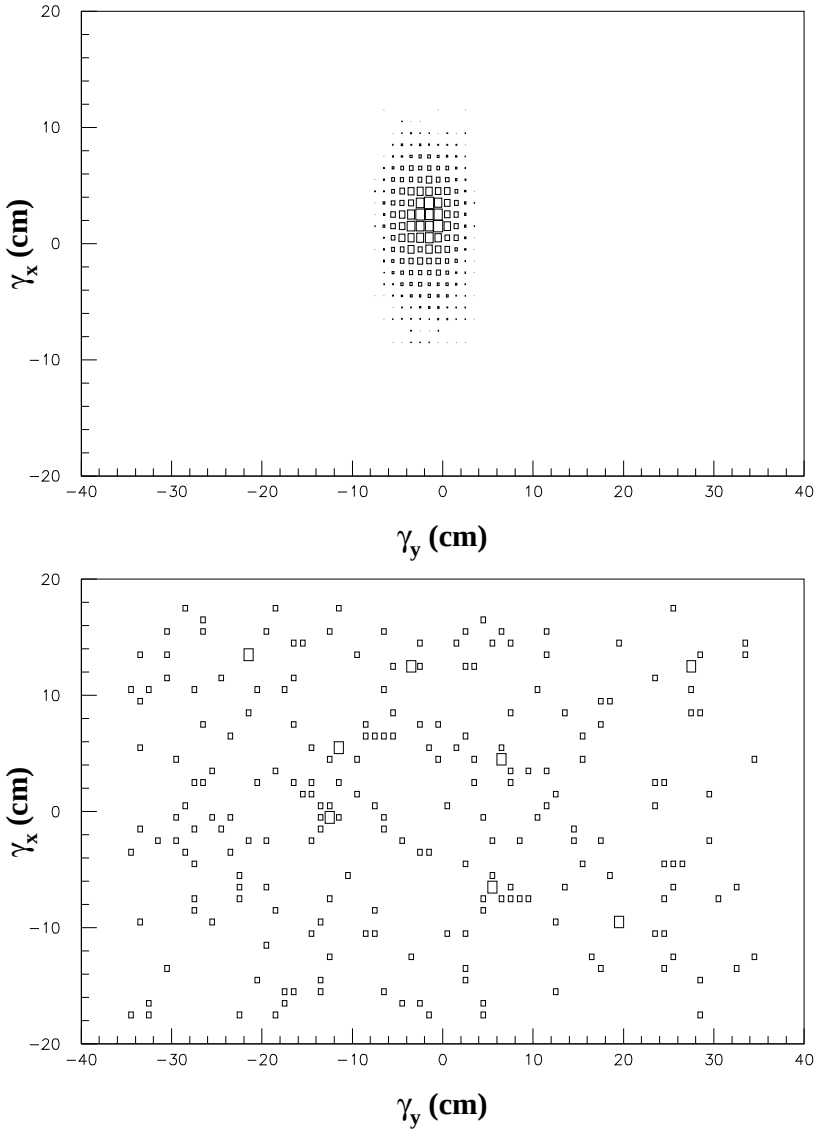

Figure 4.17: Top: Plot of simulated position distribution of the γ rays at the plane of the wire chamber. These γ rays are associated with the neutrons from the $^1H(\pi^-, n)\gamma$ reaction that are transported to detector 2 without scattering. Bottom: Simulated γ -ray position distribution at the plane of the wire chamber for the $^1H(\pi^-, n)\gamma$ reaction. The γ rays in this distribution are associated with neutrons that scatter once before hitting neutron detector 2.

related to the differential cross sections of $^1H(n,n)$ or $C(n,n)$ at the energy of the incident neutron. The differential cross sections for $^1H(n,n)$ scattering take the shape of $cos(\psi)$ in the lab. system. The angle integrated value is the total cross section at the energies relevant to our experiment. The differential cross sections for the $C(n,n)$ scattering were obtained from the National Nuclear Data Center (NNDC) at Brookhaven National Laboratory (BNL).

The effects from cross talk were included in the MC simulations. Because the energy of the emitted neutrons from the $^1H(\pi^-,n)\gamma$ reaction is singly valued and the relative directions of the emitted neutron and γ ray from this reaction is highly constrained, the effects of cross talk are apparent in the experimental spectra. Comparisons of the simulated NTOF and θ_3 spectra with the measured spectra were used to validate the simulations.

From the simulation, we found that the contribution of cross talk was about 1.5% of the total counts for the $^1H(\pi^-,n)\gamma$ reaction. Obviously, neutrons that scatter from one detector into another travel an extra distance (the distance between adjacent detectors) before being detected. Therefore, the neutrons detected as a result of the cross-talk process have a longer TOF due to the increased flight-path length and to a lesser extent (except for scattering from hydrogen) due to the energy reduction caused by the scattering in the first detector.

Cross Talk contributes more to the spectra for the neutron detectors in the central area of the detector array than to the spectra for the detectors on the outer loop of the detector array. Figure 4.19 shows contributions to the θ_3 spectra by the direct neutrons (top plot) and the single-scattered neutrons (bottom plot). Figure 4.20 shows contributions to the NTOF spectra by the direct neutrons and the single-scattered neutrons. The cross-talk process is shown schematically in Figure 4.21. In the simulations the cross talk is modeled using forced-scattering MC techniques. For two arbitrary detectors i

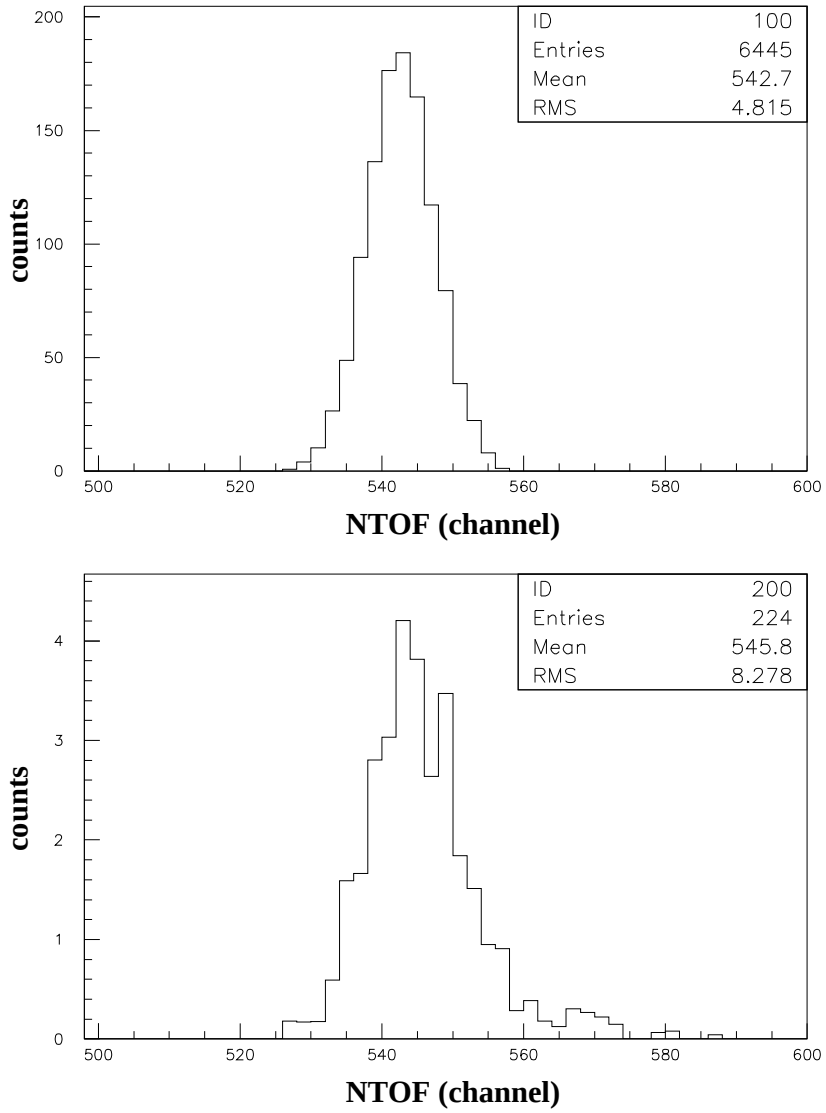

Figure 4.18: Top: TOF spectrum for neutrons from the $^1H(\pi^-, n)\gamma$ reaction that travel from the creation site to detector 2 without scattering. Bottom: Same as the top plot except for neutrons that scatter once in the target material (the liquid hydrogen cell and the cryostat wall) before hitting neutron detector 2. Note the vertical axis scale difference between the top and bottom plots.

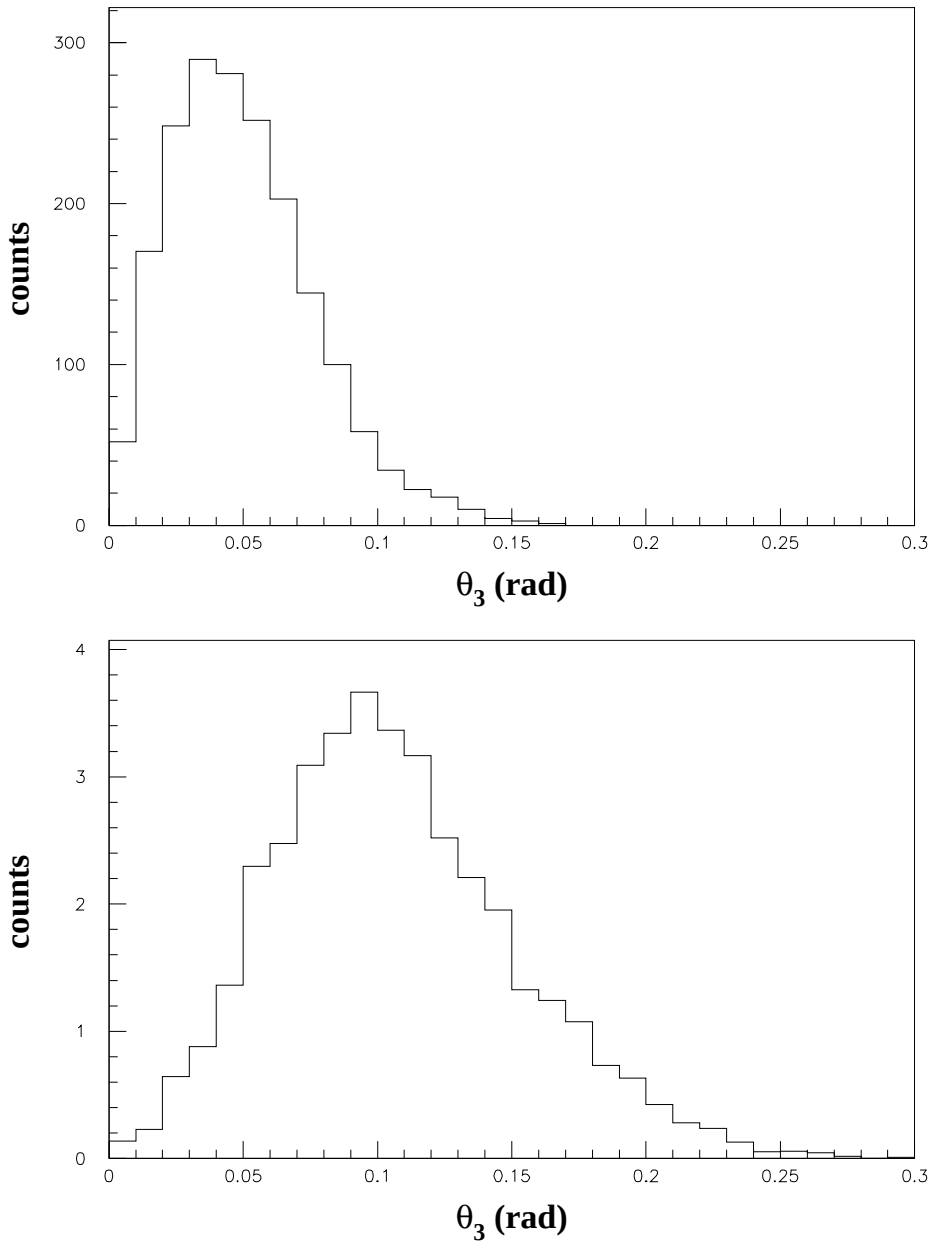

Figure 4.19: The top plot shows the contribution from direct neutrons for detector 2 for the $^1H(\pi^-, n)\gamma$ reaction. The bottom plot shows the contribution of cross talk for the target. Note the vertical axis scale difference between the top and bottom plots.

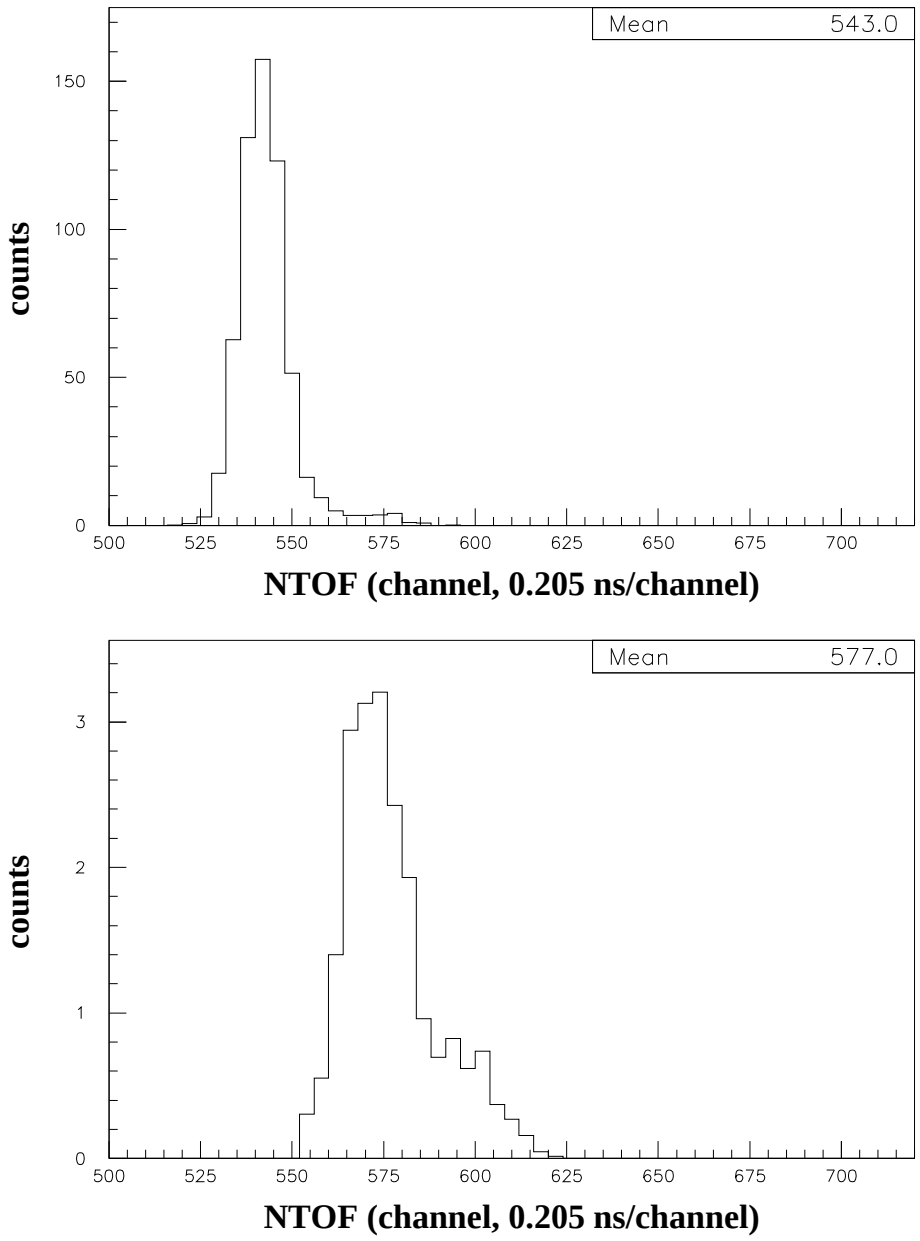

Figure 4.20: The top plot shows the contribution from direct neutrons for detector 2 for the $^1H(\pi^-, n)\gamma$ reaction. The bottom plot shows the contribution of cross talk for the target. Note the vertical axis scale difference between the top and bottom plots.

and j in the array, the probability for an incident neutron to be scattered by carbon nuclei at position A in detector i to unit area at position B in detector j and be detected by detector j is:

$$prob = \frac{n_c \, t \, \sigma(E_n, \psi) \, \epsilon(E_n^{'})}{r_{12}^2} \ . \tag{4.28}$$

The symbol t is the thickness of detector i, n_c is the number density for carbon nuclei in detector i, $\sigma(E_n, \psi)$ is the differential cross section for n+C elastic scattering, r_{12} is the distance between position A in detector i and position B in detector j. In the case of cross talk due to ${}^1H(n,n)$ scattering in detector i, the number density of hydrogen and the np cross section are used.

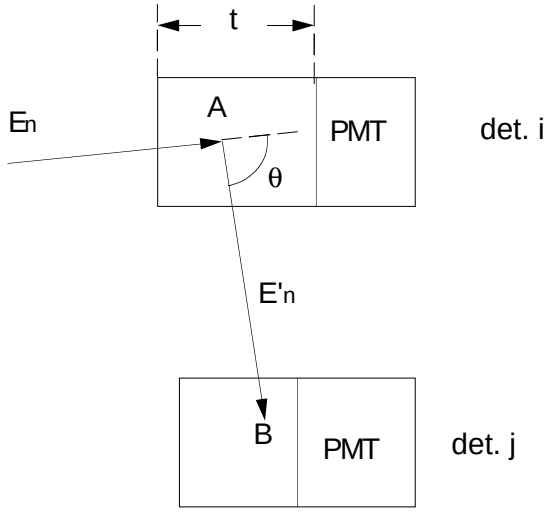

Figure 4.21: Cross Talks between adjacent detectors.

The differential cross sections for n+C scattering were taken from phase-shift analysis data obtained from [Bra97]. The differential cross sections for $H(n,n)$ scattering can be easily obtained using Figure G.1 and the feature that the angular distribution of np elastic scattering takes the shape of $\cos(\psi)$ in the laboratory system.

The probability for cross talks due to $H(n,n)$ scattering is much smaller than from the $C(n,n)$ scattering because the energies of the np scattered neutrons are typically lower than threshold (one third Cs) in the second detector. But for completeness np cross talk was included in the simulation in the same manner as n+C cross talks.

4.5 Independent Measurement of the Efficiencies of the Neutron Detectors

All physical process that influence the shape of the NTOF spectrum for the $^2H(\pi^-, n\gamma)n$ reaction are important in the determination of a_{nn}. One process that greatly influences the spectral shape is the energy dependence of the neutron detection efficiency of the liquid organic scintillators. The efficiency of each neutron detector used in LAMPF Exp1286 was determined in an independent set of measurements at TUNL. See section 2.2 for details of those measurements. Because in the MC simulations the detector efficiency were needed in fine neutron energy (0.1 MeV) steps, the efficiencies from the PTB code were used instead of the measured data. The uncertainties resulting from using the calculations were small because the PTB code predictions were in excellent agreement with the measured efficiencies, see Figure 2.2.

4.6 Simulation of the $^2H(\pi^-, n\gamma)n$ Reaction

The critical geometry and detector calibration parameters were determined using the $^1H(\pi^-, n\gamma)$ capture reaction as described in section 4.4. These parameters, with slight adjustments to account for the differences in the π^- beam tune between the hydrogen- and deuterium-target runs, were used as input into the $\pi^- d$ capture simulations. In this section we describe how the stopped π^- distribution is determined from the $\pi^- d$ capture data and discuss the results from the simulations for the deuterium target.

4.6.1 Distribution of Stopped π^- in the Deuterium Target

Starting with the results obtained from the $\pi^- p$ data, the stopped π^- distribution in the deuterium target was determined similarly as that for the hydrogen target (see section 4.4).

In the case of the ${}^2H(\pi^-, n\gamma)n$ reaction, there are three particles in the exit channel. The relative angles and energies between the γ ray and the neutrons are much less restrained than in the case of the ${}^1H(\pi^-, n\gamma)$ reaction. Therefore, there is no one-to-one correspondence between the position of the γ ray hitting the WC and the position of an associated neutron hitting the neutron-detector array. The position spectrum of γ rays associated with neutrons detected by a neutron detector is less sensitive to the distribution of stopped pions in the target than in the case of the hydrogen target. However, there is sufficient sensitivity to make slight adjustments to the distribution obtained from the $\pi^- p$ data, particularly in the vertical direction.

The sensitivity of the shape of the NTOF spectrum for $\pi^- d$ capture is illustrated in Figure 4.7 (top). However, since the shape of the NTOF spectrum for small θ_3 angles (see Figure 3.4) is strongly dependent on the value of a_{nn}, it can not be used to extract information about the stopped π^- distribution in the target. At θ_3 angles greater than 0.3 radians the NTOF spectrum becomes insensitive to a_{nn} and can be used to verify the π^- distribution in the target.

The stopped π^- distribution in the deuterium target was obtained by comparing the data to the simulated γ-ray position spectra for γ_x and γ_y as described in the previous section. The sensitivity of the γ_x and γ_y spectra to a_{nn} was negligible relative to our experimental precision. The distribution is checked using data and simulations of NTOF spectra for θ_3 greater than 0.3 radians. Because the shapes of the γ_x and γ_y spectra are only weakly sensitive

to the distribution of the stopped π^- distribution, a χ_2 analysis of the γ_x and γ_y spectra was done to find the best stopped π^- distribution. (see Figure 4.22 and Figure 4.23).

Figure 4.22 illustrates the sensitivity of the simulated γ_x spectra to the centroid of the vertical beam position. The uncertainty in the centroid of the vertical beam position was about 0.1 cm. This value was estimated from the plot of χ^2 versus the profile centroid in Figure 4.22 (middle) by adding one unit to the minimum value, χ^2_{min}. The position uncertainty is the difference in the positions corresponding to χ^2_{min} and $\chi^2_{min} + 1$.

Figure 4.23 illustrates the sensitivity of the simulated γ_y spectra to the centroid of the horizontal beam position (in the direction perpendicular to the beam direction). From the central plot of Figure 4.23 it is obvious that the simulated γ_y spectra are not sensitive to the centroid of the horizontal beam position. Therefore, we take the uncertainty in the centroid of the horizontal beam position from a similar analysis for the hydrogen target, which is about 0.2 cm. The stopped π^- distribution along this direction should be very stable because we were monitoring the counting rate. If the centroid of the stopped π^- distribution along this direction shifts, the attenuation of the neutron flux changes too. Therefore, the counting rate would change.

The sensitivity of the NTOF spectrum to the horizontal profile of the π^- distribution for θ_3 angles greater than 0.3 radians is shown in Figure 4.24. The high quality of the description of the experimental NTOF spectrum validates the values of the geometry and detector calibration parameters used in the $\pi^- d$ capture simulations.

4.6.2 Effects of Neutron Scattering in the Target

As mentioned in the previous section, neutron scattering in the target material has important influence on the shape of the NTOF spectrum and consequently

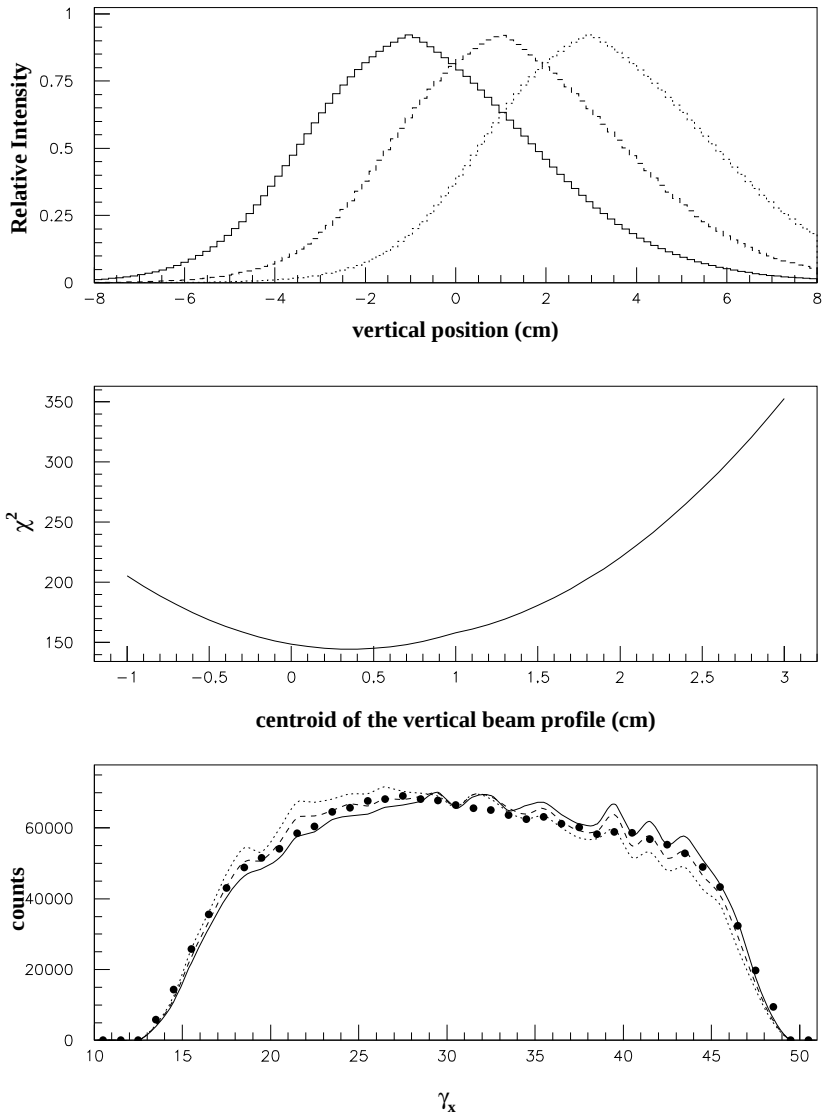

Figure 4.22: This figure demonstrates the sensitity of the γ_y spectrum versus the vertical beam profile. Top: several stopped π^- distributions along the vertical direction. Middle: χ^2 for the centroid of the vertical beam profile. Bottom: Comparison of simulated and experimental γ_x spectrum. The bold dots are the experimental data. The solid, dashed and dotted curves in the bottom plot are the simulated results corresponding to beam profiles decribed by the solid, dashed and dotted curves in the top plot, respectively.

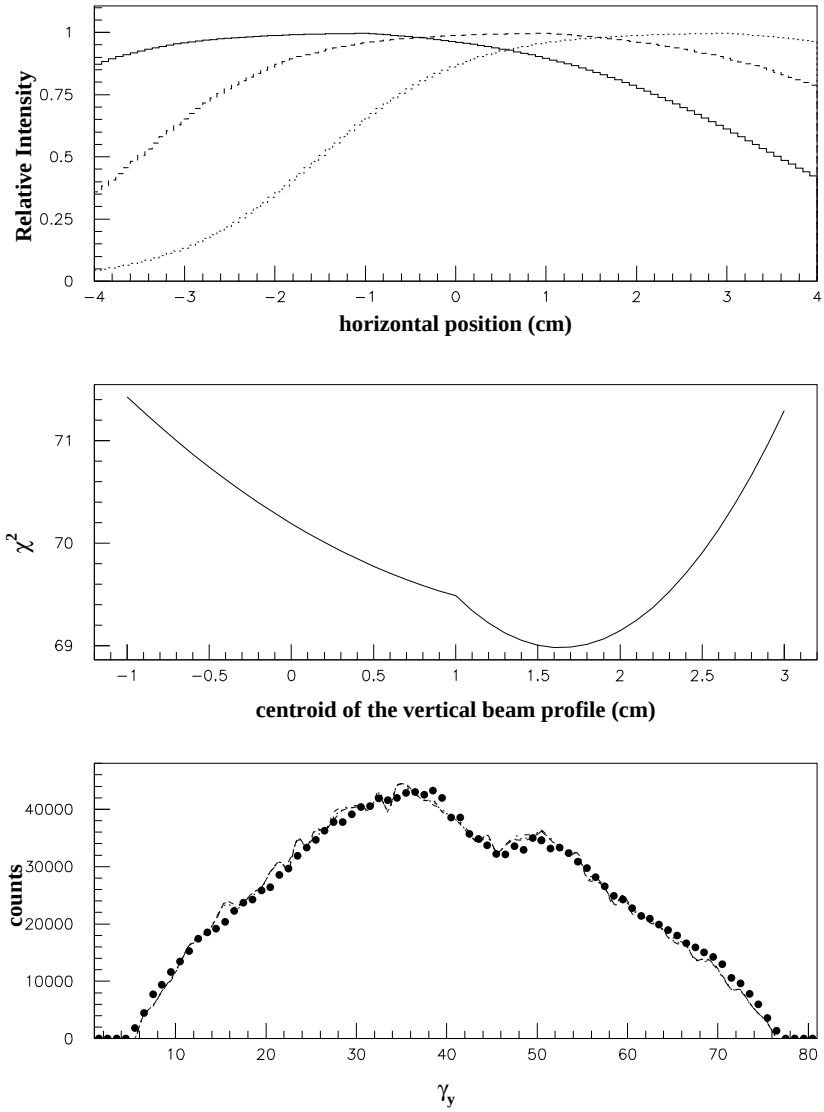

Figure 4.23: This figure demonstrates the sensitity of the simulated γ_x spectrum to the stopped π^- distributions along the horizontal direction perpendicular to the π^- beam direction. Top: several beam profiles along the horizontal direction. Middle: χ^2 for the centroid of the horizontal beam profile. Bottom: Comparison of simulated and experimental γ_y spectrum. The bold dots are the experimental data. The solid, dashed and dotted curves in the bottom plot are the simulated results corresponding to beam profiles decribed by the solid, dashed and dotted curves in the top plot, respectively.

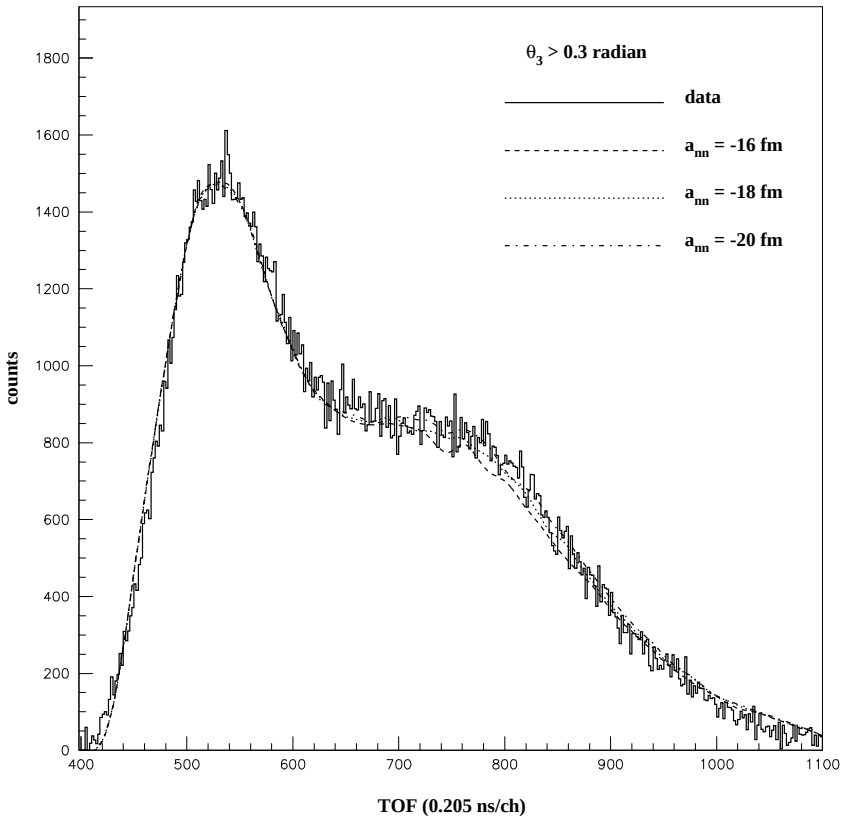

Figure 4.24: Plot of NTOF spectra for θ_3 values greater than 0.3 radian. The spectra are for the entire neutron-detector array. The solid curve is the experimental data. The dashed, dotted, and dotted-dashed curves are MC simulations made with a_{nn} =-16, -18 and -20 fm, respectively.

on the value of a_{nn} inferred by fitting the measured NTOF spectrum. Errors in simulating the effects of neutron scattering on the NTOF spectrum map directly into errors in the inferred a_{nn} value. For convenience, in our discussion we separate scattering into two types: "out-scattering" and "in-scattering". We refer to out-scattering as the process in which a neutron headed towards a detector is scattered before exiting the target material and subsequently missed the detector. We refer to in-scattering as the process in which a neutron that was not headed towards one of the detectors gets scattered into the detector. From the simulation, we found the contribution to the neutron TOF spectrum due to in-scattering to be about 4%. This number is comparable to a similar value cited in [Sch87], where the experimental setup (geometry, target size, events) was similar to ours and the authors claimed that 3% of the events were due to scattering in the liquid target.

For the $^2H(\pi^-, n\gamma)n$ reaction, it is difficult to separate counts caused by in-scatterings from those due to direct neutrons in the NTOF spectrum. It is equally difficult to isolate the in-scattering events in the γ-position spectrum. In the experimental spectra, the counts due to in-scattered neutrons are part of a continuous distribution with no clear distinction. However, in the simulation the in-scattered and direct neutrons can be tagged to identify their locations in the NTOF and γ-ray position spectra.

One characteristic of the TOF of the in-scattered neutrons apparent in the simulations is that the TOF of the in-scattered neutrons is consistently longer than that for the direct neutrons. The reason is the same as in the case of the $^1H(\pi^-, n\gamma)$ reaction discussed above. The longer TOF is reflected by the larger mean value in the bottom plot of Figure 4.25.

4.6.3 Effects of Cross Talk

As mentioned in section 4.4.6, detector cross talk is due to neutron scattering in the liquid scintillator array. From the simulation, the contribution of cross

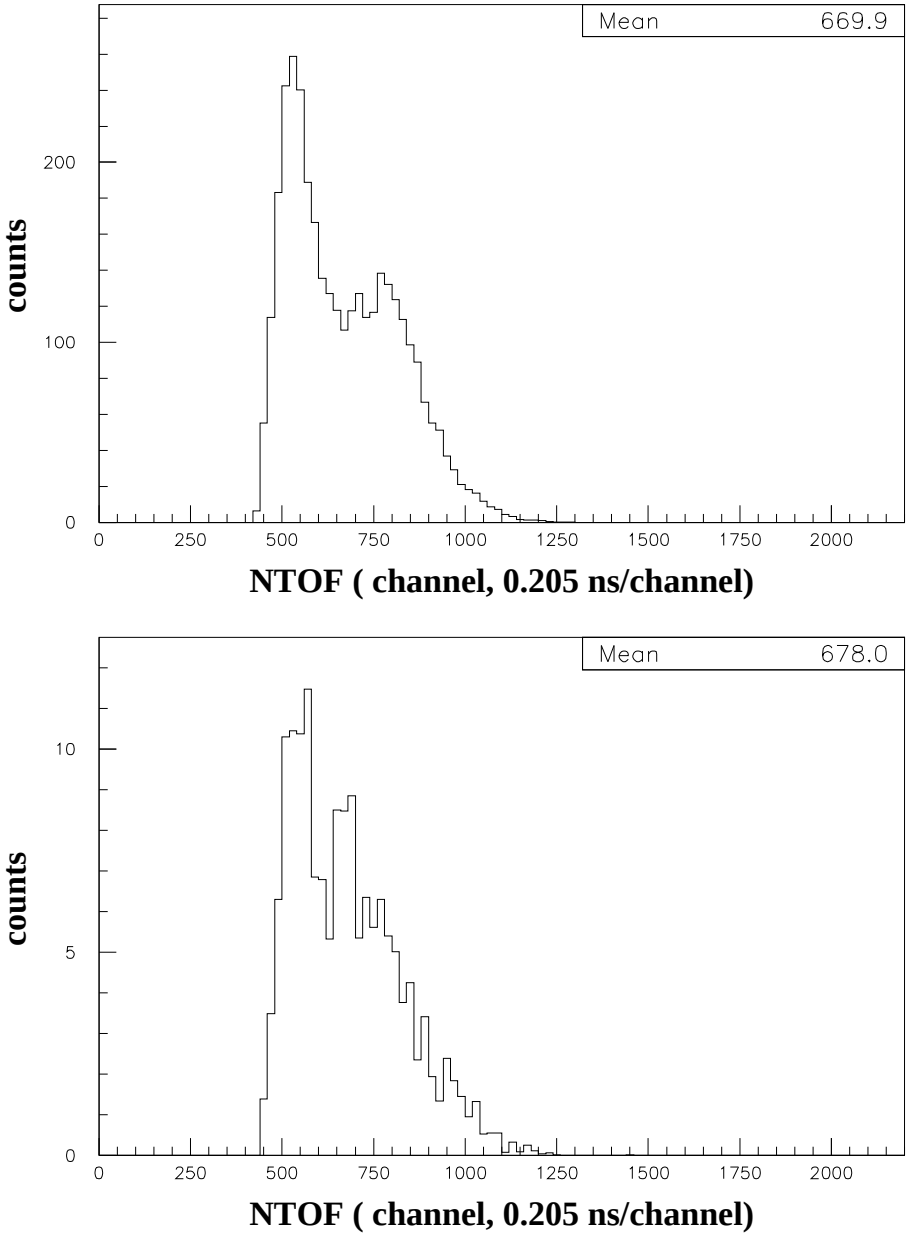

Figure 4.25: The top plot shows the contribution from direct neutrons for detector 2 for the ${}^2H(\pi^-, n\gamma)n$ reaction. And the bottom plot shows the contribution of single scattering for the same reaction. Note the vertical axis scale difference between the two plots.

talk is similar to that in the case of $^1H(\pi^-, n\gamma)$ reaction.

Figure 4.26 on the following page shows the contributions of the direct neutrons and the single scattering neutrons to the NTOF spectra. It clearly indicates that the scattered neutrons reach the neutron detectors later than the direct neutrons.

4.6.4 The γ-ray Detector Efficiency

As can be seen from Figure 3.5, the shape of the simulated NTOF spectrum is dependent on the θ_3 angle, which is determined from the momentum vectors of the emitted neutrons and γ ray in the $^2H(\pi^-, n\gamma)n$ reaction.

In the data analysis, the direction of the neutron momentum vector was defined to point from the origin of the target coordinate system (assumed to be the center of the target cell) to the center of the hit neutron detector. The direction of the γ-ray momentum was taken as the vector pointing from the origin of the target coordinate system to the position of the γ-ray position at the location of the WC. The θ_3 distribution has a strong dependence on the γ-ray position at the WC and the location of the neutron detectors, consequently, position-dependent efficiencies in the WC or in the neutron-detector array must be included in the simulation. A failure to properly model the position-dependent efficiencies in the detectors could cause an angle mismatch between the simulated NTOF spectra and the data. Because of the sharp angle dependence of the shape of the NTOF spectra, such a mismatch could bias our extracted values of a_{nn} . The relative efficiencies of the neutron detectors were measured to an accuracy of $\pm 1\%$ (see section 2.2) and were included in the simulation.

At the early stage of the MC simulation, we assumed a flat γ-ray detection efficiency over the cross section of the wire chamber. This assumption did not work well. The comparison of a simulated γ_y spectrum with data revealed that there was a dip in the data that was not reproduced in the simulation.

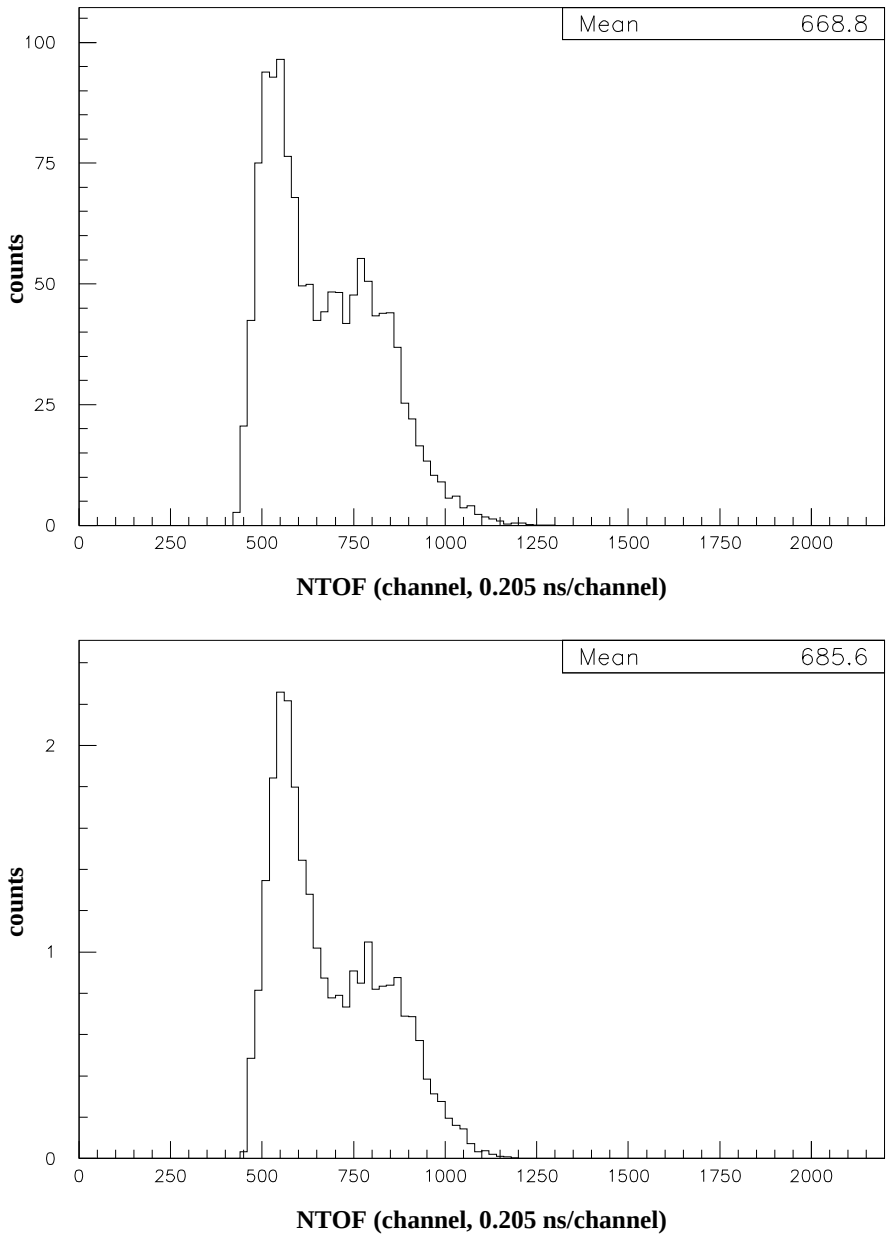

Figure 4.26: Top: the contribution from direct neutrons for detector 2 for the ${}^2H(\pi^-, n\gamma)n$ reaction. Bottom: the contribution to the NTOF spectrum of detector 2 from neutrons that cross talk in the adjacent detectors. Note the vertical axis scale differences between the two plots.

This observation led us to the idea that the γ-ray detection efficiency was not constant across the area of the γ detector. The efficiency of the γ-ray detector is the product of the efficiencies of the BGO converters, the WC and the CsI crystals. Each could have a position dependent efficiency. Rather than attempting to determine the efficiency of each detector separately, we investigated the position dependence of the efficiency of the aggregate system. The position dependence of the γ-ray detector was determined from the accidental background events. The accidental events were chosen because there should be no directional correlation between the neutron and γ ray, i.e., the γ-ray detector should be uniformly illuminated. The accidental events were selected by putting a software cut on the NTOF event parameter for TOF values faster than the arrival time of the prompt γ ray. The statistical accuracy of the $\pi^- p$ capture data was not sufficient for determining the γ-ray detector efficiency, so the $\pi^- d$ data was used.

Our analysis of the two-dimensional γ-ray position spectra for the accidental background clearly revealed that the efficiency of the γ-ray detector was position dependent.

Such two-dimensional background γ-ray position spectra should be flat if the efficiency of the γ-ray detector is independent of position. We observed that the shapes of these 2-dimensional background γ-position spectra had no neutron detector dependency, proving our original assumption that the directions of the detected neutron and γ ray were uncorrelated. The relative γ-ray detection efficiency was estimated by using the 2-dimensional background γ-ray position spectrum. Only the relative detection efficiency was needed for the simulations. Unlike the data for the accidental events, the shapes of the foreground 2-dimensional γ-ray position spectra (gated by the NTOF region corresponding to physical events) changes with neutron detectors.

The two-dimensional γ-ray position spectrum from the $\pi^- d$ capture data is shown in Figures 4.27. Because these data had some abrupt edges in some

regions, we applied 3-point smoothing to it. The A smoothed version of the spectrum is shown in Figures 4.28. The position dependent γ-ray detection efficiency was included in the simulation as an event weighting factor. The dip in the efficiency in the range $\gamma_y < 10$ was found to be caused by faulty CsI detectors. Relative efficiency curves at several γ_y positions are shown in Figures 4.29. Finally, several relative efficiency curves at different γ_x positions are shown in Figures 4.30.

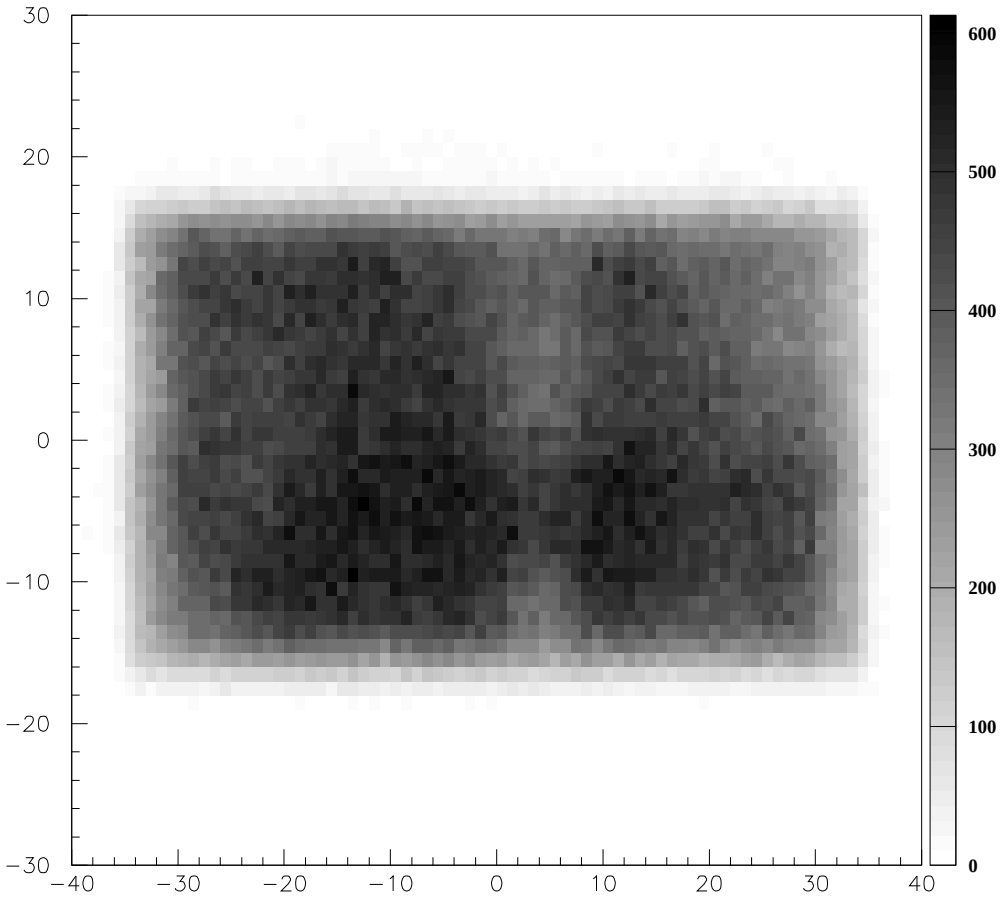

Figure 4.27: Two-dimensional γ-position spectrum for accidental background events. The gray-scale levels are indicated on the side bar.

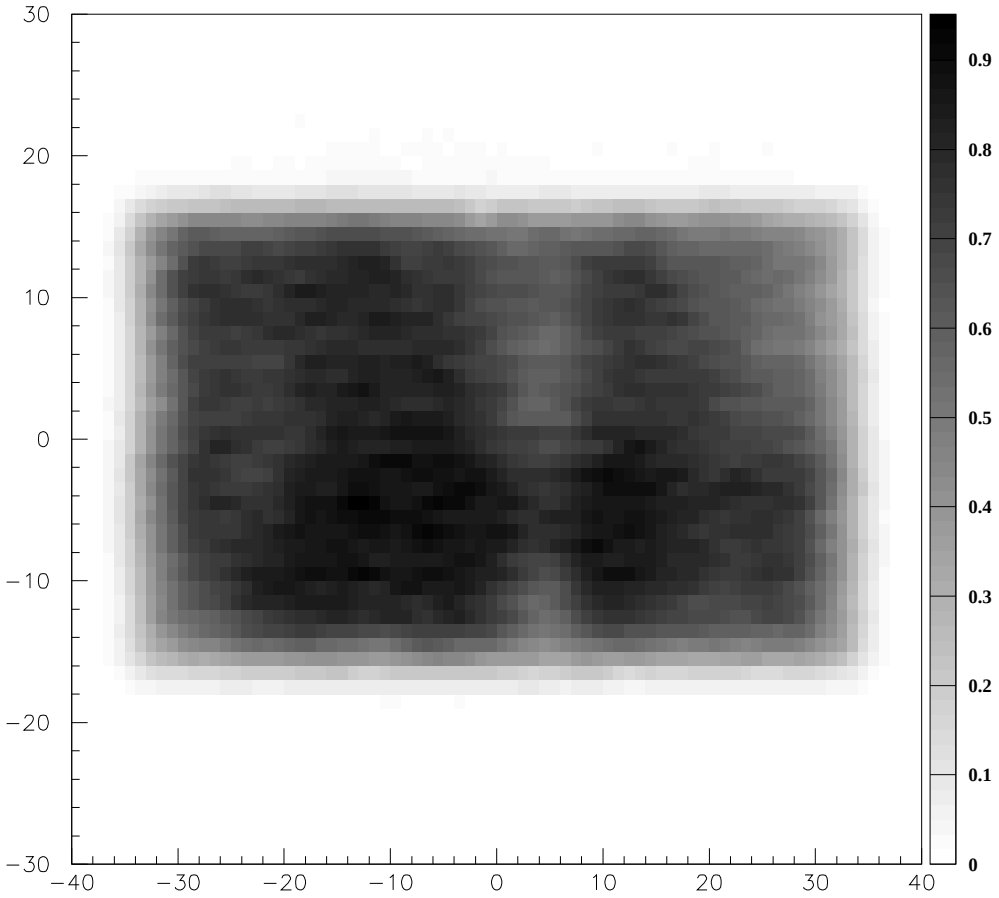

Figure 4.28: Two-dimensional relative efficiency of the γ detector system, which includes the efficiencies of the BGO converter, the wire chamber and the CsI detector array. The data in this plot is a smoothed version of the data shown here is the smoothed result of Figure 4.27

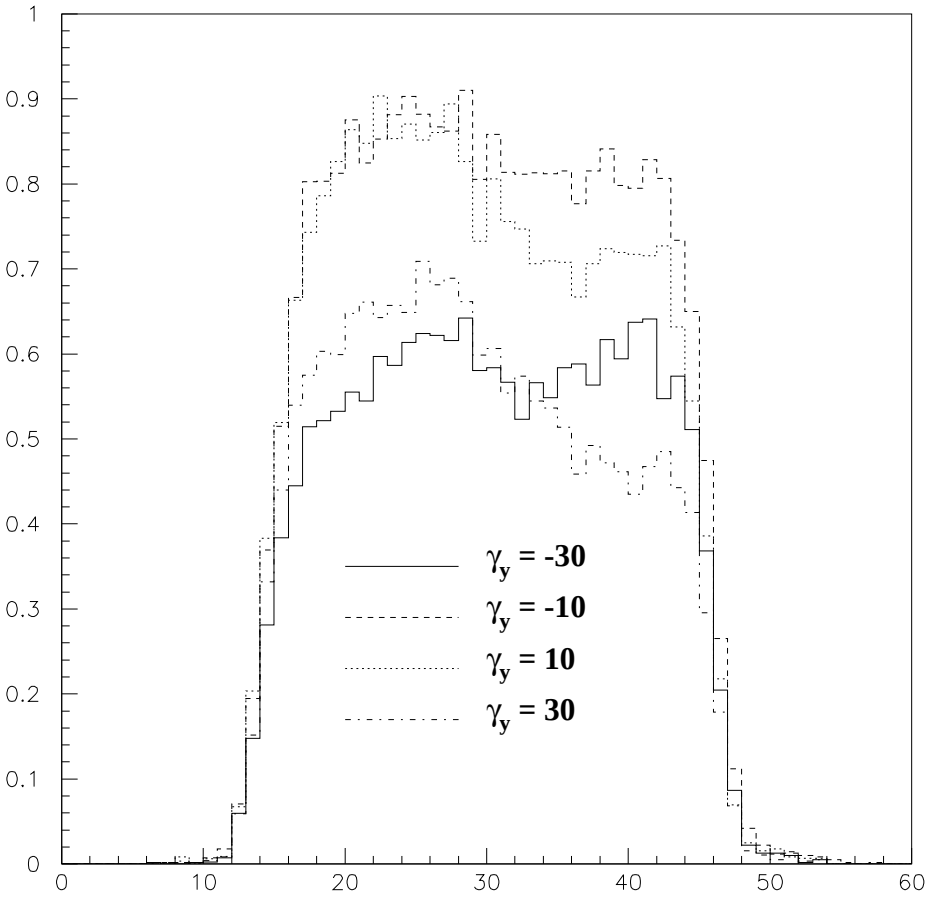

Figure 4.29: Wire Chamber efficiency as a function of γ_x for several γ_y positions, i.e., these are γ_y slices from the 2D plot in Figure 4.28.

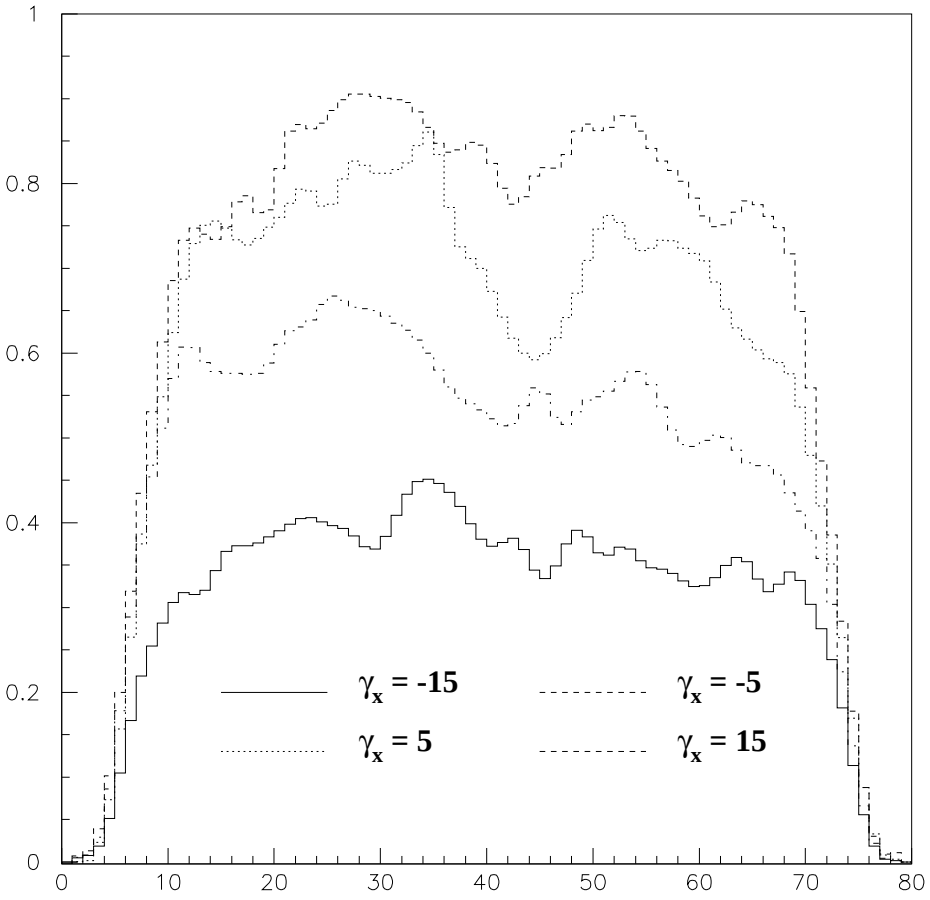

Figure 4.30: Wire Chamber efficiency as a function of γ_y for several γ_x positions, i.e., these are γ_x slices from the 2D plot in Figure 4.28.

Chapter 5

Data Analysis

In this Chapter we describe our techniques for extracting the value of a_{nn} from comparing the shapes of the experimental neutron TOF spectra and discuss the important issues involved in the extraction. Because statistical fitting of the NTOF spectra from the $\pi^- d$ capture data was central to our method of determining a_{nn} , it was necessary for us to identify and model any systematic (non-statistical) structures in the spectra before proceeding. We started the analysis by checking whether the fluctuations in the experimental TOF spectra in kinematically forbidden regions (outside those allowed by the $^1H(\pi^-, n\gamma)$ reaction for the hydrogen target data and outside those allowed by the $^2H(\pi^-, n\gamma)n$ reaction for the deuterium target data) were purely statistical.

5.1 Check for Non-Statistical Structures

A background region of the NTOF spectrum for data taken with the liquid hydrogen target is shown in the top part of Figure 5.1. The events recorded in LAMPF Exp1286 had normal statistical properties as other nuclear events. For example, in the flat region of a NTOF spectrum (the entire TOF spectrum for the $\pi^- p$ data with the exception of the TOF values around the 9 MeV peak and the channels corresponding to TOF values faster than those of the γ-ray peak in the $\pi^- d$ data) the number of counts at each channel should be more or less the same as the average counts in that region. Let the average be n for the n_c channels considered, then 68% of the channels should have counts between $n - \sigma$ and $n + \sigma$ with σ equal to $\sqrt{n}$, and 95% between $n - 2\sigma$ and

$n + 2\sigma$. If this is not the case, then there could be some systematic behavior in the measured spectra.

From our analysis of the background regions in the NTOF spectra, we concluded that the fluctuations in the NTOF spectra for the $\pi^- p$ data were purely statistical. Our results are displayed in the bottom part of Figure 5.1. In the figure, the symbol δc is defined as:

$$\delta c = c(i) - bg(i) \ , \tag{5.1}$$

where $c(i)$ stands for the number of counts at channel i and $bg(i)$ is the height of the straight line at channel i (i.e., the average counts in the region). As shown in Figure 5.1 only 5% of channels have counts beyond $\pm 2\sigma$, where σ is $\sqrt{\overline{c}}$.

A similar analysis was done on the experimental NTOF spectra for the data taken with the deuterium target. In this case we used the region corresponding to particle flight times shorter than that for the prompt γ rays. We found no non-statistical fluctuations.

5.2 Instrumentation Stability and Statistical Precision

The stability of the detection system was critical to the success of our project. During data acquisition, several key parameters (γ_x , γ_y , θ_3 and NTOF) were monitored to gauge the stability of the system. The spectrum for each monitored parameter was found to be consistent from run to run. The system was extra-ordinarily stable and robust. During the data analysis, we re-checked parameters such as the γ-ray peak, QFS peak and FSI peak in the NTOF spectra, the centroids of the γ_x and γ_y spectra for all the runs. We found that they were very consistent.

As mentioned in Chapter 1, the goal of Exp1286 was to determine the value

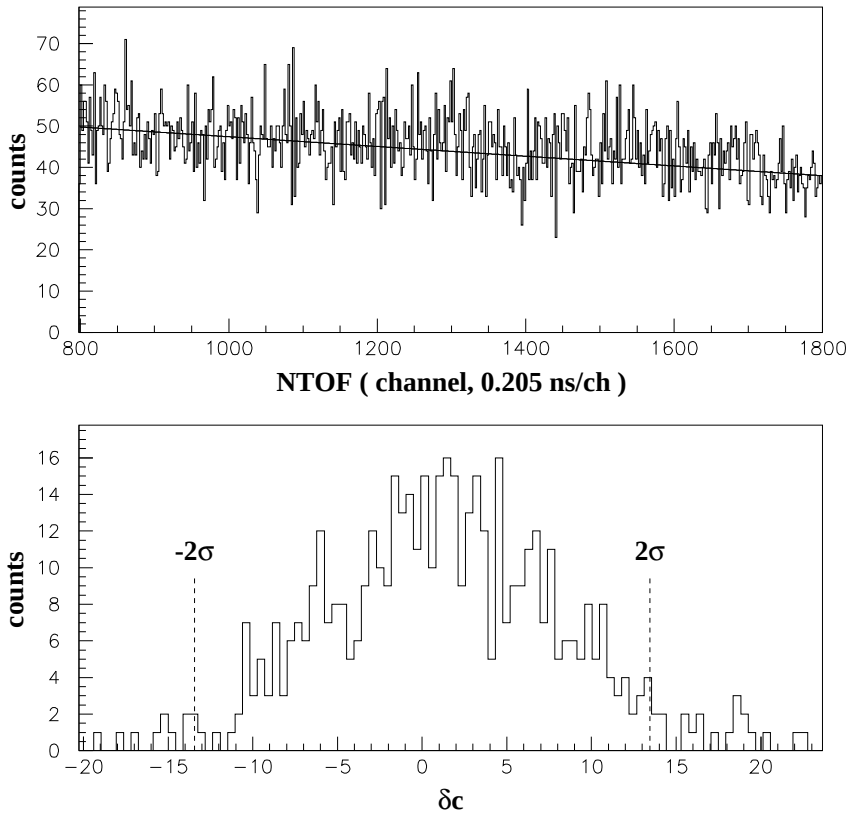

Figure 5.1: Top: plot of NTOF spectrum in the background region for the hydrogen target data. Bottom: plot of the distribution from the average value in the background region of the NTOF spectrum shown in the top plot.

of a_{nn} with high accuracy. The statistical error can be one of the main uncertainties contributing to the total uncertainty in our value of a_{nn}. The only way to reduce the relative error caused by statistical fluctuations in a measured quantity is to increase the number of counts. In Exp1286, the geometry parameters (mainly the flight-path length of the neutron detectors, and the matching distance from the target to the γ-ray detector) were chosen to maximize counting rate while maintaining the minimum neutron energy resolution. The geometry of the setup was held fixed throughout the data-acquisition phase. About eighty production runs were taken with the liquid deuterium target. The deuterium runs in Exp1286 are summarized in Table I.1.

From Table I.1 it can be easily seen that the background was reduced significantly by applying PSD cuts (this shows the power of n/γ discrimination and justifies our use of liquid scintillators for the neutron detection).

5.3 Hydrogen Contamination

In section 2.1.1 we described the hydrogen contamination problem in the deuterium target, which we mentioned earlier in Chapter 2. We repeat that we cannot extract the value of a_{nn} without considering the hydrogen contamination. To be more specific, since we extract a_{nn} for different θ_3 cuts, and the θ_3 spectra for the $^1H(\pi^-, n)\gamma$ reaction are mainly in the region of 0.0 to 0.2 radian, the hydrogen contamination is not a problem for spectra with associated θ_3 cuts beyond 0.2 radian. Before we compare the shapes of the experimental NTOF spectra with the simulated ones for a specific θ_3 (remember that the shapes of the NTOF spectra changes with θ_3), instead of trying to remove the hydrogen contamination from the experimental spectra, we added hydrogen contamination into the deuterium target in the MC simulation in the H/D events ratio that we will describe below. The simulated NTOF spectra obtained using this mixing procedure matches the experimental spectra very well.

The size of the contamination was determined by comparing the yields from the $\pi^- d$ capture reaction to those from the $\pi^- p$ capture. By normalizing the simulated NTOF spectrum to the valley between the QFS and FSI peaks in the experimental spectrum, we obtained an estimate of the $\pi^- p$ capture yields. The $\pi^- p$ capture yields are taken to be the difference between the data and the normalized simulated spectrum in the QFS region.

In analyzing the NTOF for the first θ_3 cut (0.00 to 0.05 radian), we found that the QFS peak (centered around channel 520) was much sharper than in the simulated spectrum. Our initial comparisons of the simulated spectra to data are shown in Figure 5.2. The aggregate NTOF spectrum was simulated for three values of a_{nn}, -16, -18 and -20 fm. The simulated spectra were normalized to the data in the NTOF channel range from 600 to 660. None of the simulated spectra describe the QFS peak for this angle cut. We found that the sharp structure in the QFS region of the NTOF spectrum was due to π^- capture on a hydrogen contaminant in the deuterium target. Therefore, an appropriate amount of hydrogen was added to the simulation for the deuterium target.

From the analysis of Figure 5.2 we find

$$\frac{Y_1(\pi^- p)}{Y_1(\pi^- d)} = 2.9\% \ , \tag{5.2}$$

where Y is the yield and subscript "1" indicates "θ_3 cut 1", which includes the θ_3 region between 0.0 and 0.05 radian. Also, we have:

$$\frac{Y_1(\pi^- d)}{Y_{all}(\pi^- d)} = 8.0\% \quad \text{and} \quad \frac{Y_1(\pi^- p)}{Y_{all}(\pi^- p)} = 74.6\% \ , \tag{5.3}$$

where the subscript "all" indicates all events (i.e., no θ_3 cut).

The relative number density of hydrogen to deuterium is given by the ratio of the total yields for $\pi^- p$ to that of $\pi^- d$ capture:

$$\frac{Y_{all}(\pi^- p)}{Y_{all}(\pi^- d)} = \frac{\frac{Y_1(\pi^- p)}{0.746}}{\frac{Y_1(\pi^- d)}{0.08}} = 0.31\% \ . \tag{5.4}$$

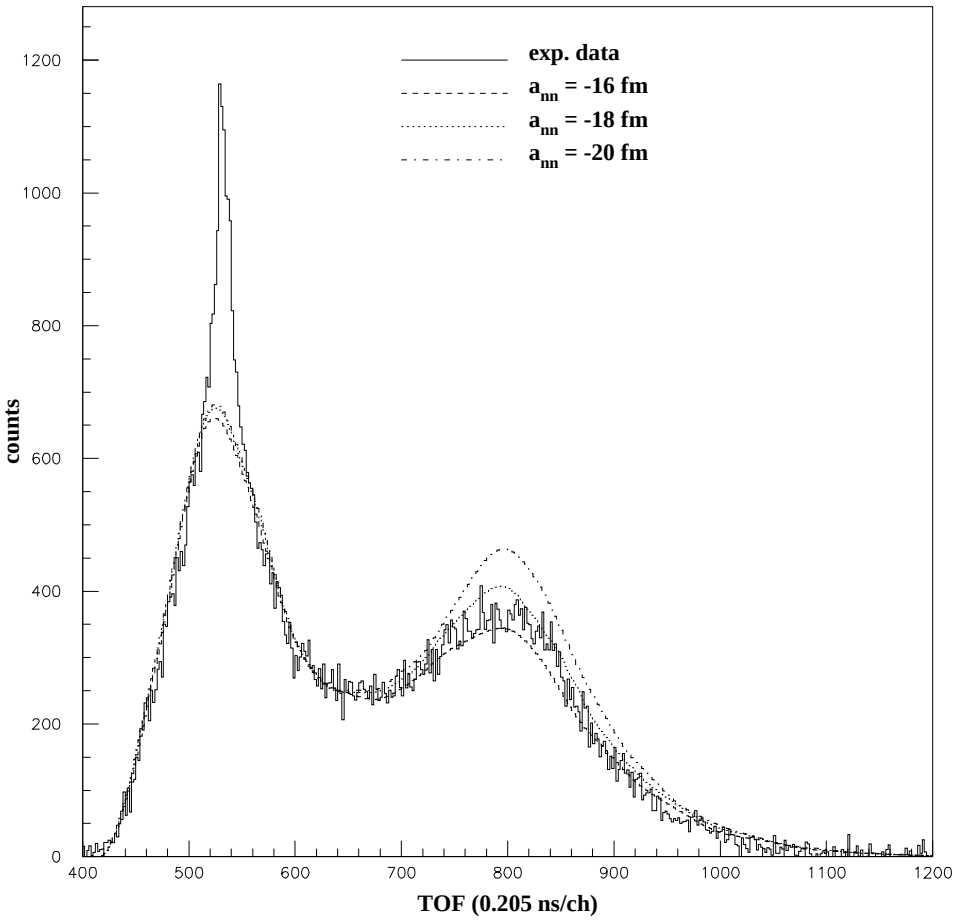

Figure 5.2: Plot of NTOF spectra for the entire detector array for θ_3 cut 1 ($0 \leq \theta_3 \leq 0.05$ radian). The plot made with the bold solid curve is the experimental spectrum. The other plots are MC simulations made with a_{nn} =-16 fm (dashed), a_{nn} =-18 fm (dotted) and a_{nn} =-20 fm (dashed-dotted). The simulated spectra were normalized to have the same area as the experimental spectrum in the region between channels 600 and 660.

The angle-integrated $\pi^- p$ and $\pi^- d$ capture cross sections are about equal [Gib75b]. In other words, in Exp1286 a spectrum obtained with the deuterium target contained 0.31% of the counts from the $^1H(\pi^-, n)\gamma$ reaction when no θ_3 cut was applied.

The relative contribution of π^- capture on the contaminant hydrogen in the deuterium target is shown in Figure 5.3. The contributions from the 0.31% hydrogen contaminants were added to the simulated NTOF spectra before comparison to data.

A value of a_{nn} and a statistical uncertainty were determined from each of the five θ_3 angle cuts following the fitting procedure described earlier in this section. The results are graphically displayed in Figure 5.4 and in Figure 5.7 through Figure 5.10.

5.4 Fitting the Experimental NTOF Spectra

In our method, a_{nn} was determined by fitting the $\pi^- d$ NTOF spectra with the simulated spectra using only one free parameter, a_{nn} .

In this section, we describe a technique for extracting the value of a_{nn} from the experimental neutron TOF spectra. As stated previously, this method requires the precise modeling of the experiment. The simulated spectra were smoothed to take out statistical fluctuations. The formula for 3 point smoothing is

$$C_i = \frac{C_{i-1} + 2\ C_i + C_{i+1}}{4}\ , \tag{5.5}$$

where C_{i-1}, C_i and C_{i+1} are counts for channel (i-1), i and (i+1), respectively. Usually, a 3-point smoothing was applied twice. However, in cases of high statistical fluctuations in the simulated spectra, the 3-point smoothing algorithm was applied three or four times consecutively to reduce the impact of statistical fluctuations.

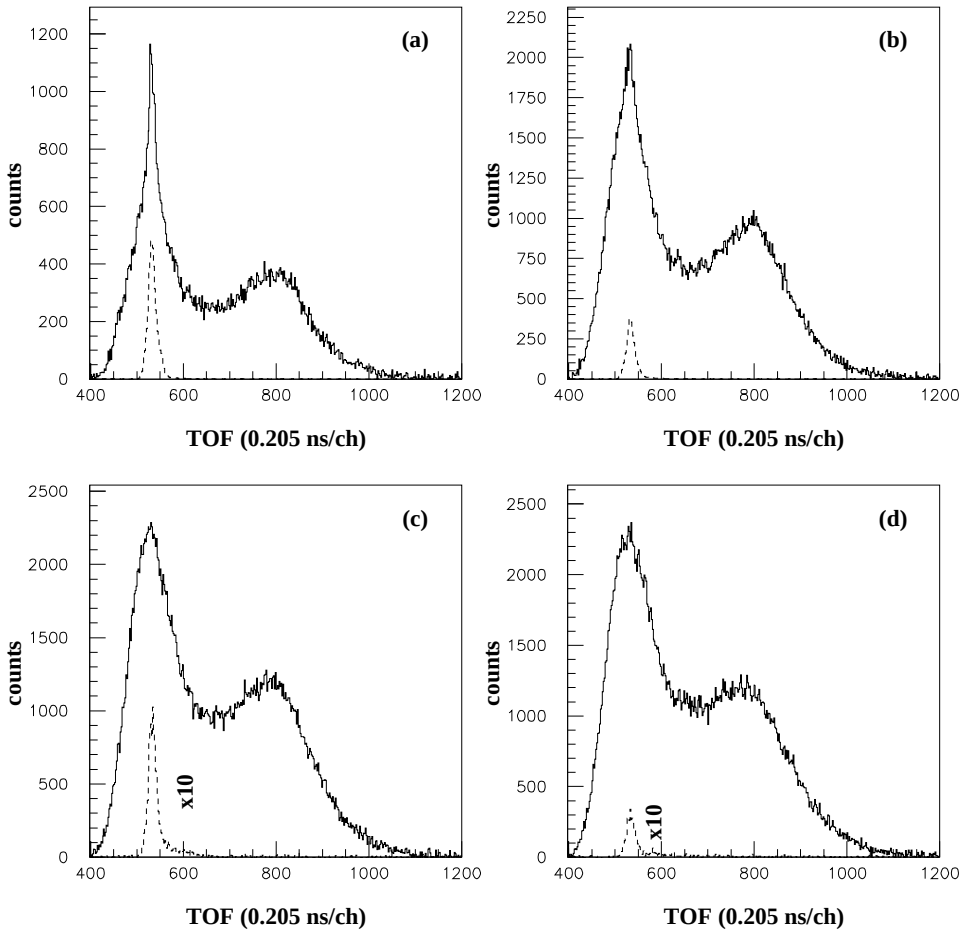

Figure 5.3: Experimental neutron TOF spectra for the deuterium target (solid curves) and for the hydrogen target (dashed curves). The hydrogen-target data have been normalized to make the integrated yields 0.31% of those for the deuterium target. The four spectra are for θ_3 cuts: (a) cut 1, (b) cut 2, (c) cut 3, (d) cut 4. For cut 3 and 4, the spectra for the hydrogen target were magnified to be visible.

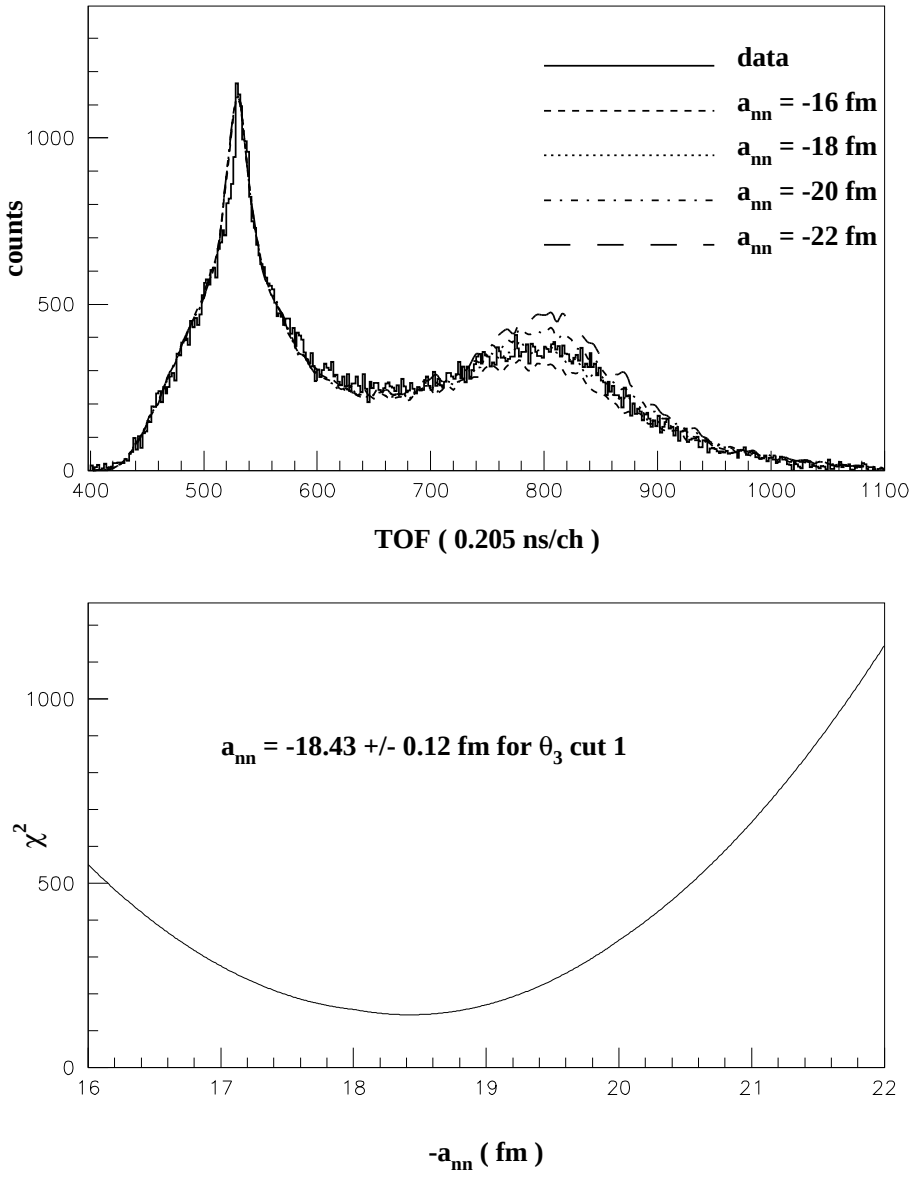

Figure 5.4: The top plot is a comparison of the shape of the experimental NTOF spectrum with that of the corresponding Monte Carlo simulated TOF spectrum for a θ_3 cut between 0.00 and 0.05 radian. The spectra are for the entire neutron-detector array. The bottom plot is the total χ^2 vs. a_{nn} .

After smoothing the simulated neutron TOF spectra were normalized to have the same number of counts in the QFS peak (in Figure 5.4, it corresponds to the area between channels 450 and 650) as the experimental spectra. The value of a_{nn} was extracted from the experimental NTOF spectra by fitting them with the simulation using χ^2 analysis in the region of the FSI peak. The FSI peak area corresponds to the area between channels 720 and 920 in Figure 5.4. The χ^2 values from the fit were computed as

$$\chi^2 = \sum_{i_s}^{i_e} \frac{(C_i^{mc} - C_i^{exp})^2}{(\delta C_i^{exp})^2} \ , \tag{5.6}$$

where i_s and i_e are the starting and ending channels of the range use for calculating the total χ^2. The symbol δC_i^{exp} is the statistical experimental error for the counts in channel i, C_i^{mc} is the counts in channel i for the MC simulated spectrum and C_i^{exp} is the counts in channel i for the experimental spectrum. The δC_i^{exp} is calculated according to

$$\delta C_i^{exp} = \sqrt{C_i^{exp}} \ . \tag{5.7}$$

Monte-Carlo simulations were run for four values of a_{nn} , -16 fm, -18 fm, -20 fm and -22 fm, see Figure 5.4. Spectra for other a_{nn} values were obtained by linearly interpolating between the above values. The simulated spectra for an arbitrary value of a_{nn} , for example, $a_{nn} = x$, where x is between -16 fm and -18 fm, is given by

$$C_i(x) = r_1 C_i(-16) + r_2 C_i(-18) \ , \tag{5.8}$$

where $C_i(-16)$ and $C_i(-18)$ are the counts in channel i for the case of $a_{nn} =$ -16 fm and $a_{nn} =$ -18 fm, respectively. The symbols r_1 and r_2 were defined as

$$r_1 = \frac{x + 18}{2} \ \text{ and } \ r_2 = 1 - r_1 \ . \tag{5.9}$$

Using the interpolation between simulated spectra, continuous curves of χ^2 as a function of a_{nn} , as shown in the bottom of Figure 5.4, were generated. The

extracted a_{nn} corresponds to the value that gave the minimum χ^2 value. The statistical errors were determined from the χ^2 curve by drawing a horizontal line at the value of $\chi^2_{min} + 1$. The a_{nn} values where the line intercepts the χ^2 curve give the minimum and maximum values, a_{nn}^{min} and a_{nn}^{max}, respectively, that are within one standard deviation of the optimum value. The method for obtaining a_{nn} and $\triangle a_{nn}$ from the χ^2 plots is illustrated in Figure 5.4.

One note to make is that the simulated θ_3 spectrum for all the detectors did not match the corresponding experimental θ_3 spectrum beyond 0.2 radian (see Figure 5.6). Therefore, when extracting a_{nn} values for θ_3 cuts beyond 0.2 radian, i.e., cuts beyond cut 4, we averaged the simulated NTOF spectra for θ_3 cut i and $i+1$ before comparing it with the experimental NTOF spectra for θ_3 cut i (i is an integer not less than 4).

The sensitivity of the shape of the NTOF spectrum to the n-γ opening angle $\theta_{n\gamma}$, see bottom plot in Figure 3.3, provided a tool for diagnosing systematic errors in our techniques. Values of a_{nn} were determined as a function of θ_3, the supplement to $\theta_{n\gamma}$. Since the extracted values of a_{nn} should be independent of angle, an angular dependence would indicate a systematic problem with the simulation. A problem of this type is likely to be caused by either a geometry misalignment (relative to the experimental setup) or an error in describing the experimental stopped π^- distribution in the simulations. The data were analyzed in 0.05-radian wide bins of θ_3 over the range $0 \leq \theta_3 \leq 0.25$. The measured yields from π^- capture in the deuterium target as a function of θ_3 is shown in Figure 5.6. Values for a_{nn} were extracted from the aggregate NTOF spectra for five θ_3 cuts: $0 \leq \theta_3 \leq 0.05$, $0.05 < \theta_3 \leq 0.10$, $0.10 < \theta_3 \leq 0.15$, $0.15 < \theta_3 \leq 0.20$, $0.20 < \theta_3 \leq 0.25$ radians. The upper limit on θ_3 was set to keep the magnitude of the scattering-length term in the low-energy limit equation, Equation 1.9, a factor of 10 greater than that for the effective-range term. Beyond our maximum limit, the sensitivity of the NTOF spectra to

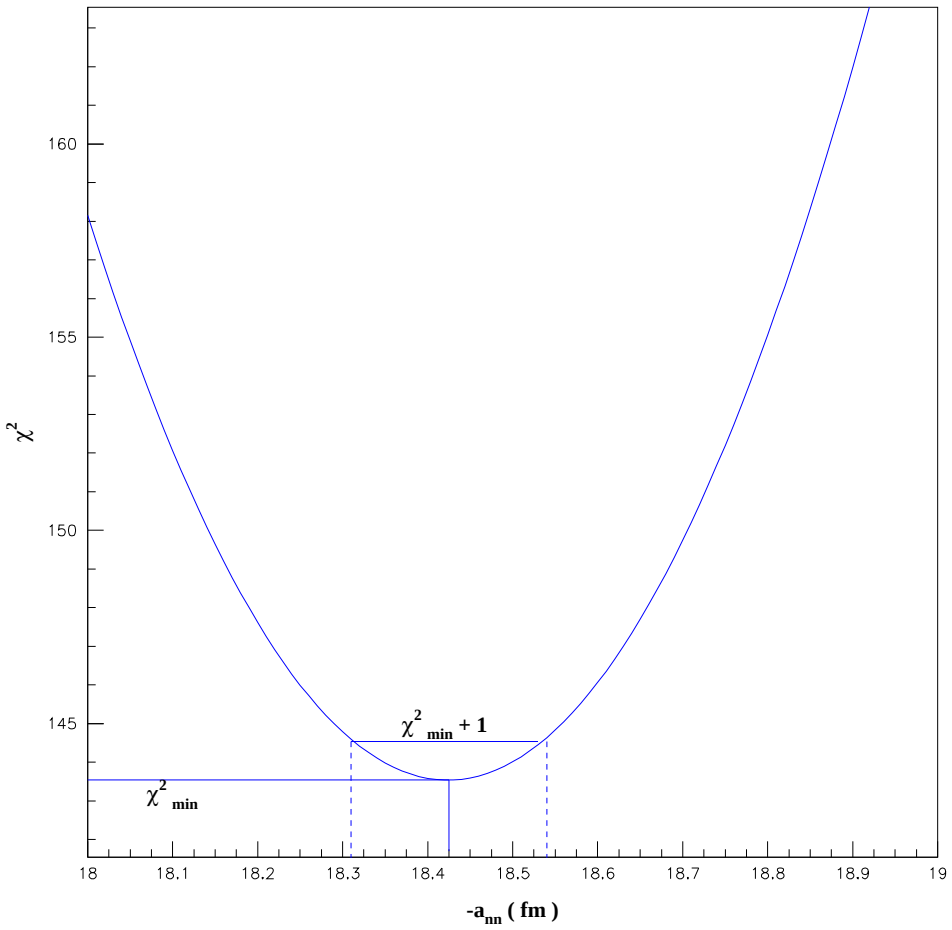

Figure 5.5: Plot of χ^2 as a function of a_{nn} resulting from the fit in the top of Figure 5.4. The plot shown here is a manification of the region between -18 and -19 fm in Figure 5.4.

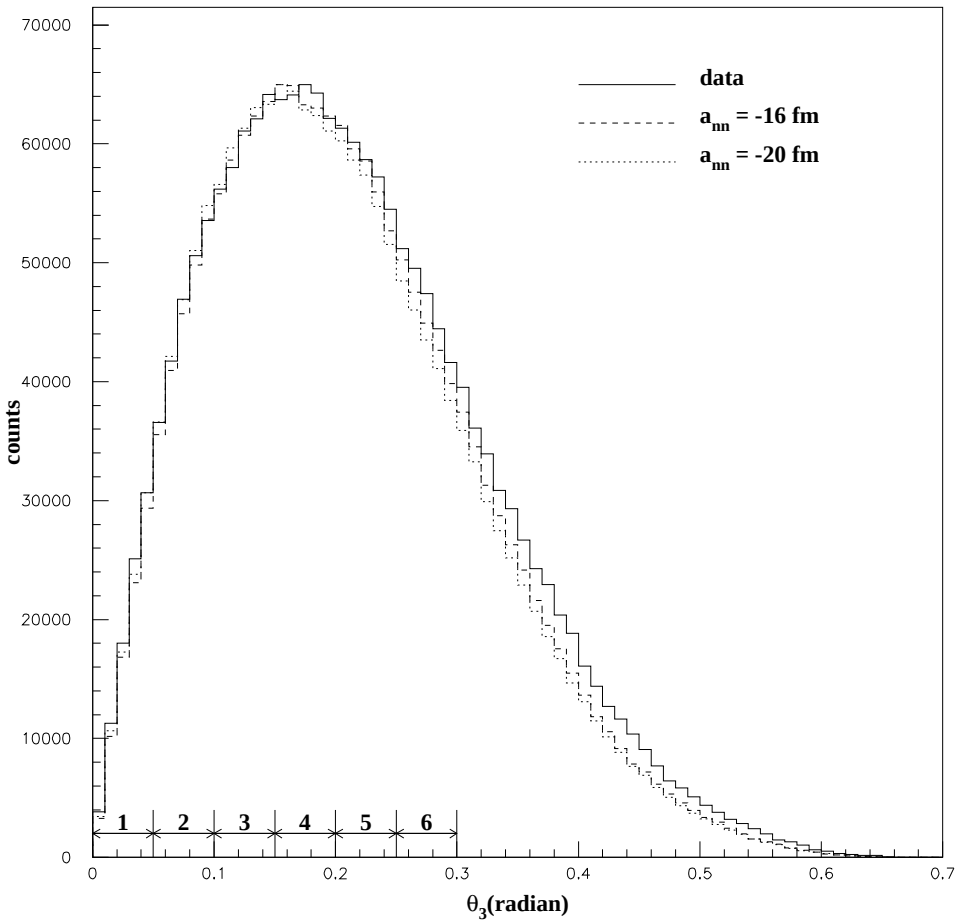

Figure 5.6: Plot of the measured yields (n-γ coincidences) for π^- capture in the deuterium target as a funciton of θ_3 . This spectrum was accumulated using the entire neutron-detector array. It contains about 98% of the total data taken in Exp1286.

a_{nn} diminished, and the NTOF spectra for θ_3 cuts larger than our limits would add little to the statistical accuracy of the final results.

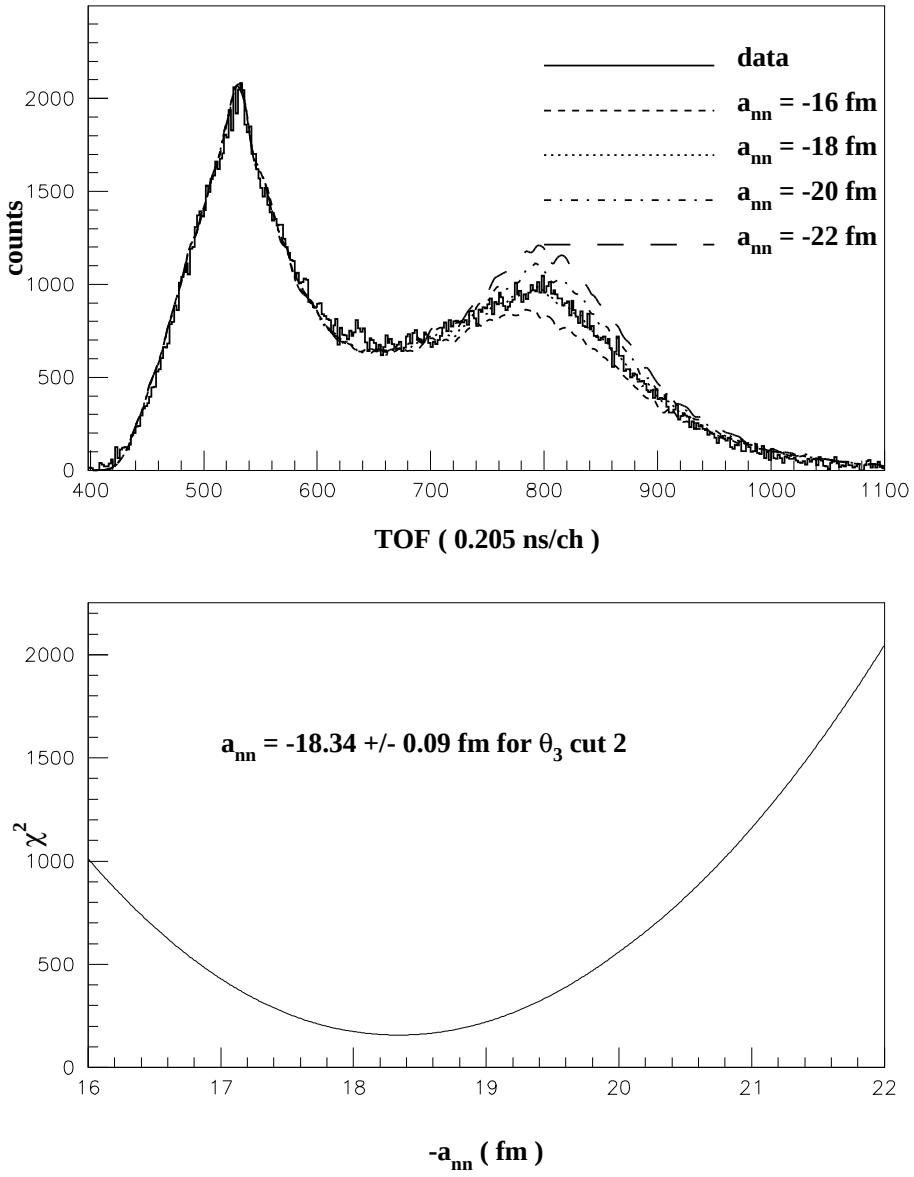

Figure 5.7: Same as Figure 5.4 except for θ_3 cut 2 (between 0.05 and 0.10 radian).

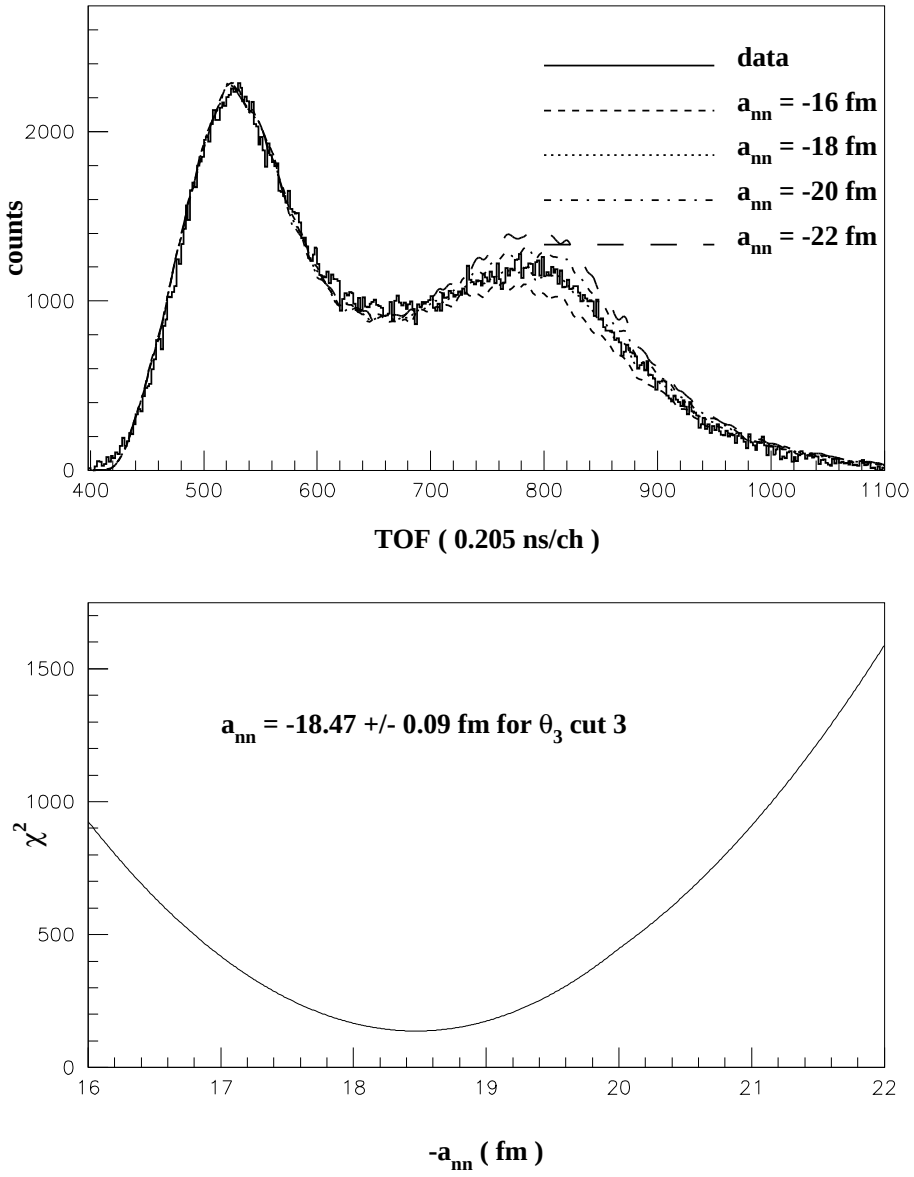

Figure 5.8: Same as Figure 5.4 except for θ_3 cut 3 (between 0.10 and 0.15 radian).

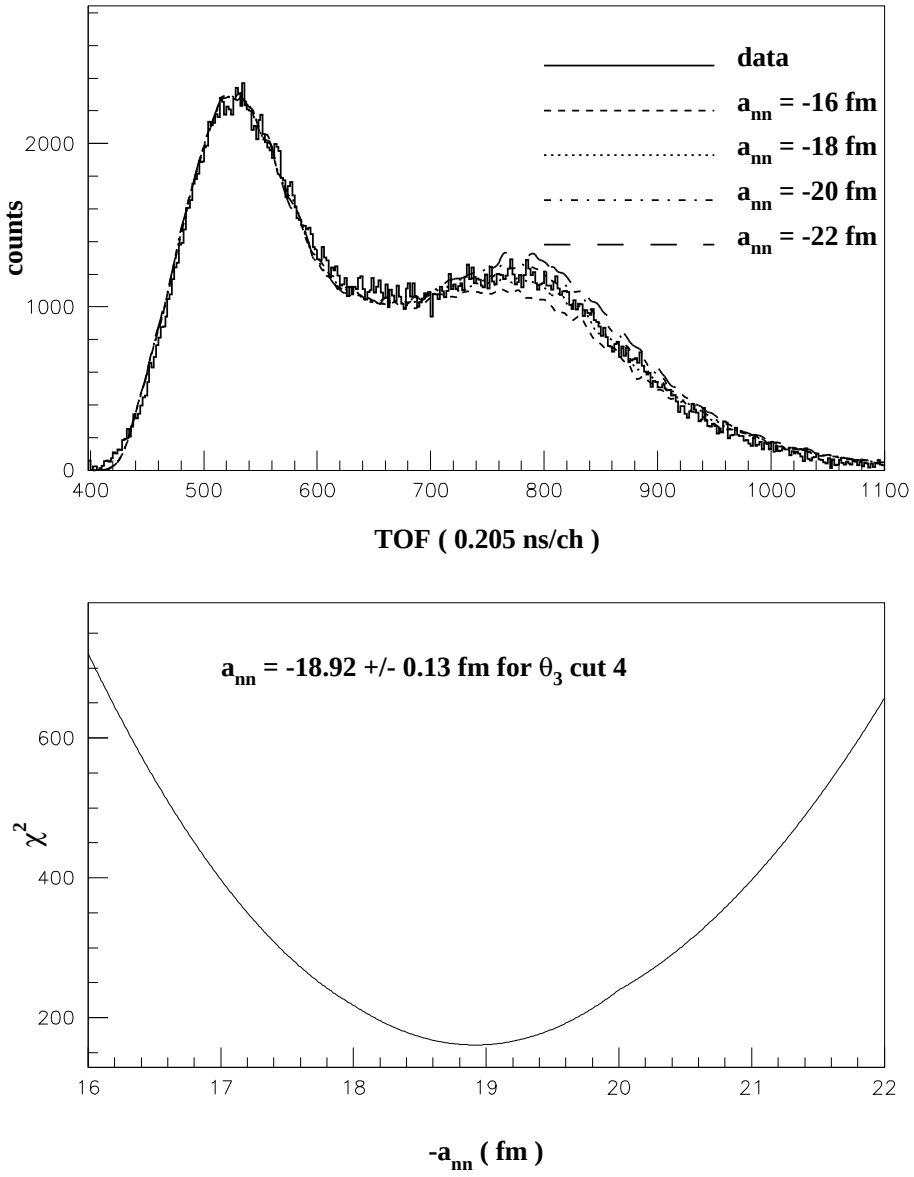

Figure 5.9: Same as Figure 5.4 except for θ_3 cut 4 (between 0.15 and 0.20 radian).

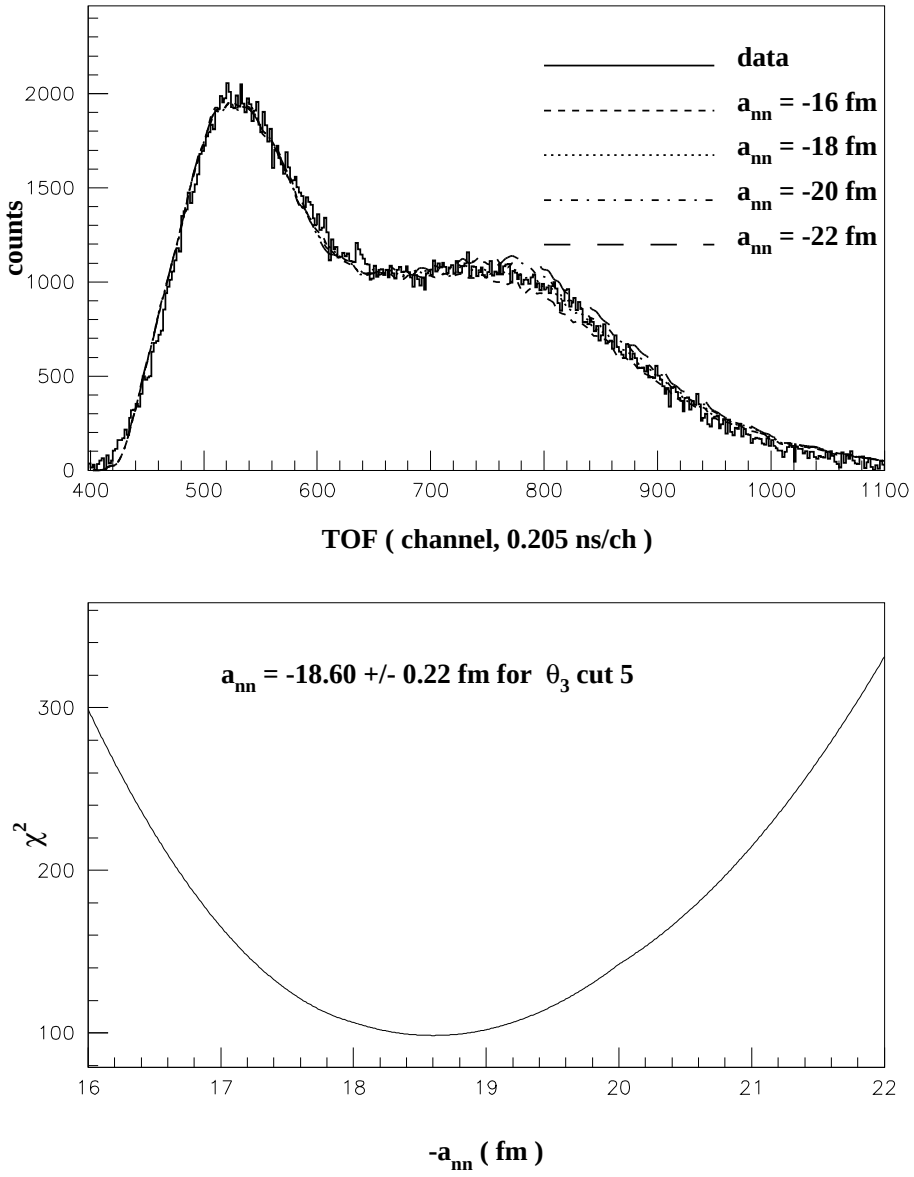

Figure 5.10: Same as Figure 5.4 except for θ_3 cut 5 (between 0.20 and 0.25 radian).

Chapter 6

Results and Conclusions

In section 5.4 we described our method for extracting the value of a_{nn} from the experimental neutron TOF spectra. In this chapter, we evaluate the effects of some key experimental candidates on the determination of a_{nn} from the NTOF spectra and present our final results.

In the sections to follow values of a_{nn} are determined by fitting the experimental NTOF spectra with increasingly more sophisticated MC simulations. The first is a point-geometry simulation, the second includes the finite-geometry of our setup but neglects neutron scattering, the third simulation includes all effects except scattering in the neutron-detector array (cross talk), and the final simulation is the full modeling.

6.1 Results from Point Geometry

In this section we determine a value of a_{nn} from the experimental NTOF spectra using a point-geometry MC simulation. In these simulations the π^- capture takes place in a point deuterium target and the emitted neutrons are detected by point detectors. The point target is located at the origin of the coordinate system and each point detector is located at the center of the corresponding neutron detector. Scattering (both out-scattering and in-scattering) inside the target system and cross talk between detectors are ignored in the present calculations. Using the χ^2 procedure described in Chapter 5, a_{nn} values were obtained from the combined spectrum for all the detectors for the θ_3 cuts listed in Table 6.1.

Please note that the θ_3 cut has the same meaning throughout this chapter,

θ_3 cut	θ_3 range (rad)	a_{nn} (fm)	$\triangle a_{nn}$
1	0.00 to 0.05	-17.40	0.15
2	0.05 to 0.10	-17.40	0.10
3	0.10 to 0.15	-17.30	0.15
4	0.15 to 0.20	-17.10	0.15
5	0.20 to 0.25	-17.30	0.20
6	0.25 to 0.30	-17.60	0.35
7	0.30 to 0.35	-18.50	0.35

Table 6.1: Values of a_{nn} extracted from the combined NTOF spectra of all detectors with different θ_3 cuts. Point geometry was assumed in the simulation and only direct neutrons were considered in the simulation. The uncertainties are purely statistical and were derived as explained in section 5.4.

and the θ_3 range of each θ_3 cut will not be repeated in other tables. The weighted average value of a_{nn} for the cuts in Table 6.1 is

$$a_{nn} = -17.37 \pm 0.06 \text{ fm} . \tag{6.1}$$

The uncertainty in the above value is purely statistical.

6.2 Results with Finite Geometry

In this section, the geometric size of the target and the neutron detectors are taken into account. As in the previous section neutron scattering in the target and cross talk in the neutron detectors are not taken into account in these simulations. The results are tabulated in Table 6.2.

θ_3 cut	a_{nn} (fm)	$\triangle a_{nn}$
1	-17.70	0.15
2	-17.80	0.15
3	-17.90	0.15
4	-17.70	0.15
5	-17.50	0.25
6	-17.90	0.45

Table 6.2: Same as Table 6.1, except a_{nn} extracted using a MC simulation that included the finite geometry of the experimental setup.

The average value of a_{nn} and its statistical uncertainty for the cuts in Table 6.2 is

$$a_{nn} = -17.76 \pm 0.07 \text{ fm} . \tag{6.2}$$

From the difference of this result with the one in the previous section, we can conclude that the effect of the finite geometry of our experimental setup on the extracted value of a_{nn} is

$$\delta a_{nn} = 0.39 \pm 0.10 \text{ fm} . \tag{6.3}$$

6.3 Results with Finite Geometry and Scattering inside Target System

In this section, we present the a_{nn} values by comparing experimental results with Monte-Carlo simulated results with finite geometry and scattering taken into account. The effects of scattering inside the target has been discussed in section 4.6.2. The effects were estimated by assuming that all neutrons from the $^2H(\pi^-, n\gamma)n$ reaction originated at the center of the target. Here we use Monte-Carlo techniques to model the effects of the target size and density. The details are given in Chapter 4.

The first step in the event generation procedure is to randomly select a site within the liquid target where the $\pi^- d$ capture reaction is to occur. A neutron from the reaction is then transported through the target materials (the liquid deuterium and the cryostat wall). Some of the neutrons traversing the material in the target assembly scatter before exiting. Because the probability of scattering is energy dependent, the scattering process alters the shape of the NTOF spectrum. There are two distinguishable scattering processes that have opposite effects on the experimental spectra. The dominant type, called "out-scattering", removes counts from the experimental spectra. Because this process removes counts , it is commonly referred to as attenuation. The impact

of neutron attenuation inside the target on the shapes of the NTOF spectra is shown in Figure 4.7. The other process is referred to as "in-scattering". It adds counts to the experimental spectra. Though the effects of these processes are in the opposite direction, they generally are not compensating for each other and must be modeled separately. The results of the simulations which includes these scattering processes are given in Table 6.3.

θ_3 cut	a_{nn} (fm)	$\triangle a_{nn}$
1	-18.60	0.15
2	-18.70	0.15
3	-18.80	0.15
4	-18.60	0.20
5	-18.30	0.20
6	-18.30	0.25

Table 6.3: Values of a_{nn} from NTOF spectra of all detectors with different θ_3 cuts. The MC simulation took into account finite geometry and neutron scattering in the target.

The average value of a_{nn} for the cuts in Table 6.3 is

$$a_{nn} = -18.61 \pm 0.07 \text{ fm} . \tag{6.4}$$

This result indicates that the inclusion of neutron scattering in the target assembly in the MC simulations increases the absolute value of a_{nn} extracted by fitting the NTOF spectra by about 1 fm.

6.4 Results from Full Monte-Carlo Simulation

In this section, we present the results of the full simulation, our most complete attempt to model the experiment. We use the full simulation to investigate the systematic behavior of simulation model we were using and to test for consistency of the extracted values of a_{nn} . More specifically, we will see if the values of a_{nn} are consistent when we extract a_{nn} from different perspectives. We will first extracte a_{nn} from the NTOF spectra of individual detectors with a θ_3 cuts

between 0.0 and 0.25 radian (because in this region, the simulated θ_3 spectrum is in excellent agreement with the experimental θ_3 spectrum for each neutron detector). Then, a_{nn} is extracted from the aggregate NTOF spectra for different θ_3 cuts. Finally, a_{nn} is extracted from the NTOF spectra of a specific type of neutron detector with a specific θ_3 cut.

6.4.1 Values of a_{nn} from NTOF Spectra of Individual Detectors

Because the statistics is very poor when a θ_3 cut is put on the experimental NTOF spectrum of an individual detector and the simulated θ_3 spectrum does not match the experimental θ_3 spectrum very well beyond 0.25 radian, we chose to apply a θ_3 cut of 0.0 to 0.25 radian when extracting the value of a_{nn} from the NTOF spectra of individual detectors.

The values of a_{nn} obtained by fitting the NTOF spectra of individual detectors are listed in Table 6.4.

det #	a_{nn}	$\triangle a_{nn}$	det #	a_{nn}	$\triangle a_{nn}$
1	-18.90	0.25	2	-18.40	0.25
3	-18.48	0.28	4	-18.80	0.20
5	-17.55	0.25	6	-17.95	0.40
7	-18.95	0.25	8	-18.55	0.25
9	-18.83	0.28	10	-19.13	0.23
11	-19.05	0.20	12	-18.68	0.28
13	-19.10	0.25	14	-17.98	0.48
15	-19.58	0.38	16	-18.90	0.45
17	-17.30	0.23	19	-17.18	0.33
20	-19.33	0.33	21	-18.83	0.33
22	-16.38	0.33	23	-17.20	0.35
25	-19.33	0.33	26	-18.55	0.35

Table 6.4: Values of a_{nn} from the NTOF spectra of individual neutron detectors. A θ_3 cut of 0.0 to 0.25 radian was applied on the NTOF spectra. The values were obtained with the full simulation.

Referring to Figure 2.6, we can see that there does not appear to be any

spatial dependence on the measured values of a_{nn}. Again, the results indicate small alignment errors in the simulation.

The weighted average value of a_{nn} from Table 6.4 is

$$a_{nn} = -18.51 \pm 0.06 \text{ fm} . \tag{6.5}$$

Here uncertainties are statistical only. The a_{nn} values from the different detectors are spread over the range from -16.38 fm to -19.58 fm with no apparent dependencies on detector types or detector positions, indicating that there is no systematic uncertainty between different detectors.

6.4.2 Values of a_{nn} from the Aggregate NTOF Spectrum with Different θ_3 Cuts

The aggregate NTOF spectrum for a particular θ_3 cut is formed by treating the entire neutron-detector array as a single detector, i.e., adding together the histograms of the individual detectors. Since we have reasonable statistics in the aggregate NTOF spectra for each θ_3 cut, the consistency of the values of a_{nn} determined in the cuts gives one measure of systematic uncertainties in our techniques. The a_{nn} values extracted from the aggregate NTOF spectrum for different θ_3 cuts are listed in Table 6.5.

θ_3 cut	a_{nn}	$\triangle a_{nn}$
1	-18.43	0.12
2	-18.34	0.09
3	-18.47	0.09
4	-18.92	0.13
5	-18.60	0.22
6	-18.48	0.24

Table 6.5: The a_{nn} values extracted from the aggregate NTOF spectrum for different θ_3 cuts using a full MC simulation (finite geometry, neutron scattering in the target and cross talk contributions are all considered).

The average value of a_{nn} for the cuts in Table 6.5 is

$$a_{nn} = -18.50 \pm 0.05 \text{ fm} . \tag{6.6}$$

Here, uncertainties are statistical only. The a_{nn} values from the different cuts are in agreement within statistical errors, indicating that alignment errors in the simulation are small.

6.4.3 Values of a_{nn} from Different Types of Detectors

Now we determine a value of a_{nn} for each detector type for θ_3 cut 3. This cut was chosen because the NTOF spectrum for this cut had the highest statistical precision. The extracted a_{nn} values are listed in Table 6.6. The dimensions of the different types of detectors are listed in Table 2.1.

det type	a_{nn}	$\triangle a_{nn}$
Type 1	-18.24	0.22
Type 2	-18.22	0.13
Type 3	-19.29	0.21
Type 4	-18.54	0.27

Table 6.6: The a_{nn} values extracted from the accumulated data for different types of neutron detectors for the θ_3 cut 3. The values were obtained using the full simulation.

The weighted average value of a_{nn} from Table 6.6 is

$$a_{nn} = -18.47 \pm 0.09 \text{ fm} . \tag{6.7}$$

Here, as in all the average values quoted above, the errors are statistical only.

The values of a_{nn} determined using the four detector types agree within the statistical precision of the measurements. These results validate the neutron detector efficiency curves used in the simulations. They also reinforces the finding in the previous section, i.e., detector alignment errors in the simulation are small. The latter observation stems from the fact that the detector of each type were spatially grouped together in the array.

6.5 Systematic Uncertainties

Here we will consider some systematic uncertainties that may exist in the MC simulation. Since both the beam profile and the neutron detector efficiencies have uncertainties, we will consider their influence on the extracted value of a_{nn} separately.

6.5.1 Systematic Uncertainties due to Uncertainties in Absolute Time of Flight

Since there is an uncertainty of about 0.4 ns in the absolute time of flight, an uncertainty of 0.13 fm is introduced to the value of a_{nn} by such an uncertainty.

6.5.2 Systematic Uncertainties due to Uncertainties in Background Subtraction

Since there is an uncertainty in the background subtraction when we tried to get the net experimental NTOF spectrum by subtracting the background from the experimental NTOF spectrum. Since the background is basically at a constant level and we have a lot of counts that belongs to the background, the background subtraction can be done very accurately. For example, for θ_3 cut 1, we have about 60,000 counts in the background from channels 200 to 1600. That is about 43 counts per channel or about 86 counts per bin. The uncertainty for each bin is about $86/\sqrt{(60,000)}$, which is approximately 0.35. We bring this up to 1 and calculated the uncertainty to the value of a_{nn} is 0.01 fm.

6.5.3 Systematic Uncertainties due to Uncertainties in θ_3

Since there is an uncertainty in θ_3 , we estimate this uncertainty to be about 0.013 radian. Then we do a χ^2 fitting by comparing the experimental NTOF spectrum with an angle-shifted simulated NTOF spectrum and obtained the uncertainty to the value of a_{nn} is about ± 0.23 fm.

6.5.4 Systematic Uncertainties due to Uncertainties in Distribution of Stopped Pions

To estimate the uncertainty in the value of a_{nn} associated with the beam profile, we changed the width and centroid of the beam profile along each direction in the MC simulation and compared the resulting spectra to experimental data. The most sensitive observable to changes in the beam profile was the γ-ray position. For each beam profile, we compared the resulting simulated γ-ray position spectrum to the measured one. The quality of the agreement between the simulated and measured spectra was quantified using a χ^2 calculation. Two examples of comparison of simulated γ-ray position spectrum to data are shown in Figure 4.22 and Figure 4.23.

We observed that the vertical γ-ray position (γ_x) spectrum is more sensitive to the changes in the beam profile in the vertical direction than to the changes in the horizontal direction (either along the beam axis or perpendicular to it). Similarly, the horizontal γ-ray position (γ_y) spectrum is more sensitive to the changes in the beam profile in the horizontal direction than to the changes in the vertical direction. Also, we find that the γ-ray position spectra are more sensitive to the changes in the centroid of the beam profile than to changes to its width.

Using spectra like in Figure 4.22 and Figure 4.23, we were able to determine the uncertainties associated with the width and centroid of the beam profile

uncertainty	along x (cm)	along y (cm)	along z (cm)
beam width	0.80	0.80	0.40
beam centroid	0.20	0.40	0.70

Table 6.7: Summary of uncertainties in beam profile.

along each direction. They are shown in Table 6.7.

After determining the uncertainty in the beam profile parameters, we run a separate MC simulation for each a_{nn} with the width and centroid of the distribution of the stopped pions along each direction changed by the amount shown in Table 6.7. These simulations were used to extract the a_{nn} value following the same procedure as described in Chapter 5. When other conditions are the same, we found that the change in the values of a_{nn} is 0.05 fm or less for uncertaity in the distribution of the stopped pions in the vertical direction, 0.05 fm or less for uncertainty in the distribution of the stopped pions in the beam direction, and 0.20 fm or less for uncertainty in the distribution of the stopped pions in the horizontal direction perpendicular to π^- beam direction. Assuming uncorrelated errors, we assign a systematic uncertainty of $\sqrt{0.05^2 + 0.05^2 + 0.20^2}$ (=0.21 fm) to our value of a_{nn} due to uncertainties in our modeling of the stopped π^- beam distribution in the target.

6.5.5 Systematic Uncertainty from Neutron-Detector Bias Uncertainty

Since the biases for the neutron detectors could change slightly during the experiment due to various reasons, such changes might change the shapes of the measure NTOF spectra and consequently bring an uncertainty to the values of the extracted a_{nn} . For an estimate of this effect, we proceed again by comparing the shapes of the experimental NTOF spectra with simulated ones

to extract values of a_{nn} . For convenience, let us define

$$\eta_{pp} = \frac{\text{number of counts at the FSI peak in a NTOF spectrum}}{\text{number of counts at the QFS peak in the same NTOF spectrum}} , \quad (6.8)$$

and

$$E_{pp} = \frac{\text{detector efficiency for neutrons at the FSI peak}}{\text{detector efficiency for neutrons at the QFS peak}} . \quad (6.9)$$

In Figure 5.4 η_{pp} changed from 31% to 36% when a_{nn} was changed from -16 fm to -18 fm. That is, η_{pp} changed 15% absolutely when a_{nn} was changed by 2 fm. From Figure 2.10, E_{pp} changed from 1.82 in the case of using one-quarter Cs bias to 1.79 in the case of using one-third Cs bias. In other words, E_{pp} changed 1.7% when the detector bias changed from one-quarter Cs to one-third Cs. Roughly the change in η_{pp} is about the same as that in E_{pp}. Therefore, even if the neutron detector bias changes from one-third Cs to one-quarter Cs, the change in the extracted values of a_{nn} would be less than 0.20 fm. During the experiment, the change in the detector biases was much less than the change from one-quarter Cs to one-third Cs. Therefore, it is safe to say that the uncertainty to the extracted value of a_{nn} caused by the uncertainty in detector efficiency is less than 0.10 fm.

6.5.6 Systematic Uncertainty from Neutron Detector Efficiency Uncertainty

When the biases for neutron detectors are perfectly fixed, there is still uncertainty in the neutron detector efficiencies. From experiences this uncertainty is about 1%. It is reasonable to assume that E_{pp} has an uncertainty of about 1%. Follow the same arguments as we used in section 6.5.5, the uncertainty to the value of a_{nn} caused by the detector-efficiency shape is about 0.05 fm.

reason of the uncertainty	uncertainty in a_{nn} (fm)
absolute time of fligth	0.13
background subtraction	0.01
θ_3	0.23
distribution of stopped pions	0.21
detector efficiency shape	0.05
detector bias setting	0.10

Table 6.8: Summary of the systematic uncertainties to a_{nn} .

6.5.7 Total Systematic Uncertainty

Now let us summarize the result from section 6.5.1 to section 6.5.6 in Table 6.8. And the total systematic uncertainty to the value of a_{nn} for the present work is 0.36 fm.

6.6 Final Results and Conclusions

From the a_{nn} value obtained from the present work, we can conclude that the N-N interaction is not charge symmetric and it is not charge independent either.

Our final result for a_{nn} is $a_{nn} = -18.50 \pm 0.06 \pm 0.36 \pm 0.30$ fm, where 0.06 fm is the statistical error, 0.31 fm is the systematic error and 0.30 fm is the theoretical error. If we sum the uncertainties together in quadrature, then, the final result can be written to

$$a_{nn} = -18.5 \pm 0.5 \text{ fm}. \tag{6.10}$$

This result agrees with the other a_{nn} investigation at TUNL using the $n - d$ breakup reaction [Gon98], where the author reported an a_{nn} value of -18.7 ± 0.6 fm. Our result also agrees with the ones from the two PSI reports [Gab81, Sch87], where values for a_{nn} were extracted from $\pi^- d$ capture experiments by analyzing the γ-ray energy spectra and the neutron energy spectra, respectively. The results reported by PSI are $a_{nn} = -18.35 \pm 0.65$ fm

and $a_{nn} = -18.70 \pm 0.60$ fm. Based on the a_{nn} value from our work and the a_{pp} value cited in Chapter 1, we verified that charge-symmetry breaking exists.

Earlier in Chapter 1, we summarized the a_{nn} values in section 1.2, where sizable differences among the values of a_{nn} measured by $^2H(\pi^-, n\gamma)n$ experiments were described. One value is close to that obtained with the $^2H(n, nn)p$ reaction in fairly old kinematically complete experiments, and the other is larger by about 2 fm. Our result agrees with the recent result obtained at TUNL [Gon98] using the $^2H(n, nn)p$ reaction and, for the first time, a rigorous theoretical analysis of the data This rules out the existence of a sizable three-body force

Also, from Chapter 3 it follows that the theory we used is not adequate if the relative energy of the two outgoing neutrons from the $^2H(\pi^-, n\gamma)n$ reaction is too high. That means θ_3 cannot be too large. Our simulation verified this. At large θ_3 cuts, the extracted a_{nn} values are significantly different from the ones obtained from lower θ_3 cuts.

In Chapter 3 we mentioned that the calculated value for the charged-symmetry breaking based on one of the most recent NN model for the difference between a_{nn} and a_{pp} is [Mil90]

$$\Delta a_{CSB}^{calc} = a_{pp}^N - a_{nn}^N = 1.5 \pm 0.5 \text{ fm} \tag{6.11}$$

Using the a_{nn} value from this work, we get

$$\Delta a_{exp}^{calc} = (-17.3 \pm 0.4) - (-18.5 \pm 0.6) \text{ fm} = 1.2 \pm 0.7 \text{ fm} \ , \tag{6.12}$$

which is in excellent agreement with Equation 6.11.

As far as the Monte-Carlo simulation is concerned, we achieved the goals we set in Chapter 1. That is, we used the MC simulation to model the experiment successfully. We were able to extract an accurate value of a_{nn} from the $\pi^- d$ data we obtained from LAMPF Exp1286.

What might be done in the future? I think, there are a few things which could have been done better or be improved in future experiments. For example, a better E_γ resolution, and better time calibrations for the NTOF spectra is desirable. And when possible we would like to have better statistics for the $^1H(\pi^-, n)\gamma$ reaction so that we can better determine the beam profile, the neutron scattering in the target system and neutron cross talks between detectors, because it is easier to identify the contributions of multiple scattering and cross talk in the case of the hydrogen target. Also if we can determine how many events are from the first half of the target and how many from the other half of the target, that would be very helpful for us to determine the distribution of the stopped π^- .

From the uncertainties we reported above, the statistical uncertainty is not the dominant part of the total uncertainty. The main uncertainty comes from the theoretical uncertainty.

On the MC code side, it would be nice to combine the simulation code which generates the events with the FORTRAN routines that call the HBOOK (histogramming) and NTUPLE (save events like what relational database does, so the relationships between different variables in the tuple can be analyzed later) routines from the library so that the demand on hard disk space could be dramatically reduced. After this upgrade to the MC code, we shall be able to write an event into HBOOK files and NTUPLE files whenever we have a valid event.

Again, our final results from Exp1286 for a_{nn} is

$$a_{nn} = -18.50 \pm 0.06 \pm 0.36 \pm 0.30 \text{ fm} \ , \tag{6.13}$$

or

$$a_{nn} = -18.50 \pm 0.47 fm \ . \tag{6.14}$$

Appendix A

How to run the MC code on a UNIX system

A.1 Use *Makefile* to generate the code

Since the complete MC code includes tens of files (about a total amount of 20,000 lines), it would be a pain if we do not have some tools to help us compile the source files and link the object files and the C library. Fortunately, on UNIX systems, there is usually a nice utility program called *make*, which makes updates of a big code very convenient. Whenever you change part of the code (either in one file or in several files), *make* will compare the modification time of the object file and the source file and only recompile the files that have been updated since the last compilation. Below is the file *Makefile* I used:

```
.SUFFIXES: .c
.c.o:
      $(CC) $(CFLAGS) -c -O3  $<
CC = gcc
# The following flag is for debug purpose
CFLAGS = -g
# use ``make clean'' to clean garbage
clean:
      /bin/rm *.o core
book_keep1p.o: new.h
crosstalk1p.o: ndet.array.h new1.h
dcs_nfe1.o: new1.h
diff_cs.o: nC_dcs.h new1.h
find_direction1.o: new1.h
gammapos1.o:  new1.h
input1.o:   new1.h
kin_pid3.o:  main1.h new1.h
kin_pip1.o:  new1.h
lib2.o:  constants.h main1.h new1.h
mc3p.o:  main.h main1.h new1.h smear.h
mclib2p.o:  gxy_ratio.h gxy_ratio1cm.h \
      gxy_ratio1cm_smooth.h main1.h new1.h
mloop1n1p.o:  new1.h
```

```
mloop2.o:  new1.h
mloop3.o:  new1.h
ndetpos1.o:  new1.h
ninh.o:  new1.h
output.o:  new1.h
pick_target.o:  new1.h smear.h
scatt1p.o:  dcs_nd.h new1.h
scattpos_new1p.o:  new1.h
smear.o:  new.h smear.h
snweight.o:  new1.h
total_cs.o:  dcsD/nd.h dcsfe/nfe.h
track1.o:  new1.h
tracknn.o:  new1.h
trans.o:  new1.h
trans_ms.o:  new.h
trav_tar1.o:  new1.h
voleff.o:  new1.h
OBJECTS = annp.o book_keep1p.o crosstalk1p.o dcs_nfe1.o \
      diff_cs.o find_direction1.o gammapos1.o \
      init_wc_eff.o input1.o iron.o kin_pid3.o kin_pip1.o \
      lib2.o line_plane.o legendre.o mc3p.o mclib2p.o \
      mloop1n1p.o mloop2.o mloop3.o ndetpos1.o ninh.o \
      output.o pick_target.o scatt1p.o scattpos_new1p.o \
      smear.o smtof.o total_cs.o track1.o tracknn.o \
      trans.o trans_ms.o trans_nair.o trav_tar1.o voleff.o
new6p: $(OBJECTS)
      \$(CC) \$(CFLAGS) -o pid_mc $(OBJECTS) -lm
```

With the file $Makefile$, we can use $make\ new6p$ on a shell command line to generate the executable file *pid_mc* after each update.

Table A.1 lists all the functions and gives each function a very brief description.

Table A.1: Description of all the functions in MC code

function name	brief description
annp.c	main code, set up input and output file names based
	on user input
book_keep1p.c	bookkeeping
crosstalk1p.c	deal with cross talk
dcs_nfe1.c	deal with differential cross sections for $Fe(n,n)$ scattering
diff_cs.c	deal with differential cross sections
find_direction1.c	given a random direction and an angle, find a random direction so that the angle between the two directions equals the specified angle

continued on next page

continued from previous page	
function name	brief description
gammapos1.c	select γ position in wire chamber
init_wc_eff.c	initialize wire chamber efficiency
input1.c	read data from various input data files
iron.c	deal with $Fe(n,n)$ scattering
kin_pid3.c	deal with the kinematics for $^2H(\pi^-, n\gamma)n$ reaction
kin_pip1.c	deal with the kinematics for $^1H(\pi^-, n)\gamma$ reaction
lib2.c	my own library, functions for general purposes
line_plane.c	find where a line meets a plane
legendre.c	calculate values for Legendre polynomials
mc3p.c	heart of the code
mclib2p.c	my own library, mainly functions related to this MC simulation
mloop1n1p.c	main function to track neutron
mloop2.c	bookkeeping for viewing results in text mode
mloop3.c	calculate various transmission coefficients
ndetpos1.c	select random position in a neutron detector
ninh.c	deal with $^1H(n,n)$ scattering
output.c	write events to binary file
pick_target.c	pick positions in target
scatt1p.c	deal with $^2H(n,n)$ scattering
scattpos_new1p.c	predict scattering position
smear.c	a smear function
smtof.c	a smear function for NTOF spectrum
total_cs.c	find total cross sections for various reactions
track1.c	functions for tracking neutrons
tracknn.c	functions for tracking neutrons
trans.c	calculate transmission coefficients
trans_ms.c	calculate transmission coefficients
trans_nair.c	calculate transmission coefficients in air
trav_tar1.c	calculate transmission coefficients in target

A.2 Script *new6pall_d.auto*

Once we get the executable code, we would like to use the code to generate event files. To save disk space, data are stored in binary files, which only take one third of disk space required by the corresponding ASCII file. But we have

to sort the binary data files in order to visualize the result. In our case, we use the HBOOK and NTUPLE system in PAW. All of these can be done using a script. Below is the script *new6pall_d.auto*:

```
#!/bin/csh -f
if ( $#argv < 3 ) then
echo "     "
echo syntax: new6pall_d.auto switch ann matrix_choice
echo this script will do MC simulation and will generate
echo several HBOOK files when necessary, also, it will
echo generate NTUPLE files if necessary
echo "     "
exit 1
endif
echo date
date
set mcdatadir="~/scott/mc"
set maindir="~/scott"
### do some clean-up at the beginning
echo cd $mcdatadir
cd $mcdatadir
echo "  "
echo TO save disk space
set binfile=short_$2.$1.tmp
if -f $binfile then
echo /bin/rm $binfile
/bin/rm $binfile
endif
### go back to $maindir
echo cd $maindir
cd $maindir
echo "     "
### generate binaray data file
### new6p.auto is another script which deals
### the input data files nicely and will be attached
### in the section~\ref{section:new6p-auto}
echo new6p.auto d $1 $2 $3
new6p.auto d $1 $2 $3
echo cd $mcdatadir
cd $mcdatadir
pwd
### if you do not want the HBOOK stuff, use the following
#goto ntuple
### dmc_replayp.in.auto is a script which generates
### the input data file for several FORTRAN codes.
### These FORTRAN codes are: dmc_replayp, dmc_replayssp
### and dmc_replay30.
dmc_replayp.in.auto d $1 $2
### the following sections do the HBOOK stuff for all the
### events in the data file
set exe=dmc_replayp
set infile=dmc_replayp_$1.$2.in
```

```
set logfile=$exe\_$2.$1.log
echo $exe \< $infile \>\! $logfile
$exe < $infile >! $logfile
echo " "
### the following section do the HBOOK stuff for the events
### generated by direct neutrons only
ssonly:
if ( $1 >= 100 ) then
  set exe=dmc_replayssp
  set logfile=$exe\_$2.$1.log
  if ( ! -f $exe ) then
    make $exe
    if ( $status > 1 ) exit 1
  endif
  echo $exe \< $infile \>\! $logfile
  $exe < $infile >! $logfile
  echo " "
endif
### the following section do the HBOOK stuff, excluding the
### events generated by neutrons due to cross talk
@ x = $1 % 100
if ( $x >= 10 ) then
  set exe=dmc_replay30
  set logfile=$exe\_$2.$1.log
  echo $exe \< $infile \>\! $logfile
  $exe < $infile >! $logfile
  echo " "
endif
### if you do not want the NTUPLE stuff, use the following
goto target
### do the NTUPLE for double events
ntuple:
echo dmc_ntp.auto d $1 $2
dmc_ntp.auto d $1 $2
if ( $status > 0 ) exit 1
### do the HBOOK for beam profile
target:
echo dotarget d $1 $2
dotarget d $1 $2
if ( $status > 0 ) exit 1
end:
echo goint to delete the binary file to save disk space
set binary_file=$binary_file
if -f $binary_file then
  echo ls -l $binary_file
  ls -l $binary_file
  echo /bin/rm $binary_file
  /bin/rm $binary_file
endif
echo date
date
echo "  "
```

```
echo normal terminatin of new6pall_d.auto $1 $2 $3
echo "  "
exit 0
```

After we get the HBOOK files, we can compare data with simulations using some handy *kumac* files in PAW. All the *kumac* files are in directory $\sim$*chenqk/scott/mc* (On a UNIX system, $\sim$ followed by a user name stands for a user's home directory). When you are in PAW, (on the TUNL unix system, enter "pawX11" on the shell command line will enable you to enter PAW), use "exec kumac_file_name 0" to get infomation for a specific *kumac* file.

If we want to calculate χ^2 and get a χ^2 vs. a_{nn} curve, we need to get HBOOK files for three or four a_{nn} (for interpolation purpose). Then, we go to directory $\sim$ *chenqk/scott/mc/chisq*, and use the *kumac* file named *get_chisq.kumac*. This *kumac* file will calculate χ^2 and generate a χ^2 vs. a_{nn} curve, using whatever θ_3 cut and smoothing mechanism we specify on the PAW command line. It also gives the value of a_{nn} corresponding to χ^2_{min} and the values of a_{nn} corresponding to $\chi^2_{min} + 1$.

A.3 Script *new6p.auto*

The script *new6p.auto* will get input data files ready and use the executable file to do the actual Monte-Carlo calculations.

```
#!/bin/csh -f
# script name: new6p.auto
if ( $#argv < 2 ) then
  echo "     "
  echo syntax: new6p.auto target switch ann matrix_choice
  echo ann and matrix_choice are necessary only for target d
  echo available values for ann: 16,18,20 and 22
  echo available values for matrix_choice: 0 or 1
  echo "     "
  exit 1
endif
### This section generates the file dseed*.tmp which stores the
### seed for random number generator and the file new6p*.in
### which contains what is required to input via keyboard when
### working in interactive mode
```

```
if ( $3 == '' ) then
  echo cp dseed.dat dseed_$2.tmp
  cp dseed.dat dseed_$2.tmp
  echo "echo $1 $2  \>\! new6p_$1.$2.in"
  echo $1 $2  >! new6p_$1.$2.in
else
  echo cp dseed.dat dseed_$3.$2.tmp
  cp dseed.dat dseed_$3.$2.tmp
  echo "echo $1 $2 $3 $4 0\>\! new6p_$1.$2.$3.in"
  echo $1 $2 $3 $4 0>! new6p_$1.$2.$3.in
endif
### This section do the actual Monte-Carlo simulation.
### Standard output is pipelined to a log file for monitoring
### purpose.
if ( $3 == '' ) then
  echo new6p.out \< new6p_$1.$2.in \>\! new6p_$1.$2.log
  new6p.out < new6p_$1.$2.in >! new6p_$1.$2.log
else
  echo new6p.out \< new6p_$1.$2.$3.in \>\! new6p_$1.$2.$3.log
  new6p.out < new6p_$1.$2.$3.in >! new6p_$1.$2.$3.log
endif
if ( $status > 0 ) exit 1
if ( $3 == '' ) then
  echo most of your output files have suffix $2.tmp
else
  echo most of your output files have suffix $3.$2.tmp
endif
```

Appendix B

Participants in project Exp1286

S.T. Carman	Lawrence Livermore National Laboratory.
Q. Chen	TUNL, Duke University.
W.R. Gibbs	New Mexico State University.
B.F. Gibson	Los Alamos National Laboratory.
F. Guber	Joint Institute for Nuclear Research,Dubna, Russia.
C.R. Howell	TUNL, Duke University.
A.H. Hussein	University of North British Columbia, Canada.
G. Mertens	University of Tübingen, Germany.
C.F. Moore	University of Texas.
C.L. Morris	Los Alamos National Laboratory.
A. Obst	Los Alamos National Laboratory.
E. Pasyuk	Joint Institute for Nuclear Research,Dubna, Russia.
C.D. Roper	TUNL, Duke University.
F. Salinas	TUNL, Duke University.
I. Slaus	Rudjer Boskovick Institute, Zagreb, Croatia.
S.M. Sterbenz	Los Alamos National Laboratory.
W. Tornow	TUNL, Duke University.
R.L. Walter	TUNL, Duke University.
C. Whitley	University of Texas.
M. Whitton	Los Alamos National Laboratory.

Note: Q. Chen and S.T. Carman became involved in the project after the experiment was done.

Appendix C

Tabulated PTB efficiencies

Here, from Table C.1 to Table C.7 we tabulate the absolute neutron detector efficiency calculated using the PTB code for the four types of neutron detectors used in Exp1286.

Table C.1: PTB efficiency for the four types of detectors used for E_n between 0.1 and 2.0 MeV.

En(MeV)	arg1	arg2	liv	bic
0.1000	0.00000	0.00000	0.00000	0.00000
0.2000	0.00000	0.00000	0.00000	0.00000
0.3000	0.00000	0.00000	0.00000	0.00000
0.4000	0.00000	0.00000	0.00000	0.00000
0.5000	0.00000	0.00000	0.00000	0.00000
0.6000	0.00000	0.00000	0.00000	0.00000
0.7000	0.00073	0.00050	0.00088	0.00097
0.8000	0.00921	0.00904	0.00915	0.01053
0.9000	0.03409	0.04216	0.04291	0.04666
1.0000	0.08005	0.10013	0.09834	0.09896
1.1000	0.12568	0.16344	0.15101	0.15749
1.2000	0.16564	0.22480	0.20644	0.21603
1.3000	0.19510	0.28229	0.24367	0.26746
1.4000	0.22407	0.31561	0.27987	0.29493
1.5000	0.24136	0.35186	0.30245	0.31950
1.6000	0.25569	0.36870	0.32421	0.34416
1.7000	0.25892	0.37750	0.33202	0.34844
1.8000	0.26370	0.39588	0.34580	0.35967
1.9000	0.26632	0.39923	0.33973	0.36039
2.0000	0.27470	0.39916	0.34868	0.36346

Table C.2: PTB efficiency for the four types of detectors used for E_n between 2.1 and 5.0 MeV.

En(MeV)	arg1	arg2	liv	bic
2.1000	0.27786	0.40025	0.34985	0.36664
2.2000	0.27370	0.41107	0.35104	0.36809
2.3000	0.27460	0.40581	0.35418	0.36787
2.4000	0.27740	0.40982	0.35162	0.36608
2.5000	0.27629	0.40053	0.35421	0.36689
2.6000	0.27417	0.40290	0.35408	0.36667
2.7000	0.27189	0.41124	0.35184	0.36277
2.8000	0.27417	0.40211	0.34793	0.35909
2.9000	0.27679	0.40482	0.35169	0.35631
3.0000	0.26871	0.39599	0.34702	0.35800
3.1000	0.27143	0.39659	0.34174	0.35276
3.2000	0.27370	0.40293	0.34304	0.35070
3.3000	0.27244	0.39581	0.34230	0.34435
3.4000	0.27135	0.39927	0.33896	0.35056
3.5000	0.26986	0.39094	0.34062	0.34726
3.6000	0.26666	0.39166	0.33476	0.34414
3.7000	0.26927	0.39241	0.34086	0.34349
3.8000	0.26335	0.38451	0.33906	0.34111
3.9000	0.25482	0.38638	0.33046	0.33850
4.0000	0.25904	0.38264	0.33698	0.33913
4.1000	0.25776	0.38046	0.32224	0.34068
4.2000	0.25223	0.37530	0.32291	0.33661
4.3000	0.24770	0.36923	0.31972	0.33703
4.4000	0.23651	0.36771	0.31112	0.33347
4.5000	0.23471	0.36386	0.31338	0.32689
4.6000	0.23325	0.35406	0.30359	0.32053
4.7000	0.23135	0.35873	0.30501	0.31866
4.8000	0.22584	0.34838	0.29490	0.31590
4.9000	0.22480	0.34761	0.29889	0.31251
5.0000	0.21943	0.34000	0.29278	0.30568

Table C.3: PTB efficiency for the four types of detectors used for E_n between 5.1 and 8.0 MeV.

En(MeV)	arg1	arg2	liv	bic
5.1000	0.22149	0.34009	0.28827	0.30438
5.2000	0.22154	0.33454	0.28431	0.29979
5.3000	0.21619	0.33275	0.28405	0.29587
5.4000	0.21450	0.33219	0.28256	0.29153
5.5000	0.20872	0.33172	0.27523	0.28892
5.6000	0.21008	0.32272	0.27097	0.29029
5.7000	0.20994	0.31540	0.27634	0.28343
5.8000	0.20243	0.32069	0.27130	0.28270
5.9000	0.20500	0.31250	0.26844	0.27878
6.0000	0.20084	0.31003	0.26697	0.28015
6.1000	0.20031	0.31213	0.26703	0.27673
6.2000	0.21559	0.31739	0.27155	0.27735
6.3000	0.20076	0.30972	0.26681	0.27242
6.4000	0.19624	0.30636	0.26112	0.27291
6.5000	0.19300	0.30263	0.25960	0.27009
6.6000	0.19566	0.30029	0.25429	0.27148
6.7000	0.18946	0.29660	0.25632	0.26585
6.8000	0.19201	0.29998	0.25365	0.26681
6.9000	0.18968	0.29255	0.24743	0.26077
7.0000	0.18692	0.29298	0.25037	0.26140
7.1000	0.18585	0.28908	0.24804	0.26032
7.2000	0.18125	0.29096	0.24969	0.25456
7.3000	0.18246	0.29218	0.24310	0.25823
7.4000	0.18872	0.28857	0.24665	0.25852
7.5000	0.18900	0.29759	0.24472	0.25408
7.6000	0.19178	0.29050	0.24765	0.25141
7.7000	0.19243	0.29864	0.24045	0.25156
7.8000	0.18707	0.28920	0.24315	0.24838
7.9000	0.18280	0.28538	0.23987	0.24486
8.0000	0.18068	0.28639	0.24441	0.24720

Table C.4: PTB efficiency for the four types of detectors used for E_n between 8.1 and 11.0 MeV.

En(MeV)	arg1	arg2	liv	bic
8.1000	0.17744	0.28152	0.23842	0.24544
8.2000	0.16998	0.27308	0.23369	0.24107
8.3000	0.17139	0.27109	0.22484	0.23826
8.4000	0.17177	0.26972	0.22580	0.23834
8.5000	0.16694	0.26721	0.22381	0.23146
8.6000	0.16703	0.26550	0.22359	0.23189
8.7000	0.16500	0.26260	0.22055	0.23154
8.8000	0.16526	0.26096	0.21526	0.22908
8.9000	0.16450	0.25701	0.21574	0.22705
9.0000	0.16567	0.25984	0.21774	0.22567
9.1000	0.16381	0.26101	0.21972	0.23084
9.2000	0.16626	0.25803	0.21895	0.22839
9.3000	0.16343	0.25895	0.21624	0.22754
9.4000	0.16013	0.25736	0.21704	0.22630
9.5000	0.15821	0.25514	0.21420	0.22576
9.6000	0.15846	0.25463	0.21651	0.22391
9.7000	0.15862	0.25148	0.22015	0.22339
9.8000	0.15568	0.25350	0.21372	0.22040
9.9000	0.15477	0.25343	0.21376	0.22253
10.0000	0.15816	0.25016	0.21227	0.22107
10.1000	0.15306	0.24554	0.21111	0.21786
10.2000	0.15497	0.24944	0.20709	0.21802
10.3000	0.15062	0.24611	0.20746	0.21620
10.4000	0.15013	0.24834	0.20544	0.21727
10.5000	0.14833	0.24287	0.20480	0.21609
10.6000	0.15101	0.24325	0.20410	0.21527
10.7000	0.14813	0.24010	0.20341	0.21075
10.8000	0.14874	0.23932	0.20162	0.21105
10.9000	0.14680	0.24128	0.20376	0.21056
11.0000	0.14378	0.23994	0.20434	0.20846

Table C.5: PTB efficiency for the four types of detectors used for E_n between 11.1 and 14.0 MeV.

En(MeV)	arg1	arg2	liv	bic
11.1000	0.14495	0.23513	0.19735	0.20698
11.2000	0.14721	0.23397	0.19992	0.20622
11.3000	0.14408	0.24178	0.19915	0.21050
11.4000	0.14483	0.23818	0.20449	0.20933
11.5000	0.14291	0.24026	0.20216	0.20588
11.6000	0.14508	0.23894	0.20344	0.20711
11.7000	0.14649	0.23823	0.20137	0.20770
11.8000	0.14472	0.23806	0.19866	0.20694
11.9000	0.14240	0.23708	0.20298	0.21317
12.0000	0.14451	0.24011	0.20021	0.21178
12.1000	0.14625	0.24210	0.20468	0.21164
12.2000	0.14572	0.24294	0.20011	0.21168
12.3000	0.14548	0.23712	0.20495	0.21005
12.4000	0.14445	0.23776	0.20140	0.21082
12.5000	0.14570	0.23644	0.19889	0.21069
12.6000	0.14528	0.23733	0.20124	0.21146
12.7000	0.14630	0.23570	0.19812	0.21035
12.8000	0.14379	0.23102	0.20201	0.20894
12.9000	0.13903	0.23636	0.20092	0.20877
13.0000	0.13852	0.23205	0.19548	0.20657
13.1000	0.14217	0.22723	0.19754	0.20604
13.2000	0.13850	0.22734	0.19838	0.20453
13.3000	0.13928	0.23197	0.19807	0.20270
13.4000	0.13819	0.23248	0.19642	0.20385
13.5000	0.13935	0.22822	0.19387	0.20229
13.6000	0.13986	0.22863	0.19680	0.20330
13.7000	0.13994	0.23082	0.19503	0.20236
13.8000	0.13644	0.22755	0.19904	0.20625
13.9000	0.13880	0.23617	0.19866	0.20399
14.0000	0.13849	0.23476	0.19666	0.20575

Table C.6: PTB efficiency for the four types of detectors used for E_n between 14.1 and 17.0 MeV.

En(MeV)	arg1	arg2	liv	bic
14.1000	0.13634	0.23419	0.19690	0.20368
14.2000	0.13759	0.23318	0.19334	0.20399
14.3000	0.13715	0.23173	0.19467	0.20642
14.4000	0.13688	0.23380	0.19998	0.20509
14.5000	0.13462	0.23399	0.19683	0.20454
14.6000	0.13953	0.22957	0.19677	0.20541
14.7000	0.13816	0.23403	0.19832	0.20405
14.8000	0.13551	0.23358	0.19714	0.20607
14.9000	0.13931	0.23647	0.19736	0.20583
15.0000	0.13502	0.23076	0.19712	0.20656
15.1000	0.13636	0.23244	0.19722	0.20524
15.2000	0.13639	0.23514	0.20013	0.20342
15.3000	0.13549	0.23120	0.20071	0.20569
15.4000	0.13101	0.23146	0.19738	0.20862
15.5000	0.13821	0.22954	0.19927	0.20476
15.6000	0.13431	0.22985	0.19563	0.20589
15.7000	0.13541	0.23091	0.19991	0.20484
15.8000	0.13482	0.23440	0.19435	0.20337
15.9000	0.13639	0.23018	0.19683	0.20715
16.0000	0.13573	0.23233	0.20049	0.20616
16.1000	0.13480	0.23424	0.20060	0.20484
16.2000	0.13445	0.23052	0.19594	0.20501
16.3000	0.13786	0.23593	0.19874	0.20514
16.4000	0.13163	0.22481	0.19340	0.20278
16.5000	0.13347	0.22916	0.19918	0.20420
16.6000	0.13127	0.22530	0.19180	0.20140
16.7000	0.13084	0.22643	0.19567	0.20065
16.8000	0.13212	0.22741	0.19587	0.20057
16.9000	0.13203	0.22601	0.19357	0.19954
17.0000	0.13143	0.22766	0.19687	0.20172

Table C.7: PTB efficiency for the four types of detectors used for E_n between 17.1 and 19.9 MeV.

En(MeV)	arg1	arg2	liv	bic
17.1000	0.13104	0.22598	0.19533	0.20066
17.2000	0.13204	0.23156	0.19560	0.20112
17.3000	0.12725	0.22611	0.19385	0.20122
17.4000	0.13147	0.23007	0.19497	0.20028
17.5000	0.12978	0.22322	0.19543	0.20417
17.6000	0.13105	0.22625	0.19769	0.20400
17.7000	0.13131	0.22831	0.19770	0.20374
17.8000	0.12950	0.22615	0.19497	0.20500
17.9000	0.13277	0.22859	0.19593	0.20762
18.0000	0.13055	0.22283	0.19653	0.20311
18.1000	0.13361	0.22783	0.19180	0.20457
18.2000	0.12982	0.23046	0.19383	0.20195
18.3000	0.13100	0.22716	0.19555	0.20277
18.4000	0.12944	0.22467	0.19522	0.20188
18.5000	0.12886	0.22709	0.19451	0.20036
18.6000	0.12831	0.22287	0.19455	0.19880
18.7000	0.12655	0.22358	0.18918	0.20015
18.8000	0.12972	0.22193	0.19480	0.20024
18.9000	0.12589	0.21978	0.18878	0.19685
19.0000	0.12591	0.22259	0.18771	0.19801
19.1000	0.12499	0.22780	0.18918	0.19378
19.2000	0.12815	0.21579	0.18532	0.19317
19.3000	0.12517	0.21816	0.18757	0.19681
19.4000	0.12379	0.22110	0.18893	0.19416
19.5000	0.12609	0.22370	0.19155	0.19663
19.6000	0.12648	0.21768	0.19261	0.19495
19.7000	0.11923	0.21603	0.18843	0.19214
19.8000	0.11931	0.21293	0.18309	0.18907
19.9000	0.11927	0.21439	0.17751	0.18653

Appendix D

Total Cross Sections for the n-d Reaction

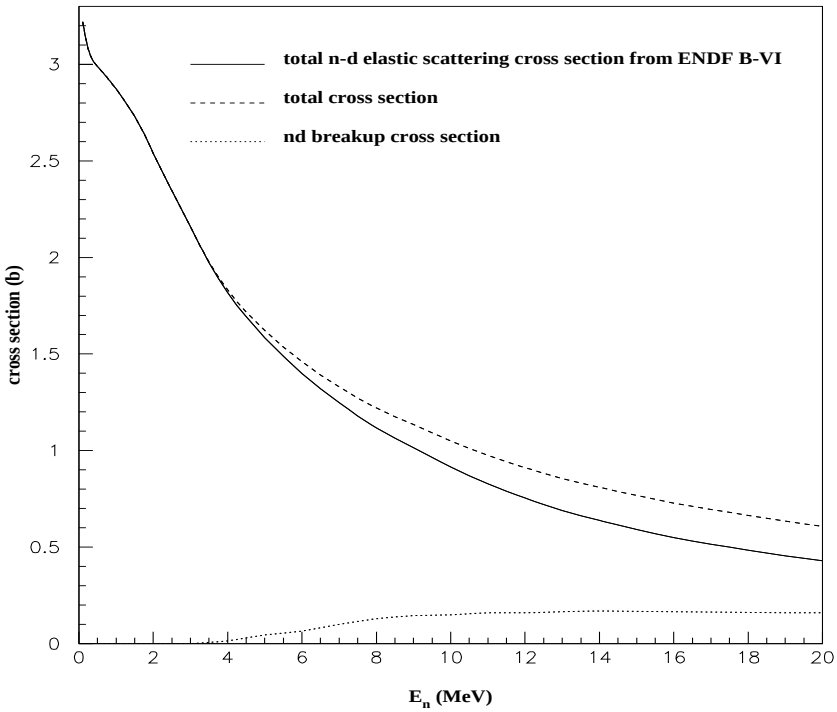

Figure D.1: Cross sections for n-d scattering. The total cross sections are almost the same as the elastic scattering cross sections when E_n is smaller than about 4 MeV. As E_n becomes larger, the ${}^2H(n,nnp)$ cross section plays a more and more important part in the total cross section.

Appendix E

Total Cross Sections for the n-^{12}C Reactions

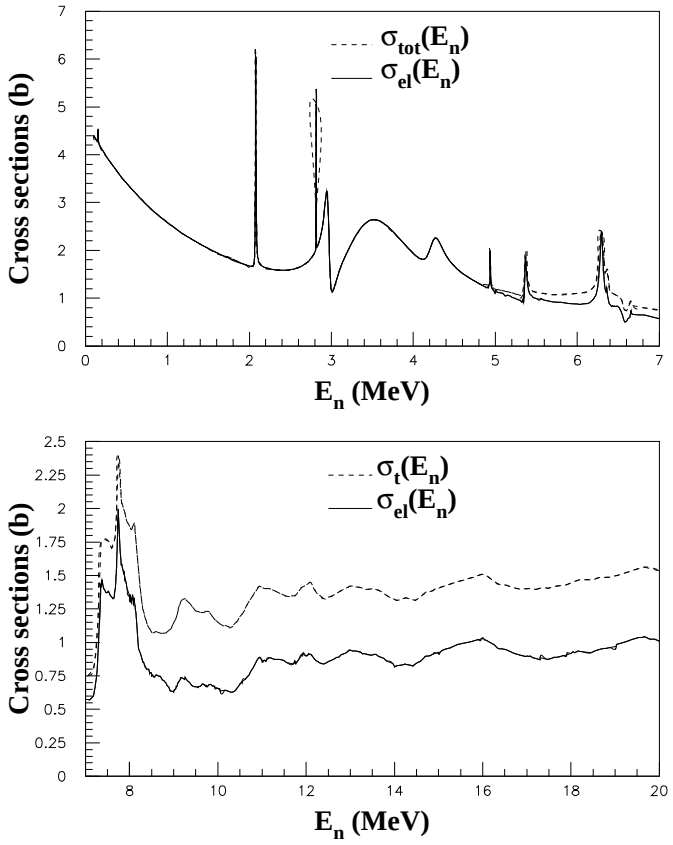

Figure E.1: Cross sections for n-^{12}C reactions. The total cross sections are almost the same as the elastic scattering cross sections when E_n is smaller than about 5.5 MeV. As E_n becomes larger, the difference between the total cross sections for the n-^{12}C reaction and that for $C(n,n)$ becomes larger too. The dashed curve represents the total cross sections for nd reaction and the solid curve is the total cross sections for n-^{12}C scattering.

Appendix F

Cross Sections of $Fe(n,n)$ Scattering

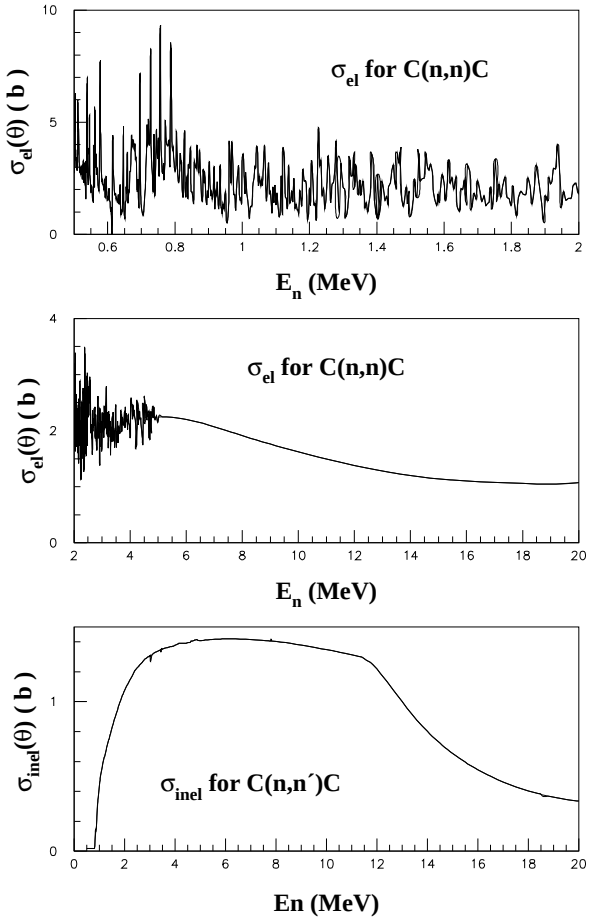

Figure F.1: The top two plots show the total n-Fe elastic scattering cross sections obtained from ENDF VI. The bottom one shows the total $Fe(n,n')$ inelastic scattering cross sections from the same source.

Appendix G

Total Cross Sections of $H(n,n)$ Scattering

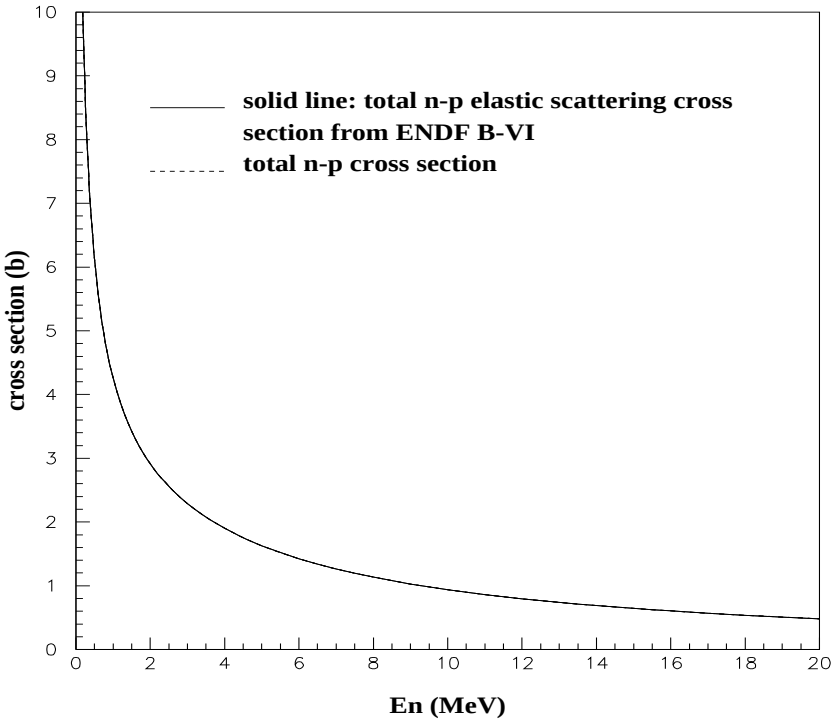

Figure G.1: Total cross sections of n-p scattering. The total cross sections are almost the same as the elastic scattering cross sections. Therefore, it is difficult to distinguish the two curves. The differential cross sections always take the shape of $\cos(\theta)$ in the lab. system.

Appendix H

Check Some Statistical Characteristics

Here, I shall describe how to check the correctness of the MC simulation. After the MC code was written, we had to make sure it worked as intended. This concern is very important to the extraction of the value of a_{nn} . In this appendix, we will check some statistical aspects of the MC simulation.

H.1 Common Geometry Parameters for Both Targets

The parameters that define the geometry of the detection system are the same for both the deuterium target and the hydrogen target. Some of the parameters are (please refer to Figure 2.4 on page 28) listed below.

1. The dimension of the wire chamber (WC) are

$$A_{wc} = 14'' \times \ 28'' = 35.56\ cm \times \ 71.12\ cm = 2529\ cm^2\ . \tag{H.1}$$

2. The distance from the target to the WC plane is $d_{gd} = 80.64\ cm$.

3. The solid angle [1] subtended by the WC to the target, Ω_{wc}, must be between Ω_1 (min.) and Ω_2 (max), with

$$\begin{aligned}\Omega_1 = & \frac{A_{wc}}{(d_{gd}^2 + 17.78^2 + 35.56^2)} \\ & \times \frac{d_{gd}}{\sqrt{d_{gd}^2 + 17.78^2 + 35.56^2}} = 0.281\ sr\ ,\end{aligned} \tag{H.2}$$

[1] In this section, we treat the target as a point.

and

$$\Omega_2 = A_{wc}/d_{gd}^2 = 0.389 \ sr \ . \tag{H.3}$$

Of course, Ω_1 is an underestimate for Ω_{wc} and Ω_2 is an overestimate for Ω_{wc}. If we simply take the average of Ω_1 and Ω_2 as Ω_{wc}, then,

$$\Omega_{wc} = \frac{\Omega_1 + \Omega_2}{2} = 0.335 \ sr \ . \tag{H.4}$$

The relative solid angle of the WC is then:

$$\Omega_{wc}^{rel} = \frac{\Omega_{wc}}{4\pi} = \frac{0.335}{4\pi} = 2.67\% \ . \tag{H.5}$$

The superscript *rel* in Equation H.5 indicates relative solid angle. Of course, Equation H.4 is an approximation. Numerical integration gives:

$$\Omega_{wc} = 0.348 \ sr \ . \tag{H.6}$$

This shows that Equation H.4 is a good approximation for Ω_{wc}.

4. The area of the neutron detector frame: (rectangular area) is (refer to Table 2.1 and Figure 2.6 on page 31):

$$\begin{aligned} A_{nfr} &= (5 \times 8.24 + 5)'' \times (4 \times 7.14 + 5)'' \\ &= (46.2'' \times 33.56'') \\ &= (117.35 \ cm \times 85.24 \ cm) = 10003 \ cm^2 \ , \end{aligned} \tag{H.7}$$

where the subscript nfr stands for the neutron detector frame. The distance from the target center to the center of the neutron detector frame is

$$d_{nd} = 250.0 \ cm \ . \tag{H.8}$$

Therefore, the solid angle subtended by the neutron detector frame from the target is:

$$\Omega_{nfr} = \frac{A_{nfr}}{d_{nd}^2} = 0.160 (< \Omega_{wc} = 0.348) \tag{H.9}$$

The corresponding relative solid angle is then

$$\Omega_{nfr}^{rel} = \frac{\Omega^{nfr}}{4\pi} = 1.27\%. \tag{H.10}$$

Obviously, $\Omega_{nfr}^{rel} < \Omega_{wc}^{rel}$.

5. Now we calculate the solid angle subtended by the neutron detectors themselves. The sum of the front surface area of all neutron detectors is (again, refer to Table 2.1 and Figure 2.6)

$$\begin{aligned} A_{ndet} &= 20 \times \pi \times 5^2/4 + 4 \times \pi \times 4.5^2/4 \\ &= 145.25 \times \pi(inch^2) \\ &= 937.09 \times \pi \ \ cm^2 (= 29.4\% \, \text{of} \, A_{nfr}) \ . \end{aligned} \tag{H.11}$$

There were 20 neutron detectors with diameter $5''$ and 4 detectors with diameter $4.5''$. The aggregate solid angle subtended by all twenty-four neutron detectors is:

$$\Omega_{ndet} \doteq \frac{A_{ndet}}{d_{nd}^2} = 0.047 \ sr \ . \tag{H.12}$$

A more accurate result for Ω_{ndet} is 0.0458 sr (given by numerical integration).

Therefore, the relative solid angle of all the neutron detectors is:

$$\Omega_{ndet}^{rel} = \frac{0.0458}{4\pi} = 0.364\%. \tag{H.13}$$

In the next two sections, we will use the numbers listed above to make gross checks that the MC code is functioning correctly.

H.2 Rudimentary Test of MC Simulation Using the Hydrogen Target

The discussion in this section is based on the following assumptions: (1) a neutron is produced inside the target and the corresponding γ is detected;

(2) the target is a point; (3) the target material is hydrogen. In this section elementary estimates of scattering probabilities are compared to the results of the MC simulation.

For the direct neutrons, the probability for a neutron to hit one of the neutron detectors (not limited to a specific neutron detector) is

$$P_{hit}^{ss} = \frac{\Omega_{wc}}{\Omega_{ndet}} = 0.0458/0.348 = 13.2\% \ . \tag{H.14}$$

This result comes purely from geometrical consideration. If we extend lines connecting a position on the boundary of the WC and the target to the neutron detector plane, all these lines will form a cone. The neutron detector frame is inside this cone. In other words, if we draw a line from a position in any neutron detector through the target and extend the line, it is guaranteed to go through the WC.

From the Monte-Carlo simulation, we observed that 26,700 neutrons out of 212,000 neutrons that were traced for direct transport (without scattering) to the detector planes were detected (26,700/212,000 = 12.6%), which is about the same as the ratio of the solid angle of all the neutron detectors (Equation H.12) to that of the wire chamber (Equation H.4).

For $H(n,n)$ scattering [2] inside the liquid target, the probability for single scattering is:

$$P_{target}^{scatt} = 1 - exp(-\sigma_{el}(E_n) * l * n) \ , \tag{H.15}$$

where l is the distance traveled by the neutron from the point of generation to where it goes out of the target boundary if unscattered, n is the nuclei number density, $\sigma_{el}(E_n)$ is the total cross section for $H(n,n)$ scattering at energy E_n . For liquid hydrogen,

$$n = 0.078 g/cm^3 * 6.022 * 10^{23} nuclei/g = 4.7 * 10^{22} nuclei/cm^3 \ . \tag{H.16}$$

[2] We deal with single scattering only because the contributions from multiple scattering are negligible compared to contribution from single scattering.

Since the neutron energy from the ${}^1H(\pi^-, n)\gamma$ capture is 8.9 MeV, for the $H(n, n)$ scattering, the total elastic scattering cross section is

$$\sigma_{el}(E_n = 8.9MeV) = 1.04b \ . \tag{H.17}$$

Assume l = radius of the target = 3.00 cm, we have:

$$P_{target}^{scatt} = 1 - exp(-0.14664) = 1 - 0.864 = 0.136 \ , \tag{H.18}$$

$$\frac{N_{scatt}^{tar}}{N_{non}^{tar}} = 0.136/(1 - 0.136) = 15.7\% \ , \tag{H.19}$$

where N_{scatt}^{tar} refers to the number of neutrons being scattered once inside the target and N_{non}^{tar} refers to the number of neutrons to pass through the target without being scattered.

From the Monte-Carlo simulation, the above ratio is 39950/212425 = 18.8%, including scattering in target and in wall.

The probability for a neutron to be scattered and to hit one of the neutron detectors (not limited to a specific neutron detector) is (refer to Equation H.13 on page 196)

$$P_{scatt}^{tar} = 0.136 * \Omega_{ndet}^{rel} = 0.136 * 0.364\% = 0.050\%. \tag{H.20}$$

If the $H(n, n)$ scattering is isotropic in the laboratory system, the ratio of the number of valid[3] single-scattering events to that of the direct neutron events is (refer to Equation H.14 on the preceding page and Equation H.20)

$$r_{dir}^{scatt} = \frac{P_{scatt}^{tar}}{P_{hit}^{ss}} = \frac{0.050}{13.2} = 0.38\% \ . \tag{H.21}$$

But there are other factors to consider:

$$\overline{\theta_{scatt}^{lab}} = 0.25rad \tag{H.22}$$

[3]By valid, I mean the event is recorded.

is the average scattering angle for n-p scattering in the laboratory system for those scattered neutrons hitting any neutron detector in the detector array. This value was obtained by choosing two random points A and B in the WC and the target respectively and another random point in one of the neutron detectors and then calculating the average angle between $\overrightarrow{AB}$ and $\overrightarrow{BC}$. This angle should be approximately equal to the average scattering angle in the cm system where

$$\sigma_{cm}(\theta) = \frac{1.04}{4\pi}\ b/sr = 82.76\ mb/sr \text{ for any } \theta \tag{H.23}$$

$$\overline{\sigma(\theta)} = \frac{1.04}{4\pi}\ b/sr = 82.76\ mb/sr\ , \tag{H.24}$$

where the subscript cm means c.m. system.

$$\begin{aligned} \sigma_{lab}(0.25rad) &= 4 * cos(0.25) * \sigma_{cm}(0.25 * 2\ rad) \\ &= 3.87 * \sigma_{cm}(0.5\ rad) \\ &= 3.87 * \overline{\sigma(\theta)}\ , \end{aligned} \tag{H.25}$$

where the subscript lab means the lab system, $(0.25 * 2\ rad)$ comes from the fact that $\theta_{cm} = 2.0\ *\ \theta_{lab}$ for elastic n-p scattering. The cosine factor is the Jacobian for transforming the cm cross section to the lab. For the purpose of convenience, we define an effective ratio to be

$$r_{eff}^{np} = \sigma_{lab}(0.25rad)/\overline{\sigma(\theta)} = 3.87\ . \tag{H.26}$$

Here, the superscript np stands for the n-p scattering. Therefore the ratio of single scattered events versus direct events should be roughly

$$r_{dir}^{ss} = r_{eff}^{np} * r_{dir}^{scatt} = 3.87 * 0.38\% = 1.47\%. \tag{H.27}$$

More exactly, once a neutron is scattered, the probability for it to be detected by any one of the neutron detectors is:

$$\frac{\int_{all\ n\ detector} \sigma(\theta, E_n) * \sin\theta d\theta\ d\phi}{\int_{4\pi} \sigma(\theta, E_n) * \sin\theta d\theta\ d\phi}\ , \tag{H.28}$$

where θ is relative to the direction of the incident neutron.

The Monte-Carlo simulation gives: 623 neutrons were detected out of 39950 neutron being scattered. The ratio is $623/39950 = 1.56\%$, consistent with the estimate based on geometry and the n-p scattering cross sections.

To check if n-p scattering is dealt with properly in the code, the average scattering angles and the distribution of the scattering angles from the simulation were computed. From the Monte-Carlo simulation, the average θ_{lab} for n-p scattering is 0.75 rad (521 data points). Since n-p scattering is isotropic in the cm system, in the lab system, we have

$$\sigma_{lab}(\theta) = \sigma_0 cos\theta \ . \tag{H.29}$$

Therefore the average n-p scattering angle in the lab system is

$$\overline{\theta_{lab}} = \frac{\int_0^{\pi/2} \theta \sigma_{lab}(\theta) sin\theta d\theta}{\int_0^{\pi/2} \sigma_{lab}(\theta) sin\theta d\theta} = \pi/4 \ . \tag{H.30}$$

Similarly, the probability for a neutron to be elastically scattered in the wall is

$$P_{wall}^{scatt} = 1 - exp(-l_{wall} * n(F_e) * \sigma_{el}) \ , \tag{H.31}$$

or approximately we have

$$P_{wall}^{scatt} \approx \frac{\sigma_{el}}{\sigma_{tot}} * (1 - exp(-l_{wall} * n(F_e) * \sigma_{tot}) \ . \tag{H.32}$$

Where l_{wall} is the distance the neutron traveled in the wall (which we assume to be the thickness of the steel wall for the purpose of this estimation), $n(Fe)$ is the number density of iron (the density of iron is 7.8 g/cm^3), σ_{el} (= 1.89 b) and σ_{tot} (= 3.27 b) are the total elastic scattering cross section and total cross section for E_n equal to 8.9 MeV, respectively. Using the above values we obtain

$$n(F_e) = \frac{7.8}{56} * 6.022 * 10^{23} = 8.39 * 10^{22}. \tag{H.33}$$

Therefore, according to Equation H.32

$$P_{wall}^{scatt} = 0.578 * (1 - exp(-0.0878)) = 4.86\% \ . \tag{H.34}$$

Just for reference, if P_{wall}^{scatt} is calculated according to Equation H.31, we have

$$P_{wall}^{scatt} = (1 - exp(-0.32 * n(F_e) * 1.89 * 10^{-24}) = 4.89\% \ . \tag{H.35}$$

These two results are actually the same. For the liquid hydrogen target itself, the scattering probability is 13.6% (Equation H.18).

To make a first estimate of the scattering probability of neutrons from the Fe nuclei in the cryostat wall we assume the n-Fe elastic scattering to be isotropic for 8.9 MeV neutrons with the average differential cross section

$$\overline{\sigma_{el}(\theta)} = \frac{\sigma_{el}}{4\pi} = \frac{1.89}{4\pi} b/sr = 0.150 \ b/sr \ . \tag{H.36}$$

Again, the average n-Fe scattering angle for those scattered neutrons which are detected is approximately 0.25 radians in the lab system.

$$\sigma_t(0.25rad) = 3.8 \ b/sr \ . \tag{H.37}$$

Assume the ratio of the differential elastic scattering cross section to the differential total cross section is the same as that of the total elastic cross section to the total cross section, i.e.,

$$\frac{\sigma_{el}(\theta)}{\sigma_t(\theta)} = \frac{\sigma_{el}}{\sigma_t} \ . \tag{H.38}$$

Then we have

$$\sigma_{el}(0.25rad) = \sigma_t(\theta) * \frac{\sigma_{el}}{\sigma_t} = 2.2 \ b/sr \ , \tag{H.39}$$

therefore, the probability for neutron to be scattered from the wall and to hit one of the neutron detectors is approximately

$$\begin{aligned} P_{wall}^{sc\&hit} &= 4.86\% * 0.364\% * \frac{\sigma_{el}(0.25rad)}{\overline{\sigma_{el}(\theta)}} \\ &= 4.86\% * 0.364\% * \frac{2.2}{0.15} = 0.26\% \ , \end{aligned} \tag{H.40}$$

or more exactly:

$$P_{wall}^{sc\&hit} = 4.86\% * 0.364\% * \frac{\int_{all\,n\,det.} \sigma(\theta,\phi,E_n) * \sin\theta d\theta\, d\phi}{\int_{4\pi} \sigma(\theta,\phi,E_n) * \sin\theta d\theta\, d\phi} \ . \tag{H.41}$$

Please notice that 0.364% is the relative solid angle. It should be slight larger, because, generally speaking, the wall is closer to the neutron detector frame than the target. Hence,

$$\frac{P_{wall}^{hit}}{P_{ss}^{hit}} \doteq \frac{0.26\%}{13.2\%} = 2.0\% \ , \tag{H.42}$$

where P_{wall}^{hit} is the probability for neutrons hitting one of the neutron detectors due to elastic scattering inside the wall, while P_{wall}^{hit} is the probability for neutron hitting one of the neutron detectors due to single scattering. This is higher than the similar ratio for double scattering inside the target (1.47% for the hydrogen target).

Note: 0.364% * 2.2/0.15 = 5.5% . As an example from the Monte-Carlo simulation, 725 neutrons out of 13483 scattered in the wall were detected. The ratio is $\frac{725}{13483} = 5.4\%$ and this is approximately equal to 5.5%. In other words, if a 8.9 MeV neutron is scattered inside the wall, 5.4% of the scattered neutrons are going to hit one of the neutron detectors.

Now, let us take a look at the scattering angles for the $Fe(n,n)$ scattering. From the Monte-Carlo simulation:

$$\overline{\theta_{scatt}} = 0.492\, rad \tag{H.43}$$

based on 1489 data points.

From the numerical analysis code in ~/scott/dcs_nfe_test.c, we obtain

$$\frac{\oint_0^{\pi} \theta\sigma(\theta)\sin\theta d\theta}{\oint_0^{pi} \sigma(\theta)\sin\theta d\theta} = 0.48\ rad \ . \tag{H.44}$$

Some factors that are not mentioned are: (1). different transmission factors for direct neutrons and scattered neutrons, 2. different neutron detectors efficiencies for single scattering and double scattering.

For the estimates made in this section, data in [Lan68] were used. Now, we can summarize the strengths of several kinds of events:

1. strength of events from direct neutrons:

   Factors to be considered in this case are, (1) WC has a relative solid angle of 2.67%, (2) when γ moves at the WC, neutron has a probability of 13.2% to hit one of the neutron detectors, if there is no neutron scattering. As a result, the strength of such events is

   $$S0 = 2.67\% * 13.2\% = 0.35\% \ . \tag{H.45}$$

   If we want to consider the flux attenuation through the target, the wall and air (for example, assume a 25% attenuation coefficient) then

   $$S0 = 0.35\% * 0.75 = 0.26\% \ . \tag{H.46}$$

2. strength of events due to neutron scattering in the target system:

   This kind of events corresponding to a γ ray that moves towards the WC and is detected and the associated neutron is scattered inside the liquid target and hits a neutron detector. Factors to be considered in this case are (1) WC has a relative solid angle of 2.67%. (2) on the average, a neutron has a probability of 17% to be elastically scattered when going out of the target system (including both the liquid target and the stainless steel wall) (3) scattered neutron has a probability of approximately. 4 * 0.364% = 1.5% to hit one of the neutron detectors, where 0.364% is the relative solid angle of all neutron detectors. The strength of such events is then

   $$S1a = 2.67\% * 17\% * 1.5\% = 0.0068\% \ . \tag{H.47}$$

3. strength of events due to scattering case 2:

   Scattering case 2 is defined as the process in which a γ ray does not move towards the WC, but is Compton scattered and detected in the WC while the associated neutron is scattered and hits any one of the neutron detectors.

   To decide the strength for scattering case 2, let us consider the following factors: (1) WC has a relative solid angle of 2.67%, (2) probability for γ not to hit WC is 1-2.67% = 97.33%, (3) probability for γ to be Compton scattered is 0.5%, (4) probability for scattered γ to be detected is approximately. 2.67%, (5) probability for neutron to be scattered 17%, (6) probability for scattered neutron to hit a neutron detector is approximately. 0.364%. Therefore, the strength of events due to scattering case 2 is

$$\begin{aligned} S1b &= 97.33\% * 0.5\% * 2.67\% * 17\% * 0.364\% \\ &= 8.0 \times 10^{-8} \ . \end{aligned} \tag{H.48}$$

   Obviously,

$$S1b \ll S1a \tag{H.49}$$

H.3 Some Considerations for the Deuterium Target Simulations

In this section, we continue the comparison of simple estimates to the results of the MC simulations. The focus here will be on the deuterium target. For geometry parameters, please refer to section H.1. The discussion is based on the assumptions that: (1) a neutron is produced inside the target and the associated γ ray is detected by the WC, (2) the target is a point, (3) only one of the two outgoing neutrons from the $^2H(\pi^-, n\gamma)n$ reaction is considered for simplicity, (4) the target material is deuterium.

The possibility that a direct neutron from the $^2H(\pi^-, n\gamma)n$ reaction will hit a neutron detector is:

$$P_{dir}^{hit} = \frac{\int_{all\,n\,detectors} \sigma(\theta, E_n) * \sin\theta \, d\theta \, d\phi \, dE_n}{\int_{4\pi} \sigma(\theta, E_n) * \sin\theta \, d\theta \, d\phi \, dE_n} \; . \tag{H.50}$$

The $\sigma(\theta, E_n)$ is the double differential cross section for the $^2H(\pi^-, n\gamma)n$ reaction. The θ and E_n are the angle between the detected neutron and the γ ray and the energy of the neutron, respectively. To obtain a very rough estimate, we assume isotropic neutron production from the $^2H(\pi^-, n\gamma)n$ reaction. The probability of one of the neutrons hitting a neutron detector is then simply the relative solid angle of the neutron detector, 0.364%. A better estimate can be made by taking the ratio of the cross section at the mean opening angle to the angle-averaged cross section. To make this approximation, we use the MC simulation to determine the mean opening angle and the mean neutron energy.

From the simulation result we notice that the average opening angle between either neutron and the γ ray is not sensitive to the value of a_{nn}. For a_{nn} = -16 fm, the average opening angle between the γ and either neutron from the $^2H(\pi^-, n\gamma)n$ reaction is 2.35 radians. That is, for all the neutrons generated, $\overline{\theta_{3\_gen}} = \pi - 2.35 = 0.79\ rad.$ The 2.35 rad angle term was obtained from a data set of over 10,000 simulated events. The average angle between the γ ray and the neutrons that are detected in the simulation is 2.89 rad. The supplement of this opening angle is $\overline{\theta_{3\_det}} = \pi - 2.89 = 0.25(rad)$.

Because of the strong dependence of the cross sections on E_n, we checked that the neutron energies picked by the MC code were reasonable. From the simulation result with $a_{nn} = -16$ fm, the average E_n for the outgoing neutrons is 4.90 MeV. From the double differential cross sections given by theory (see Chapter 4), the average E_n is 4.905 MeV (for $a_{nn} = -16$ fm). The good agreement between the point-geometry theoretical cross sections and the results of the simulation verifies that the MC code is handling the finite geometry of

the experimental setup and the cross-section lookup correctly.

On the average, the probability for an unscattered neutron (with energy 4.90 MeV) to hit one of the neutron detectors is

$$\begin{aligned} P_{dir}^{hit} &= \Omega_{ndet}^{rel} * \frac{\sigma(\overline{\theta})}{\overline{\sigma(\theta)}} = \frac{\sigma(2.89rad)}{\overline{\sigma(\theta)}} * 0.364\% \\ &= \frac{0.10}{0.2149/(4\pi)} * 0.362\% = 2.13\% \end{aligned} \tag{H.51}$$

where σ refers to the differential cross sections for the $^2H(\pi^-, n\gamma)n$ reaction at the average E_n mentioned above. For a n-γ opening angle of 2.89 rad the differential cross section has a value of 0.10 mb/sr·MeV [4].

The mean differential cross section $\overline{\sigma(\theta)}$ is computed as the total cross section divided by 4π sr. The total cross section at E_n = 4.90 MeV is 0.2149 mb/MeV.

From the simulation, out of 5,407,000 neutrons generated with E_n between 0.3 and 20 MeV before tracing, 241480 were detected, 241500/5407000 = 4.47%. This is comparable to the number in Equation H.51 [5].

In the code, if E_n is not between 0.3 and 20 MeV, we simply do not trace the neutron. In some events one of the neutrons elastically scatters inside the target. The probability for a neutron to elastically scatter from the deuterium target is

$$P_{scatt}^{tard} = 1 - exp(-\sigma_t(E_n) * l * n_d) * \frac{\sigma_{el}}{\sigma_t}. \tag{H.52}$$

At low energies (E_n < 10 MeV) $\frac{\sigma_{el}}{\sigma_t} \doteq 1.0$ for the n-d reaction. In equation H.52, l is the distance an unscattered neutron travels before reaching the tar-

[4] Actually the unit is arbitrary because the maximum differential cross section is normalized to unity. We have the same situation when talking about the differential cross section for the $^2H(\pi^-, n\gamma)n$ reaction.

[5] Since the differential cross section for the $^2H(\pi^-, n\gamma)n$ reaction changes dramatically both in magnitude and in shape from E_n = 0.3 MeV to E_n = 20 MeV, we do not expect the estimate to be very accurate. Nevertheless, the order of magnitude is right.

get boundary, and n_d is the nuclei number density ($nuclei/cm^3$). For liquid deuterium, we have

$$n_d = \frac{\rho_{ld}}{A_d} * N_A = (0.156/2) * 6.022 * 10^{23} = 4.7 * 10^{22} cm^{-3} \ , \tag{H.53}$$

where ρ_{ld} is the density of the liquid deuterium and A_d is the atomic weight of deuterium, N_A is Avogadro's number. You may have noticed that n_d is the same as that in the case of the hydrogen target. The average E_n is

$$\overline{E_n} = 4.9 MeV \ , \tag{H.54}$$

and the total n-d cross section at the average E_n is

$$\sigma_t(\overline{E_n}) = 1.89 * 10^{-24} cm^2 \ . \tag{H.55}$$

Assume all neutrons are produced at the center of the target, i.e.,

$$l = \text{radius of the target} = 3.00 \ cm \ . \tag{H.56}$$

From Equation H.52 we have

$$P_{scatt}^{tard} = 1 - exp(-0.2665) = 1 - 0.766 = 0.234 \ , \tag{H.57}$$

where P_{scatt}^{tard} is the probability for a neutron to be scattered in the deuterium target. Thus, the probability for a neutron to be unscattered in the target is

$$P_{dir}^{tard} = 1 - P_{scatt}^{tard} = 0.766 \ , \tag{H.58}$$

where the subscript dir stands for the direct (or unscattered) neutrons. Hence the ratio of scattered neutrons to unscattered ones is:

$$\eta = \frac{\text{number of neutrons being scattered}}{\text{number of neutrons unscattered}} = \frac{P_{scatt}^{tard}}{P_{dir}^{tard}} = 30.5\% \ . \tag{H.59}$$

From the Monte-Carlo simulation, for E_n between 0.3 and 20 MeV, 205k neutrons were scattered in the deuterium target and 664k were unscattered, i.e.,

$$P_{scatt}^{tard} = 205/(205 + 664) = 0.236 \ . \tag{H.60}$$

This is almost the same as predicted in Equation H.57. Using this result we have

$$\eta = 205/664 = 30.9\% \ . \tag{H.61}$$

This is in good agreement with Equation H.59. The scattering probability in the target, P_{scatt}^{tard}, from the simulation could be slightly different from that predicted by Equation H.57. The reason for this possible difference is that the effective center of the target in the simulation can be slightly different from its physical center.

Now we consider scattered neutrons and compute the probability for a scattered neutron to hit one of the neutron detectors. We shall refer to this probability as P_{scatt}^{hit}. Again, if an isotropic neutron-deuteron (n-d) elastic scattering is assumed then

$$P_{scatt}^{hit} = \Omega_{ndet}^{rel} = 0.364\% \ . \tag{H.62}$$

For this result, we find that the ratio of the number of neutrons hitting the neutron detectors due to n-d elastic scattering inside the liquid target to that due to direct neutrons is

$$R_{dir}^{scatt} = \eta * \frac{P_{scatt}^{hit}}{P_{dir}^{hit}} = 0.305 * 0.364/2.13 = 5.2\%. \tag{H.63}$$

But there are other factors to consider. For example, n-d scattering is not isotropic in the laboratory system. A better estimate takes into account the anisotropy of the n-d scattering cross sections,

$$P_{scatt}^{hit} = \frac{\sigma_{lab}(\overline{\theta_{lab}})}{\overline{\sigma(\theta_{lab})}} * \Omega_{ndet}^{rel} \ . \tag{H.64}$$

The $\sigma_{lab}(\overline{\theta_{lab}})$ is the n-d elastic scattering cross section in the lab system at the mean E_n and the average lab scattering angle $\overline{\theta_{lab}}$. The Ω_{ndet}^{rel} is the relative solid angle of the neutron detector array.

Now we start to evaluate Equation H.64 for P_{scatt}^{hit} by using reasonable estimates of the relevant parameters. In the case of the hydrogen target the directions of the γ ray and the neutron from the $^1H(\pi^-, n)\gamma$ reaction are exactly opposite. However, this is no longer true in the case of the deuterium target. The direction distribution of the incident neutrons is much more complicated and estimating the $\overline{\theta_{lab}}$ is not trivial for the neutrons that are scattered from deuterons and detected by one of the neutron detectors. From the MC simulation,

$$\overline{\theta_{lab}} = 0.59\, rad\ . \tag{H.65}$$

This should be different from that in the hydrogen target because the initial neutron direction is different from that in the case of hydrogen target and the differential cross section for n-d scattering is different from that for n-p scattering. For $E_n\ = 4.0$ MeV (assume $\overline{\theta_{lab}}$ is 0.59 rad too) we have

$$\begin{aligned} \theta_{cm} &= \theta_{lab} + asin(\frac{m_n}{m_d} sin\theta_{lab}) \\ &= 0.59 + \arcsin(0.5 * \sin(0.59)) \\ &= 0.59 + 0.28 = 0.87\ rad\ , \end{aligned} \tag{H.66}$$

$$\sigma_{cm}(\theta_{cm}) = 0.194\, b/sr\ , \tag{H.67}$$

$$\begin{aligned} R_{dir}^{scatt} &= \eta\, \frac{P_{scatt}^{hit}}{P_{dir}^{hit}} = 5.2\% * \frac{\sigma_{lab}(0.59 rad)}{\overline{\sigma(\theta)}} \\ &= 5.2\% * \frac{0.38}{0.15} = 13.2\%\ , \end{aligned} \tag{H.68}$$

where 5.2% is the value for the ratio when assuming isotropic n-d scattering.

$$\begin{aligned}
\sigma_{lab}(\theta_{lab}) &= \sigma_{cm}(\theta_{cm}) * \frac{(1 + cos\theta_{cm} + (m_n/m_d)^2)^{3/2}}{1 + cos\theta_{cm} m_n/m_d} \\
&= \sigma_{cm}(\theta_{cm}) * \frac{(1 + 0.25 + \cos(\theta_{cm}))^{1.5}}{1 + 0.5\cos(\theta_{cm}))} \\
&= \frac{2.61}{1.32} * \sigma_{cm}(\theta_{cm}) = 1.98 * \sigma_{cm}(\theta_{cm}) \\
&= 1.98 * 0.194\, b/sr = 0.38\, b/sr \text{ with } \theta_{lab} = 0.59\, rad\ .
\end{aligned} \tag{H.69}$$

The average differential cross section for n-d scattering at $E_n = 4.0$ MeV is

$$\overline{\sigma(\theta)} = \frac{1.89}{4\pi} = 0.15\, b/sr\ , \tag{H.70}$$

therefore, the ratio of scattered neutron events to direct neutron events (remember, this ratio is 5.2%, if we assume n-d scattering is isotropic) is roughly:

$$R_{dir}^{scatt} = \eta\, \frac{P_{scatt}^{hit}}{P_{dir}^{hit}} = 5.2\% * \frac{\sigma_{lab}(0.59 rad)}{\overline{\sigma(\theta)}} = 5.2\% * \frac{0.38}{0.15} = 13.2\%\ . \tag{H.71}$$

This number seems too large. Again, we should use ratio of integrals for more precise results, i.e.,

$$\begin{aligned}
R_{dir}^{scatt} &= \eta\, \frac{P_{scatt}^{hit}}{P_{dir}^{hit}} \\
&= 5.2\% * \frac{\int\int \sigma_{lab}(\theta, E_n) d\theta d\phi dE_n \text{over the n det. array}}{\int\int \sigma_{lab}(\theta, E_n) d\theta d\phi dE_n \text{over the whole space}}\ .
\end{aligned} \tag{H.72}$$

The R_{dir}^{scatt} from the MC simulation is compared to the above estimates. From the MC simulation, we found that out of 2051321 neutrons being scattered in deuterium target, 13446 of them were detected, 13446/2051321 = 0.68%. This result is nearly a factor of two larger than the relative solid angle of the neutron detectors, 0.364%, indicating that the n-d cross section is enhanced in the direction of $\overline{\theta_{lab}}$. And this factor is approximately the same as the ratio of $\sigma(\overline{\theta_{lab}})$ to $\overline{\sigma(\theta)}$.

From the simulation, 65k scattered neutrons (by the deuterium target) and 1400k direct neutrons were detected, i.e.,

$$R_{dir}^{scatt} = 65/1400 = 4.6\% \ . \tag{H.73}$$

This indicate Equation H.71 is a very rough estimate for R_{dir}^{scatt}.

Now let us turn our attention to the cryostat wall. We will follow the same approach. The n-Fe cross sections are used to compute the relevant probabilities. The probability of a neutron elastically scattering from the stainless steel target container before being detected is calculated similarly to that for n-d scattering, by evaluating Equation H.57. The total cross section for n-Fe reactions at the mean neutron energy emitted from the ${}^2H(\pi^-, n\gamma)n$ reaction is

$$\sigma_t(4.0MeV) = 3.65b \ . \tag{H.74}$$

The angle-integrated elastic scattering cross section is

$$\sigma_{el}(4.0MeV) = 2.18b \ . \tag{H.75}$$

Both values are taken from tables in [Lan68]. For the iron wall of the cryostat, which has a thickness of 1/8" (i.e., 0.32 cm), the probability for neutrons to be elastically scattered P_{scatt}^{wall} is

$$\begin{aligned} P_{scatt}^{wall} &= 1 - exp(-l_{wall} * n(F_e) * 2.18 * \sigma_{el}(\overline{E_n})) \\ &= 1 - exp(-0.32 * n(F_e) * 2.18 * 10^{-24}) \ , \end{aligned} \tag{H.76}$$

where l_{wall} stands for the length of the neutron flight path in the wall and $n(Fe)$ is the number density of Fe nuclei in the wall. Using the nuclear number density from Equation H.33, we obtain

$$P_{scatt}^{wall} = 1 - exp(-0.0585)) = 5.7\% \ . \tag{H.77}$$

For the liquid target itself, this number is 23.4% (P_{scatt}^{tard}, see Equation H.57).

Next we compute the angle averaged cross section for the n-Fe scattering. For 4.0 MeV neutrons, using the similar approach to that used for n-d scattering, we get

$$\overline{\sigma_{el}(\theta)} = \frac{\sigma_{el}}{4\pi} = \frac{2.18}{4\pi}\, b/sr = 0.173\, b/sr \ . \tag{H.78}$$

For the $Fe(n,n)$ scattering, $\theta_{lab} \approx \theta_{cm}$, since Fe is 56 times heavier than the neutron. It follows that

$$\sigma_{lab}(\theta_{lab}) \approx \sigma_{cm}(\theta_{cm}) \ . \tag{H.79}$$

From the simulation, the average scattering angle for the scattered neutrons that are detected is 0.42 rad. Then we have

$$\sigma(\overline{\theta_{lab}}) = \sigma_{el}(0.42rad) = 1.15\, b/sr \tag{H.80}$$

for E_n = 4.0 MeV. So, the probability for the neutron that is scattered off the stainless steel wall to hit one of the neutron detectors (P^{hit}_{scatt}) is

$$\begin{aligned} P^{hit}_{scatt} &= \Omega^{rel}_{ndet} \frac{\sigma_{el}(0.42rad)}{\overline{\sigma_{el}(\theta)}} \\ &= 0.364\% * 1.15/0.173 = 2.42\% \ . \end{aligned} \tag{H.81}$$

The ratio of scattered neutrons (by the wall) to direct neutrons is

$$\eta = \frac{P^{wall}_{scatt}}{1 - P^{wall}_{scatt}} = 6.0\% \ . \tag{H.82}$$

Therefore, the ratio of the scattered neutron events (due to n-Fe scattering) to the direct neutron events is

$$R^{scatt}_{dir} = \eta \frac{P^{hit}_{scatt}}{P^{hit}_{dir}} = 6.0\% * 2.42\%/2.13 = 6.8\% \ . \tag{H.83}$$

From the Monte-Carlo simulation, out of 207k neutrons scattered by the iron wall, 33k of them are detected. This ratio ($33/207 = 1.6\%$) is comparable

to what we obtained in Equation H.81. In the same simulation, 1403k direct neutrons are detected. We then have

$$R_{dir}^{scatt} = 33/1403 = 2.4\% \ . \tag{H.84}$$

This is comparable to Equation H.83. You may have noticed that the quality of the estimates made for the ${}^2H(\pi^-, n\gamma)n$ reaction is much worse than that for the ${}^1H(\pi^-, n)\gamma$ reaction. The main reason is that the latter produces mono-energetic neutron and the relationship between the directions of the outgoing particles is very simple.

As we have seen the contribution of single scattering is less than 10%. It is reasonable to assume that the contribution of double scattering is one order of magnitude smaller than that of single scattering. Therefore, we can ignore the contributions from double scattering in the target system[6].

As a reminder, when we made the estimates above, we did not take into account the following factors: (1) different transmission factors for single scattered neutrons and double scattered neutrons, (2) different neutron detectors efficiencies for single scattered and double scattered neutrons.

[6]The target system includes the target itself and the target container.

Appendix I

Summary of deuterium runs in Exp1286

In Table I.1, we list the number of counts we obtained for each production run and the number of counts we lost due to different cuts in Exp1286. In the table, the symbol n_t stands for the total number of events for each run, n_e is the number of valid double events from the whole detection system after all the cuts we applied (see below for details), n_{tr} is the number of triple events for each run, n_1 is the number of lost events due to the requirement on the TOF spectrum (the NTOF channel number must be between 0 and 2200), n_2 is the number of lost events due to the requirement on the Pulse-Shape Discrimination (PSD) spectrum [1], n_3 is the number of lost events due to the requirement on the pulse-height spectrum (which must be higher than the preset threshold, in our case, it was set to be equivalent to one third Cs), n_4 is the number of lost events due to restrictions on E_γ [2], and n_5 is the number of lost events due to restrictions on the γ-ray positions (which must be in the effective area of the wire chamber). Since we did not include triples in the histograms for doubles, we have

$$n_t = n_e + n_{tr} + n_1 + n_2 + n_3 + n_4 + n_5 \tag{I.1}$$

(to be continued)

[1] The purpose of this is to supress the counts in the NTOF, γ_x, γ_y and θ_3 spectra caused by detection of γ rays in the neutron detectors.

[2] The γ-ray energy E_γ must be between 120 MeV and 159 MeV. This is equivalent to put restrictions on the relative energy of the outgoing neutrons from the $^2H(\pi^-, n\gamma)n$ reaction. This is necessary for the theory we cited in Chapter 3 to hold.

Table I.1: Summary of the deuterium runs in Exp1286, to be continued.

run#	n_t	n_v	n_{tr}	n_1	n_2	n_3	n_4	n_5
197	80292	32230	1931	6684	33362	4036	1855	194
198	77475	31161	1858	6378	32138	3849	1885	206
199	197651	70922	6034	17673	86691	9634	6213	484
200	181244	64046	5803	16373	79859	9101	5635	427
205	239455	81932	8147	21996	108067	11414	7332	567
206	199005	67411	6679	18432	90688	9417	5916	462
207	198066	66977	6792	18457	90139	9252	6005	444
208	260160	90060	8670	23936	116614	12371	7917	592
209	213818	76239	7094	19265	93239	10350	7107	524
210	206493	73728	6859	18623	90179	10184	6418	502
211	188626	68696	6166	16590	81504	9120	6101	449
212	96687	35767	3144	8627	40988	4691	3234	236
213	282762	100987	9318	25328	124690	13111	8685	643
214	262144	91010	8687	23936	118531	11964	7458	558
215	234685	82382	7617	21236	105054	10969	6904	523
216	156808	54580	5204	14209	70519	7368	4589	339
217	189922	66834	6113	17050	85157	8624	5697	447
218	174204	61134	5685	15859	78126	7847	5115	438
219	218641	75406	7023	19921	99452	9906	6390	543
220	169955	59565	5377	15429	76442	7671	5122	349
221	197648	68953	6574	18198	88791	8743	5949	440
222	232341	81192	7710	20833	104096	11104	6861	545
223	208000	72411	6850	19002	93199	9867	6177	494
224	176481	61255	5883	16147	79123	8402	5256	415
225	201318	70975	6745	18285	88997	9742	6134	440

run#	n_t	n_v	n_{tr}	n_1	n_2	n_3	n_4	n_5
226	225864	80967	7482	20107	98682	11050	7024	552
227	234507	84051	7774	21077	102215	11548	7274	568
228	153865	55679	4936	13804	66416	7760	4906	364
229	231252	83490	7410	20348	101381	10996	7130	497
230	103888	37459	3297	9314	45399	5054	3132	233
232	89446	32096	2864	7972	39162	4318	2820	214
234	226821	79707	7654	20713	100399	10658	7126	564
235	214939	75489	7231	19421	95678	9878	6749	493
236	236128	84021	7460	21236	105164	10807	6909	531
237	193570	68944	6325	17005	86208	8870	5731	487
238	192067	68395	6165	16929	85786	8707	5628	457
239	439226	157031	14130	38805	195167	19944	13074	1075
240	244782	89329	7709	21217	106992	11724	7221	590
241	197201	72131	6229	17220	86244	9067	5838	472
242	205624	74408	6663	17834	90452	9679	6075	513
243	184047	66734	5848	16245	80741	8525	5503	451
244	173897	63047	5469	15335	76463	7965	5162	456
245	180806	65580	5727	15615	79674	8234	5487	489
246	204992	74421	6431	17950	90114	9164	6395	517
247	186775	68390	5977	16451	81453	8345	5705	454
249	185333	67495	5908	16119	81373	8370	5570	498
250	180738	65843	5756	15681	78677	8740	5583	458
251	175375	63710	5558	15250	76630	8476	5291	460
252	176376	64071	5494	15348	77351	8511	5162	439
253	19364	7133	581	1766	8286	972	572	54
254	25883	9455	834	2293	11169	1295	774	63
255	133052	47928	4247	11535	59016	6093	3893	340
256	172992	62903	5490	14981	76388	7819	4969	442
257	177753	63792	5596	15765	79064	8115	5006	415
258	177663	63158	5684	15541	79569	8201	5066	444
259	194825	69402	6112	16908	87531	8728	5651	493
260	211999	75677	6802	18555	94355	9789	6315	506
261	220608	78961	7056	19117	97894	10690	6328	562
262	177466	63490	5844	15301	78612	8701	5054	464
263	178670	64039	5709	15696	78986	8602	5214	424
264	264541	94297	8696	23265	117033	12803	7803	644
265	176100	62441	5643	15302	78806	8367	5104	437

(to be continued)

run#	n_t	n_v	n_{tr}	n_1	n_2	n_3	n_4	n_5
266	208200	73658	6689	18464	93069	9940	5892	488
267	185430	65003	5983	16206	83726	8777	5253	482
268	182471	64417	5831	16213	81749	8535	5285	441
269	158948	56116	5111	13834	71099	7772	4624	392
270	176443	61326	5659	15697	79703	8591	5027	440
271	171629	59195	5745	15021	78204	8081	4978	405
275	173575	59673	5727	15347	79807	7932	4680	409
276	189932	64193	6333	16963	88201	8707	5068	467
277	177013	59971	5784	15868	81932	8184	4814	460
296	198603	70335	6570	17276	88571	9305	5973	573
297	174575	59927	5720	15411	80259	7927	4895	436
298	232188	80613	7516	20420	105874	10615	6569	581
299	182205	63488	5838	15900	83243	8237	5026	473
300	185152	62380	6100	16650	86197	8155	5233	437
302	170981	60082	5501	14880	77762	7517	4804	435
303	191623	67767	5962	16556	86777	8563	5495	503

Bibliography

[Aar65] R. Aaron, R. D. Amado, and Y. Y. Yam. *Calculations of Neutron-Deuteron Scattering.* Physical Review, **140**(1965) B1291–B1300.

[Abe86] R. Abegg, D. Bandyopadhyay, et al. *Test of Charge Symmetry in Neutron-Proton Elastic Scattering at 477 MeV.* Physical Review Letters, **56**(1986) 2571.

[Ald79] J. C. Alder et al. *A High-resolution Pair Spectrometer for Medium Energy Photons.* Nuclear Instrument and Methods, **A160**(1979) 93–114.

[All76] L. J. Allen, T. A. Rijken, and J. J. Fiedeldey. *Charge Symmetry as an Off-Shell Constraint on the Nuclear Force for Finite Range Transformation.* Nuclear Physics, **A260**(1976) 213–225.

[Arn73] R. A. Arndt, J. Binstock, and R. Bryan. *Nucleon-Nucleon Scattering Near 50 MeV. I. Phase-Shift Analysis of the Data.* Physical Review, **D8**(1973) 1397–1408.

[Arn87] R. A. Arndt, J. S. Hyslop III, and L. D. Roper. *Nucleon-Nucleon Parital-Wave Anslysis to 1100 MeV.* Physical Review, **D35**(1987) 128–144.

[Bae81] H. W. Baer et al. *Design, Construction, and Performance of a Hight-Resolution π^0 Spectrometer for Nuclear Physics Experiments.* Nuclear Instrument and Methods, **180**(1981) 445–449.

[Ban64] M. Bander. *Low-energy Neutron-neutron Scattering Parameters.* Physical Review, **134**(1964) B1052–B1058.

[Bar66] A. C . L. Barnard, J. B. Swint, and T. B. Clegg. *Cross Sections as a Function of Angle and Complex Phase Shifts for the Scattering of*

Protons from ^{12}C. Nuclear Physics, **86**(1966) 130–144.

[Bet64] H. Bethe et al. *Meson Factories–A Report of the Ad Hoc Panel to the U.S. Office of Science and Technology (USA)*, 1964.

[Bev69] P. R. Bevington. *Data Reduction and Error Analysis for the Physical Sciences*. McGraw-Hill Book Company, 1969.

[Bic] Bicron Corporation, 12345 Kinsman Road, Newbury, OH 44065.

[Big61] J. A. Biggerstaff, R. L. Becker, and M. T. McEllistrem. *Charged Particle Discrimination in a CsI(Tl) Detector*. Nuclear Instruments and Methods, **10**(1961) 327–332.

[Bin74] J. Binstock and R. Bryan. *Nucleon-Nucleon Scattering Near 50 MeV. II. Sensitivity of Various n-p Observables to Phase Parameters*. Physical Review, **D9**(1974) 2528–2538.

[Bla79] J. M. Blatt and V. F. Weisskopf. *Theoretical Nuclear Physics*. Dover Publications, Inc., 1979.

[Bra97] 1997. R. T. Braun, Private communication.

[Bri71] D. M. Brink and G. R. Satchler. *Angular Momentum*. Oxford University Press, second edition, 1971.

[Bug85] D. V. Bugg. *Nucleon-Nucleon Physics up to 1 GeV*. Annual Review in Nuclear and Particle Sciences, **35**(1985) 295–320.

[Cam74] H. S. Camarda. *P-wave Neutron Strength-Function Measurements and the Low-Energy Optical Potential*. Physical Review, **C9**(1974) 28–37.

[Che50] G. F. Chew and M. L. Goldberger. *The Production of Fast Deuterons in High Energy Nuclear Reactions*. Physical Review, **77**(1950) 470.

[Che57a] G. F. Chew, M. L. Goldberger, F. E. Low, and Y. Nambu. *Applications of Dispersion Relations to Low-Energy Meson-Nucleon Scattering*. Physical Review, **106**(1957) 1337.

[Che57b] G. F. Chew, M. L. Goldberger, F. E. Low, and Y. Nambu. *Relativistic Dispersion Relation Approach to Photomeson Production.* Physical Review, **106**(1957) 1345.

[Che59] G. F. Chew and F. E. Low. *Calculations of Neutron-Deuteron Scattering.* Physical Review, **113**(1959) 1640.

[Che85] W. Cheney and D. Kincaid. *Numerical Mathematics and Computering.* Brooks/Cole Publishing Company, 2nd edition, 1985.

[Che87] Z. Chen. *Neutron Attenuation Measurements for Shielding Materials.* Measurements made with the TUNL neutron time-of-flight group, 1987.

[Coo87] S. A. Coon and R. C. Barrett. *$\rho-\omega$ Mixing in Nuclear Charge Asymmetry.* Physical Review C, **36**(1987) 2189.

[Cub89] J. Cub, E. Finckh, K. Gebhardt, K. Geissdörfer, R. Lin, and J. Strate. *The Neutron Detection Efficiency of NE213 Detectors measured by Means of a ^{252}Cf source.* Nuclear Instruments and Methods in Physics Research, **A274**(1989) 217–221.

[Die78] G. Dietze. *SPEKT - A Dialog Program for Multichannel Spectra Analysis.* Technical Report PTB-ND-13, Physikalisch-Technische Bundesanstalt, Bundesallee 100, W-3300 Braunschweig, 1978.

[Die82a] G. Dietze and H. Klein. *Gamma-Calibration of NE213 scintillator counters.* Nuclear Instruments and Methods in Physics Research, **A194**(1982).

[Die82b] G. Dietze and H. Klein. *NRESP4 and NEFF4 Monte Carlo Codes for the Calculation of Neutron Response Functions and Detection Efficiencies for NE 213 Scintillation Detectors.* Technical Report PTB-ND-22, Physikalisch-Technische Bundesanstalt, Bundesallee 100, W-3300 Braunschweig, 1982.

[Dro78] M. Drosg. *Unified Absolute Differential Cross Sections for Neutron Production by the Hydrogen Isotopes for Charge-Particle Energies Between 6 and 17 MeV.* Nuclear Science and Engineering, **67**(1978) 190–220.

[Eas73] R. J. Eastgate, W. J. Thompson, and R. A. Hardekopf. *A Nuclear Optical Model Code for Small Computers.* Computer Physics Communications, **5**(1973) 69–79.

[Eri91] T. E. O. Ericson, V. W. Hughes, and D. E. Nagle. *The Meson Factories.* University of California Press, 1991.

[Fad61] L. D. Faddeev. *Scattering Theory for a Three-Particle System.* Journal of Experimental and Theoretical Physics (U.S.S.R.), **12**(1961) 1014–1019.

[Fin87] E. Finckh, K. Geissdörfer, R. Lin, S. Schindler, and J. Strate. *Method for Data Analysis of Three Particle Experiments by Monte Carlo Simulation.* Nuclear Instruments and Methods in Physics Research, **A262**(1987) 441–443.

[Fit86] D. H. Fitzgerald et al. *Forward Angle Cross Sections for Pion-nucleon charge exchange between 100 and 150 MeV/c.* Physical Review C, **34**(1986) 619–626.

[Fra83] J. S. Frank et al. *Measurement of Low-Energy Elastic $\pi^{\pm}p$ Differential Cross Sections.* Physical Review, **D28**(1983) 1569–1585.

[Ful73] R. L. Fulton. *Mechanic Design of the LAMPF Low-Energy Pion Channel.* LA-5222-MS, Informal Report UC 34 & 38, LAMPF, Los Alamos, Nex Mexico 87544, 1973.

[Gab79] B. Gabioud et al. *n-n Scattering Length from the Photon Spectra of the Reactions $\pi^- d \to nn\gamma$ and $\pi^- p \to \gamma n$.* Physical Review Letters, **42**(1979) B1508–B1511.

[Gab81] B. Gabioud et al. *n-n Effective Range from the photon spectrum of the Reactions $\pi^- d \to nn\gamma$.* Physics Letters, **103B**(1981) 9–12.

[Gab84] B. Gabioud, J.-C. Adler, C. Joseph, J.-F. Loude, N. Morel, A. Perrenoud, J.-P. Perroud, M. T. Tran, E. Winkelmann, W. Dahme, H. Panke, D. Renker, G. Strassner, P. Truöl, and G.F. de Téramond. *nn Scattering Parameters a_{nn} and r_{nn} from the Photon Spectrum of the Reaction $\pi^- d \to nn\gamma$.* Nuclear Physics, **A420**(1984) 496–524.

[Gar90] H. Garcilazo and T. Mizutani. *πNN Systems.* World Scientific, 1990.

[Gib75a] W. R. Gibbs, B. F. Gibson, and G.J. Sephenson Jr. *Erratum: Extraction of a_{nn} from the reaction $\pi^- d \to nn\gamma$.* Physical Review, **C12**(1975) 2130.

[Gib75b] W. R. Gibbs, B. F. Gibson, and G.J. Sephenson Jr. *Extraction of a_{nn} from the reaction $\pi^- d \to nn\gamma$.* Physical Review, **C11**(1975) 90–99.

[Gib77] W. R. Gibbs, B. F. Gibson, and G.J. Sephenson Jr. *Threshold charged-pion photoproduction and radiative pion capture II. $\pi^- d \to nn\gamma$.* Physical Review, **C16**(1977) 327–332.

[Gib78] W. R. Gibbs, B. F. Gibson, and G.J. Sephenson Jr. *Erratum: Threshold charged-pion photoproduction and radiative pion capture II. $\pi^- d \to nn\gamma$.* Physical Review, **C17**(1978) 856.

[Gib97] 1997. B. F. Gibson, Private communication.

[Gla85] D. N. Glasgow et al. *Radiative Pion Capture II. $\pi^- d \to nn\gamma$.* Rad. Effects, **92**(1985) 913.

[Glö96] W. Glöckle, H. Witała, D. Hüber, and J. Golack. *The Three-Nucleon Continuum: Achievements, Challenges and Applications.* Physics Reports, **274**(1996) 107–286.

[Gon98] D. E. González Trotter. *Extraction of the $^1S_0$ Neutron- Neutron Scattering Length From A Kinematically complete n-d Breakup Experiment.* Ph.D. thesis, Duke University, 1998.

[Haa86] D. G. Haase, C. R. Gould, and W. L. Seagondollar. *A Brute Force Polarized Target for Neutron Scattering Experiments.* Nuclear Instruments and Methods, **A243**(1986) 305–311.

[Had65] R. P. Haddock et al. *Measurement of the Neutron-neutron S-wave Scattering Length from the Raaction $\pi^- d \to nn\gamma$.* Physical Review Letters, **14**(1965) 318–323.

[Hen69] E. M. Henley. *Charge Independence and Charge Symmetry of Nuclear Forces.* In D. H. Wilkinson, editor, *Isospin in Nuclear Physics*, chapter 2, pages 17–72. North Holland Physics Publishing, 1000 AC Amsterdam, The Netherlands, 1969.

[Hol85] L. Holm, H. W. Fielding, and G. C. Neilson. *Gain Stabilization of Phototubes Using a LED Diode Scheme.* Nuclear Instrument and Methods, **A324**(1985) 518–520.

[Hus92] 1992. A. H. Hussein and others, LAMPF proposal #1286.

[Knu71] D. E. Knuth. *The Art of Computer Programming*, volume 2. Addison-Wesleyohn Publishing Company, Inc., 1971.

[Knu90] L. Knutsen et al. *A Test of Charge Symmetry in n-p Scattering at E_n = 183 MeV.* Nuclear Physics A, **508**(1990) 185c.

[Kra86] K. S. Krane. *Nuclear Orientation Formalism.* In N. J. Stone and H. Postma, editors, *Low-Temperature Orientation*, chapter 2, pages 31–112. North Holland Physics Publishing, 1000 AC Amsterdam, The Netherlands, 1986.

[Kra88] K. S. Krane. *Introductory Nuclear Physics.* John Wiley & Sons, Inc., 1988.

[Kre69] M. Krell and T. E. O. Ericson. *Energy Levels and Wave Functions of Pionic Atoms.* Nuclear Physics, **B11**(1969) 521.

[Lac80] M. Lacombe, B. Loiseau, J. M. Richard, and R. Vinh Mau. *Parametrization of the Paris N-N Potential.* Physical Review, **C21**(1980) 861–873.

[Lan68] I. Langner, J. J. Schmidt, and D. Woll. *Tables of evaluated neutron cross sections for fast reactor materials.* Gesellschaft Für Kernforschung M.B.H, Karlsruhe, 1968.

[LB85] S. I. Eidelman B. I. Khazin M. Yu. Lelchuk V. S. Okhapkin E. V. Pakahtusova S. I. Redin N. M. Ryskulov Yu. M. Shatunov A. I. Shekhtman B. A. Shwartz V. A. Sidorov A. N. Skrinsky V. P. Smakhtin L.M. Barkov, A. G. Chilingarov and E. P. Solodov. *Electromagnetic Form Factor in the Timelike Region.* Nuclear Physics, **B256**(1985) 365–384.

[Leo71] M. Leon. *Parametrization of the Paris N-N Potential.* Physics Letter, **37B**(1971) 87.

[Leo94] W.R. Leo. *Techniques for Nuclear and Particle Physics Experiments.* Springer-Verlag, 1994.

[Mac87] R. Machleidt, K. Holinde, and Ch. Elster. *The Bonn Meson-Exchange Model for the Nucleon-Nucleon Interaction.* Physics Reports, **149**(1987) 1–89.

[McL88] V. McLane, C. L. Dunford, and P. F. Rose. *Neutron Cross Section Curves*, volume 2. Academic Press, Boston, MA, 1988.

[McV61] K. W. McVoy. *Neutron-Neutron Scattering Length.* Physical Review, **121**(1961) 1401–1410.

[Men] F. S. Meneses. Ph.D. thesis.

[Mes61] A. Messiah. *Quantum Mechanics*, volume 1. North-Holland Puslishing Co., Amsterdan, 1961.

[Mil90] G. A. Miller, B. M. K. Nefkens, and I. Slaus. *Charge Symmetry, Quarks and Mesons.* Physics Reports, **194**(1990) 1–116.

[Mon68] T. R. Mongan. *Separable-Potential Fits to Neutron-Neutron Scattering Data.* Physical Review, **175**(1968) 1260.

[Mon69] T. R. Mongan. *Separable-Potential Models of the Nucleon-Nucleon Interaction.* Physical Review, **178**(1969) 1597.

[Mug84] S. F. Mughabghab. *Neutron Cross Sections*, volume 1. Academic Press, Inc., Orlando, FL 32887, 1984.

[Nag78] M. M. Nagels, T. A. Rijken, and J. J. de Swart. *Low-Energy Nucleon-Nucleon Potential from Regge-Pole Theory.* Physical Review, **D17**(1978) 768–776.

[Ngu95] L. P. Nguyen. *π^- -p $\rightarrow$ π^0 n Cross Sections in the Region of the $\triangle$(1232) Resonance.* Ph.D. thesis, University of Maryland, 1995.

[Nol69] J. A. Nolen and J. P. Schiffer Jr. *Coulomb Energies.* Annual Review of Nuclear Science, **19**(1969) 471–526.

[Nov93] Jan K. Novak et al. *Experiment 1286 Liquid Hydrogen Target Hazard Management Plan.* Technical Report MP-SOP-1043.00, Los Alamos National Lab., Los Alamos, New Mexico, 1993.

[One78] Y. Onel, R. C. Brown, J. A. Edington, N. M. Stewart, and I. M. Blair. Nuclear Physics, **A304**(1978) 51.

[Ped78] E. Pedroni. *A Study of Charge Independence and Symmetry from π^+ and π^- Total Cross Sections on Hydrogen and Deuterium near the 3,3 Resonance.* Nuclear Physics, **A300**(1978) 321–347.

[Ped86] R. S. Pedroni. *Cross Sections and Analyzing Powers in the 8- to 17-MeV Range for Neutron Scattering from $^{54,56}Fe$ $^{58,60}Ni$ ^{93}Nb and ^{120}Sn.* Ph.D. thesis, Duke University, 1986.

[Phi54] R. H. Phillips and K. M. Crowe. *An Indirect Measurement of the n-n Interaction.* Physical Review, **96**(1954) 484.

[Pic71] H. S. Picker, E. F. Redish, and Jr. G. J. Stephenson. *Two-Nucleon T Matrix Half Off the Energy Shell: A Direct Approach.* Physical Review C, **4**(1971) 287.

[Pic73] H. S. Picker and E. F. Redish. *Remarks on Wave-Function Models of the Half-Shell T Matrix for Two Nucleons.* Physical Review C, **8**(1973) 2495.

[Pre92] W. H. Press, S. A. Teukolsky, W. T. Vetterling, and B. P. Flannery. *Numerical Recipes in* FORTRAN*: The Art of Scientific Computing.* Cambridge University Press, second edition, 1992.

[Rei68] R. V. Reid, Jr. *Local Phenomenological Nucleon-Nucleon Potentials.* Annals of Physics, **50**(1968) 411–448.

[Ros69] L. Rosen. *The Los Alamos Meson Factory.* Science Journal, **5A**(1969) 2–8.

[RS92] M. W. Rawool-Sullivan et al. *A New Multiplexing Scheme for Cathode-Strip Readout Chambers.* Nuclear Instrument and Methods, **A311**(1992) 168.

[Sal75] R. W. Salter, Jr., R. P. Haddock, M. Zeller, D. R. Nygren, and J. B.

Czirr. *The n-n S-wave Scattering Length from the Neutron Spectra of the reaction $\pi^- d \to nn\gamma$* . Nuclear Physics, **A254**(1975) 241–268.

[Sat76] H. Sato. *On the Coulomb Displacement Energy.* Nuclear Physics, **A269**(1976) 378–396.

[Sat83] G. R. Satchler. *Direct Nuclear Reactions.* Oxford University Press, 1983.

[Sch87] O. Schori, B. Gabioud, C. Joseph, J.-P. Perroud, D. Rüegger, M. T. Tran, P. Truöl, E. Winkelmann, and W. Dahme. *Measurement of the neutron-neutron scattering length a_{nn} with the reaction $\pi^- d \to nn\gamma$ in complete kinematics.* Physical Review C, **35**(1987) 2252–2257.

[Set95] H. R. Setze. *Differential Cross Section for the Neutron-Induced Deuteron Breakup Reaction at $E_n = 13.0$ MeV.* Ph.D. thesis, Duke University, 1995.

[Shk73] G. M. Shklyarevskii. *Determination of the Neutron-Neutron Scattering Length from the reaction $\pi^- d \to nn\gamma$* . Soviet Journal of Nuclear Physics, **16**(1973) 700.

[Sla82] I. Slaus, Y. Akaishi, and H. Tanaka. *Three Body Forces and Neutron-Neutron Effective Range Parameters.* Physical Review Letters, **48**(1982) 993–996.

[Sla89] I. Slaus, Y. Akaishi, and H. Tanaka. *Neutron-Neutron Effective Range Parameters.* Physics Reports, **173**(1989) 257–300.

[Sot76] M. Sotana and E. Truhlik. *Radiaive Capture of Negative Pions in Deuterium.* Nuclear Physics, **A262**(1976) 400–412.

[Tab] F. Tabakin.

[Tak51] M. Taketani, S. Nakamura, and M. Sasaki. *On the Method of the Theory of Nuclear Forces.* Progress of Theoretical Physics, **VI**(1951) 1000.

[Tér77] G. F. de Téramond. *Final State Interactions and Neutron-neutron Scattering Parameters.* Physical Review C, **16**(1977) 1976–1983.

[Tér80] G. F. de Téramond, J. Páez, and C.W. Soto Vargas. *Off-Shell Rescattering Effects in the reaction $\pi^- d \rightarrow nn\gamma$.* Physical Review C, **21**(1980) 2542–2546.

[Tér87] G. F. de Téramond and B. Gabioud. *Charge Asymmetry of the Nuclear Interaction and Neutron-Neutron Scattering Parameters.* Physical Review C, **36**(1987) 691–701.

[Tér89] G. F. de Téramond. *Charge Symmetry of the Nuclear Interaction and the N-N Scattering Parameters.* In *Proc. Workshop on Spin and Symmetries*, volume TRI-89-5, pages 235–244, 1989.

[Tho] A. W. Thomos.

[Tho84] W. J. Thompson. *Computing in Applied Science.* John Wiley and Sons, 1984.

[Tic92] M. Tichy, H. Klein, and J. Pulpan. *Calibration of an NE-213 Scintillator.* Technical Report PTB-7.2-92-1, Physikalisch-Technische Bundesanstalt, Bundesallee 100, W-3300 Braunschweig, 1992.

[Tor] W. Tornow, Private communication.

[Tor75] W. Tornow, H. Spiegelhauer, and G. Mack. *Simulation of a Double-Scattering Polarization Experiment with Fast Neutrons by Means of Monte Carlo Calculations.* Nuclear Instrument and Methods, **125**(1975) 373–389.

[Tor96] W. Tornow, H. Witala, and R. T. Braun. *Determinations of the Neutron-Neutron Scattering Length from Kinematically Incomplete Neutron-Deuteron Breakup Experiments.* Few Body Systems, **21**(1996) 97–130.

[Tra79] M. T. Tran et al. *Differential Cross Sections for Radiative Capture of Pions on Hydrogen in the $\delta(1232)$ Region: A test of the isospin structure and t-symmetry of hadronic electromagnetic interactions.* Nuclear Physics, **A324**(1979) 301–334.

[Tsa74] Yung-Su Tsai. *Pair Production of Bremsstrahlung of Charged Leptons.* Review of Modern Physics, **46**(1974) 815.

[Wat51] K. M. Watson and R. N. Stuart. *On the γ -Ray Spectrum Resulting from the Absorption of π-mesons in Deuterium.* Physical Review, **82**(1951) 738.

[Wat52] K. M. Watson. *The Effect of Final State Interactions on Reaction Cross Sections.* Physical Review, **88**(1952) 1163.

[Whi91] C. A. Whitton, Jr. *Correction Procedures for Variable Intensity Neutron Time-of-flight Measurements.* Nuclear Instrument and Methods, **A309**(1991) 264–274.

[Wil72] D. H. Wilkinson. *Some Experimental Aspects of Symmetries.* In Ivo Slaus et al., editors, *Few Particle Problems in the Nuclear Interaction*, pages 191–220. North Holland / American Elsevier, 1972.

[Wil87] A. G. Williams, A. W. Thomas, and G. A. Miller. *Charge Symmetry Breaking in Neutron-proton Elastic Scattering.* Physical Review C, **36**(1987) 1956–1967.

[Wit88] H. Witała, W. Glöckle, and Th. Cornelius. *Nucleon-induced deuteron breakup: Analysis of 14.1 MeV data by rigorous Faddeev calculations with meson-exchange NN interactions.* Physical Review C, **39**(1988) 384.

[Wit96] H. Witała, D. Hüber, W. Glöckle, W. Tornow, and D. E. González Trotter. *Extraction of the Neutron-Neutron Scattering Length a_{nn} from Kinematically Complete Neutron-Deuteron Breakup Experiments.* Few Body Physics, **20**(1996) 81–92.

[Yam54] Y. Yamaguchi. *Two-Nucleon Problem When the Potential Is Nonlocal but Separable. I.* Physical Review, **95**(1954) 1628.

[Zei74] B. Zeitnitz. *Neutron-Neutron Effective Range Parameters from Kinematically Complete Experiments on the Reaction $^2H(n,2n)^1H$.* Nuclear Physics, **A231**(1974) 13–28.

Biography

Name:	Qiankun Chen
Born:	Hunan Province, P.R.China
	October 1, 1963
Education:	B.S. Tsinghua University, Beijing, China, 1984
	M.S. Tsinghua University, Beijing, China, 1987
	M.A. Duke University, Durham, North Carolina, 1995
Positions:	Research Assistant, Duke University, 1994-1997
	Teaching Assistant, Duke University, 1992-1994
	Lecturer, Tsinghua University, 1990-1992
	Assistant Professor, Tsinghua University, 1987-1990
Memberships:	American Physical Society

PUBLICATIONS:

1. W. Tornow, C.R.Howell, R.T. Braun, Q. Chen, D.E.Gonzalez Trotter, C.D. Roper, F. Salinas, H.R. Setze, R.L. Walter and H. Witala *Selected Topics of the Few-Nucleon Research Program at TUNL*, Few Body Systems Supplementum **8**, p161, 1995

2. Huiquan Qi, Hongbin Chen, Yingtang Chen, Qiankun Chen, Zhenpeng Chen and Zemin Chen *Small Angle Scattering Cross Sections of 14.8 MeV Neutrons for Iron, Nickel and Chromium*, Nuclear Science and Engineering, **111**, No.3, p309, 1992

3. Huiquan Qi, Yingtang Chen, Qiankun Chen, Zhenpeng Chen and Zemin Chen *Fast Neutron Scattering Cross Section at Small Angles and Optical Model Parameters*, Physical Review C, **48**, No.4, p1779, 1993

4. H. Qi, Y. Chen, Z. Chen, Z. Chen, Q. Chen and H. Li *Small angle scattering cross sections of 14.7 MeV neutrons for U-238*, *Proceedings of the international conference on nuclear data for science and technology*, Mito, Japan, 1988, p799

5. Qi Huiquan, Chen Guojie, Chen Yingtang, Chen Qiankun, Chen Zhenpeng, Chen Zemin *The Small Angle Scattering Cross Section of 14.8 MeV Neutrons from Al-27 and O-16*, Chinese Journal of Nuclear Physcis, **14**, p15, 1992,

6. Qi Huiquan, Chen Qiankun, Chen Yingtang, Chen Hongbin, Chen Zhenpeng, Deng Jingkang, Chen Zemin, Tang Hongqing and Qi Bujia *Small Angle Scattering Cross Section of 12 MeV Neutrons from U-238 and and Fe*, Chinese Journal of Nuclear Physics, **13**, p343, 1991,

7. H. Qi, Y. Liu, Z. Chen, Z. Wu, W. Wang, Q. Chen and G. Xu *Measurements of neutron scattering cross sections at small angles*, INDC [3] (CPR)-006/L, 1985,

8. H. Qi, Y. Liu, Z. Chen, Z. Wu, W. Wang, Q. Chen and G. Xu *Study on position-sensitive neutron detection system*, INDC(CPR)-005/G, 1985

CONFERENCE REPORT:

1. Q. Chen, C.R. Howell, C.D. Roper, F. Salinas, H.R. Setze, W. Tornow, R.L. Walter *Results of the LAMPF neutron-neutron scattering length experiment* Bulletin of American Physics Society, **42**, p936, 1997

[3]INDC: International Nuclear Data Center

2. F. Salinas, C.R. Howell, W. Tornow, D.E. Gonzalez Trotter, T.S. Carman, Q. Chen, C.D. Roper, H.R. Setze, R.L. Walter *The TUNL(Triangle Universities Nuclear Laboratory) neutron-proton scattering length experiment*, Bulletin of American Physics Society, **40**, p1045, 1995

3. D.E. Gonzalez Trotter, W. Tornow, C.R. Howell, F. Salinas, T.S. Carman, Q. Chen, C.D. Roper, H.R. Setze, R.L. Walter *The TUNL(Triangle Universities Nuclear Laboratory) neutron-neutron scattering length experiment*, Bulletin of American Physics Society, **40**, p1045, 1995

4. T.S. Carman, Q. Chen, C.R. Howell, C.D. Roper, F. Salinas, I. Slaus, W. Tornow, R.L. Walter *The neutron-neutron scattering length using 2H(pion, n n gamma) reaction: LAMPF(Los Alamos Meson Physics Facility) E1286 (Experiment 1286)* Bulletin of American Physics Society, **40**, p1629, 1995

5. R.T. Braun, W. Tornow, Q. Chen, D.E. Gonzalez Trotter, C.R. Howell, C.D. Roper, F. Salinas, H.R. Setze, R.L. Walter *Neutron-Proton Analyzing Power at 12 MeV and pion-nucleon-nucleon coupling constant* Bulletin of American Physics Society, **39**, p1007, 1994